

# **The Physics of High-Velocity Ions in the Hall Thruster Near-Field**

Thesis by  
Regina Sullivan

In Partial Fulfillment of the Requirements  
for the Degree of  
Doctor of Philosophy

California Institute of Technology  
Pasadena, California

2010  
(Defended March 3, 2010)



Dedicated to my parents and my brother, for their unconditional love and support.



# Acknowledgements

I would like to take the opportunity to thank the following individuals:

- Jan, Pat, and Owen Sullivan, the *sine qua non* of my life and academic career. (Thanks for always being there to answer the phone at 3 am!)
- Lee Johnson, my mentor for the past 7 and 1/2 years and my PhD advisor at JPL, for teaching me how to be a good researcher, for always showing great patience with my non-so-well-thought-out questions, and also for helping me learn many valuable life skills (motorcycle riding, guitar playing, etc.).
- Joseph Shepherd, my PhD advisor, for his academic, research, and career advice, and for giving me a crash course in numerical methods for solving differential equations.
- David Conroy, my officemate, for providing good advice, good music, and good conversation.
- Michelle Scharfe, for her invaluable assistance with modeling, for writing some code for me, and for being really nice to me the first summer I interned at JPL.
- Yiangos Mikellides, for helping me develop my sheath model, and for figuring out a way to implement those pesky boundary conditions.
- Rich Hofer, for providing me with the HPHall code and answering my many questions about it.
- Ray Swindlehurst and Al Owens, for helping me in the machine shop.
- Paul Bellan and Dale Pullin, for taking time out of their undoubtedly busy schedules to serve on both my candidacy and thesis defense committees.
- My ice hockey teammates, for helping to keep me sane.

I would also like to thank the following programs/institutions for funding my research:

- National Science Foundation Graduate Research Fellowship Program
- Air Force Research Laboratory
- California Institute of Technology

# Abstract

A study of the physics underlying high velocity ion trajectories within the near-field region of a Hall thruster plume is presented. In this context, “high velocity” ions are ions that have been accelerated through the full potential drop of the thruster (sometimes referred to as “primary energy” or “primary beam energy” ions). Results from an experimental survey of an SPT-70 thruster plume are shown, along with simulated data from a Hall thruster code and from a plasma sheath model. Two main features are examined: the central jet along the Hall thruster centerline, and the population of high velocity ions at high angles.

In the experimental portion of the investigation, three diagnostic instruments were employed: (1) a Faraday probe for measuring ion current density, (2) an ExB velocity filter for mapping ions with the primary beam energy, and (3) a Retarding Potential Analyzer (RPA) for determining ion energy distributions. In the numerical portion, two codes were employed: (1) a hybrid-PIC Hall thruster code known as HPHall, and (2) a model of the plasma sheath near the exit plane of the thruster, which was developed by the author.

A comparison between the measured and simulated data sets is made, to analyze the degree to which different mechanisms are responsible for the evolution of the thruster plume in the near-field region. This analysis shows that the central jet is both a function of symmetric expansion of the ion beam as well as asymmetry in the internal potential field of the thruster. Additionally, it is suggested that high energy, high angle ions could be generated given a specific internal electric field configuration, while oscillations are ruled out as the cause of these ions. The results from the sheath model show that while the sheath can change trajectory angles by 10 to 20 degrees, it can not fully explain the presence of high angle ions with high energies.



# Contents

<b>Acknowledgements</b>	<b>v</b>
<b>Abstract</b>	<b>vii</b>
<b>Nomenclature/Symbols</b>	<b>xxii</b>
<b>1 Introduction</b>	<b>1</b>
1.1 Hall Thruster Overview . . . . .	1
1.2 Previous Research . . . . .	4
1.3 Motivation . . . . .	4
1.4 Problem Statement and Approach . . . . .	5
<b>2 Experimental Method</b>	<b>7</b>
2.1 SPT-70 Thruster . . . . .	7
2.2 Vacuum Facility . . . . .	8
2.3 Diagnostic Instruments - Faraday Probe . . . . .	10
2.3.1 Instrument Overview . . . . .	10
2.3.2 Instrument Design and Data Acquisition System . . . . .	12
2.3.3 Uncertainty Analysis . . . . .	12
2.4 Diagnostic Instruments - ExB Velocity Filter . . . . .	13
2.4.1 Instrument Overview . . . . .	13
2.4.2 Instrument Design and Data Acquisition System . . . . .	15
2.4.3 Uncertainty Analysis . . . . .	21
2.5 Diagnostic Instruments - Retarding Potential Analyzer . . . . .	24
2.5.1 Instrument Overview . . . . .	24

2.5.2	Instrument Design and Data Acquisition System . . . . .	25
2.5.3	Uncertainty Analysis . . . . .	28
2.6	Summary of Scans . . . . .	30
<b>3</b>	<b>Simulation Approach - HPHall</b>	<b>34</b>
3.1	Hybrid-PIC Model Overview . . . . .	34
3.1.1	Electron Sub-model . . . . .	35
3.1.2	Heavy Particle Sub-model . . . . .	38
3.1.3	Wall Interactions . . . . .	40
3.2	HPHall at the Jet Propulsion Laboratory . . . . .	41
3.3	Application to the Ion Trajectory Problem . . . . .	43
3.3.1	HPHall Solution Domain . . . . .	43
3.3.2	Magnetic Field and Electron Mobility Analysis . . . . .	43
3.3.3	Ion Tracking and Energy Distributions . . . . .	49
3.3.4	Oscillation Analysis . . . . .	50
<b>4</b>	<b>Simulation Approach - Corner Sheath Model</b>	<b>52</b>
4.1	Corner Sheath Model - Motivation . . . . .	52
4.2	Sheath Equations . . . . .	54
4.3	Boundary Conditions . . . . .	55
4.4	Numerical Method . . . . .	57
4.5	Model Verification . . . . .	60
4.6	“Quasi”-2D Application . . . . .	60
<b>5</b>	<b>Experimental Results and Discussion</b>	<b>66</b>
5.1	Results and Discussion - ExB Filter and Faraday Probe . . . . .	66
5.1.1	Transverse Scans . . . . .	68
5.1.1.1	200 W Results . . . . .	74
5.1.1.2	650 W Results . . . . .	80
5.1.2	Axial Scans . . . . .	80
5.2	Uncertainty in the ExB Data . . . . .	85
5.3	RPA Analysis . . . . .	87
5.4	Uncertainty in the RPA Data . . . . .	96

5.5	Sputter Yield Analysis . . . . .	96
<b>6</b>	<b>HPHall Results and Discussion</b>	<b>102</b>
6.1	HPHall Run Conditions . . . . .	103
6.2	Time Averaged Results from HPHall . . . . .	103
6.2.1	650 W Results . . . . .	103
6.2.2	200 W Results . . . . .	116
6.2.3	Asymmetry of Ion Density Plots . . . . .	128
6.2.4	Comparison of averaged data to existing studies . . . . .	130
6.3	Faraday Probe and ExB Plots from HPHall . . . . .	132
6.3.1	Faraday Probe Results . . . . .	132
6.3.2	ExB Probe Results . . . . .	137
6.4	RPA Results from HPHall . . . . .	147
6.4.1	650 W results . . . . .	147
6.4.2	200 W results . . . . .	152
6.5	Repeatability of the Simulated Results . . . . .	156
6.6	Effect of Oscillations . . . . .	159
<b>7</b>	<b>Corner Sheath Model Results and Discussion</b>	<b>165</b>
7.1	Boundary Conditions . . . . .	165
7.2	Potential Profile . . . . .	166
7.3	Ion Trajectories Through the Sheath . . . . .	172
<b>8</b>	<b>Comparison of Experimental and Simulated Results</b>	<b>182</b>
8.1	Formation of the Central Jet . . . . .	183
8.2	Angles of Ion Trajectories within the Near Field Plume . . . . .	184
8.3	High Velocity High Angle Ions . . . . .	186
<b>9</b>	<b>Conclusions and Recommendations</b>	<b>192</b>
9.1	Conclusions . . . . .	192
9.2	Recommendations for Future Work . . . . .	193
<b>A</b>	<b>Additional Experimental ExB Data</b>	<b>197</b>

<b>B Additional Experimental RPA Data</b>	<b>211</b>
B.1 Raw RPA Data . . . . .	211
B.2 Differentiated RPA Data (not normalized) . . . . .	218
B.3 Sputter Yield Data . . . . .	225
<b>C Additional HPHall Oscillation Results</b>	<b>227</b>
<b>D Additional HPHall Simulated ExB Probe Results</b>	<b>235</b>
<b>E Additional Corner Sheath Model Trajectory Results</b>	<b>243</b>

# List of Figures

1.1	Hall thruster cross section . . . . .	3
1.2	SPT-70 plume . . . . .	3
2.1	SPT-70 thruster . . . . .	9
2.2	SPT-70 erosion . . . . .	9
2.3	Big Green vacuum chamber . . . . .	10
2.4	Translation stage schematic . . . . .	11
2.5	Faraday probe schematic . . . . .	11
2.6	Faraday probe used in the experiment . . . . .	13
2.7	Faraday probe data acquisition system . . . . .	14
2.8	ExB schematic . . . . .	15
2.9	ExB sample trace . . . . .	16
2.10	Colutron Model 300 velocity filter . . . . .	16
2.11	ExB probe used in experiment . . . . .	17
2.12	ExB alignment . . . . .	18
2.13	ExB potential distribution . . . . .	19
2.14	ExB magnetic field . . . . .	19
2.15	ExB data acquisition system . . . . .	20
2.16	ExB resolution . . . . .	22
2.17	RPA schematic . . . . .	24
2.18	RPA sample trace . . . . .	25
2.19	RPA photo . . . . .	26
2.20	RPA data acquisition system . . . . .	27
2.21	Example result from Simion . . . . .	29
2.22	Transverse and axial scans . . . . .	31

2.23	RPA scans . . . . .	32
3.1	HPHall program flow . . . . .	36
3.2	SPT-70 solution domain . . . . .	37
3.3	Transformation from r-z to $\xi - \eta$ plane . . . . .	38
3.4	Shape of plasma sheath at wall . . . . .	40
3.5	Possible potential distributions . . . . .	44
3.6	Measured SPT-70 magnetic field, 200 W case . . . . .	45
3.7	Measured SPT-70 magnetic field, 650 W case . . . . .	46
3.8	Simulated Faraday probe trajectory projection . . . . .	50
3.9	Simulated RPA trajectory projection . . . . .	51
4.1	Bending of ion trajectories due to the sheath . . . . .	53
4.2	Corner sheath model program flow . . . . .	58
4.3	Comparison of 1D to 2D model, example 1 . . . . .	61
4.4	Comparison of 1D to 2D model, example 2 . . . . .	62
4.5	Comparison of 1D to 2D model, example 3 . . . . .	63
4.6	Corner sheath model solution domain . . . . .	64
4.7	Applying the 2D solver in a quasi-2D fashion . . . . .	65
5.1	Transverse scans taken with the ExB filter . . . . .	68
5.2	Compiled ExB results, 200 W . . . . .	69
5.3	Compiled ExB results, 650 W . . . . .	70
5.4	Compiled FP results, 200 W . . . . .	71
5.5	Compiled FP results, 650 W . . . . .	72
5.6	ExB results, 200 W case, at 50 mm . . . . .	76
5.7	ExB results, 200 W case, at 100 mm . . . . .	77
5.8	ExB results, 200 W case, at 150 mm . . . . .	78
5.9	Faraday probe results, 200 W case . . . . .	79
5.10	ExB results, 650 W case, at 50 mm . . . . .	81
5.11	ExB results, 650 W case, at 100 mm . . . . .	82
5.12	ExB results, 650 W case, at 150 mm . . . . .	83
5.13	Faraday probe results, 650 W case . . . . .	84

5.14	ExB axial results, 200 W . . . . .	86
5.15	ExB axial results, 650 W . . . . .	86
5.16	Differentiated RPA data at 200 W, 0 to 40° . . . . .	90
5.17	Differentiated RPA data at 200 W, 45 to 65° . . . . .	91
5.18	Differentiated RPA data at 200 W, 70 to 90° . . . . .	92
5.19	Differentiated RPA data at 650 W, 0 to 40° . . . . .	93
5.20	Differentiated RPA data at 650 W, 45 to 65° . . . . .	94
5.21	Differentiated RPA data at 650 W, 70 to 90° . . . . .	95
5.22	Example of sputter yield calculation. . . . .	98
5.23	Sputter yield estimate for C, 200 W . . . . .	99
5.24	Sputter yield estimate for Si, 200 W . . . . .	99
5.25	Sputter yield estimate for Al, 200 W . . . . .	99
5.26	Sputter yield estimate for Ti, 200 W . . . . .	100
5.27	Sputter yield estimate for C, 650 W . . . . .	100
5.28	Sputter yield estimate for Si, 650 W . . . . .	100
5.29	Sputter yield estimate for Al, 650 W . . . . .	101
5.30	Sputter yield estimate for Ti, 650 W . . . . .	101
6.1	Averaged plasma potential from HPHall, 650 W upstream run . . . . .	106
6.2	Averaged axial electric field from HPHall, 650 W upstream run . . . . .	107
6.3	Averaged radial electric field from HPHall, 650 W upstream run . . . . .	108
6.4	Averaged electron temperature from HPHall, 650 W upstream run . . . . .	109
6.5	Averaged ion density from HPHall, 650 W upstream run . . . . .	110
6.6	Averaged plasma potential from HPHall, 650 W downstream run . . . . .	111
6.7	Averaged axial electric field from HPHall, 650 W downstream run . . . . .	112
6.8	Averaged radial electric field from HPHall, 650 W downstream run . . . . .	113
6.9	Averaged electron temperature from HPHall, 650 W downstream run . . . . .	114
6.10	Averaged ion density from HPHall, 650 W downstream run . . . . .	115
6.11	Averaged plasma potential from HPHall, 200 W upstream run . . . . .	118
6.12	Averaged axial electric field from HPHall, 200 W upstream run . . . . .	119
6.13	Averaged radial electric field from HPHall, 200 W upstream run . . . . .	120
6.14	Averaged electron temperature from HPHall, 200 W upstream run . . . . .	121

6.15	Averaged ion density from HPHall, 200 W upstream run . . . . .	122
6.16	Averaged plasma potential from HPHall, 200 W downstream run . . . . .	123
6.17	Averaged axial electric field from HPHall, 200 W downstream run . . . . .	124
6.18	Averaged radial electric field from HPHall, 200 W downstream run . . . . .	125
6.19	Averaged electron temperature from HPHall, 200 W downstream run . . . . .	126
6.20	Averaged ion density from HPHall, 200 W downstream run . . . . .	127
6.21	Plasma potential from HPHall at different axial locations, 650 W upstream run	129
6.22	Plasma potential from HPHall at different axial locations, 650 W downstream run . . . . .	129
6.23	Plasma potential from HPHall at different axial locations, 200 W upstream run	129
6.24	Plasma potential from HPHall at different axial locations, 200 W downstream run . . . . .	130
6.25	Faraday probe traces created from HPHall data, 650 W runs . . . . .	134
6.26	Faraday probe traces created from HPHall data, 200 W runs . . . . .	135
6.27	Faraday probe traces created from HPHall data, 25mm, all runs . . . . .	136
6.28	ExB probe traces created from HPHall data at 50 mm, 650 W runs . . . . .	139
6.29	ExB probe traces created from HPHall data at 50 mm, 650 W runs, ion current	140
6.30	ExB probe traces created from HPHall data at 100 mm, 650 W runs . . . . .	141
6.31	ExB probe traces created from HPHall data at 150 mm, 650 W runs . . . . .	142
6.32	ExB probe traces created from HPHall data at 50 mm, 200 W runs . . . . .	144
6.33	ExB probe traces created from HPHall data at 100 mm, 200 W runs . . . . .	145
6.34	ExB probe traces created from HPHall data at 150 mm, 200 W runs . . . . .	146
6.35	RPA traces created from HPHall data, 650 W runs, 0 to 40 deg . . . . .	149
6.36	RPA traces created from HPHall data, 650 W runs, 45 to 65 deg . . . . .	150
6.37	RPA traces created from HPHall data, 650 W runs, 70 to 80 deg . . . . .	151
6.38	RPA traces created from HPHall data, 200 W runs, 0 to 40 deg . . . . .	153
6.39	RPA traces created from HPHall data, 200 W runs, 45 to 65 deg . . . . .	154
6.40	RPA traces created from HPHall data, 200 W runs, 70 to 80 deg . . . . .	155
6.41	Bound on the simulated RPA data . . . . .	157
6.42	Oscillation tracking in HPHall, 650 W upstream run . . . . .	162
6.43	Oscillation tracking in HPHall on a shorter time scale, 650 W upstream run .	163
6.44	Frequency spectrum, 650 W upstream run . . . . .	164

7.1	Boundary conditions for the corner sheath model, 650 W upstream run . . .	167
7.2	Boundary conditions for the corner sheath model, 650 W downstream run . .	168
7.3	Boundary conditions for the corner sheath model, 200 W upstream run . . .	169
7.4	Boundary conditions for the corner sheath model, 200 W downstream run . .	170
7.5	Plasma potential from the corner sheath model, 650 W upstream run . . . .	170
7.6	Plasma potential from the corner sheath model, 650 W downstream run . . .	171
7.7	Plasma potential from the corner sheath model, 200 W upstream run . . . .	171
7.8	Plasma potential from the corner sheath model, 200 W downstream run . . .	171
7.9	Trajectories from the corner sheath model, 650 W upstream run, $U_0 = 2.5$ .	174
7.10	Trajectories from the corner sheath model, 650 W upstream run, $U_0 = 5.0$ .	175
7.11	Trajectories from the corner sheath model, 650 W downstream run, $U_0 = 2.5$	176
7.12	Trajectories from the corner sheath model, 650 W downstream run, $U_0 = 5.0$	177
7.13	Trajectories from the corner sheath model, 200 W upstream run, $U_0 = 2.5$ .	178
7.14	Trajectories from the corner sheath model, 200 W upstream run, $U_0 = 5.0$ .	179
7.15	Trajectories from the corner sheath model, 200 W downstream run, $U_0 = 2.5$	180
7.16	Trajectories from the corner sheath model, 200 W downstream run, $U_0 = 5.0$	181
8.1	Potential profiles from HPHall versus theoretical potential profile . . . . .	189
A.1	ExB results, 200 W case, at $0^\circ$ . . . . .	198
A.2	ExB results, 200 W case, at $10^\circ$ . . . . .	199
A.3	ExB results, 200 W case, at $20^\circ$ . . . . .	200
A.4	ExB results, 200 W case, at $30^\circ$ . . . . .	201
A.5	ExB results, 200 W case, at $40^\circ$ . . . . .	202
A.6	ExB results, 200 W case, at $50^\circ$ . . . . .	203
A.7	ExB results, 200 W case, at $60^\circ$ . . . . .	204
A.8	ExB results, 650 W case, at $0^\circ$ . . . . .	205
A.9	ExB results, 650 W case, at $10^\circ$ . . . . .	206
A.10	ExB results, 650 W case, at $20^\circ$ . . . . .	207
A.11	ExB results, 650 W case, at $30^\circ$ . . . . .	208
A.12	ExB results, 650 W case, at $40^\circ$ . . . . .	209
B.1	RPA raw data, 200W, from 0 to $40^\circ$ . . . . .	212

B.2	RPA raw data, 200W, from 45 to 65° . . . . .	213
B.3	RPA raw data, 200W, from 70 to 90° . . . . .	214
B.4	RPA raw data, 650W, from 0 to 40° . . . . .	215
B.5	RPA raw data, 650W, from 45 to 65° . . . . .	216
B.6	RPA raw data, 650W, from 70 to 90° . . . . .	217
B.7	RPA differentiated data, 200W, from 0 to 40° . . . . .	219
B.8	RPA differentiated data, 200W, from 45 to 65° . . . . .	220
B.9	RPA differentiated data, 200W, from 70 to 90 degrees . . . . .	221
B.10	RPA differentiated data, 650W, from 0 to 40° . . . . .	222
B.11	RPA differentiated data, 650W, from 45 to 65° . . . . .	223
B.12	RPA differentiated data, 650W, from 70 to 90° . . . . .	224
B.13	Sputter yield, Carbon . . . . .	225
B.14	Sputter yield, Silicon . . . . .	225
B.15	Sputter yield, Aluminum . . . . .	226
B.16	Sputter yield, Titanium . . . . .	226
C.1	Oscillation tracking in HPHall, 650 W downstream run . . . . .	228
C.2	Frequency spectrum, 650 W downstream run . . . . .	229
C.3	Oscillation tracking in HPHall, 200 W upstream run . . . . .	230
C.4	Frequency spectrum, 200 W upstream run . . . . .	231
C.5	Oscillation tracking in HPHall, 200 W downstream run . . . . .	232
C.6	Frequency spectrum, 200 W downstream run . . . . .	233
D.1	ExB probe traces created from HPHall data at 50 mm, 650 W runs, ion current	236
D.2	ExB probe traces created from HPHall data at 100 mm, 650 W runs, ion current	237
D.3	ExB probe traces created from HPHall data at 150 mm, 650 W runs, ion current	238
D.4	ExB probe traces created from HPHall data at 50 mm, 200 W runs, ion current	239
D.5	ExB probe traces created from HPHall data at 100 mm, 200 W runs, ion current	240
D.6	ExB probe traces created from HPHall data at 150 mm, 200 W runs, ion current	241
E.1	Trajectories from the corner sheath model, 650 W upstream run, $U_0 = 7.5$ .	243
E.2	Trajectories from the corner sheath model, 650 W upstream run, $U_0 = 10.0$ .	244
E.3	Trajectories from the corner sheath model, 650 W downstream run, $U_0 = 7.5$	245

- E.4 Trajectories from the corner sheath model, 650 W downstream run,  $U_0 = 10.0$  246
- E.5 Trajectories from the corner sheath model, 200 W upstream run,  $U_0 = 7.5$  . 247
- E.6 Trajectories from the corner sheath model, 200 W upstream run,  $U_0 = 10.0$  . 248
- E.7 Trajectories from the corner sheath model, 200 W downstream run,  $U_0 = 7.5$  249
- E.8 Trajectories from the corner sheath model, 200 W downstream run,  $U_0 = 10.0$  250

# List of Tables

2.1	Faraday probe dimensions . . . . .	12
2.2	RPA uncertainty due to ion optics . . . . .	30
2.3	Summary of Faraday probe scans . . . . .	32
2.4	ExB scan summary . . . . .	33
2.5	RPA scan summary . . . . .	33
3.1	Cathode and anode parameters for HPHall . . . . .	43
3.2	Description of the four cases modeled in HPHall . . . . .	48
3.3	Performance parameters of the cases modeled in HPHall . . . . .	48
6.1	Description of the four runs modeled in HPHall . . . . .	103
6.2	Averaged data from previous HPHall studies . . . . .	131
6.3	Averaged data from current HPHall study . . . . .	131
6.4	Maximum error in the simulated Faraday probe data . . . . .	156
6.5	Maximum error in the simulated ExB data . . . . .	158
6.6	Maximum error in the simulated RPA data . . . . .	158
6.7	Summary of oscillation data from HPHall . . . . .	161
7.1	Trajectories through sheath, $U_0 = 2.5$ , 650 W upstream run . . . . .	174
7.2	Trajectories through sheath, $U_0 = 5.0$ , 650 W upstream run . . . . .	175
7.3	Trajectories through sheath, $U_0 = 2.5$ , 650 W downstream run . . . . .	176
7.4	Trajectories through sheath, $U_0 = 5.0$ , 650 W downstream run . . . . .	177
7.5	Trajectories through sheath, $U_0 = 2.5$ , 200 W upstream run . . . . .	178
7.6	Trajectories through sheath, $U_0 = 5.0$ , 200 W upstream run . . . . .	179
7.7	Trajectories through sheath, $U_0 = 2.5$ , 200 W downstream run . . . . .	180
7.8	Trajectories through sheath, $U_0 = 5.0$ , 200 W downstream run . . . . .	181

E.1	Trajectories through sheath, $U_0 = 7.5$ , 650 W upstream run . . . . .	243
E.2	Trajectories through sheath, $U_0 = 10.0$ , 650 W upstream run . . . . .	244
E.3	Trajectories through sheath, $U_0 = 7.5$ , 650 W downstream run . . . . .	245
E.4	Trajectories through sheath, $U_0 = 10.0$ , 650 W downstream run . . . . .	246
E.5	Trajectories through sheath, $U_0 = 7.5$ , 200 W upstream run . . . . .	247
E.6	Trajectories through sheath, $U_0 = 10.0$ , 200 W upstream run . . . . .	248
E.7	Trajectories through sheath, $U_0 = 7.5$ , 200 W downstream run . . . . .	249
E.8	Trajectories through sheath, $U_0 = 10.0$ , 200 W downstream run . . . . .	250

# Nomenclature/Symbols

$\mu_0$  = permeability of free space =  $1.26 \times 10^{-6}$  m kg s<sup>-2</sup> A<sup>-2</sup>

$\epsilon_0$  = permittivity of free space =  $8.85 \times 10^{-12}$  m<sup>-3</sup> kg<sup>-1</sup> s<sup>4</sup> A<sup>2</sup>

$k$  = Boltzmann constant =  $1.38 \times 10^{-23}$  m<sup>2</sup> kg s<sup>-2</sup> K<sup>-1</sup>

$e$  = elementary charge =  $1.60 \times 10^{-19}$  C

$\sigma$  = magnetic potential function

$\lambda$  = magnetic stream function

$n_i$  = ion density

$n_e$  = electron density

$n_n$  = neutral density

$T_e$  = electron temperature

$u_i$  = ion velocity

$\phi$  = plasma potential

$\mu_{e\perp}$  cross-field electron mobility

$\Omega_e$  = electron Hall parameter

$\omega_{ce}$  = electron cyclotron frequency

$\nu_e$  = total effective electron collision frequency

$\nu_{en}$  = electron-neutral collision frequency

$\nu_{ei}$  = electron-ion collision frequency

$\nu_w$  = electron-wall collision frequency

$\nu_b$  = anomalous collision frequency

$\lambda_D$  = debye length

$u_s$  = ion acoustic speed

$\tilde{\nabla}$  = non-dimensional partial derivative

$\tilde{n}$  = non-dimensional ion density

$\vec{U} = \vec{M}$  = non-dimensional ion velocity

$\chi$  = non-dimensional plasma potential

$\tilde{E}$  = non-dimensional electric field

$\Gamma$  = secondary electron emission yield

$\mu$  = ratio of electron mass to ion mass

$\zeta$  = non-dimensional axial (z) position

$\rho$  = non-dimensional radial (r) position



# Chapter 1

## Introduction

### 1.1 Hall Thruster Overview

As with other types of electric propulsion (EP) devices, Hall thrusters offer the benefits of high efficiencies and long lifetimes. Such advantages make these thrusters well-suited for a variety of in-space applications, especially those requiring adjustments to spacecraft velocity over long periods of time. For example, satellite station-keeping and planetary exploration are some of the more prominent applications of EP technology over its nearly 50-year development history. Hall thrusters, notably, were used on Russian satellites as early as 1974 [1]. Recently, Hall thrusters have been employed on a variety of missions. Space Systems/Loral, for example, has used the Russian manufactured SPT-100 thruster on a number of their commercial satellites [2]. Additionally, the TacSat-2 mission conducted by the U.S. Air Force was the first use of a U. S. developed Hall thruster on a satellite [3]. Hall thrusters also provided the propulsion for the ESA SMART-1 lunar orbiter [4].

Hall thrusters, and their close counterparts, ion thrusters, are able to achieve high specific impulses (and thus low propellant masses) due to the high exhaust velocities that they produce. In both of these types of thrusters, electrical energy is converted to kinetic energy through the acceleration of an ionized gas. However, in an ion thruster this acceleration occurs between two grids, while in a Hall thruster the acceleration region is not defined by a physical barrier. For this reason, the behavior of the resulting ion exhaust is less easily predicted in the case of the Hall thruster.

Hall thrusters generate thrust by using a system of perpendicular electric and magnetic fields to ionize and accelerate propellant atoms. Figure 1.1 shows the main components of the Hall thruster, along with the directions of the internal fields. During operation, the

propellant gas (usually Xenon) is introduced at the upstream end of the insulated cylindrical channel. At the same time, electrons are generated at the cathode. Due to their thermal motion, the electrons distribute themselves across the face of the thruster, while the presence of the positive anode draws them into the channel.

As these electrons migrate upstream, they encounter the radial magnetic field and begin to undergo orbits about these field lines, essentially becoming trapped in the region of high magnetic field. This decrease in electron mobility causes a primarily axial electric field to develop along the length of the channel. Propellant atoms, moving from upstream, undergo collisions with the trapped electrons. If the energy of a collision is sufficient, ionization will occur. The ions generated will then be accelerated out of the channel by the axial electric field, producing an annular ion beam [5].

In a conventional chemical rocket nozzle, the thrust force is transmitted to the thruster body through direct contact with the propellant. However, in a Hall thruster, the argument has been made that the thrust force is transmitted through the magnetic field [5]. This occurs because of the "partially magnetized" nature of the plasma, in which the electrons are trapped on magnetic field lines while the ions are not. As the ions are accelerated downstream by the electric field, they tend to want to drag the electrons with them. However, the Lorentz force ( $F_{mag} = q(\vec{v} \times \vec{B})$ ) keeps the electrons from being pulled along with the ions. The magnetic field thus exerts a force on the electrons that is in the upstream direction. The equal and opposite force between the electrons and the magnetic field, in the downstream direction, is the thrust force.

As illustrated in Figure 1.2, although the ion plume produced by a Hall thruster starts off as a well-collimated beam, it quickly changes from an annular structure to a central "jet" with a more diffuse population of ions surrounding it. This transition occurs within several thruster diameters downstream of the exit plane, in a region referred to the "near-field" of the Hall thruster. Since the ion beam is evolving considerably in this region, in order to have a full understanding of the plume behavior it is vital to know what physical interactions influence ions in the near-field.

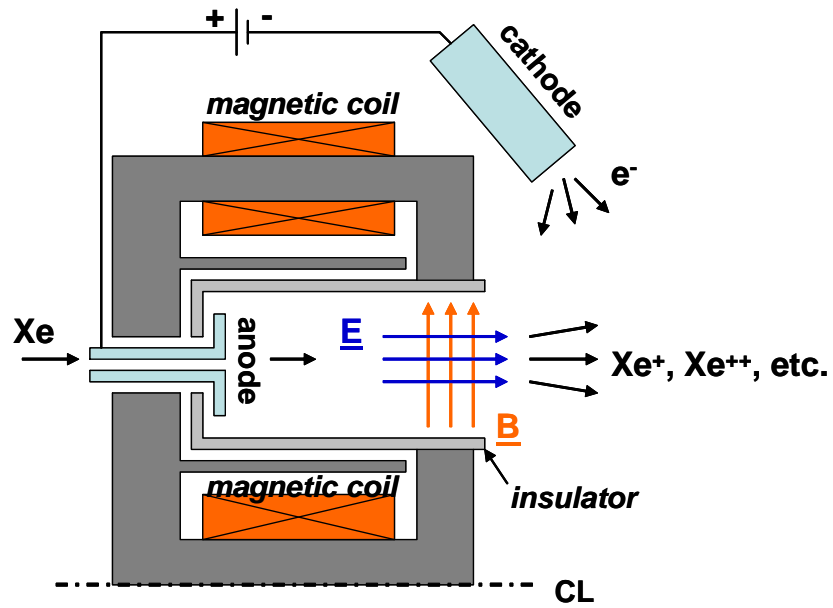


Figure 1.1: Hall thruster cross section. Note that the full thruster is cylindrically symmetric about the centerline.

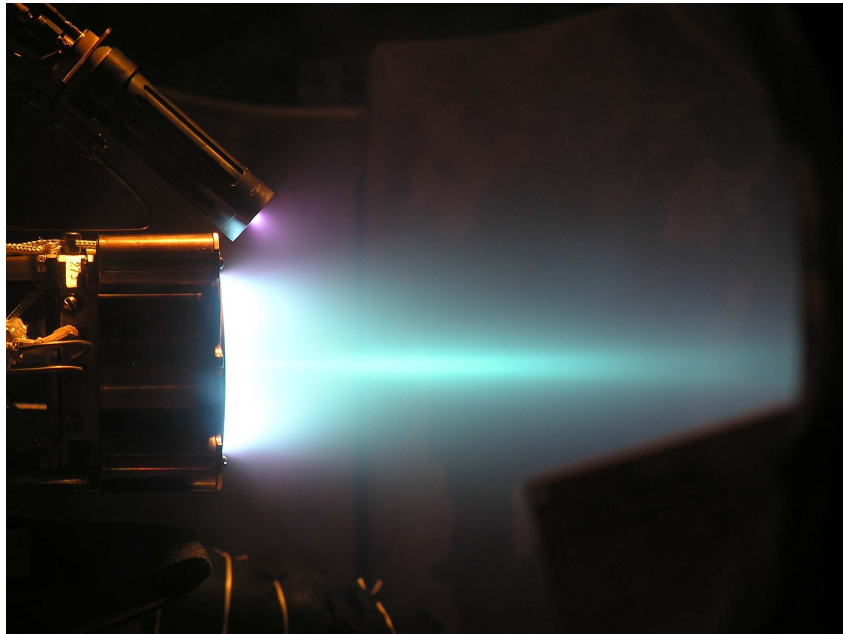


Figure 1.2: SPT-70 plume. This photograph shows that the formation of a central jet occurs within several thruster diameters of the exit plane.

## 1.2 Previous Research

In terms of experimental research, some studies have been conducted that focus on ion trajectories within the near-field region of the Hall thruster plume. For example, Laser-Induced-Fluorescence (LIF) techniques have been used by the researchers at the Air Force Research Laboratory (AFRL) to investigate ion velocities near the exit plane of a Hall thruster [6–9]. However, most experimental studies of the Hall thruster near-field region have looked at plasma parameters such as potential, ion density, and electron temperature [10–12], because these parameters can be measured using fast moving probes that cause minimal disturbance to the thruster plasma. For the most part, experimental investigations of ion energy and trajectory angles have used diagnostics that were located far from the thruster exit plane [12, 13].

Simulations of Hall thrusters have focused primarily on two areas: (1) the internal physics inside the thruster channel, and (2) the "far-field" region that is several thruster diameters downstream of the exit plane. The method that has been most widely used to model the thruster channel is the "hybrid-PIC" approach which treats electrons as a fluid and ions as particles-in-cell. Most research groups involved in the modeling of Hall thrusters have developed codes which use this method [14–18]. In these codes, the simulation domain usually consists of the Hall thruster channel plus a small region downstream of the exit plane within the near-field. In regards to the far-field codes, these simulations typically use DSMC methods to model collisions within the thruster plume [19, 20]. While these codes do a suitable job of modeling plume expansion, they require an input boundary condition to work. If the input condition that is applied poorly reflects the actual situation, then the far-field codes will not produce accurate results.

## 1.3 Motivation

In both the internal and far-field Hall thruster codes, the physics of the near-field region are not adequately modeled. This is understandable, since neither type was developed with the intention of simulating the near-field region. The initial motivation for developing the internal, hybrid-PIC based models was to investigate the plasma physics within the channel, and in particular, examine the acceleration of ions within the channel [14]. As a

result, the simulation region of most hybrid-PIC codes only extends out a few centimeters downstream of the exit plane, and thus cannot fully capture near-field phenomena. As far as the far-field simulations are concerned, these codes were created with the goal of modeling the behavior of the thruster plume at a wide range of operating conditions, to help predict plume/spacecraft interactions [20]. Since the applied magnetic and electric fields are negligible across most of the thruster plume, assumptions were made that reduced the complexity of the electrodynamic equations in these models. This allowed for the entire plume to be simulated in 3D, but reduced the accuracy of these models near the exit plane.

To be able to link the internal and far-field codes, one needs a strong understanding of the missing piece of the plasma physics puzzle, i.e., the mechanisms that govern plasma behavior within the near-field region. As will be discussed in this thesis, there are two important features of the plume which are thought to develop in the near-field of the Hall thruster and which are not fully captured by the current models. One is the formation of the central jet, and the other is the creation of high energy ions at high angles off the thruster centerline. The characteristics of the central jet are directly linked to thruster performance and beam divergence and, thus, the central jet is significant from a thruster operation standpoint. High angle, high energy ions, on the other hand, are important from a thruster integration standpoint. These ions can cause significant damage to spacecraft surfaces and therefore it is imperative to understand how they are created. Since both of these phenomena significantly influence how these thrusters can be used in actual missions, it is necessary to fully understand the underlying physics that cause them, and then to correctly implement them in Hall thruster simulations.

## **1.4 Problem Statement and Approach**

The goal of the research detailed in this thesis was to investigate the physics of high velocity ions in the Hall thruster near-field region using both experimental methods and simulations. Note that in this context, "high velocity" ions are ions that have been accelerated through the full potential applied between the anode and the cathode of the thruster. (These ions may also be referred to in the text as "primary energy" or "primary beam energy" ions.) During the course of this research, several specific questions pertaining to the central jet and the high angle, high energy ion population, were addressed.

In regards to the formation of the central jet, one of the major questions was whether the jet is due solely to symmetric expansion of the cylindrical ion beam, or due in part to asymmetries in the thruster design. Previous research suggested, for example, a link between jet formation and the magnetic field configuration [21], but the specific impact of the field on ion trajectories had not yet been assessed. To investigate this issue, ion trajectories were tracked in an experimental survey and then compared to the results of a Hall thruster code that included the internal plasma physics of the thruster. This allowed for a qualitative assessment of the impact of different parameters on the central jet.

In regards to the high energy, high angle ions, the main question that arose was how these ions could be accelerated out to high angles, since Hall thrusters are designed so that most of the primary energy ions are accelerated axially. The experimental data clearly revealed substantial populations of primary energy ions at angles from 60 to 80 degrees off centerline, but it was not immediately apparent how they were generated. One approach that was used to investigate these ions was to see if a hybrid-PIC code could reproduce the electric field necessary to generate them. Additionally, it was hypothesized that the area of non-neutrality near the corners of the thruster channel (the plasma sheath) could provide additional radial acceleration, so a model was developed to investigate this possibility.

Ultimately, the application of this research is to bridge the gap between the internal physics of the Hall thruster and the far-field physics of the plume. If the mechanisms which govern ion trajectory development within the near-field are well understood, then it may be possible to develop a fully-integrated framework that accurately models the channel, near-field, and far-field regions of the Hall thruster. Such a framework would be extremely valuable due to its predictive capabilities, and would help to diminish the need for thorough experimental investigations of the thruster plume. At the very least, the data could be used to help determine correct input conditions for the far-field plume codes. Certainly, although experimental data is always desirable, a well-validated code could eliminate the need for testing a thruster over long periods at a number of operating conditions, and thus lower the overall mission cost as well as aid in mission planning.

## Chapter 2

# Experimental Method

In the experimental portion of this research, measurements of a SPT-70 Hall thruster were taken using three different types of diagnostic instruments. To investigate the formation of the central jet, maps of the high velocity ion current density were taken using an ExB velocity filter. High energy, high angle ions were examined using a type of parallel grid energy analyzer known as a Retarding Potential Analyzer (RPA). Additionally, measurements of the total ion current density were taken using a Faraday probe, for comparison with the ExB and RPA data. Two thruster power levels were tested: the nominal condition of 650 W and the low power level of 200 W.

This chapter describes the experimental apparatus, including the thruster, vacuum facility, and diagnostic probes. Each probe description includes a basic overview of how the device works, the electronic equipment needed to operate it, and an estimate of the uncertainty in its measurements. A summary of the individual scans taken with the different instruments is also included.

### 2.1 SPT-70 Thruster

The SPT-70, pictured in Figure 2.1, is a Hall thruster developed by the Fakel Design Bureau in Russia. Its “SPT” designation stands for “stationary plasma thruster,” the Russian term for a Hall thruster with dielectric walls and an extended acceleration region [22]. Originally created for satellite station-keeping and orbit management, it has a flight history dating back to the 1980s [23, 24]. The SPT-70 was chosen for this experiment for several reasons. Due to its small size and relatively low operating power, it can be tested in a vacuum chamber that does not require the use of liquid nitrogen, thus substantially reducing facility costs.

Additionally, the SPT-70 has a simple channel geometry that makes it straightforward to model.

In terms of its channel geometry, which is shown in Figure 2.2, the SPT-70 has a cylindrical channel consisting of an inner and outer wall made of BN-SiO<sub>2</sub>. At the start of its lifetime, the outer diameter of the channel is 70 mm, while its inner diameter is 35 mm, and the length of the channel is 29 mm [14]. It should be noted, however, that the thruster used in this experiment had already been operated for several hundred hours, and thus sustained substantial erosion due to ions impacting its dielectric walls. The effect of this erosion is shown in Figure 2.2.

In addition to the thruster itself, an outer cathode is required to supply electrons for the plasma discharge and for beam neutralization. In this case, a hollow barium-oxide cathode was employed. This cathode was not designed specifically for use with the SPT-70, but nonetheless produced the necessary electron current for thruster operation. The cathode was mounted externally, out of the thruster exit plane, at an angle of about 45°, as can be seen in Figure 2.1.

During the experiment, the SPT-70 was run at 2 different power levels: 200 W and 650 W. The 650 W level represents the nominal operating point for the thruster, while the 200 W case was selected based on the nominal power level of the commercially produced Busek BHT-200 [6]. Note that it was not necessarily expected that the SPT-70 would behave like the BHT-200 at 200 W, but rather the purpose of operating at lower power was to see what would happen to ion trajectories at an off-nominal condition. To achieve 200 W, the discharge voltage was set at 250 V, the discharge current was set at 0.8 A, and the magnet current was set at 1.25 A. For a 650 W discharge, these values were 300 V, 2.17 A, and 2.17 A, respectively.

## 2.2 Vacuum Facility

The experiments were carried out at the Jet Propulsion Laboratory in Pasadena, California, in the “Big Green” vacuum facility pictured in Figure 2.3. This chamber has a diameter of approximately 2 m and a length of 5.5 m. To create vacuum, it uses a set of three diffusion pumps, as well as a set of four cryogenic pumps. The diffusion pumps alone can be used to achieve pressures in the 10<sup>-6</sup> torr range. Turning on the cryo-pumps, in addition to the

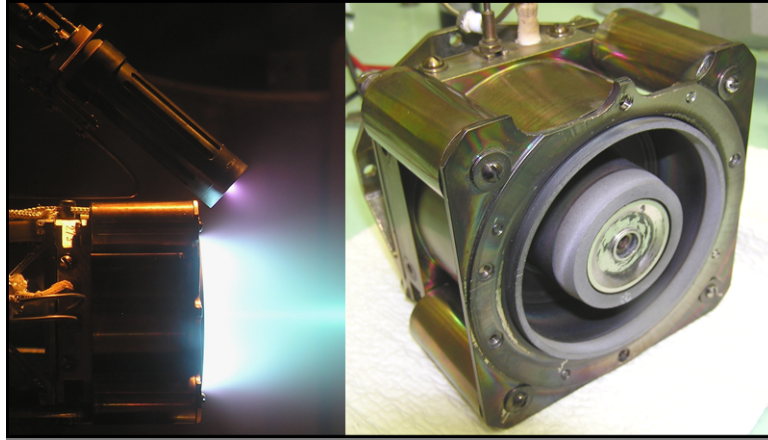


Figure 2.1: SPT-70 thruster from side (L) and from front (R). Note that the cathode is not pictured in the right-hand photograph.

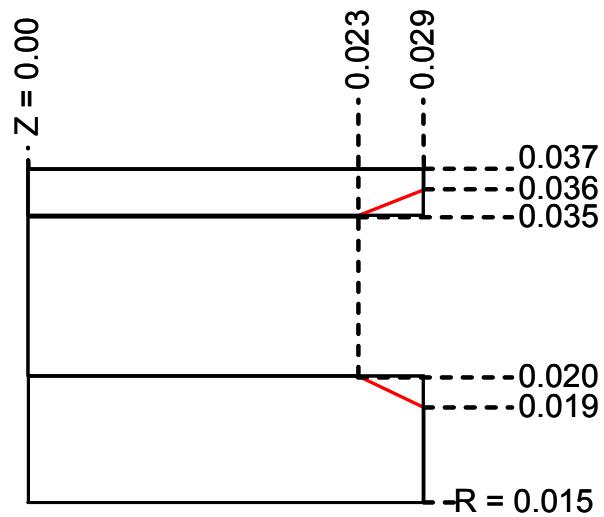


Figure 2.2: SPT-70 channel geometry, new (black) and eroded (red). Dimensions are in meters,  $Z = 0$  corresponds to the anode,  $R = 0$  corresponds to the thruster centerline.

diffusion pumps, can lead to even lower pressures, in the  $10^{-7}$  torr range. As previously mentioned, the SPT-70 thruster can be operated in this chamber without the use of liquid nitrogen.

Inside the chamber, a computer-controlled two-dimensional  $x - y - \theta$  stage allows the researcher to position various diagnostic probes within the plume of the Hall thruster. As shown in Figure 2.4, the range of the stage is roughly -100 to 1500 mm in the x-direction and -500 to 500 mm in the y-direction, relative to the thruster. Additionally, the stage can rotate from  $-90$  to  $90^\circ$ . The stage is fixed in the z-direction, so the height of the probes is set so that they are at the same height as the thruster center. In the experiment, the cathode was positioned so that it was out of the plane of motion of the probes.

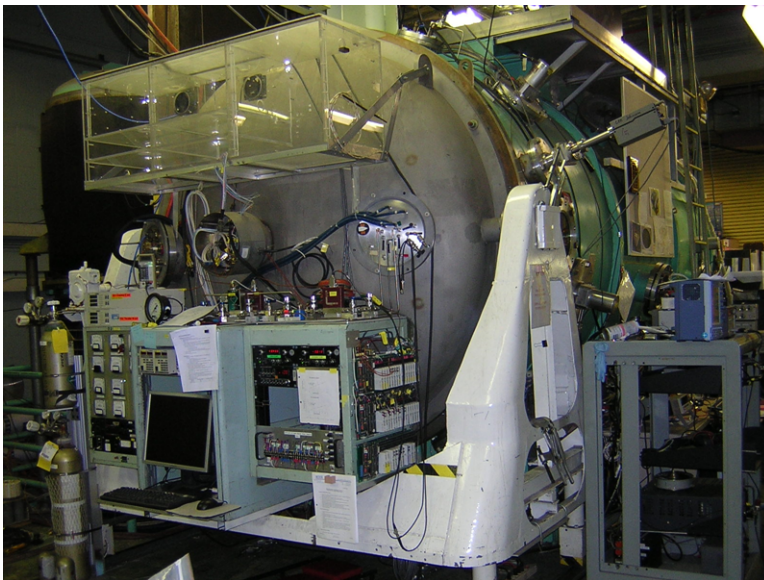


Figure 2.3: "Big Green" vacuum chamber.

## 2.3 Diagnostic Instruments - Faraday Probe

### 2.3.1 Instrument Overview

A Faraday probe was used to obtain measurements of ion current density. As shown in Figure 2.5, a Faraday probe consists of a current collector surrounded by an outer "ring", both of which are electrically isolated from one another by an insulating spacer. The gap between the two is sized so that it is smaller than the plasma Debye length. This ensures

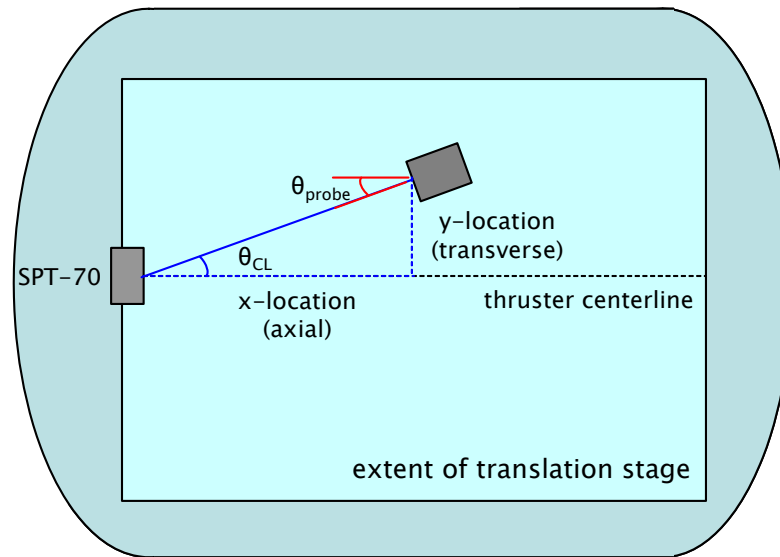


Figure 2.4: Translation stage schematic. The probes are set at a fixed height so that they move within a horizontal plane intersecting the thruster centerline. In the experiment, the thruster cathode was “above” this plane of motion. The extent of the translation stage is about -100 to 1500 mm in the x-direction, and -500 to 500 mm in the y-direction

that the potential on the face of the collector is uniform. To obtain a measurement of ion current density, both the collector and the ring are biased at a low negative potential relative to ground, to reject electrons. The current on the collector face is then measured and divided by the corresponding area [25].

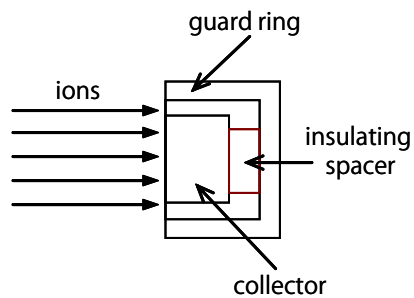


Figure 2.5: Faraday probe schematic.

Table 2.1: Faraday probe dimensions.

Total length	31.1 mm
Collector diam.	1.3 mm
Collector/ring gap	0.13 mm
Ring outer diam.	15.9 mm
Ring inner diam.	2.8 mm
Length of taper	6.5 mm

### 2.3.2 Instrument Design and Data Acquisition System

The particular Faraday probe used in this experiment is shown in Figure 2.6. Although most faraday probes are of the simple "button" construction shown in Figure 2.5, employing a cylindrical outer ring, this probe has a tapered outer ring. This allows for a smaller collector face and also reduces the total surface area that is exposed to the thruster plasma, thus minimizing the probe-plasma interaction. The relevant dimensions are shown in Table 2.1. Both the collector and ring were machined from graphite. During operation, both the collector and ring were connected to two separate Keithley 2400 SourceMeters, and each were biased at -20 V. The current measurement was also taken using these source-meters. The data acquisition system is shown in Figure 2.7.

Since a faraday probe is essentially just a current collector, any charged particle that reaches its face will be measured, regardless of angle of incidence of charge species. The angle of acceptance of the device can therefore be assumed to be roughly  $180^\circ$ , and current measured represents the total ion current. Other instruments are required if one wants to pinpoint trajectory direction or velocity with any accuracy. The faraday probe data was taken so that it could be later combined with the data from the other probes to estimate flux-dependent parameters such as material erosion due to ions. See Section 2.6 for the specific scans taken with the faraday probe.

### 2.3.3 Uncertainty Analysis

There are two possible sources of error for the faraday probe. One is secondary electron emission (SEE) from the collector surface. SEE occurs when an ion with sufficient energy collides with a surface, liberating an electron from the material. The other is the potential distribution on the probe's surface. If the potential is curved, for instance, near the edge of the collector, this can cause a slight bending of ion trajectories. Both of these sources of

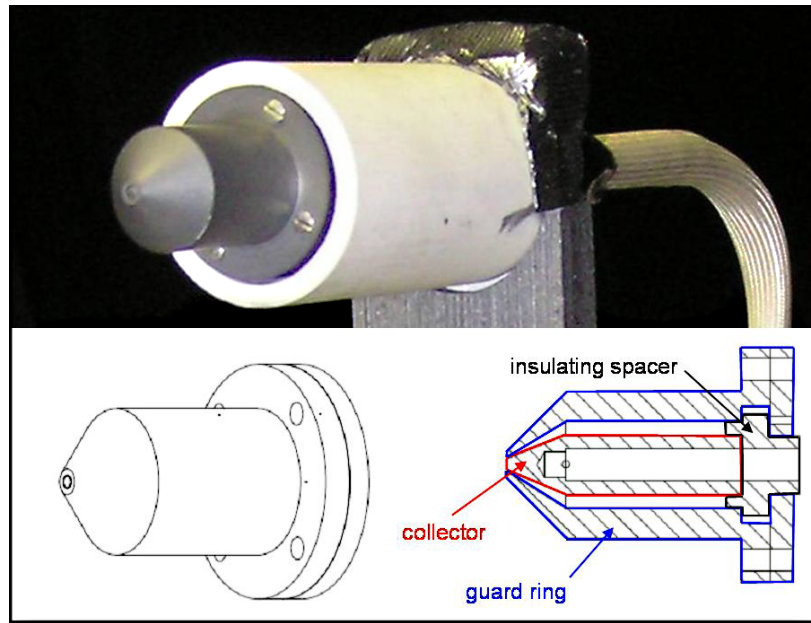


Figure 2.6: Faraday probe photo and drawing. Note that there is a small gap of 0.13 mm between the tip of the collector and the guard ring. Drawing created by Ray Swindlehurst.

error have been mitigated by the design of the probe itself, namely the use of a low SEE yield material (graphite) and a outer guard ring. As mentioned, the gap between the guard ring and the collector has been sized so that it is less than a plasma Debye length, so that the potential remains flat on the collector surface.

## 2.4 Diagnostic Instruments - ExB Velocity Filter

### 2.4.1 Instrument Overview

An ExB velocity filter was used to determine the distribution of high velocity ions as a function of location in the SPT-70 plume. This type of device measures ion velocity by employing a system of orthogonal electric and magnetic fields to filter incoming ions. As shown in Figure 2.8, the two fields are perpendicular to each other and to the incident ion beam [12].

The physics of the ExB filter are straightforward; one simply applies the Lorentz equation:

$$\vec{F} = q \left( \vec{E} + \vec{v} \times \vec{B} \right). \quad (2.1)$$

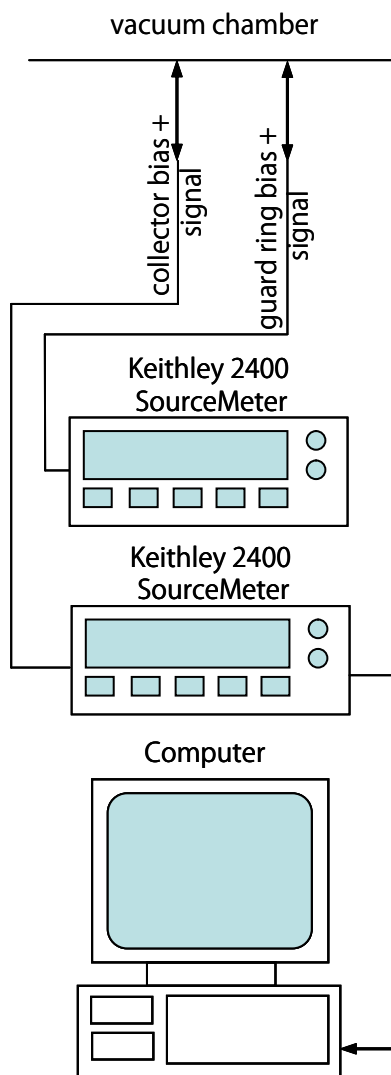


Figure 2.7: Faraday probe data acquisition system.

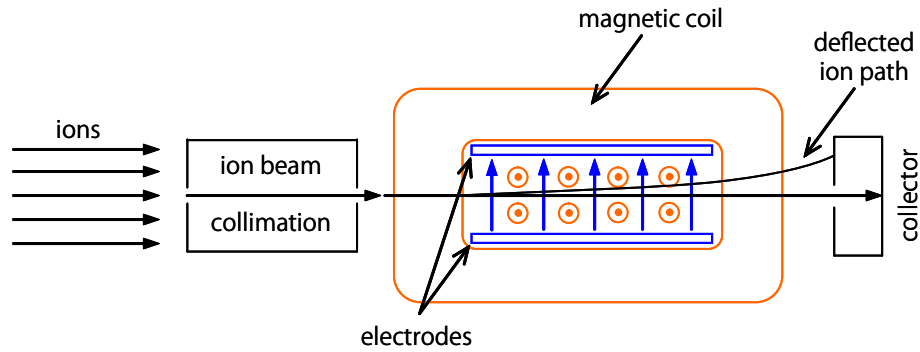


Figure 2.8: ExB Schematic.

Since all three vectors on the right side of the equation are perpendicular to each other, the force on the ion is in the direction of the magnetic field, and can be expressed as:

$$F = q(E - vB). \quad (2.2)$$

If the force on an ion is equal to zero, the ion will pass through the filter and be measured by the collector plate at the rear of the device. This occurs if  $v_i = E/B$ . Therefore, to obtain a distribution of ion velocities, one must simply sweep the  $E/B$  ratio over a range of values. This is typically what is done when an ExB filter is used, and for a Hall thruster the results on the thruster centerline generally look like Figure 2.9. (Note that this diagram is simply for illustration purposes, and does not represent actual experimental data).

#### 2.4.2 Instrument Design and Data Acquisition System

The particular filter used in this experiment was a Colutron Model 300 velocity filter, as shown in Figure 2.10. This commercial filter can produce an electric field of up to 12,500 V/m and a magnetic field of up to 0.11 T. It uses a set of metal shims to create an electric field across a 17.5 mm gap, while two solenoids provide a magnetic field perpendicular to this electric field. Thus, either the voltage on the shims or the current through the solenoids can be changed to produce the desired  $E/B$  ratio.

The filter itself was placed in a stainless steel housing, as shown in Figure 2.11. The housing consisted of a stainless steel box with a tapered "nose-cone" (a tapered MDC

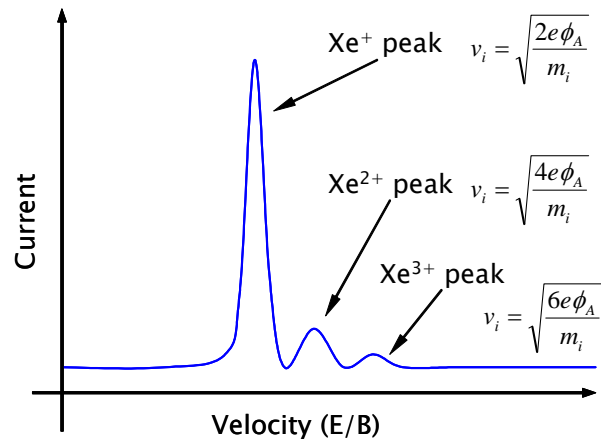


Figure 2.9: ExB sample trace. This trace is representative of the ion velocity distribution on the centerline of the thruster.

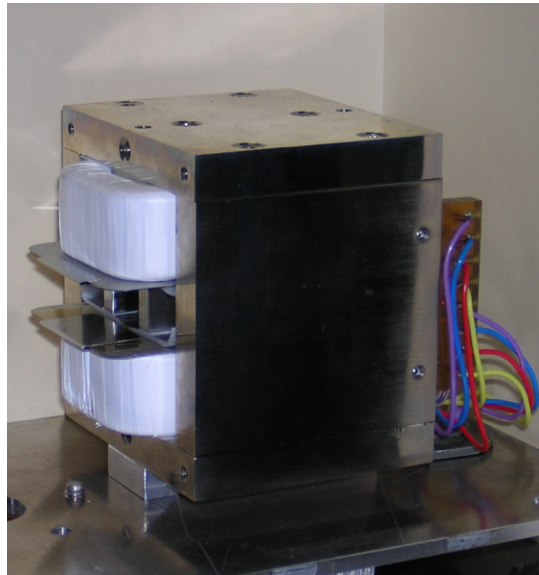


Figure 2.10: Colutron Model 300 velocity filter. The white structures are the magnetic coils, which create a vertical magnetic field across the channel.

vacuum flange). On the bottom of the box there was a 25 mm diameter hole, covered by a stainless steel mesh, which reduced the number of neutral particles and low energy ions that could build up inside the box and cause anomalous measurements due to charge exchange interactions. The entire housing was coated in graphite to prevent sputtering of the metallic surface.

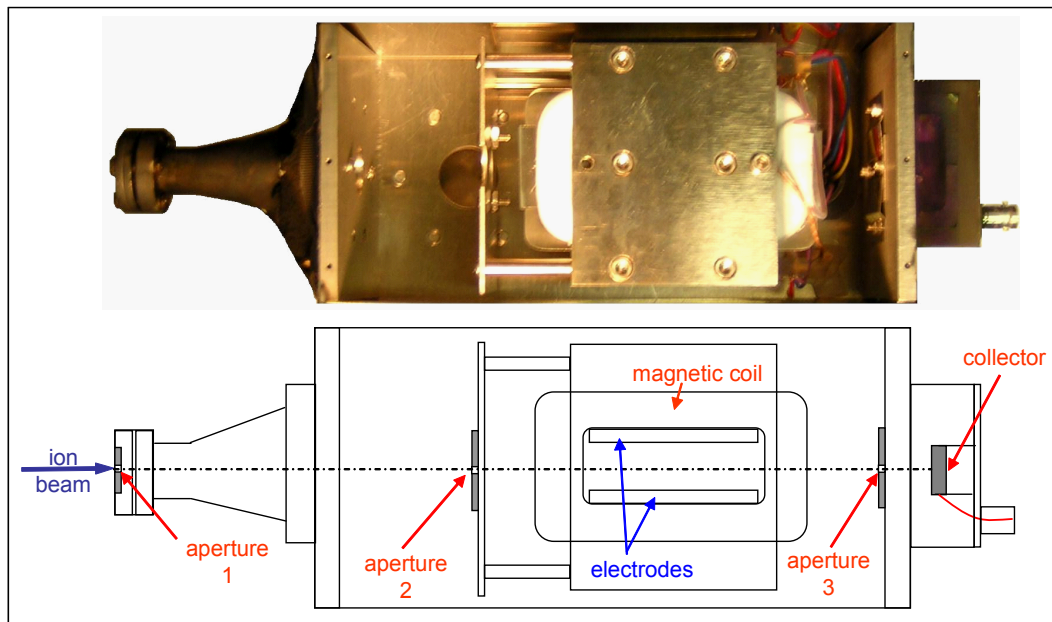


Figure 2.11: ExB photo and schematic.

There were 3 apertures mounted inside the housing, as shown in Figure 2.11. The first two apertures both had a diameter of 0.97 mm and were made of 0.03 mm thick tantalum foil. The purpose of these two apertures was to collimate the beam. The third aperture was slit-shaped, with a height of 30 mm, width of 0.8 mm, and thickness of 0.8 mm. The distance between apertures 1 and 2 was 143.0 mm, the distance between 2 and 3 was 159.5 mm, and the distance between aperture 3 and the collector was 17.3 mm. Given the geometry and spacing of the apertures, the acceptance angle of the device was  $0.8^\circ$  (full angle). It is important to note that this very small viewing angle allowed the origin of the measured ion trajectories to be determined with a very high degree of accuracy. To ensure accuracy, the probe had to be carefully aligned relative to the thruster when it was mounted on the stage. This task was accomplished by mounting a laser pointer where the collector anode was normally located, then shining the beam through backwards through the device,

as shown in Figure 2.12.

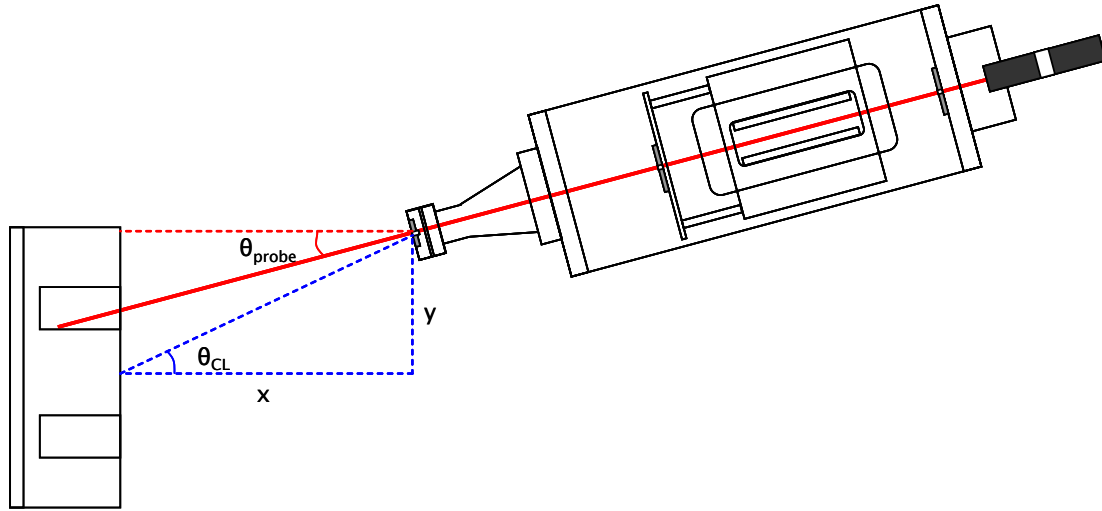


Figure 2.12: Alignment of ExB probe. A laser pointer was mounted in place of the collector plate, and its beam aligned with all 3 apertures. The probe was then mounted on the translation stage, and the probe's position and rotation angle was calibrated relative to the thruster. This was important due to the very small angle of acceptance of the device.

Before using the filter, the electric and magnetic fields were calibrated. To achieve an approximately linear electric field distribution in the filter channel, the voltages on the metal shims within the channel were adjusted using a voltage divider (manufactured by Colutron and provided with the filter). Figure 2.13 shows the resulting potential distribution within the channel. To ensure that the desired magnetic field was achieved, the field strength as a function of solenoid current was measured using a gaussmeter. This information is contained in Figure 2.14.

Rather than operate the ExB probe in the typical fashion, as described above, the filter E/B ratio was set so that only  $\text{Xe}^+$  ions that had been accelerated through the full potential of the thruster (the leftmost peak in Figure 2.9) were measured. That is, the filter was set to measure a specific velocity and species, and then moved around in the plume. This E/B ratio was selected experimentally, by aligning the ExB filter with the center of the thruster channel, at an angle of  $0^\circ$ , and then determining the velocity corresponding to the primary  $\text{Xe}^+$  peak. For this reason, it may be more appropriate to call the device a

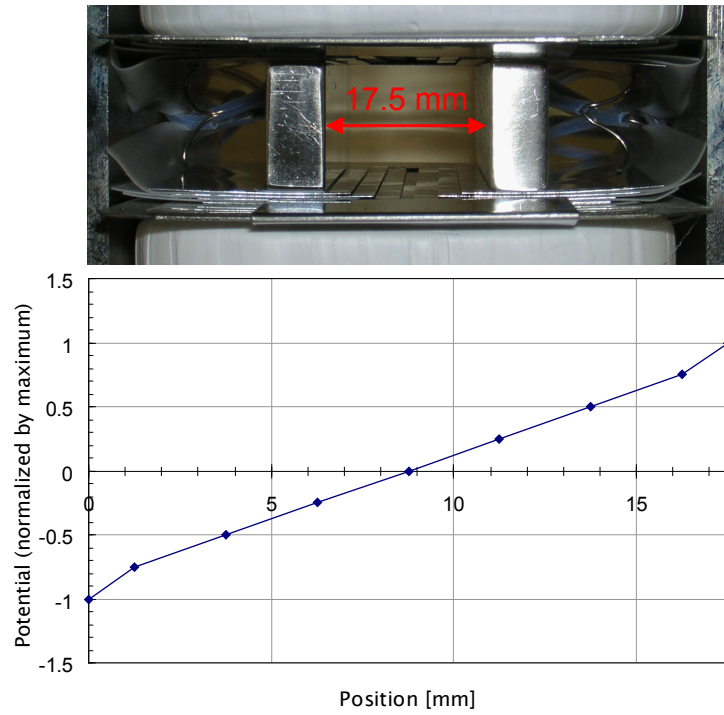


Figure 2.13: ExB potential distribution across filter channel.

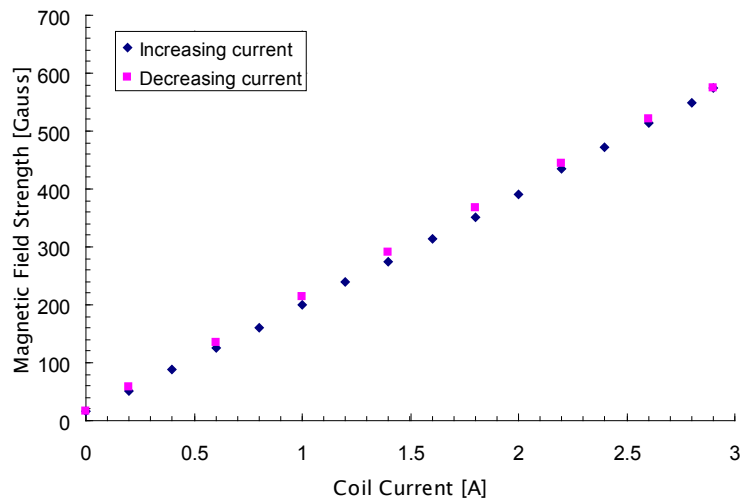


Figure 2.14: ExB magnetic field calibration

"high velocity ion probe" rather than refer to it as an ExB filter in the traditional sense. By employing the probe in this fashion, it was possible to create a map of the high velocity ion current produced by the SPT-70. The specific scans taken by the instrument are detailed in Section 2.6.

The data acquisition system for the ExB is shown in Figure 2.15. In this system, the potential for the electric field plates was supplied by a Keithley 2400 SourceMeter, and was balanced using the voltage balancing box supplied with the Colutron filter. A Keithley 6284A power supply was used to supply the DC current for the magnet coils. The collector current signal was sent to the computer and recorded, along with position information from the translation stage.

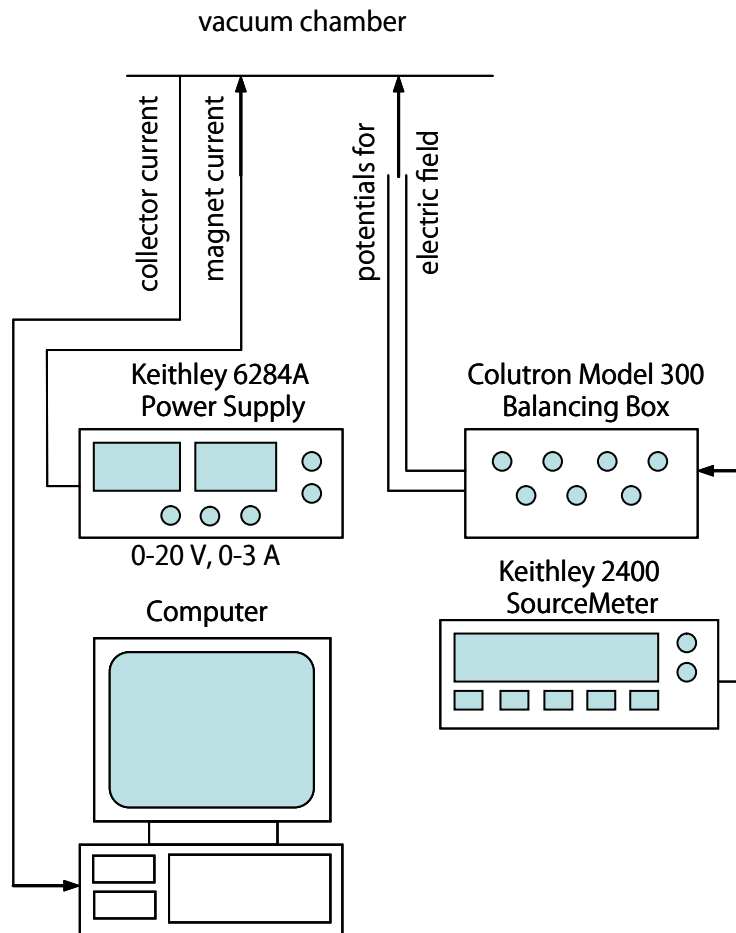


Figure 2.15: ExB data acquisition system

### 2.4.3 Uncertainty Analysis

There were several sources of error and uncertainty in the ExB results, including internal CEX collisions, interactions between the probe and the thruster plume, and spread in the ion velocities due to collector and aperture sizing. As mentioned previously, there was a mesh-covered hole in the bottom of the ExB housing, so that neutrals could not build up inside the device. This was done to reduce neutral density inside the device, so that the high velocity  $\text{Xe}^+$  signal could not be attenuated due to CEX collisions between  $\text{Xe}^+$  and neutral Xe atoms. However, although this decreased the neutral density, it was impossible to completely eliminate the density of neutrals within the device. Because of the size of the hole, it was assumed that the density inside the device equilibrated to the background neutral density.

In the 650W case, the background density of neutrals was significantly higher than in the 200W case, as evidenced by a higher vacuum pressure within the chamber. Additionally, the background neutral density was likely higher near the exit plane of the thruster than far from it. This change in neutral density is hard to quantify without a direct measurement, but from a qualitative standpoint it is fair to say that there is likely greater signal attenuation at smaller axial distances, and also that the signal attenuation is more significant for the 650 W case.

It also should be mentioned that there was some unavoidable interaction between the probe housing and the thruster plume. Although attempts were made to minimize the surface area that was exposed to the thruster plume, for example by adding a conical taper to the front of the device, there was still visible interaction between the ion beam and the device. The other countermeasure that was taken was to reduce the amount of time that the probe spent in front of the thruster plume during the scan. A shorter time scale for the scan also helped to decrease the neutral buildup inside the device due to neutrals entering through the front aperture.

One quantifiable uncertainty in the ExB data is the spread in ion velocities and trajectory angles that could be measured as a result of the aperture and collector sizing. This is illustrated in Figure 2.16. Because the collector and apertures have a finite width and acceptance angle, the device can measure ions that are not completely orthogonal to the electric and magnetic fields, and also ions that have a velocity that is not exactly equal

to the  $E/B$  value.

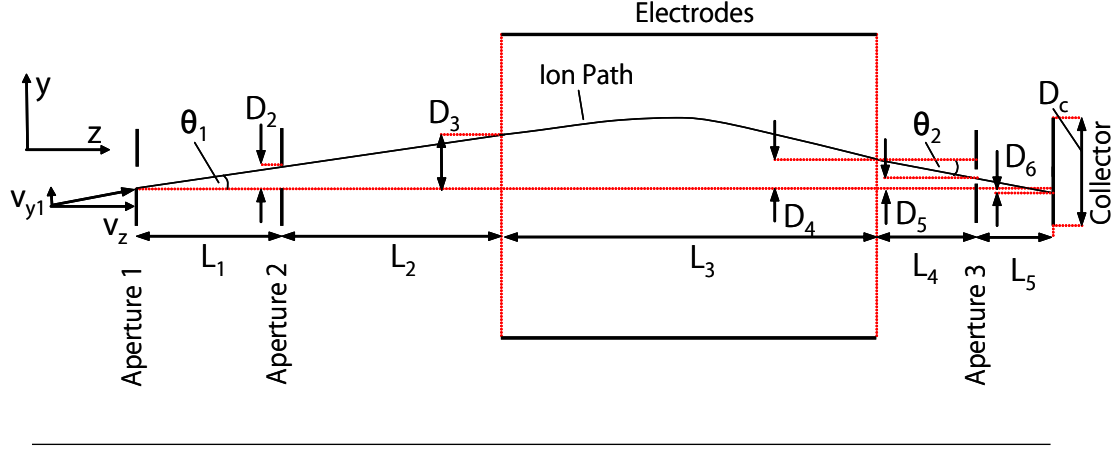


Figure 2.16: ExB resolution calculation

The spread in the data can be calculated as follows. First, start by calculating the maximum input angle,  $\theta_1$ , for ions:

$$\theta_1 = \tan^{-1} \left( \frac{D_2}{L_1} \right). \quad (2.3)$$

This allows the y-position of the ion at the entrance of the filter to be calculated ( $D_3$ ):

$$D_3 = (L_1 + L_2) \tan(\theta_1). \quad (2.4)$$

Then, by applying the Lorentz force equation (Eqn. 2.1) and assuming that acceleration in the z-direction is negligible, this allows the acceleration in the y-direction to be calculated:

$$a_y = -\frac{q}{m} (E - v_z B). \quad (2.5)$$

Note that the ratio of  $E/B$  is set to measure a certain ion velocity:

$$v_{set} = \frac{E}{B}. \quad (2.6)$$

So Eqn 2.5 can be rewritten as:

$$a_y = -\frac{q}{m} (v_{set} - v_z) B. \quad (2.7)$$

The time it takes for the ion to transit the filter can be estimated by dividing the filter length by the axial velocity:

$$t_3 = \frac{L_3}{v_z}. \quad (2.8)$$

If transit time and acceleration are known, then the position and velocity of the ion at the end of the filter can be calculated, as well as the value of  $\theta_2$ :

$$D_4 = D_3 + (v_{y1}) t_3 + \frac{1}{2} a_y t_3^2 \quad (2.9)$$

$$v_{y4} = v_{y1} + a_y t_3 \quad (2.10)$$

$$\theta_2 = \tan^{-1} \left( \frac{v_{y4}}{v_z} \right). \quad (2.11)$$

Finally, the y-position at the z-position of the third aperture ( $D_5$ ) and at the collector ( $D_6$ ) are:

$$D_5 = D_4 + L_4 \tan(\theta_2) \quad (2.12)$$

$$D_6 = D_5 + L_5 \tan(\theta_2). \quad (2.13)$$

In order for the ion to pass through the third aperture, the condition on  $D_5$  must be:

$$|D_5| \leq \frac{D_{A3} + D_2}{2}, \quad (2.14)$$

where  $D_{A3}$  is the width of the third aperture. Additionally, for the ion to hit the collector, the condition on  $D_6$  is:

$$|D_6| \leq \frac{D_c + D_2}{2}. \quad (2.15)$$

So if the ion trajectory satisfies the two conditions above, then it will be measured. Using this set of equations, it was determined that the spread in velocities that could be measured was less than one percent of the desired velocity as defined by the E/B ratio.

## 2.5 Diagnostic Instruments - Retarding Potential Analyzer

### 2.5.1 Instrument Overview

A retarding potential analyzer (RPA) was used to take energy distribution measurements in the SPT-70 plume. A RPA is a parallel grid electrostatic analyzer that uses an applied potential (the "retarding" potential) to accept or reject ions based on their energies. Figure 2.17 shows a schematic of a typical RPA. The front grid is usually allowed to float at the plasma potential, while the "screen" grid is biased at a low negative potential to keep out electrons. The "retarding" grid potential is ramped from zero to several hundred or thousand volts, depending on the acceleration voltage of the thruster being examined. Sometimes, a "suppressor" grid is used to prevent secondary electrons (i.e., electrons produced due to ions colliding with the collector) from causing a false current reading. A collector at the back of the device measures the ion current.

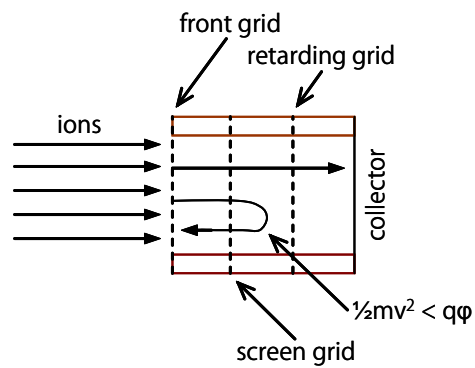


Figure 2.17: RPA Schematic.

The device operates on the principle of energy conservation:

$$\frac{1}{2}mv^2 = q\phi. \quad (2.16)$$

That is, ions with enough kinetic energy to overcome the potential barrier will pass through the retarding grid and reach the collector. In this way, the RPA acts as a "high-pass" filter for ion energies [26]. The raw data produced by the RPA, as illustrated in Figure 2.18, represents the "integrated" ion current, i.e., the total current of ions with energies *above* the specified energy. To determine the current of ions *at* a given energy, one must take the

derivative of the raw data, also shown in Figure 2.18.

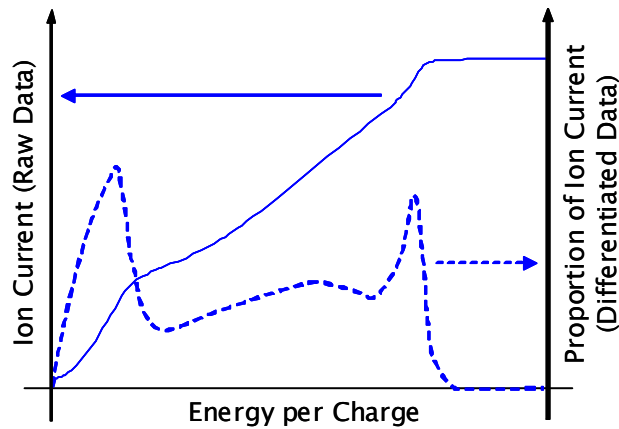


Figure 2.18: RPA sample trace. Taking the derivative of the raw data gives the energy distribution.

One other point to note is that the RPA does not distinguish between charge species. According to Equation 2.16, a double ion must have twice the kinetic energy as a single ion to overcome the same potential barrier. However, using RPA data it is not possible to make the distinction between a single ion that is moving with a certain kinetic energy and a double ion that is moving with twice that energy.

## 2.5.2 Instrument Design and Data Acquisition System

The particular RPA used in the experiment employed 3 grids, as shown in Figure 2.19. The front grid was mounted so that it was flush with the face of the RPA housing. Both the front face and grid were electrically isolated from the body of the RPA, which was grounded. The screen grid was mounted 1 mm behind the front grid, and during operation was set at -20 V. Behind the screen grid was the "retarding" grid, to which the voltage ramp was applied to decelerate ions entering the device. The spacing between the screen and retarding grids was 2.5 mm. The collector anode was located 1.0 mm behind the retarding grid.

Each of the grids were isolated from each other using Celazole spacers with an inner diameter of 14.3 mm and an outer diameter of 23.1 mm. The front grid had a pattern of twenty-seven 0.4 mm diameter holes, thus establishing an effective input area of  $3.39 \times 10^{-6} \text{ m}^2$ . The front grid was manufactured from 0.1 mm thick molybdenum. The screen and

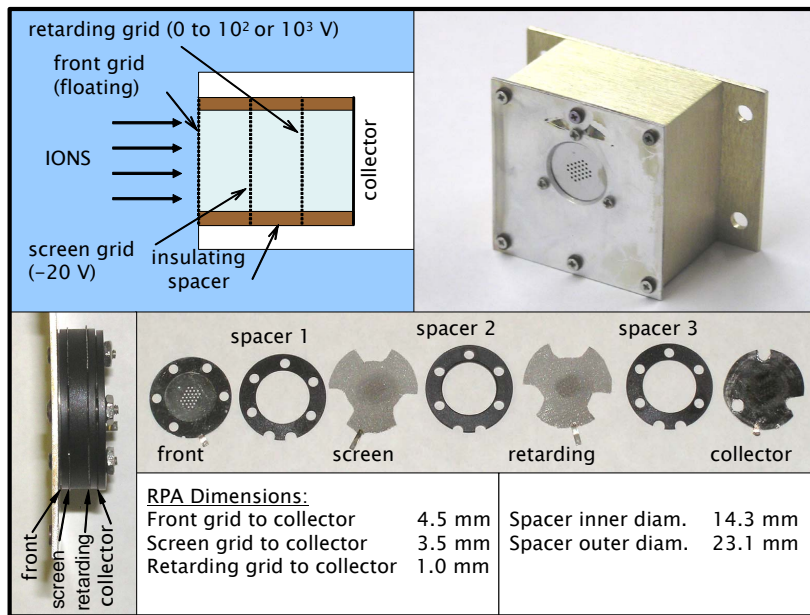


Figure 2.19: RPA photo and schematic.

retarding grids were both made out of a stainless steel mesh, 0.2 mm thick, with an open area fraction of 0.36. These two grids were positioned such that the holes in the mesh were not aligned, to prevent secondary or tertiary alignment patterns (Moire patterns) depending on the angle of the device relative to the ion source. All of the grids had an outer diameter of 22 mm. The collector anode consisted of a 22 mm diameter, 0.1 mm thick, tungsten disk. The angle of acceptance of the device was 15 deg (full angle) and was determined experimentally [27].

The components of the RPA data acquisition system are shown in Figure 2.20. A standard DC power supply was used to apply a potential of -20 V to the screen grid, while a function generator plus a high-voltage amplifier were used to create the ramp voltage for the retarding grid. The current to the collector was amplified using a gain of  $10^5$  to  $10^8$ , depending on the magnitude of the signal. The voltage from the signal generator was sent to the control computer through a data acquisition box, and this signal was synched to the acquisition of the current measurement. The resolution of the data acquisition system could be varied using a Labview control program.

During operation, the RPA was placed at a specific angle relative to the thruster centerline and a potential sweep was made. This allowed the energy distribution of ions to

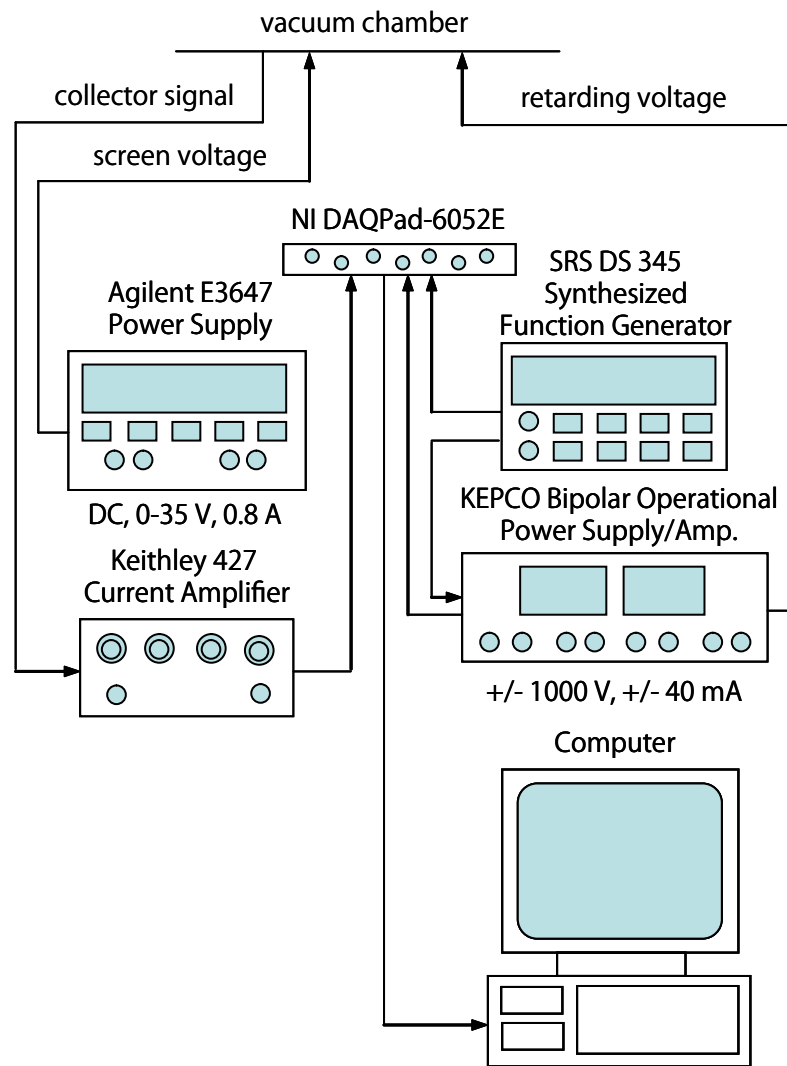


Figure 2.20: RPA data acquisition system.

be determined at specific locations in the plume. See Section 2.6 for a description of the scans taken with the RPA.

### 2.5.3 Uncertainty Analysis

Uncertainty and errors in the RPA results comes from a number of sources, namely: charge exchange (CEX) collisions inside the device, ion optics of the grids, and the differentiation method that was used. In some of the RPA scans that are close to the thruster centerline (0 deg and 10 deg cases, for example, in Figures 5.16 and 5.19), one can see ions with energies per charge that are greater than the acceleration potential of the device. Theoretically, one should not see ions that have kinetic energies greater than that which can be obtained by acceleration through a certain potential drop (250 eV in the 200W case, 300 eV in the 650 W case).

One explanation for ions with energies per charge that are higher than the acceleration potential is that these ions that have gone from  $\text{Xe}^{2+}$  to  $\text{Xe}^+$  in a CEX collision. Such ions can have an energy/charge greater than 300eV/q. If you look at the energy conservation equation ( $q\phi = 1/2mv^2$ ), a doubly charged ion will have double the kinetic energy as a singly charged ion if accelerated through the same potential. In a CEX collision between a  $\text{Xe}^{2+}$  ion and a Xe atom in which two  $\text{Xe}^+$  are produced, one of the  $\text{Xe}^+$  ions will attain the kinetic energy of the  $\text{Xe}^{2+}$  ion after the collision, and thus will have twice the energy per charge as the  $\text{Xe}^{2+}$  ion.

They are most likely generated at locations where the neutral density is high, such as near the thruster exit plane. However, an  $\text{Xe}^+$  ion generated through this process would likely appear at around twice the acceleration potential, since it will have been the result of a collision between a neutral and a  $\text{Xe}^{2+}$  ion that had been accelerated through the full thruster potential. Instead, what is seen in the experimental data is a tail extending from the primary beam energy peak. This tail is more likely the result of CEX interactions inside the RPA, where the incoming  $\text{Xe}^{2+}$  ions have been slowed by the applied retarding potential before they undergo a CEX collision. As will be seen, the fact that this tail is a significant contributor to the ion current in the 650 W case, but not so much in the 200 W case, suggests that the higher densities associated with the 650 W case are a factor. Additionally, CEX interactions with surfaces inside the RPA (in which the  $\text{Xe}^{2+}$  loses an electron to a surface atom) are also a possible contributor to this phenomena.

Another source of uncertainty relates to the ion optics of the grids. As the potential on the retarding grid increases, a larger range of ion energies can be accepted through the grid holes due to the fact that the potential drops slightly within each hole. To simulate ion trajectories near a grid hole inside the RPA, a program called Simion was used [28]. Simion calculates the electrostatic potential distribution for a given configuration in 2D, and also simulates ion trajectories through the configuration. An example of a Simion calculation for the problem at hand is shown in Figure 2.21. This figure shows that the potential barrier is slightly lower within the hole, meaning that an ion with an energy per charge lower than the retarding potential can pass through it. The results of the Simion simulations are shown in Table 2.2. These results suggest that the uncertainty is roughly 2-3 percent of the applied retarding voltage.

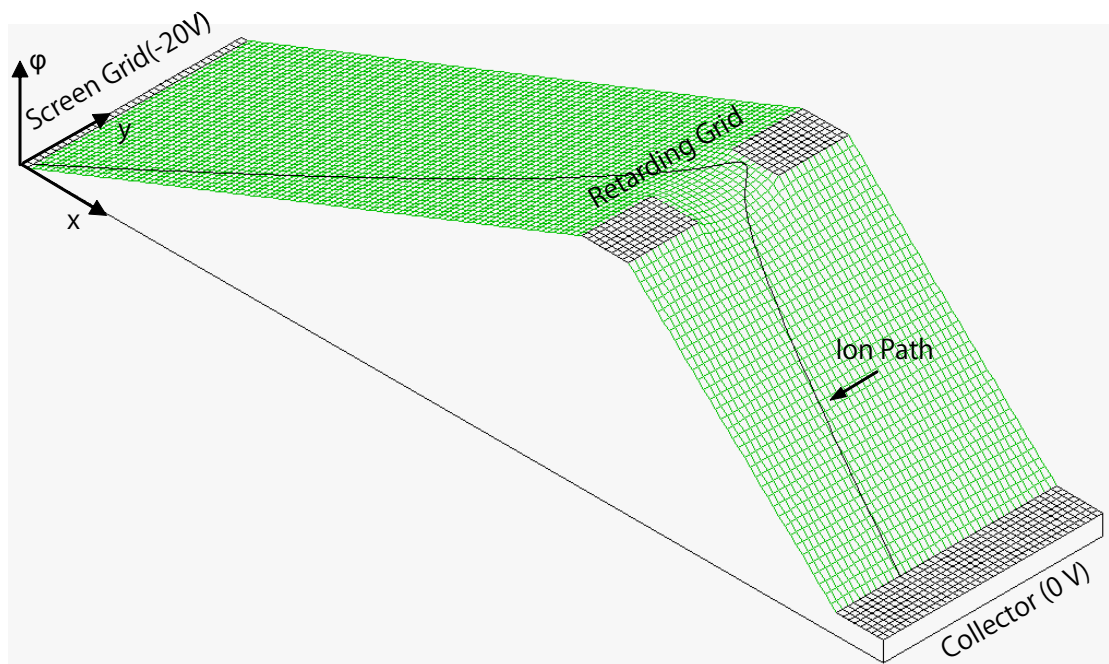


Figure 2.21: Example result from Simion. The height of the graph represents the potential,  $\phi$ . In this particular case the retarding potential was set to 200V, with the screen grid voltage at -20V and the collector at 0 V. The ion had an initial kinetic energy of 119.5 eV, which is lower than the 120 eV that would be needed to get over the potential barrier if the grid hole was not present.

In addition to uncertainty in the data caused by the grid optics, the way in which the derivative of the raw data is taken determines the uncertainty in the energy distribution

Table 2.2: RPA uncertainty due to ion optics

Retarding Voltage [V]	Lowest Accepted Energy/Charge [eV/q]	$\Delta V$ [V]	Proportion of Retarding Voltage
50	48.8	-1.2	0.024
100	97.8	-2.2	0.022
150	146.7	-3.3	0.022
200	195.7	-4.3	0.022
250	244.7	-5.3	0.021
300	293.5	-6.5	0.022
350	342.6	-7.4	0.021
400	391.5	-8.5	0.021

calculation. In this study, there was a sufficient amount of noise that some averaging of the raw data had to be done. It was found that an average over 20 points was sufficient. This, therefore, reduced the number of data points in the file from 10,000 to 500. Additionally the slope of the data at a given point was calculated using the following algorithm:

$$\frac{dI}{dV} = \frac{n \sum V_{avg} I_{avg} - \sum V_{avg} \sum I_{avg}}{n \left( \sum V_{avg}^2 - (\sum V_{avg})^2 \right)}, \quad (2.17)$$

where  $n$  is the number of data points over which the slope was calculated, and the sums are taken over each set of  $n$  data points, using the averaged current and voltage values (such that the center point of each sum is a data point in the differentiated data set). In the 200 W case it was determined that  $n=3$  led to a differentiated curve with a satisfactory amount of smoothness, so after the differentiation the number of points in the data set was 166. In the 650 W case, it was necessary to set  $n = 5$ , so the number of points was reduced to 100. Since both scans were taken from -50 to 450 V, for a total change of 500 V, the uncertainties were  $500/166 = 3.01$  eV/q for the 200 W case and  $500/100 = 5.00$  eV/q for the 650W case.

## 2.6 Summary of Scans

In the case of the faraday probe, for all scans the instrument angle was set to zero degrees and it was moved in the transverse ( $y$ ) direction, across the thruster face, as shown in Figure 2.22. Each scan was taken at a different axial ( $x$ ) location. The probe angle was

set at zero and not changed due to its large angle of acceptance. Table 2.3 summarizes the data collected using the faraday probe.

In the case of the ExB filter, two types of scans were taken: transverse and axial. During a transverse scan, the axial location and angle was fixed and the probe was moved perpendicular to the thruster centerline. Because the angle of acceptance of the ExB filter was less than a degree, the probe angle was varied to determine the dependence of ion current on angle. During an axial scan, the transverse location was fixed and the probe was moved in the direction of the thruster, parallel to the thruster centerline. Table 2.4 summarizes the data collected using the ExB filter.

Unlike the other probes, the RPA could not be moved while it was taking data. Instead, it was positioned at a specific angle off of the thruster centerline, at a specific distance away from the thruster, as shown in Figure 2.23. For most of the scans, the distance was 400 mm, but in some cases the RPA had to be moved further away, to ensure that the device used to amplify its signal was not saturated, and also to prevent electrical shorts inside the probe. Table 2.5 summarizes the data collected using the RPA.

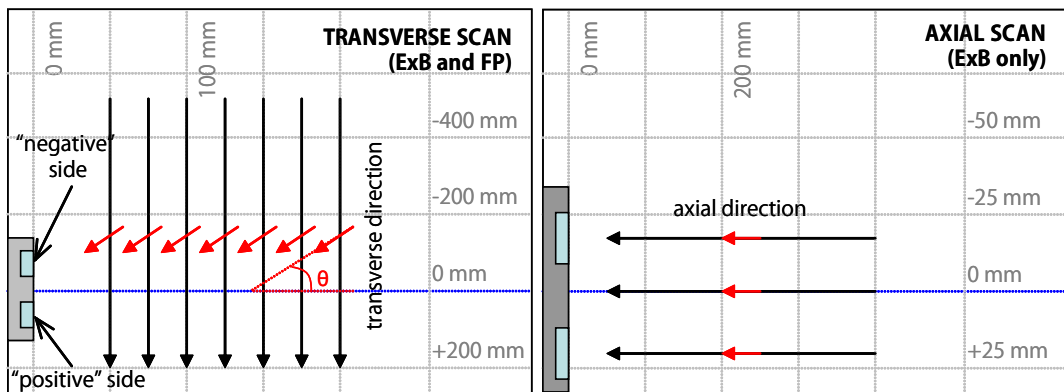


Figure 2.22: Transverse and axial scans. Note that the angle of the Faraday probe was set to 0

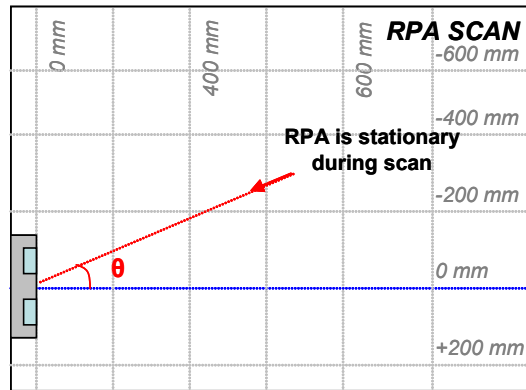


Figure 2.23: RPA scans. During each scan, the RPA position was fixed.

Table 2.3: Summary of Faraday probe scans

Thruster Operating Point	Axial Position [mm]	Transverse Position [mm]	Angle of Faraday Probe [°]	Chamber Pressure [torr]	Cathode Float Voltage [V]
200 W	15 to 1500	-477 to 223	0	$3.0 \times 10^{-6}$	-14.0
650 W	15 to 1500	-477 to 223	0	$6.5 \times 10^{-6}$	-23.0

Table 2.4: ExB scan summary

Thruster Operating Point	Type of Scan	Axial Position [mm]	Transverse Position [mm]	Angle of ExB Probe [°]	ExB Setting	Chamber Pressure [torr]	Cathode Float Voltage [V]
200 W	Trans.	50, 75, 100, 125, 150, 175, 200	-477 to 223	0, 10, 20, 30, 40, 50, 60, 70	ON (set at Xe <sup>+</sup> location)	$2.5 \times 10^{-6}$	-15.4
200 W	Trans.	50, 75, 100, 125, 150, 175, 200	-477 to 223	0, 10, 20, 30, 40, 50, 60, 70	OFF (no deflection)	$2.5 \times 10^{-6}$	-15.4
650 W	Trans.	50, 75, 100, 125, 150, 175, 200	-477 to 223	0, 10, 20, 30, 40	ON (set at Xe <sup>+</sup> location)	$6.0 \times 10^{-6}$	-35.5
200 W	Axial	400 to 50	-27, -4, 0, 23	0	ON (set at Xe <sup>+</sup> location)	$2.5 \times 10^{-6}$	-15.4
200 W	Axial	400 to 50	-27, -4, 0, 23	0	OFF (no deflection)	$2.5 \times 10^{-6}$	-15.4
650 W	Axial	400 to 50	-27, -4, 0, 23	0	ON (set at Xe <sup>+</sup> location)	$6.0 \times 10^{-6}$	-35.5

Table 2.5: RPA scan summary

Thruster Operating Point	Distance from Thruster Center [mm]	Angle Off of Thruster Centerline [°]	Chamber Pressure [torr]	Cathode Float Voltage [V]
200 W	400	0, 10, 20, 30, 40, 45, 50, 55, 60, 65, 70, 75, 80, 85, 90	$2.5 \times 10^{-6}$	-15.0
650 W	400	45, 50, 55, 60, 65, 70, 75, 80, 85, 90	$8.0 \times 10^{-6}$	-14.0
650 W	600	10, 20, 30, 40, 45	$8.0 \times 10^{-6}$	-14.0
650 W	1000	0	$8.0 \times 10^{-6}$	-14.0

## Chapter 3

# Simulation Approach - HPHall

In the simulation portion of this research, two approaches were used. The first was an existing hybrid-PIC Hall thruster code known as HPHall, which was used to investigate both the central jet and high angle, high energy ions. As was mentioned previously, internal hybrid-PIC codes only simulate a small portion of the near-field. Nonetheless, this type of model can still give insight into the acceleration of ions inside the channel and immediately outside the exit plane, even if it does not capture the full extent of the near-field region. Furthermore, a better alternative (such as a well-validated fully-kinetic or fluid-based model) was not readily available.

This chapter describes the simulation method used by the hybrid-PIC model. In the case of HPHall, since it was an existing code with a substantial development history, most of the information is summarized from other sources, with references provided as needed.

### 3.1 Hybrid-PIC Model Overview

As stated in the introduction, HPHall is a hybrid-PIC Hall thruster code that treats electrons as a fluid and ions as particles-in-cell. HPHall was first developed by J. M. Fife and M. Martinez-Sanchez at MIT during the mid-1990s [14]. In the ensuing years, it has gained wide acceptance by the Hall thruster research community. Currently, HPHall, as well as similar codes based on hybrid-PIC methods, are used by most institutions that engage in the modeling of these thrusters [15–18]. Although other approaches exist, such as pure fluid codes that model electrons and ions as fluids [29], and fully kinetic codes that handle both species using a particle-based method [30, 31], none are as widely used as hybrid-PIC.

For the definitive reference on HPHall, one should consult the Ph.D. thesis of J.

M. Fife [14] (unless otherwise noted, the content of this section represents a summary of the information presented in this document). In spite of the modifications that have been made to HPHall since its initial creation, the basic solution method and assumptions have not changed. As illustrated in Figure 3.1, the basic method is as follows. First, the solution grid and magnetic field are generated by separate solvers outside of HPHall. These files are required by HPHall to initiate the solution process, as well as a third file that specifies the input parameters of the code. Initially, the solution domain is not populated by particles, unless files from a previous HPHall run are used. The grid, magnetic field, and input parameter information is then fed into the fluid solver and the solution process initiated.

During the solution process, HPHall integrates the electron fluid equations on a two-dimensional domain, then moves the ions based on the results from the electron sub-model. The major assumptions of the code are as follows: (1) the plasma is quasi-neutral (i.e.,  $n_e = n_{Xe^{1+}} + n_{Xe^{2+}}$ ), (2) the induced magnetic field is small compared to the applied field and can be neglected, (3) the problem is axisymmetric about the thruster centerline. Using these assumptions, the code simulates the plasma between two boundaries, the “anode line” and the “cathode line”. Both the anode and cathode “lines” correspond to  $\lambda$ -lines, the magnetic streamlines that will be described in the following sub-section. On these boundaries, plasma parameter values, such as potential and electron temperature, are specified. An example solution domain for the SPT-70 is shown in Figure 3.2.

### 3.1.1 Electron Sub-model

In the electron sub-model, the electrons are assumed to be strongly-magnetized, so electron motion can be split into two clear parts: motion along and motion across magnetic field lines. The magnetic field can be described using Maxwell's equations:

$$\nabla \cdot \vec{B} = 0 \quad (3.1)$$

$$\nabla \times \vec{B} = \mu_0 \left( \vec{j} + \epsilon_0 \frac{\partial E}{\partial t} \right) \approx 0. \quad (3.2)$$

In these equations, it has been assumed that the magnetic field has no azimuthal component. It has also been assumed, based on measurements, that the azimuthal current density and the electric field variation (the RHS of Eqn. 3.2) are negligible compared

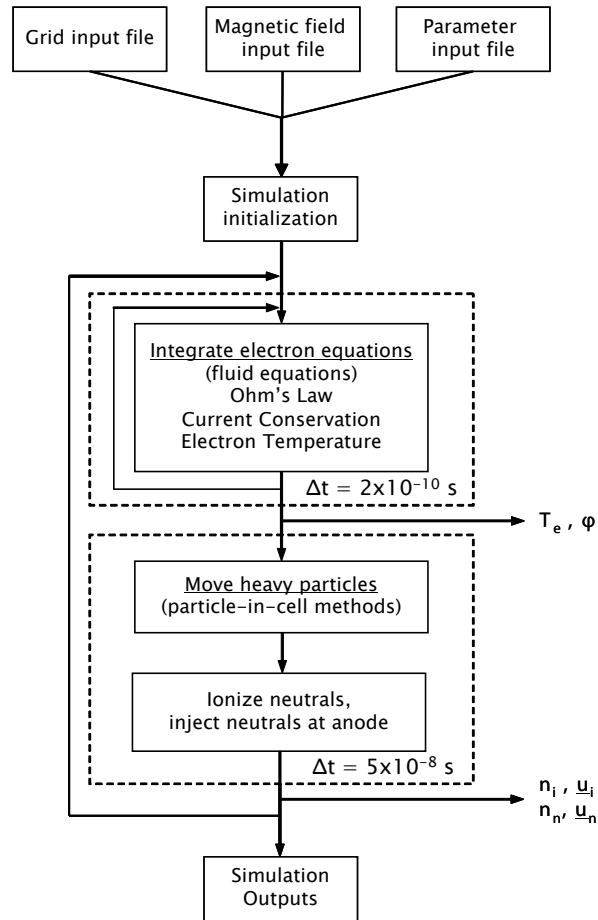


Figure 3.1: HPHall program flow. This graphic has been modified from one appearing in [14]

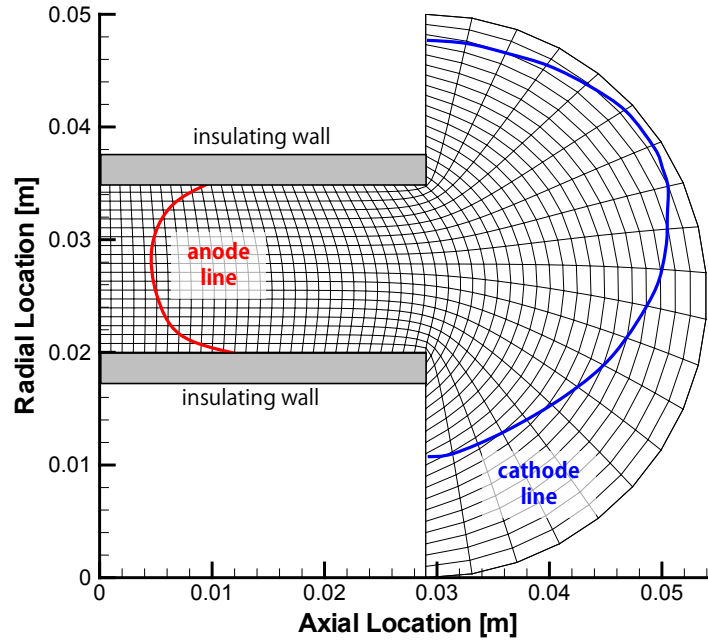


Figure 3.2: SPT-70 solution domain. Cathode and anode lines correspond to magnetic streamlines known as  $\lambda$  lines.

to the gradients in the magnetic field. Based on these equations, one can define a magnetic potential function,  $\sigma$ , and a magnetic stream function,  $\lambda$ , that satisfy the following relationships.

$$\vec{B} = \nabla\sigma \quad (3.3)$$

$$\nabla^2\sigma = 0 \quad (3.4)$$

$$\nabla\lambda = r(B_r\hat{z} - B_z\hat{r}). \quad (3.5)$$

It is the magnetic “stream-lines” or “ $\lambda$ -lines” over which the electron equations are integrated. The equations that are solved by the electron sub-model are (1) Ohm’s law, (2) current conservation, and (3) electron temperature. A Maxwellian electron distribution is assumed, and it is also assumed that the electron temperature is constant along each  $\lambda$ -line. Therefore, one can think of HPHall almost as a “quasi”-linear code, that varies

across  $\lambda$ -lines.

The derivation of the electron equations, as well as the integration method, is fairly complicated. Rather than describe the specifics here, the reader is instead referred to Fife's PhD thesis [14].

### 3.1.2 Heavy Particle Sub-model

In the heavy particle sub-model, a separate simulation mesh is used to calculate particle motion. Rather than advance the particles in physical space directly, the problem is first transferred to a simpler domain. The relatively complicated  $r - z$  mesh shown in Figure 3.3 is transformed to a rectangular  $\xi - \eta$  mesh, where  $\xi$  and  $\eta$  are represented by integer values, as shown in Figure 3.3. The particle positions, velocities, and forces are also transformed to the  $\xi - \eta$  plane. Particle motion is then calculated on this plane, and transformed back to the physical  $r - z$  plane [18].

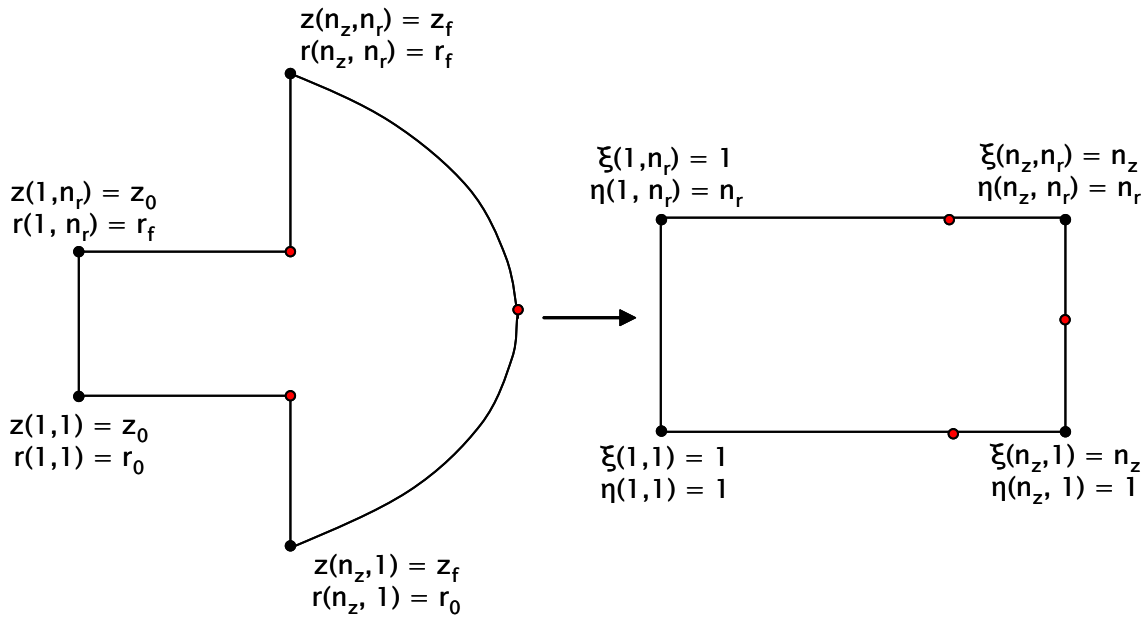


Figure 3.3: Transformation from  $r-z$  to  $\xi - \eta$  plane

Rather than modeling every particle, which would lead to unfeasible computation times, PIC methods deal with “macro” particles. Macro-particles (MPs) represent clusters of particles; in the case of HPHall, the number of actual particles per MP is scaled such that there are 20 to 50 MPs of each species (ions and neutrals) per cell, giving a total of

roughly  $1 \times 10^5$  total MPs in the simulation. Since the neutral density is about 3 orders of magnitude greater than the ion density, the number of ions per MP is about 3 orders of magnitude smaller than the number of neutrals per MP.

Ion motion is calculated using the following equations:

$$\vec{v}_{m+1/2} - \vec{v}_{m-1/2} = \Delta t \left[ \frac{q}{m_i} \left( \vec{E} + \vec{v}_{m-1/2} \times \vec{B} + \vec{R}_0 \right) \right] \quad (3.6)$$

$$\vec{x}_{m+1} - \vec{x}_m = \Delta t \vec{v}_{m+1/2}, \quad (3.7)$$

where  $m$  denotes the ion time step, and  $\vec{R}_0$  is the sum of all of the non-electromagnetic forces [18].

Neutral particles are initially injected into the domain at the anode, at a rate specified by the propellant flow rate of the thruster. Once they enter the domain, they can reflect off of the walls. Additionally, ions can recombine with electrons at the walls to produce neutrals. Neutrals are not subject to electromagnetic forces, but can undergo collisions with other species. Ionization in Hall thrusters occurs when an electron impacts a neutral or an ion. In HPHall this is modeled by a simple ionization rate coefficient, as follows:

$$\dot{n}_i^{1+} = \zeta(T_e) n_e n_n \quad (3.8)$$

$$\dot{n}_i^{2+} = \zeta^{0 \rightarrow 2}(T_e) n_e n_n + \zeta^{1 \rightarrow 2}(T_e) n_e n_i^{1+}, \quad (3.9)$$

where  $\zeta$  is the neutral to  $\text{Xe}^{1+}$  coefficient,  $\zeta^{0 \rightarrow 2}$  is the neutral to  $\text{Xe}^{2+}$  coefficient, and  $\zeta^{1 \rightarrow 2}$  is the  $\text{Xe}^{1+}$  to  $\text{Xe}^{2+}$  coefficient. All of the  $\zeta$ s are empirically-derived functions of  $T_e$  that depend on neutral/ion species.

Additionally, charge exchange (CEX) collisions have been added to the JPL version HPHall. Charge exchange is a process by which a fast ion and a slow neutral collide to produce a slow ion and a fast neutral. However, in the current study CEX collisions were not “turned on,” since the way in which the collisions were implemented caused an extremely large number of simulated particles, several orders of magnitude above the normal value, to be created. This slowed down the simulation to an unacceptable degree, leading to the decision to turn CEX collisions off.

### 3.1.3 Wall Interactions

In a real Hall thruster, there is a thin region of non-neutrality known as a plasma sheath. In a quasi-neutral plasma, the thermal fluxes of ions and electrons are not equal, due to the higher temperature and smaller mass of the electrons. Therefore, to keep the wall from continually becoming more negative, the wall potential takes on a steady state value that is negative relative to the potential of the plasma far from the wall, as shown in Figure 3.4. This rejects electrons and thus keeps the fluxes balanced. As will be discussed in Section 4.1, the velocity of ions into the sheath must exceed the “Bohm velocity,” i.e.:

$$v_i > \sqrt{\frac{kT_e}{m_i}}. \quad (3.10)$$

This acceleration to the Bohm velocity occurs over a region called the “pre-sheath,” as shown in Figure 3.4.

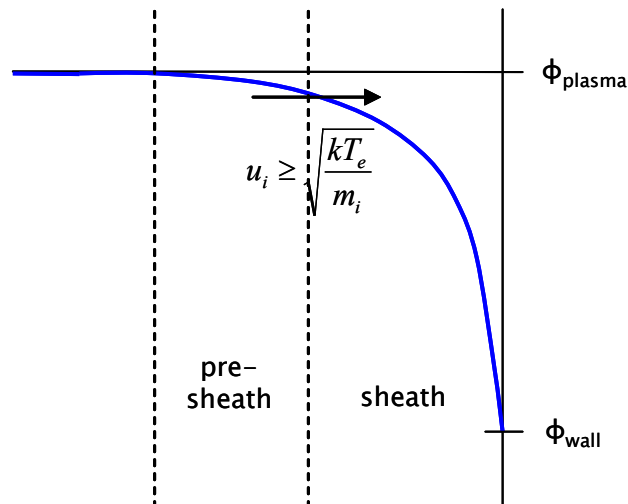


Figure 3.4: Shape of the plasma sheath at the wall.

As mentioned, one of the primary assumptions of HPHall is that the plasma is quasi-neutral, and as a consequence the sheath is not resolved. There are two methods available to ensure that the Bohm condition is satisfied at the wall. One involves changing the way the weighting is conducted at the wall, i.e., modifying how parameter values are weighted at each node of the simulation mesh adjacent to the wall. In the original version of HPHall, the method used was “one-sided” weighting, meaning that only values from the simulation-side

of the wall were used. This resulted in the underestimation of values that tended to increase towards the wall. However, it was shown that this method tends to only work if the mesh size is very fine [18, 32].

Because it was desired to find a solution to this problem that would not require a finer mesh (and hence an unacceptably long computation time), the second approach that was implemented to force the Bohm condition at the wall. This is done, in the cells adjacent to the wall, by assigning the Bohm velocity to any ions with a radial velocity that is less than the Bohm velocity [32]. Unless otherwise specified, this is the method that is used in the HPHall simulations presented in this thesis.

### 3.2 HPHall at the Jet Propulsion Laboratory

The version of HPHall used for the analysis in this thesis is one that consists of changes made to the code primarily by F. Parra at MIT and R. Hofer at JPL [18, 32–35]. The modifications implemented by F. Parra include both improvements to the code in terms of capabilities as well as physics. For example, two major additions to the code were algorithms regarding charge exchange and enforcement of the Bohm condition at the channel wall (the Bohm condition refers to the requirement that an ion must enter the region of non-neutrality near the wall with a velocity greater than its acoustic speed.). Reference [Parra JAP 2006] provides a summary of the changes implemented by F. Parra.

Further changes were made to the code by R. Hofer, I. Mikellides, and I. Katz at JPL. One major contribution to the code was an improved electron mobility model. In HPHall, electron mobility is handled by dividing the simulation domain into separate regions, with a mobility coefficient assigned to each region, and linear interpolation of the coefficient between regions. By implementing a 3-region model, as opposed to the previous 2-region model, the JPL modelers were able to improve the code's agreement with experimental results [35]. The cross-field electron mobility is defined as follows (note, Eqns. 3.11 to 3.18 are from [35]):

$$\mu_{e\perp} = \frac{e}{\nu_e m_e} \left( \frac{1}{1 + \Omega_e^2} \right), \quad (3.11)$$

where  $\Omega_e = \omega_{ce}/\nu_e$ , the electron Hall parameter, and  $\omega_{ce} = eB/m_e$ , the electron cyclotron frequency. In this case  $\nu_e$  is the total effective electron collision frequency, defined

as:

$$\nu_e = \nu_{en} + \nu_{ei} + \nu_w + \nu_b, \quad (3.12)$$

where  $\nu_{en}$  is the electron-neutral collision frequency,  $\nu_{ei}$  is the electron-ion collision frequency,  $\nu_w$  is the collision frequency of the electrons with the walls, and  $\nu_b$  is the collision frequency associated with “anomalous” transport mechanisms, such as turbulent plasma fluctuations. This collision frequency is defined as:

$$\nu_b = \frac{1}{16}\alpha\omega_{ce}, \quad (3.13)$$

where  $\alpha$  can be adjusted to match experimental results. In the 3-region model,  $\alpha$  is defined as:

$$\alpha = \begin{cases} \alpha_c & z \leq z_c, \\ \alpha_c f_c + \alpha_e f_{e1} & z_c < z < z_{e1}, \\ \alpha_e & z_{e1} < z < z_{e2}, \\ \alpha_e f_{e2} + \alpha_p f_p & z_{e2} < z < z_p, \\ \alpha_p & z \geq z_p, \end{cases} \quad (3.14)$$

where the subscripts  $c$ ,  $e$ , and  $p$  stand for values in the channel, exit, and plume regions, respectively. The fractions  $f$  are defined as:

$$f_c = 1 - f_{e1} \quad (3.15)$$

$$f_{e1} = \frac{z - z_c}{z_{e1} - z_c} \quad (3.16)$$

$$f_{e2} = 1 - f_p \quad (3.17)$$

$$f_p = \frac{z - z_{e2}}{z_p - z_{e2}}. \quad (3.18)$$

So there are three regions over which  $\alpha$  is constant, and two intermediate regions over which the  $\alpha$  values are interpolated. Overall, this makes for seven adjustable parameters:

Table 3.1: Cathode and anode parameters for HPHall.

Parameter	Value
$z_{anode}$	0.0040 m
$r_{anode}$	0.0275 m
$z_{cath}$	0.0049 m
$r_{cath}$	0.0275 m
$T_{e_{cath}}$	64678 K
$\phi_{cath}$	29.5 V

$\alpha_c, \alpha_e, \alpha_p$ , and  $z_c, z_{e1}, z_{e2}, z_p$ . In the JPL version of HPHall there is one additional adjustable parameter, called  $Te_{\perp}/Te_{\parallel}$ , which specifies the ratio of the electron temperature parallel to the magnetic field lines, versus perpendicular to the magnetic field lines.

An additional change made at JPL is an updated ionization cross section, which resulted in a greater number of  $Xe^{2+}$  ions being produced, and required an alteration to be made to the electron energy equation. Also, modifications were made to the wall sheath model that had been previously implemented by F. Parra [32]. See References [33–35] for a discussion of these changes to the code.

### 3.3 Application to the Ion Trajectory Problem

#### 3.3.1 HPHall Solution Domain

As can be seen in Figure 3.2, the HPHall solution domain includes the thruster channel, as well as a small portion of the near field. It is important to note that between the cathode line and the boundary of the domain, the solution is simply a linear interpolation between the parameter values at the two locations [35]. Figure 3.2 shows the position of the cathode line relative to the boundary and reveals that there is only a small portion of the domain that is treated in this fashion. The locations and conditions at the anode line and the cathode line are summarized in Table 3.1. Note that the “locations” of the cathode and anode are points through which the cathode and anode lines pass (HPHall calculates the line from the specified point).

#### 3.3.2 Magnetic Field and Electron Mobility Analysis

As will be discussed in Section 5.3, the experimental data suggest that the magnetic field strength may be correlated with plume collimation and high angle, high velocity ions. It was

hypothesized that the magnetic field could change the electric potential contours enough to produce the necessary radial acceleration to explain the experimental results. In a Hall thruster, since the electrons are highly magnetized, they will tend to not move perpendicular to magnetic field lines, while freely moving parallel to field lines. This causes a negligible density gradient of electrons parallel to magnetic field lines, but a large gradient perpendicular to the field lines. Thus, the electric potential contours follow the magnetic field lines, for the most part. The bottom line is that the electron mobility relative to field lines strongly affects the potential distribution.

If the magnetic field is primarily in the radial direction, then the electric field will be primarily in the axial direction. However, if the field lines have a significant axial component, then the electric field will have a substantial radial component, and thus ions could be accelerated out to high angles. Additionally, if some of the potential drop occurs outside the thruster exit plane, then the ions could experience radial acceleration within the near-field as well as within the channel. This is illustrated in Figure 3.5, and could help to explain the experimental data.

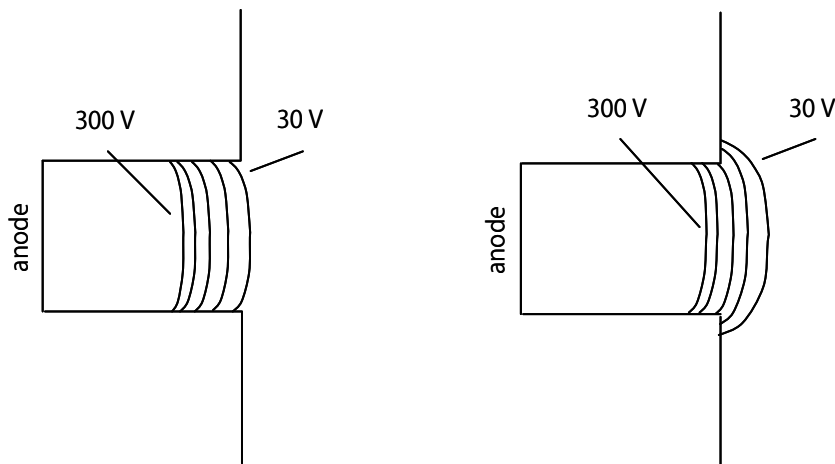


Figure 3.5: Different possible potential distributions in the Hall thruster channel. In HPHall, the location over which most of the potential drop occurs (the acceleration region) can be moved by changing the values of the mobility coefficients and the locations of the regions over which these coefficients are applied. In the lefthand drawing, most of the drop occurs just upstream of the exit plane, meaning the acceleration of ions is primarily in the axial direction. In the righthand drawing, some of the drop occurs just outside the exit, meaning that there will be greater acceleration in the radial direction.

Detailed magnetic field measurements were taken for each thruster, and are shown in

Figure 3.6 and 3.7. Axially and radially directed probes, mounted on a 2D translation stage, were used to obtain the measurements with a F.W. Bell 5060 Gaussmeter. Ideally, if one had a code with a physics-based mobility model, one could determine the effect of changing the mobility by running the code using these different field measurements. However, because of HPHall's coefficient-based approach to the mobility, it is not possible to simply change the magnetic field; one needs to change the mobility coefficients as well. Therefore, this part of the modeling effort primarily involved "knob turning," i.e., figuring out how changes in the mobility affect the potential distribution, and thus ion trajectories.

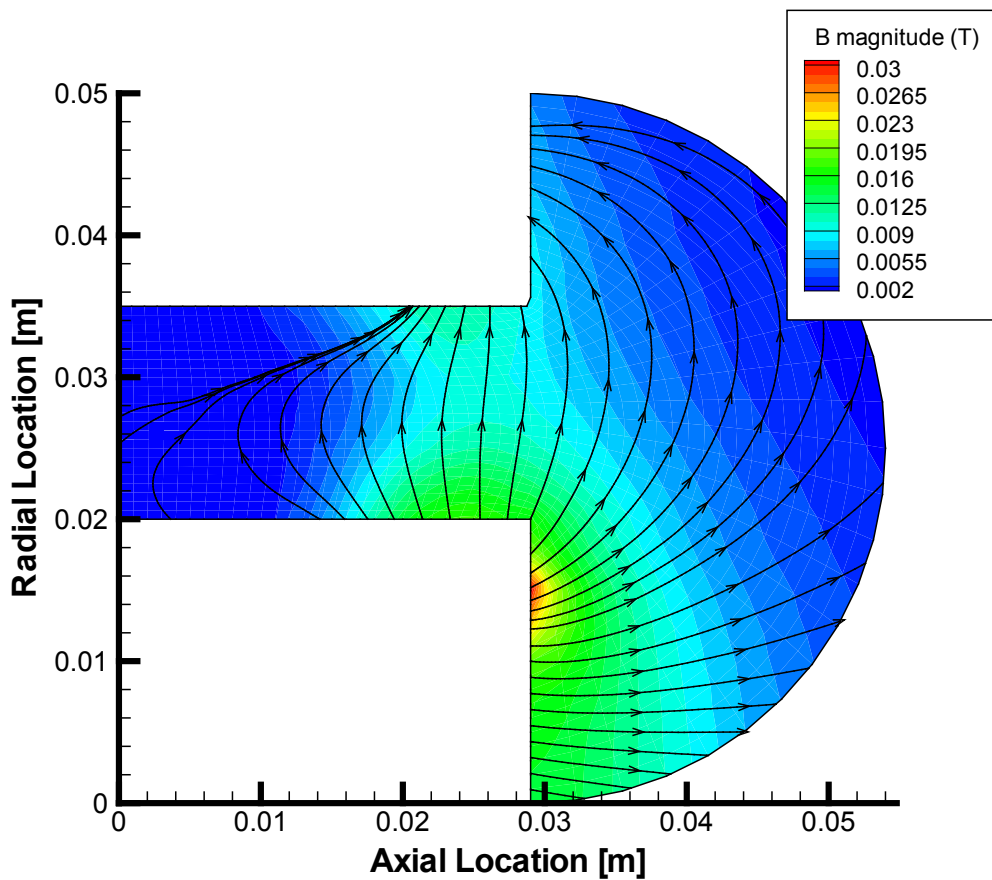


Figure 3.6: Measured SPT-70 Magnetic Field, 200 W case. Magnetic field strength in Tesla, with magnetic field lines superimposed.

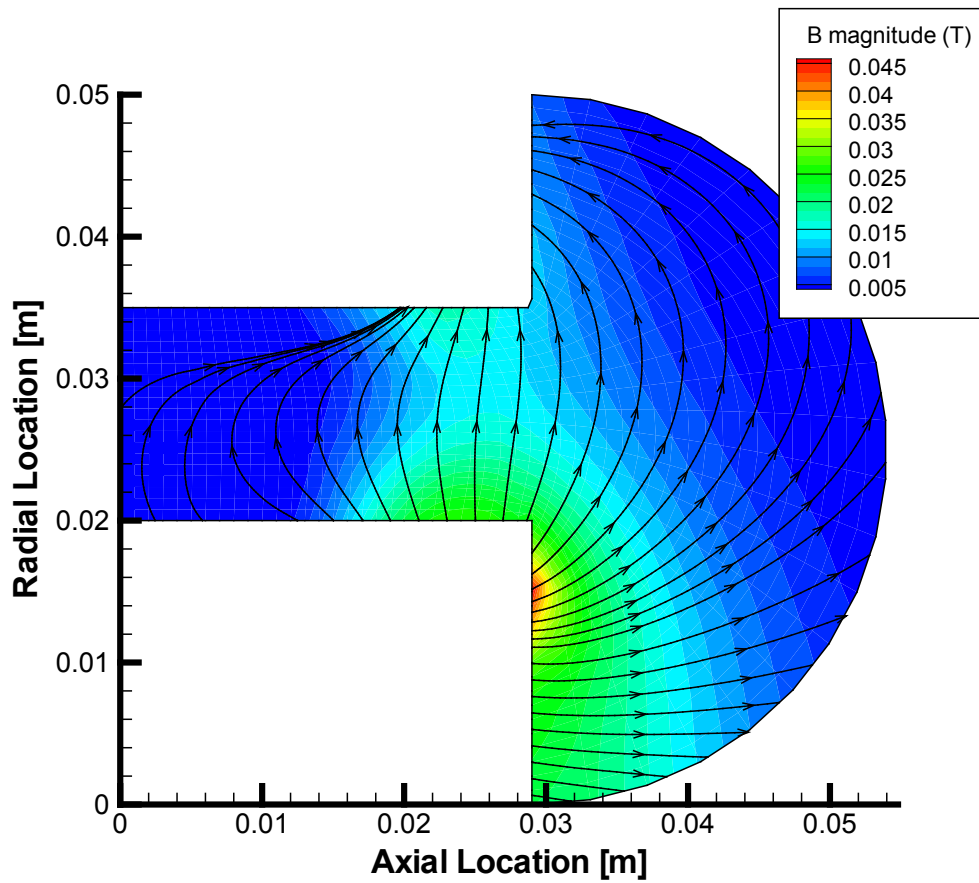


Figure 3.7: Measured SPT-70 Magnetic Field, 650 W case. Magnetic field strength in Tesla, with magnetic field lines superimposed.

A number of runs of HPHall were conducted to determine the effect of the mobility coefficients and transition locations on the simulated parameters. During each run, the simulation was first initialized by running only neutral particles for 20,000 time steps, then running in normal mode for 10,000 time steps (the simulation would reach steady state during this part of the run). Then, the simulation was run for 10,000 iterations during which time the results were recorded. The goal of these different runs was to find some configurations in which most of the potential drop occurred upstream of the exit plane, and some in which the potential drop spanned the exit plane, as described in Figure 3.5. To start with, the simulation data in the 650 W case had to be matched to the performance parameters of the thruster. Four performance parameters were selected: anode current, thrust, specific impulse, and efficiency, values for which there is experimental data available. The experimentally measured, nominal values of these parameters are 2.2 A, 0.038 N,  $1.6 \times 10^3$  s, and 0.46, respectively [14].

Matching to this nominal case was accomplished using the configuration shown in Table 3.2. Note that the values  $\alpha_c$ ,  $\alpha_e$ ,  $\alpha_p$ ,  $z_c$ ,  $z_{e1}$ ,  $z_{e2}$ ,  $z_p$  and  $T_{e\perp}/T_{e\parallel}$  are those defined previously in Section 3.1.1. After this configuration was determined, it was noticed that the flow rate in the nominal case (2.34 mg/s) did not exactly match the flow rate used in the present study for the 650 W condition (1.7 mg/s). After the flow rate input was changed, the mobility coefficients, but not the transition locations, were changed to obtain the correct ion current value. As shown in Table 3.3, the other performance parameters changed slightly but were still similar to this configuration. This configuration was labeled the “650 W upstream run,” because the performance values match the 650 W run, and also because most of the potential drop occurs upstream of the exit plane (as will be seen in Chapter 6).

The “650 W downstream” run catalogued in Table 3.2 was selected because the performance parameters of this case matched those seen in the 650 W upstream run, but also because a significant portion of the plasma potential drop was shifted downstream of the exit plane. To select the 200 W runs in Table 3.2, for which thrust, specific impulse, and efficiency data were not available, the same transition locations were used as in the 650 W runs, but the mobility coefficients were adjusted so that the current measured the value seen in the experiment. Note that the performance parameters of the 200 W upstream and downstream runs match well.

Table 3.2: Description of the four cases modeled in HPHall.

Run Name	$V_D$ [V]	$\dot{m}$ [mg/s]	Transition Locations [m]	Mobility Coefficients	$T_{e\parallel}/T_{e\perp}$
Nominal (match to experiment)	300	2.34	$z_c=0.025$ , $z_{e1}=0.027$ , $z_{e2}=0.029$ , $z_p=0.031$	$\alpha_c=0.01$ , $\alpha_e=0.1$ , $\alpha_p=1$	0.55
650 W upstream	300	1.7	$z_c=0.025$ , $z_{e1}=0.027$ , $z_{e2}=0.029$ , $z_p=0.031$	$\alpha_c=0.055$ , $\alpha_e=0.5$ , $\alpha_p=1$	0.5
650 W downstream	300	1.7	$z_c=0.034$ , $z_{e1}=0.036$ , $z_{e2}=0.036$ , $z_p=0.036$	$\alpha_c=0.125$ , $\alpha_e=1.1$ , $\alpha_p=1.1$	0.3
200 W upstream	250	0.8	$z_c=0.025$ , $z_{e1}=0.027$ , $z_{e2}=0.029$ , $z_p=0.031$	$\alpha_c=0.03$ , $\alpha_e=0.3$ , $\alpha_p=1$	0.5
200 W downstream	250	0.8	$z_c=0.034$ , $z_{e1}=0.036$ , $z_{e2}=0.036$ , $z_p=0.036$	$\alpha_c=0.13$ , $\alpha_e=1$ , $\alpha_p=1$	0.3

Table 3.3: Performance parameters of the cases modeled in HPHall.

Run Name	$V_D$ [V]	$\dot{m}$ [mg/s]	$I_A$ [A]	Thrust [N]	Isp [s]	Efficiency
Experimental values	300	2.34	2.2	0.04	$1.6 \times 10^3$	0.4
Nominal match to experiment)	300	2.34	2.2	0.04	$1.6 \times 10^3$	0.4
650 W upstream	300	1.7	2.2	0.03	$1.7 \times 10^3$	0.4
650 W downstream	300	1.7	2.2	0.03	$1.8 \times 10^3$	0.4
200 W upstream	250	0.8	0.8	0.009	$1.0 \times 10^3$	0.2
200 W downstream	250	0.8	0.8	0.008	$1.0 \times 10^3$	0.2

### 3.3.3 Ion Tracking and Energy Distributions

Ion tracking was done using an addendum to HPHall written by M. K. Scharfe at the AFRL. In this code, position, velocity, and mass values of ion and neutral macro-particles are recorded as they cross the outer boundary of the simulation domain. Both  $\text{Xe}^+$  and  $\text{Xe}^{2+}$  were tracked, in addition to the neutral particles. Additionally, the time at which the particles crossed the boundary was recorded.

To compare the ion trajectory data to the data from the experiment, post-processing codes were created that generated simulated Faraday probe, ExB, and RPA traces. To build up a Faraday probe trace, the macro-particle positions were extrapolated from the outer boundary of the simulation domain to a plane parallel to the thruster exit plane, at a specified axial distance. This plane was divided up into “bins” spanning the radial distance, as shown in Figure 3.8, and the number of projected macro-particles in each bin was counted. Note that the ions were assumed to follow straight line trajectories once they passed the simulation boundary, so the effects of mechanisms, such as collisions, are not reflected in the simulated data.

To obtain a measure of the ion current, the number of macro-particles in each bin had to be multiplied by the number of actual particles per macro-particle, then multiplied by  $q$  (the particle charge), then divided by the total time over which the simulation was run, to get the current in amps. Also, since the HPHall data represents two-dimensional data, to correctly scale the data the area accounted for by each bin had to be considered. If the HPHall data was rotated  $360^\circ$  about the centerline, the radial bins would appear as rings on the projected plane, as shown in Figure 3.8. Dividing the ion current into each bin by the area of the bin thus gave a measurement of ion current density which could be compared to the experimental Faraday probe traces.

ExB probe traces were easily created from the Faraday probe data simply by restricting the bound on the velocities and angles that the ions could have. Only ions with trajectories with angles within  $\pm 1^\circ$  of the probe angle and within  $\pm 1$  percent of the primary energy of the device were included in the ExB trace. As in the case of the Faraday probe, the ExB traces also had to be divided by the bin area to obtain a measurement that could be compared to the experimental data.

RPA traces were created by first setting the angle and distance of the probe, as

shown in Figure 3.9. From this, the axial distance of the probe was calculated, the particles were projected onto a plane at that radial distance, and the projected area of the RPA collector onto that plane was calculated. The particles were filtered based on whether they intersected this area of the plane. Additionally, the angle of acceptance of the RPA was considered, so particles were accepted as part of the RPA signal only if their trajectory angles fell within  $\pm 7.5^\circ$  of the probe angle. As with the Faraday probe and ExB data, the RPA current data had to be divided by the projected area to correctly scale it.

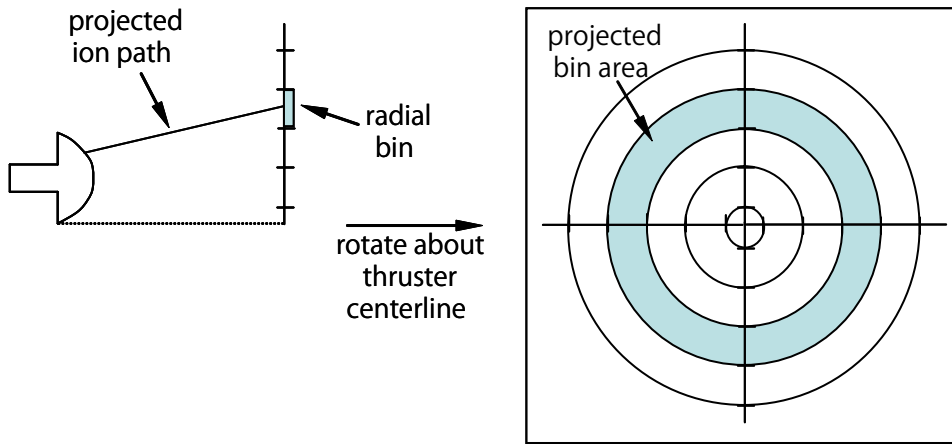


Figure 3.8: Simulated Faraday probe trajectory projection onto a plane parallel to the thruster exit plane. Note that the projected area of the radial bin forms a ring, with area  $\pi(r_2^2 - r_1^2)$ .

### 3.3.4 Oscillation Analysis

One feature of HPHall is that it successfully captures two types of oscillatory phenomena in the Hall thruster plume. It was important to consider the effect of oscillations, because instabilities can cause the potential distribution, and hence the electric field, to vary at different points in time. Breathing mode oscillations, which occur at about 20 kHz, can be described using the following equations:

$$\frac{\partial n_i}{\partial t} = \zeta(T_e) n_i n_n - n_i \frac{v_i}{L} \quad (3.19)$$

$$\frac{\partial n_n}{\partial t} = -\zeta(T_e) n_i n_n + n_n \frac{v_n}{L}, \quad (3.20)$$

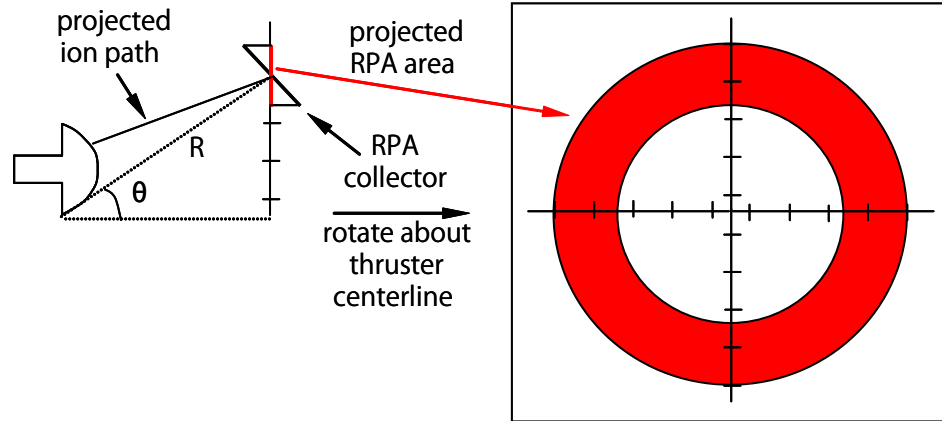


Figure 3.9: Simulated RPA trajectory projection onto a plane parallel to the thruster exit plane. The width of the ring,  $r_2 - r_1$ , is equal to the diameter of the RPA collector multiplied by the cosine of the probe angle.

where  $\zeta(T_e)$  is the ionization rate coefficient, and  $n \frac{v}{L}$  is the rate of ions leaving or neutrals entering an ionization region of length  $L$ . These equations are the same as those used to describe predator-prey relationships, and thus this type of oscillation is also referred to by that name [14, 36, 37]. Additionally, transit-time oscillations occur at the frequency of roughly 200 kHz. These fluctuations are believed to be the result of a localized rise in the electric field near the anode, which then propagates along the channel, and happens over the same time scale that it takes an ion to “transit” the thruster channel [14, 37].

The effect of oscillations were accounted for by recording parameter data at different points in the simulation. Because the ion time step is 0.05 microsec, and the time scale of the two different oscillations were 50 microsec and 5 microsec, data was taken every 10 time steps, for 5000 time steps, so that both the predator-prey and transit-time oscillations could be visualized.

## Chapter 4

# Simulation Approach - Corner Sheath Model

In addition to HPHall, an independent plasma sheath model was developed to simulate the near-wall region of the thruster near the exit plane. After initial HPHall runs did not exactly match the experimental data, it was theorized that the plasma sheath near the corner of the wall could possibly lead to a large enough radial electric field to accelerate high energy ions out to the high angles seen in the experiment. HPHall could not be used to investigate this hypothesis because it is a quasi-neutral code that does not resolve the sheath.

This chapter describes the simulation method used by the corner sheath model, which was developed by the author with help from colleagues at the Jet Propulsion Laboratory (JPL) and the Air Force Research Laboratory (AFRL). All of the information regarding the equations, numerical approach, simulation domain, and boundary conditions for this model is included in this chapter.

### 4.1 Corner Sheath Model - Motivation

During the effort to determine how high velocity ions are accelerated out to high angles, it was hypothesized that the radial electric field necessary to bend ion trajectories toward high angles could be provided by the sheath at the corner of the Hall thruster exit. In a quasi-neutral plasma, a region of non-neutrality will develop naturally at a wall due to the imbalance between the thermal electron and ion fluxes towards that surface. This non-neutral region, the sheath, has its own internal electric field that is directed towards the wall [38]. Therefore, an initially axially-moving ion that enters the sheath, as illustrated in

Figure 4.1, will be deflected by this field. By how much depends on the sheath thickness and potential profile, as well as the point at which the ion encounters the sheath.

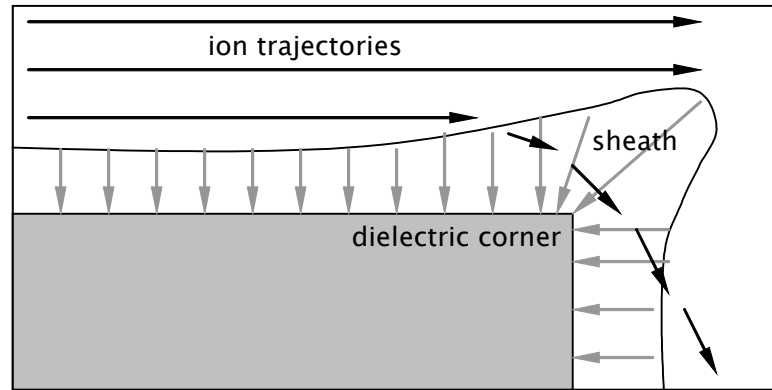


Figure 4.1: Bending of ion trajectories due to the sheath. Ions with initially axial velocities may be deflected by the sheath's internal electric field.

HPHall is insufficient to examine the effects of the sheath because it replaces the sheath with a boundary condition, and forces the ion velocity at the wall boundary to be the ion acoustic, or Bohm, velocity [32]. Efforts have been made outside HPHall to address the problem of sheath development in a flowing plasma. Hong and Emmert, for example, have investigated sheath behavior in the wake of a metal target [39]. While useful from a problem formulation standpoint (the same equations and numerical solution methods can be applied to the dielectric corner problem), the geometries examined in these cases were not similar to that of the current problem, nor were the effects of a dielectric material considered.

Studies conducted by Ahedo have treated the effects of plasma flowing past annular dielectric walls, as is the case in a Hall thruster. In Ahedo's work, a model was first developed to describe the pre-sheath (the quasi-neutral region outside the sheath) [40]. This model was then linked to equations describing the non-neutral sheath, so that ultimately the entire domain, from one wall to the other, was simulated. Secondary electron emission at the walls was also taken into account [41]. However, this approach cannot be directly applied to the problem of radial acceleration within the sheath, because it assumed a "zero-Debye length limit," i.e., the sheath was assumed to have zero thickness. Also, the presence of the corner at the exit adds a further complication to the direct application of this method to the problem at hand.

To resolve the sheath and determine whether it has a significant effect on ion trajectories, a 2D framework was developed to solve the standard sheath equations while including the effects of secondary electron emission due to ion collisions with the dielectric wall. This model solves continuity, momentum, and Poisson's equations iteratively to determine density, velocity, and potential profiles within the sheath.

## 4.2 Sheath Equations

To model the sheath, the familiar hydrodynamic sheath equations were applied [39]. These equations consist of ion continuity and ion momentum conservation, as well as Poisson's equation. Electron density is modeled using the Boltzmann relation. For reference, the direction perpendicular to the wall normal vector will be called the "axial" or "z" direction, while the direction parallel to the wall normal vector will be called the "radial" or "r" direction (as in HPHall, corresponding to Hall thruster convention). The equations, which hold for a collisionless plasma, are as follows:

$$\frac{\partial n_i}{\partial t} + \nabla \cdot (n_i \vec{u}_i) = 0 \quad (4.1)$$

$$\frac{\partial (n_i \vec{u}_i)}{\partial t} + \nabla \cdot (n_i \vec{u}_i \vec{u}_i) = -\frac{en_i}{m_i} \nabla \phi \quad (4.2)$$

$$\nabla^2 \phi = -\frac{e}{\epsilon_0} (n_i - n_e) \quad (4.3)$$

$$n_e = n_0 \exp\left(\frac{e\phi}{kT_e}\right). \quad (4.4)$$

To simplify the calculation, one can combine Eqns. 4.3 and 4.4 and introduce the following non-dimensional parameters:

$$\tilde{\nabla} = \frac{\nabla}{\lambda_D} = \frac{\nabla}{\sqrt{\epsilon k T_e / e^2 n_0}} \quad (4.5)$$

$$\tilde{n} = \frac{n_i}{n_0} \quad (4.6)$$

$$\vec{U} = \frac{\vec{u}_i}{u_s} = \frac{\vec{u}_i}{\sqrt{kT_e/m_i}} \quad (4.7)$$

$$\chi = \frac{e\phi}{kT_e}. \quad (4.8)$$

Substituting Eqn. 4.5 to 4.8 into the sheath equations gives:

$$\frac{\partial \tilde{n}}{\partial t} + \tilde{\nabla} \cdot (\tilde{n} \vec{U}) = 0 \quad (4.9)$$

$$\frac{\partial \tilde{n} \vec{U}}{\partial t} + \tilde{\nabla} \cdot (\tilde{n} \vec{U} \vec{U}) = 0 \quad (4.10)$$

$$\tilde{\nabla}^2 \chi = -(\tilde{n} - \exp(\chi)). \quad (4.11)$$

The non-dimensionalized equations, Equation 4.9 to 4.11 thus give three equations and three unknowns ( $\tilde{n}$ ,  $\vec{U}$ , and  $\chi$ ).

### 4.3 Boundary Conditions

To determine the boundary conditions, the approach of Hobbs and Wesson was used [42]. In this method, the non-dimensional electric field and potential can be determined by the following set of equations:

$$\begin{aligned} (\tilde{E}_w)^2 = 2\tilde{M}^2 \left[ \left(1 - \frac{2\chi_w}{\tilde{M}^2}\right)^{1/2} - 1 \right] - \frac{\Gamma}{1-\Gamma} (8\mu\chi_w\tilde{M}^2) \\ + 2(e^{\chi_w} - 1) \left[ 1 - \frac{\Gamma}{1-\Gamma} \left(-\frac{\mu\tilde{M}^2}{2\chi_w}\right)^{1/2} \right] \end{aligned} \quad (4.12)$$

$$\chi_w = -\ln \left[ \frac{1-\Gamma}{\tilde{M}(2\pi\mu)^{1/2}} - \frac{\Gamma}{(-4\pi\chi_w)^{1/2}} \right] \quad (4.13)$$

$$\tilde{M}^2 = 1 + \frac{\Gamma}{1-\Gamma} \mu^{1/2} \left(-\frac{\tilde{M}^2}{2\chi_w}\right)^{1/2} (1 - 2\chi_w), \quad (4.14)$$

where  $\tilde{M}$  is the non-dimensional radial ion velocity, and:

$$\mu = \frac{m_e}{m_i} \quad (4.15)$$

$$\tilde{M} = \frac{u_0}{\sqrt{kT_e/m_i}} \quad (4.16)$$

$$\chi_w = \frac{e\phi_w}{kT_e} \quad (4.17)$$

$$\left(\tilde{E}_w\right)^2 = \left(\frac{\partial\chi}{\partial\zeta}\right)_w^2 \quad (4.18)$$

$$\zeta = \frac{z}{\lambda_D}. \quad (4.19)$$

The variable  $\Gamma$  is the secondary electron emission yield, as defined by:

$$\Gamma = \frac{\Gamma_{e2}}{\Gamma_{e1}}, \quad (4.20)$$

where  $\Gamma_{e1}$  is the flux ( $nu$ ) of primary electrons towards the wall, and  $\Gamma_{e2}$  the flux of secondary electrons away from the wall. The SEE yield has been found, empirically, to be a function of electron temperature,  $T_e$ , and the wall material. Numerous fits of  $\Gamma$  as a function of  $T_e$  for boron nitride walls have been calculated. For the purposes of this study, the power fits of Dunaevsky [43] have been applied:

$$\Gamma = \left(\frac{T_e}{E_0}\right)^\alpha, \quad (4.21)$$

where  $\alpha = 0.5$ ,  $E_0 = 35$ , and  $T_e$  is in eV rather than K. Note that if  $\Gamma$  is solely a function of temperature, then Eqns. 4.12 to 4.14 are also only dependent on temperature. Knowing  $\Gamma$  allows these three equations to be solved simultaneously, as has been done in cite<sub>2007</sub>.

The above set of equations allows the electric field and potential at the wall to be determined. If the potential at the edge of the sheath is also known, then the sheath equations can be solved to find the sheath thickness. Finding the potential at the edge of the sheath is simple. Within the pre-sheath, the potential drops from its bulk value far from

the wall to the value needed to accelerate ions to the Bohm velocity. If the velocity in the bulk is assumed to be zero, then the potential at the pre-sheath/sheath boundary is:

$$\phi_s = \phi_{bulk} - \frac{1}{2} \frac{m_i}{e} v_{bohm}^2 = \phi_{bulk} - \frac{1}{2} \frac{m_i}{e} \frac{kT_e}{m_i} = \phi_{bulk} - \frac{1}{2} \frac{kT_e}{e}. \quad (4.22)$$

So the non-dimensional potential at the edge of the sheath is:

$$\chi_s = \chi_{bulk} - \frac{1}{2}. \quad (4.23)$$

So if one knows the potential far from the wall, one can easily calculate the potential at the sheath edge.

The way that the above algorithm was used was to first solve for  $\chi_s$  using Eqn. 4.23. Then, by using the electron temperature profile from HPHall, solve for  $\Gamma$ ,  $\tilde{E}_w$ , and  $\chi_w$  using Eqns. 4.12 to 4.13. After the boundary conditions were calculated, the values of  $\chi_s$  and  $\chi_w$  were fed into the model, along with a guess for the sheath thickness. From these inputs the model would calculate the value of  $\tilde{E}_w$ . If that value was within an acceptable error, then the calculated potential profile was accepted as the solution. If it was not, the model would iterate on the sheath thickness, until an acceptable solution was reached.

## 4.4 Numerical Method

The problem was divided into two separate parts: a fluid solver and a potential solver. The fluid solver determined the values of ion density and velocity from the continuity and momentum equations, given a potential field. The potential solver determined the potential field from Poisson's equation based on the ion density and the potential from the previous time step. Program flow is shown in Figure 4.2.

A finite volume approach was used to calculate the spatial derivatives of the fluid equations on a rectangular grid with uniform spacing in the axial and radial directions. First order upwind values were used to compute velocities at the boundaries of each cell, while density was calculated at the cell centers. Time derivatives were calculated using the Beam-Warming algorithm to ensure stability [39, 44], as shown in Eqn. 4.24.

$$\frac{\partial f}{\partial t} = \frac{3f^{n+1} - 4f^n + f^{n-1}}{2\Delta t}, \quad (4.24)$$

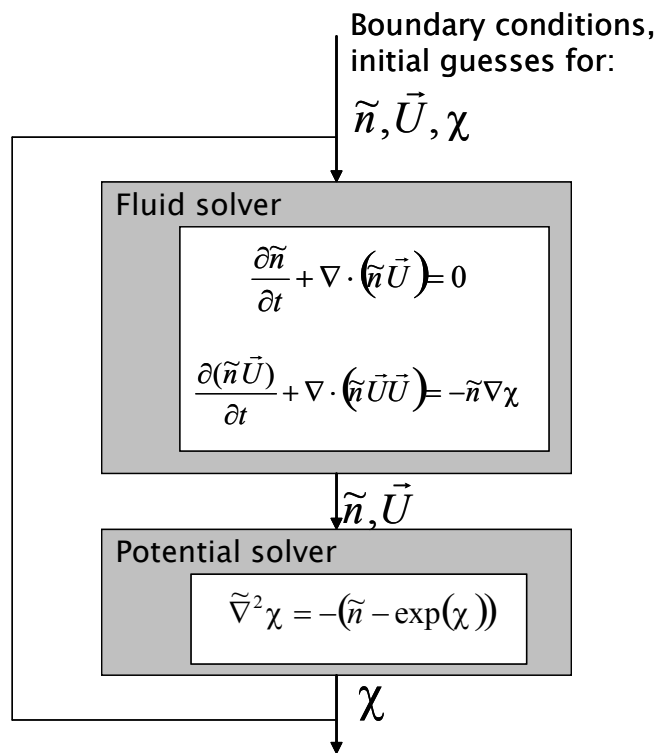


Figure 4.2: Corner sheath model program flow.

where  $f^n$  indicates the value of  $f$  at the current time index, so  $f^{n-1}$  is the value of  $f$  at the previous time step, and  $f^{n+1}$  is the value of  $f$  at the following time step.

Finite volumes were also applied to the spatial derivatives of Poisson's equation, and the potential field was solved by applying an iterative Gauss-Seidel scheme (Eqn. 4.28) [45]. Eqn. 4.11 can be discretized by writing the spatial derivatives according to the finite volume method:

$$\frac{\partial^2 \chi}{\partial x^2} = \frac{1}{\Delta x^2} (\chi_{j+1,k} - 2\chi_{j,k} + \chi_{j-1,k}) \quad (4.25)$$

$$\frac{\partial^2 \chi}{\partial y^2} = \frac{1}{\Delta y^2} (\chi_{j,k+1} - 2\chi_{j,k} + \chi_{j,k-1}), \quad (4.26)$$

where  $j$  is the x-index, and  $k$  is the y-index of the point at which the derivative is being taken. Applying Eqns. 4.25 and 4.26 at all the points in the domain, and then plugging this into Eqn. 4.11 results in a matrix equation of the form:

$$\mathbf{A} \cdot \mathbf{x} = \mathbf{b}, \quad (4.27)$$

where  $\mathbf{x}$  is a vector corresponding to the values of  $\chi$  at each point in the domain. The Gauss-Seidel algorithm can then be applied to Eqn. 4.27

$$(\mathbf{L} + \mathbf{D}) \cdot \mathbf{x}^r = -\mathbf{U} \cdot \mathbf{x}^{r-1} + \mathbf{b}, \quad (4.28)$$

where  $\mathbf{D}$  is the diagonal part of  $\mathbf{A}$ ,  $\mathbf{L}$  is the lower triangle of  $\mathbf{A}$  with zeros on the diagonal, and  $\mathbf{U}$  is the upper triangle of  $\mathbf{A}$  with zeros on the diagonal, such that:

$$\mathbf{A} = \mathbf{L} + \mathbf{D} + \mathbf{U}. \quad (4.29)$$

Note that  $r$  in Eqn. 4.28 is the index of the current iteration, and  $r - 1$  is the index of the previous iteration. Initially, a guess is made for the values of  $\mathbf{x}$ , and then  $\mathbf{x}$  is iterated on using Eqn. 4.28 until the solution reaches a steady state.

## 4.5 Model Verification

The model was validated by comparing its result to those obtained using the standard 1D sheath equations. In 1D, the non-dimensional sheath equations are:

$$\tilde{n}U = 1 \quad (4.30)$$

$$U^2 + 2\chi = 1 \quad (4.31)$$

$$\frac{\partial^2 \chi}{\partial \rho^2} = -(\tilde{n} - \exp(\chi)), \quad (4.32)$$

where  $\rho = r/\lambda_D$ . By using Eqns. 4.30 and 4.31 to solve for the ion density, one can derive the following:

$$\frac{\partial^2 \chi}{\partial \rho^2} = -\left((1 - 2\chi)^{-1/2} - \exp(\chi)\right). \quad (4.33)$$

Equation 4.33 is an ODE that can be solved using standard methods given conditions for  $\chi$  and  $\partial\chi/\partial\rho$  at the outer boundary, and either the sheath thickness (if known) or the value of  $\chi$  at the wall boundary. Figure 4.3, 4.4, and 4.5 shows a comparison of the 1D solution and the results of the 2D solver. In each case,  $\chi$ ,  $\chi_w$ , and the sheath thickness were used to determine the potential profile within the sheath. The comparisons shown in Figure 4.3 to 4.5 suggest that the 2D code solves the sheath equations with an acceptable degree of accuracy, and thus can be applied to the problem of the sheath at a dielectric corner.

## 4.6 “Quasi”-2D Application

When implementing the 2D sheath model, two major complications arose. First, the initial intent was to apply the 2D solver to a domain that encompasses the entire area surrounding the corner, as shown in Figure 4.6. However, to carry out the calculation in this region, a major obstacle must be overcome. It is important to note that as the value of the potential on the outer boundary changes, so does the thickness of the sheath. Therefore, because the 2D solver is only valid in the region inside the sheath, in order to implement the solver in

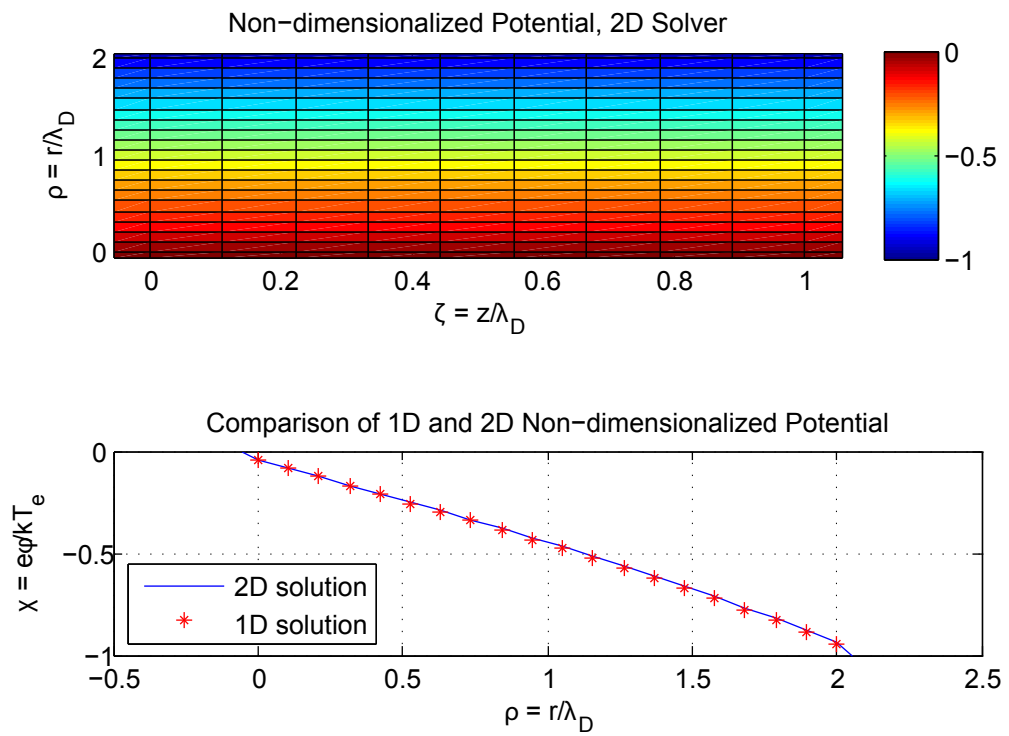


Figure 4.3: Comparison of 1D to 2D model, example 1. In this case  $\chi = 0$  at the outer boundary and  $\chi_w = -1$ . The sheath thickness was 2.

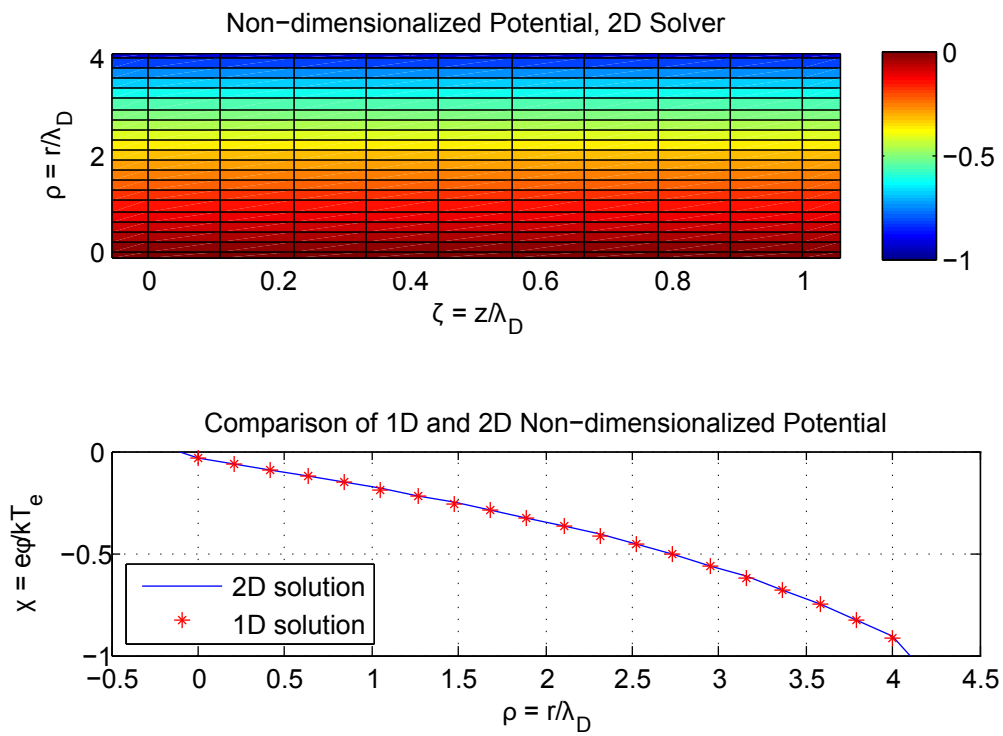


Figure 4.4: Comparison of 1D to 2D model, example 2. In this case  $\chi = 0$  at the outer boundary and  $\chi_w = -1$ . The sheath thickness was 4.

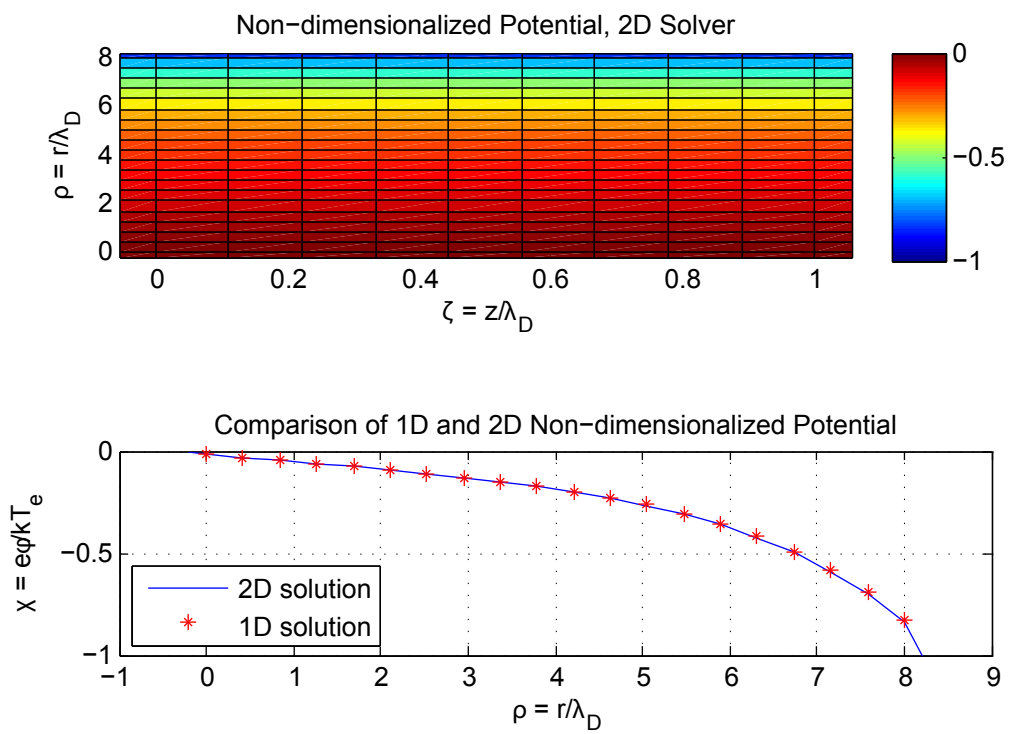


Figure 4.5: Comparison of 1D to 2D model, example 3. In this case  $\chi = 0$  at the outer boundary and  $\chi_w = -1$ . The sheath thickness was 8.

its current form, the width of the simulation domain must be allowed to vary. Alternatively, rather than having a variable-width domain, one could attempt to solve the sheath as well as the quasi-neutral region adjacent to it (the “pre-sheath”). This has been done, for instance, by Ahedo [40, 41]. Additionally, techniques for joining the two regions have been developed, such as asymptotic matching [46] and patching [47].

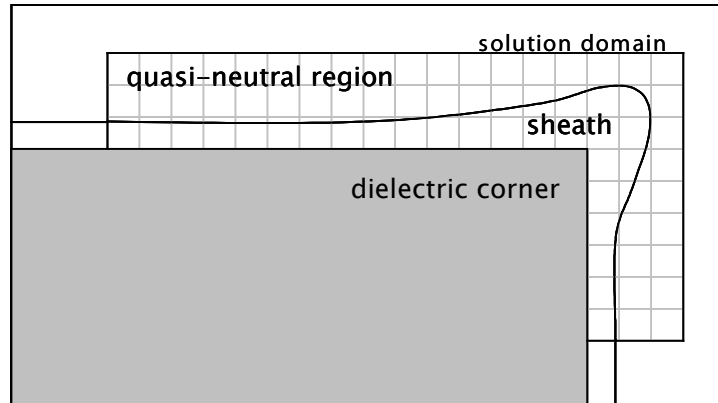


Figure 4.6: Corner sheath model solution domain. If the entire pre-sheath/sheath solution is obtained, the solution domain must be split up into two regions. If just the sheath solution is obtained, the width of the domain must vary.

Rather than start by attempting to implement a variable-width domain or solve the entire pre-sheath/sheath problem, an intermediate step was taken. In this step, the 2D solver was applied to small cells along the corner. The cells were sized such that it could be assumed that the potential, electric field, density, and velocity were constant along the outer boundary of the cell, as illustrated in Figure 4.7. Then for each cell, the 2D solver was used to find the variation of the potential within the sheath, as well as the sheath thickness. In this fashion, the variation of the sheath thickness and the electric field in the axial direction could be estimated.

Based on the results that were later obtained using this quasi-2D approach, it was determined that a full 2D application of the solver to the sheath problem was not needed. The question of whether the high angle, high velocity ions could be explained by acceleration through the sheath was answered sufficiently using the quasi-2D approach.

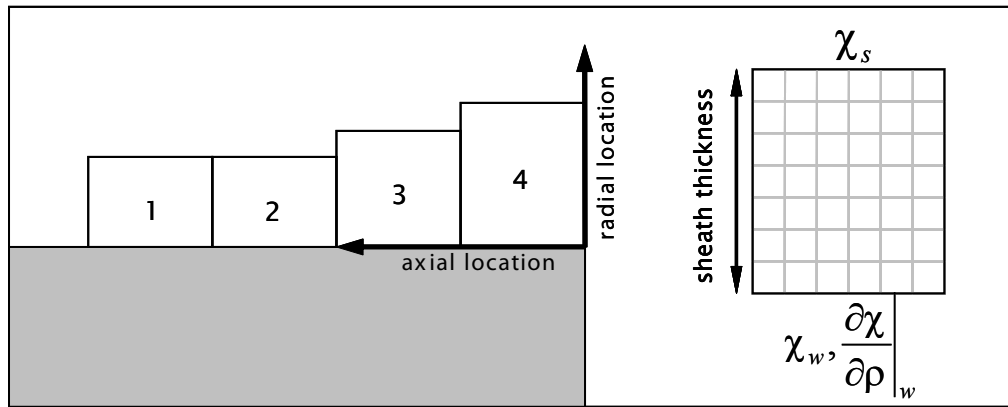


Figure 4.7: Applying the 2D solver in a “quasi”-2D fashion. The solver was applied to cells over which the boundary values could be assumed constant.

## Chapter 5

# Experimental Results and Discussion

This chapter details the results from the experimental survey of the SPT-70. Faraday probe, ExB filter, and RPA traces are shown, along with noteworthy observations and thorough analysis of the data. Uncertainty is also considered, and the results of the analysis are provided within each section. The purpose of the experimental investigation was to characterize the central jet and high angle ion trajectories for two different operating conditions (200 W and 650 W). In the process, these measurements helped to generate theories regarding the central jet formation and the generation of high energy, high angle ions.

The experimental data show some interesting features. The ExB scans suggest, for example, that the evolution of the plume is largely due to ions moving inward toward the thruster centerline as opposed to ions moving away from it. These scans also show a substantial proportion of ions in the central jet have purely axial ( $0^\circ$ ) trajectories, even though to reach the centerline they must start with trajectory angles that are greater than zero. As mentioned previously, the RPA data show that there is a substantial population of high angle, high energy ions, in particular at a power level of 200 W.

### 5.1 Results and Discussion - ExB Filter and Faraday Probe

Before discussing the ExB and Faraday probe results, it is important to explain a few concepts that will make interpretation of the data easier to understand. First, it should be noted that the ion current measured by this probe is the current of  $\text{Xe}^+$  into  $0.8^\circ$ , due to the collimation provided by the apertures (as discussed in Section 2.4). In the following sections, the ExB filter ion current density values are given in  $\text{A/m}^2$ , and simply represent the current into  $0.8^\circ$ , divided by aperture area. In contrast to the Faraday probe results, which represent the

non-collimated ion current density for all species, the ExB data represent the collimated ion current density for  $\text{Xe}^+$  ions with the primary beam energy.

In order to ensure that the ExB measurements correctly scale with the Faraday probe measurements, given the angle and velocity restrictions in the ExB data, a quick “sanity check” calculation was done. In this calculation, data from the Faraday probe was compared to data from the ExB probe at an angle of  $0^\circ$ , at an axial distance of 100 mm, for the 650 W condition. At this location, the Faraday probe measures a peak in ion current density of about  $2000 \text{ A/m}^2$  (see Figure 5.13), while the ExB probe measures a peak in current density of about  $0.007 \text{ A/m}^2$  (see Figure 5.11). To estimate the reduction in current due to the angle restriction of the aperture, it was assumed that all of the ion current emitted by the thruster exited through a half-sphere of radius 100 mm. This corresponds to a surface area of  $0.02 \text{ m}^2$ . Since the viewing area of the probe is equal to  $7.4 \times 10^{-7} \text{ m}^2$  (the aperture area), the current density should scale as  $7.4 \times 10^{-7} / 0.02 = 3.5 \times 10^{-5}$ , just due to the angle restriction alone. If it is assumed that the velocity restriction further reduces the current by a factor on the order of 1 percent, then the current density measured by the ExB filter should be roughly  $3.5 \times 10^{-6}$  times less than what is measured by the Faraday probe. This appears to be true, since  $2000 \text{ A/m}^2$  multiplied by  $3.5 \times 10^{-6}$  gives  $0.007 \text{ A/m}^2$ .

Another important aspect of the ExB scans that should be pointed out is that because of the direction of the scan and the way the probe is angled (see Figure 5.1, reproduced from Section 2.6), for a given scan angle,  $\theta$ , the probe only “sees” ions that are travelling at  $+\theta$  degrees, and not those at  $-\theta$  degrees. Therefore, for one side of the channel (marked “negative” in 5.1), the probe will only measure ions that are traveling with a radial velocity component that is outward, away from the thruster centerline. Conversely, for the other side of the channel (marked “positive” in the figure), the probe will only measure ions that are moving inward. Therefore, in the plots in the following sections, the current density peak corresponding to outward moving ions will show up to the left of the inward moving ion peak.

Finally, in all the transverse ExB plots, the projected channel locations are also shown. For a transverse scan at an angle, ions originating from the channel will not show up between  $-35$  and  $-20$  and  $+20$  and  $+35$  mm. (This occurs because of the geometry of the trajectories; an ion exiting at a certain angle and traveling a certain axial distance will move in the transverse direction.) By plotting the projection, one can see from what part of

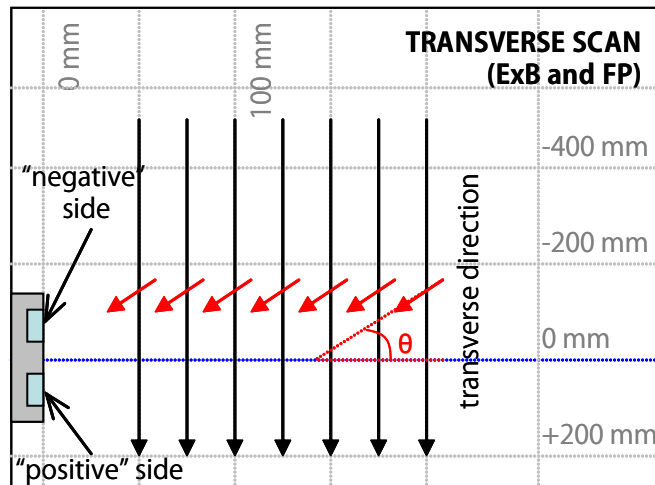


Figure 5.1: Transverse scans taken with the ExB filter.

the thruster the ions originated, assuming that the ions follow field-free trajectories outside the thruster. Additionally, one can see how much the ions needed to be accelerated in the radial direction to end up in locations outside of the projected areas.

### 5.1.1 Transverse Scans

To start the analysis, it is best to first take a look at graphs that show all the transverse results plotted together, to get an idea of the general trends shown in the data. Figure 5.2 shows the results from the transverse ExB scans at 200 W, while Figure 5.3 is the ExB data at 650 W. Note that these plots are what Matlab refers to as “pseudo-color” plots, in which a color is assigned to each rectangle in the plot based on the value of the ion current density at the location of the rectangle. So essentially they are contour plots, except rather than interpolating between points to create a distribution that looks continuous, these plots show values at discrete locations with no interpolation. Figure 5.4 and 5.5 are contour plots of the corresponding Faraday probe results for the 200 W and 650 W cases, respectively. Note that the Faraday probe data in the far-field is plotted on a log scale, while in the near-field it is plotted on a linear scale. These different scales were used so that the features of the data could be more easily visualized.

Looking at the bottom plot in Figure 5.2, for which the probe angle was set to  $0^\circ$ , one can see the transition from annular ring to central jet for the 200 W case. Note that

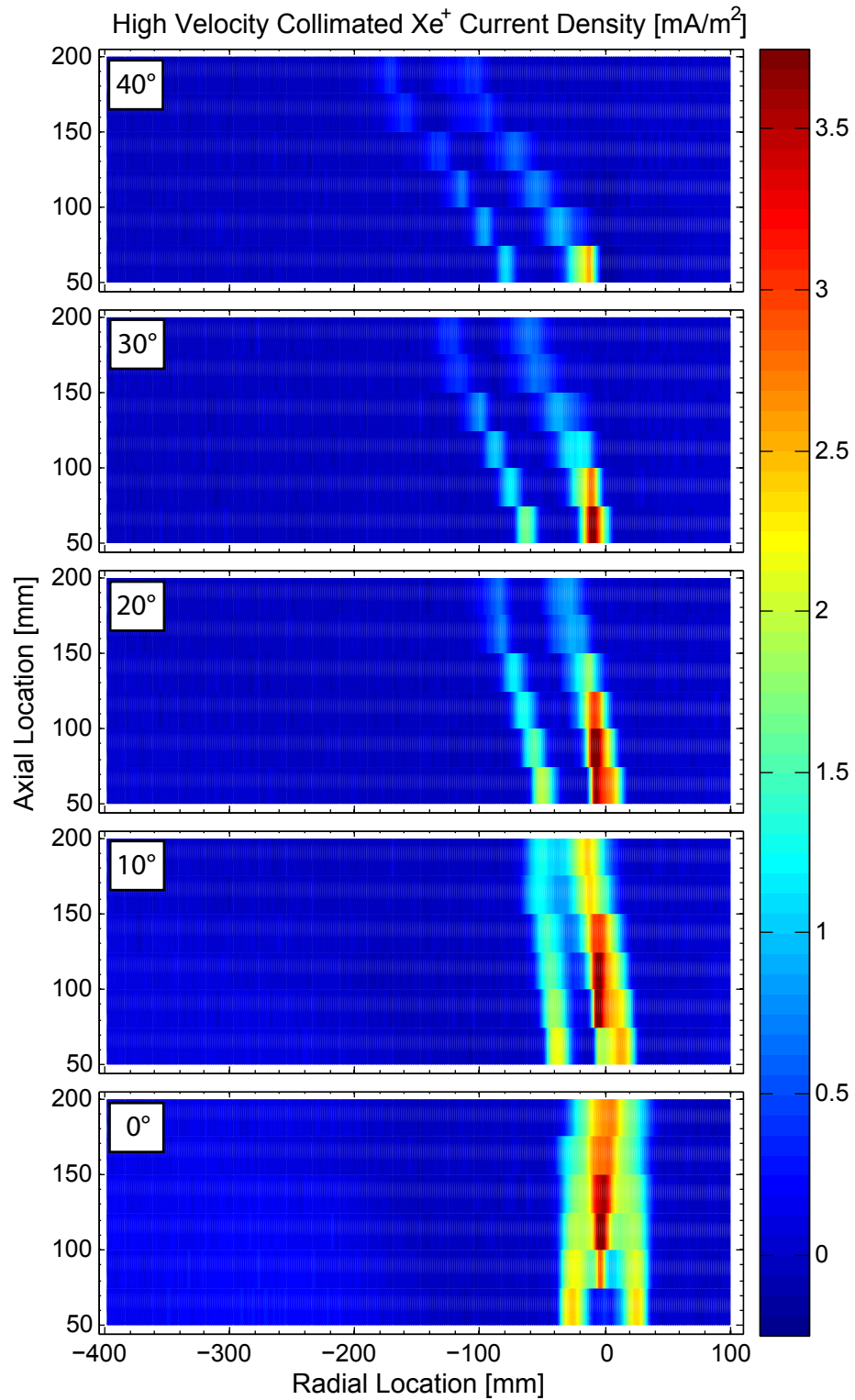


Figure 5.2: Compiled ExB results, 200 W.

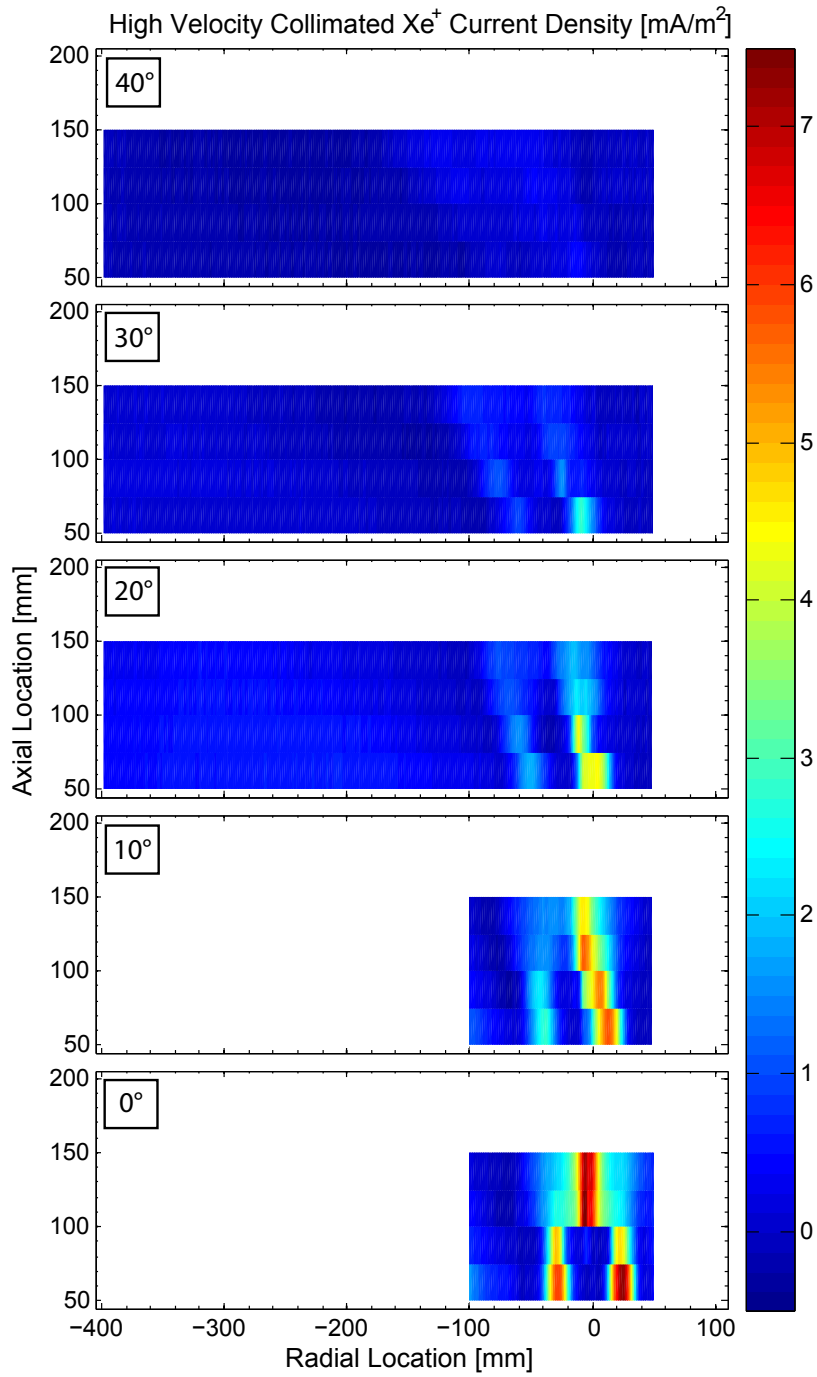
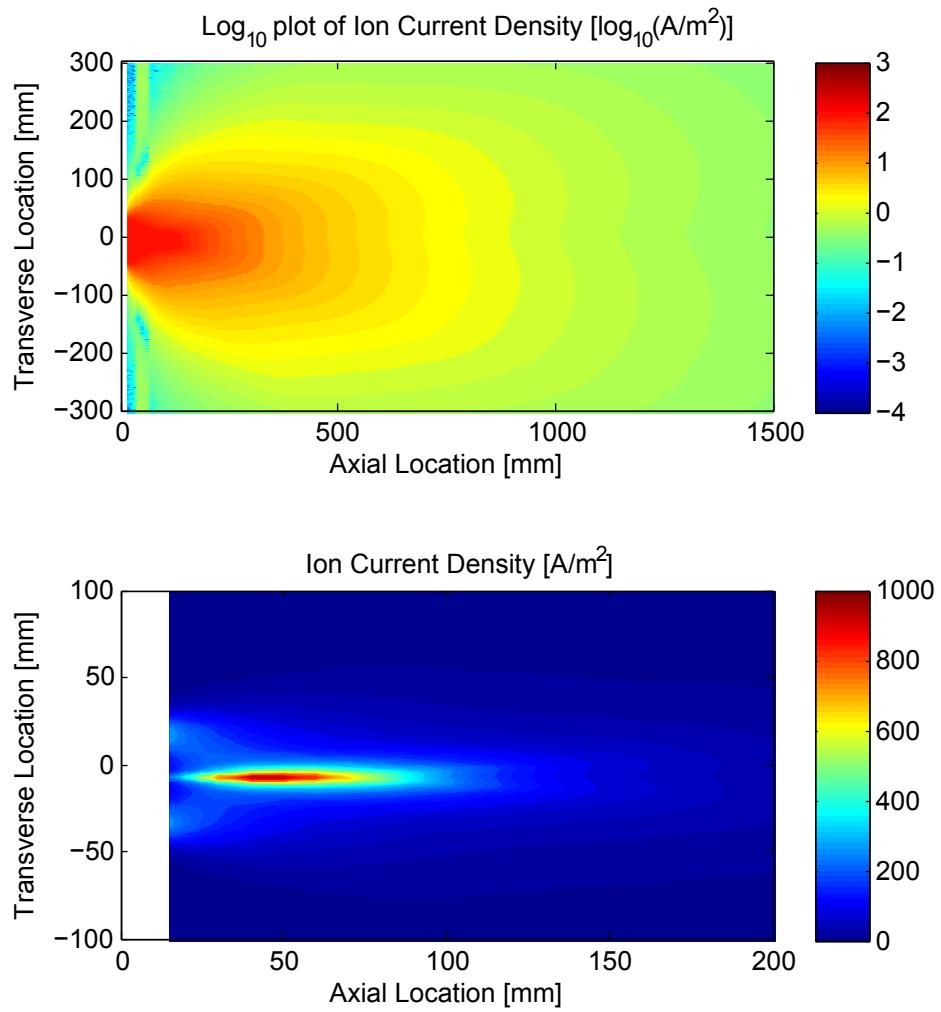
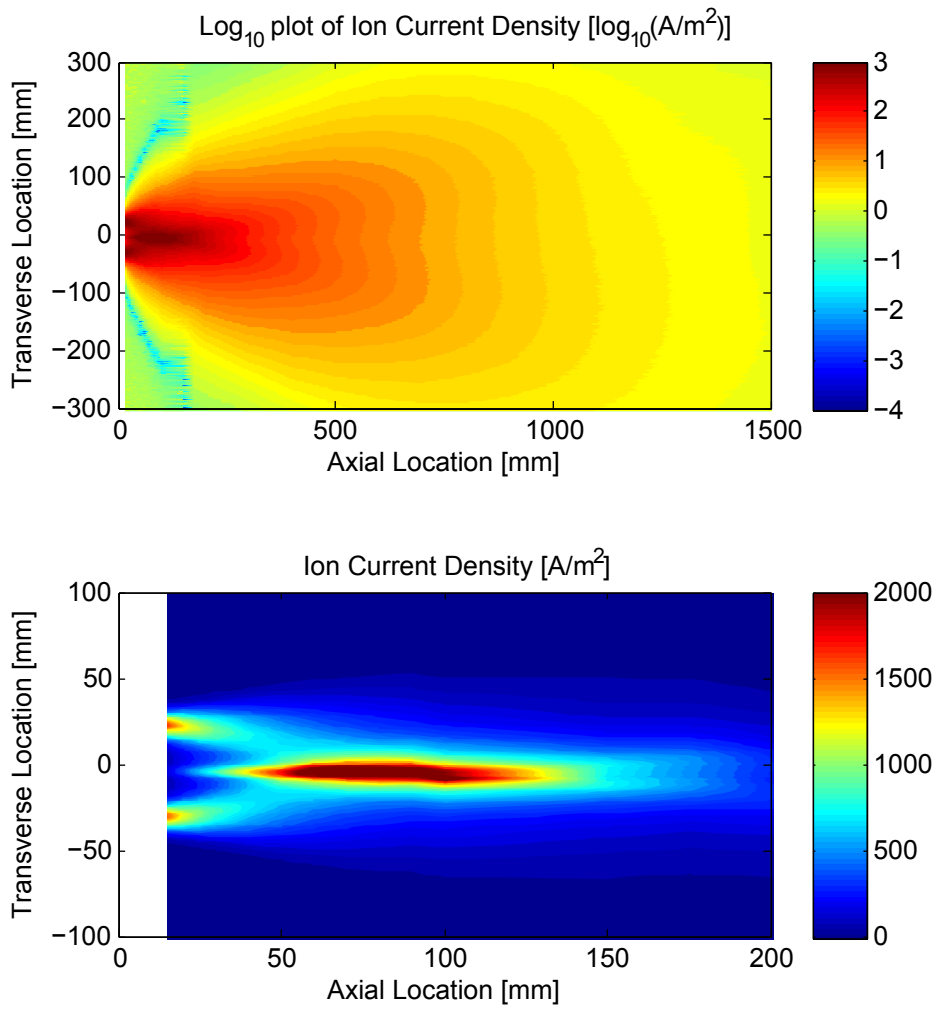


Figure 5.3: Compiled ExB results, 650 W.



---

Figure 5.4: Compiled Faraday probe results, 200 W.



---

Figure 5.5: Compiled Faraday probe results, 650 W.

the ring structure is present along with the jet structure between 75 and 100 mm from the thruster. In fact, the ring has not fully collapsed onto the central jet until about 150 mm. This suggests that the transition from one structure to the other is occurring over an axial distance of about 75 mm (from 75 mm to 150 mm). In contrast, the 650 W case has a much clearer transition from ring to jet, as shown in the bottom plot of Figure 5.3. This transition seems to happen over a distance of 25 mm, from 75 to 100 mm. One note about the 0 and 10° cases shown in Figure 5.3 is that data from -100 to -400 and 50 to 100 mm are not present, due to the fact that a substantial amount of leakage current was measured when the probe was moved to these locations. This error was discussed previously in Section 2.4.

For the 200 W case, as the angle of the probe increases, a substantial ion current density exists out to 40° off the channel centerline. As can be seen in the top plot of Figure 5.2, even at 200 mm from the thruster, there is a current density of approximately 1 mA/m<sup>2</sup> due to ions moving with trajectories that are 40° relative to the thruster centerline. In contrast, the ion current density drops off much more as the angle is increased in the 650 W case. As shown in Figure 5.3, most of the ion current is confined to within 20° of the channel centerline. Thus, it appears that the 650 W case has much better collimation than the 200 W. This is to be expected, due to the fact that the thruster has been optimized to run at 650 W.

The Faraday probe results (Figures 5.4 and 5.5) also reveal a transition from ring to central jet for both the 200 W and 650 W cases. However, the Faraday probe data show the transition happening upstream of what is suggested by ExB data. In the 200 W case, the Faraday probe data indicate that the transition region extends from roughly 15 to 30 mm, while in the 650 W case, the results suggest the region is from about 25 to 50 mm (in contrast to 75 to 150 and 75 and 100 mm, respectively). This apparent discrepancy occurs because of the much larger acceptance angle of the Faraday probe, which is essentially 180°.

The data presented in Figures 5.2 and 5.3 can be divided up into individual plots, for each transverse scan taken at a different axial position. Rather than discuss each of these plots, which would involve a large amount of repetition, several examples have been extracted and will be discussed in the following subsections. The cases that have been selected are the 50, 100, and 150 mm scans, at all angles, from both the 200 W and 650 W cases. These scans were selected because they capture the transition region of both operating conditions. For reference, all of the individual plots are contained in Appendix A.

### 5.1.1.1 200 W Results

Figure 5.6 shows the results of transverse scans for the 200 W condition, at different angles relative to the centerline, at an axial distance of 50 mm. At  $0^\circ$ , there are two roughly symmetric peaks that line up with the centers of the channel. This suggests that at 50 mm, most of the axially-directed, high velocity ion current density originates within the channel, and that both sides of the channel contribute equally. At  $10^\circ$ , in contrast, more ion current density is associated with inward moving ions, as shown by the larger area under the right peak. Also, the data show that not all inward-radial ions have taken straight paths from the channel to the probe; rather their trajectories have been bent (this is seen by the ion current density that appears to the left of the projected channel location). The same phenomenon is present at  $20$  and  $30^\circ$ . At  $40^\circ$ , the overall high velocity current density starts to decrease, and drops off considerably at  $50^\circ$ , although there are still high velocity ions present at  $60^\circ$ .

These results indicate for the collimated ExB probe at 50 mm, most of the angle-resolved high velocity ion current density falls between angles of  $0$  and  $50^\circ$ , and that the majority of current density at angles of  $10$  to  $40^\circ$  is directed inward, rather than outward. Also, at these angles there is a substantial proportion of current density that has not traveled directly from the channel. This suggests that there is a mechanism outside the exit plane which is pushing the ions inward. The data provided here thus offers clues as to the size and direction of an external electric field. Explanations include the residual electric field that exists outside the channel, as well as a disparity that exists in ion density outside the channel (since no ions are produced at the center of the thruster exit plane). A residual or induced magnetic field is not sufficient to explain these results.

Figure 5.9 shows the corresponding Faraday trace at 50 mm and with zero angle relative to the centerline. In this trace, there is a single sharp spike at the center, and the individual channel peaks are not discernable. This suggests that at 50 mm, most of the total ion current density is due to a central jet of ions rather than an annular ring, meaning at this distance the transition from one to another has already occurred. Comparing this to the ExB data suggests that although there is still a ring of axially directed ions, the non-axial contributions that make up the jet are significantly larger.

Figure 5.7 shows the results of transverse scans for the 200 W condition, at different angles relative to the centerline, for the 100 mm case. At  $0^\circ$ , rather than two distinct

peaks, there is a central peak with “shoulders” that correspond to the two sides of the channel. At  $10^\circ$ , one sees the same phenomena that were present at 50 mm, i.e., a larger contribution to the high velocity ion current density by the inward-radial ions, and ions not following straight-line paths. At  $20^\circ$  and  $30^\circ$ , the inward-radial current density is larger than the outward-radial current density.

Comparing this data to the 50 mm case suggests that the angle-resolved high velocity ion current density falls off more rapidly as the angle increases. The majority of the ion current leaves the thruster at angles less than  $30^\circ$ , whereas at 50 mm, a significant proportion of ion current density is seen at  $40^\circ$ . Thus, the high velocity ion beam appears to be more convergent at 100 mm.

Figure 5.9 shows the corresponding Faraday probe trace at 100 mm and with zero angle relative to the centerline. The overall density is smaller than at 50 mm, which is to be expected, and the peak is less sharp. This suggests that the beam is less convergent at 100 mm, which is at odds with the conclusion reached from the ExB data. However it is important to note that the Faraday probe accepts all forward velocities, so the peak may appear wider due to contributions from lower velocity ions.

Figure 5.8 shows the results of transverse scans for the 200 W condition, at different angles relative to the centerline, for the 150 mm case. The  $0^\circ$  case clearly shows that the beam has transitioned fully from the ring to jet, but in contrast to the 100 mm case, the central peak is wider and the shoulders are not as distinct. At  $10^\circ$ , the contribution of the inward moving ions is still greater than that of the outward moving ions, although the two peaks in the data appear to have merged. At  $20^\circ$ , the contributions of the two sides of the channel are separate and distinct, and the peak heights decrease in magnitude as the angle is further increased. Continuing the trend seen from the 50 mm to the 100 mm case, the beam appears to have a greater degree of collimation, as most of the ion current density is seen at angles less than  $20^\circ$ .

Figure 5.9 shows the corresponding Faraday probe trace at 150 mm and with zero angle relative to the centerline. Comparing this to the 100 mm case, one sees significant spreading of the beam, and a decrease in ion current density. Again, as in the 100 mm case, this is at odds with the ExB results, but could possibly be explained by the fact that the Faraday probe is accepting all species rather than just high velocity  $\text{Xe}^+$ .

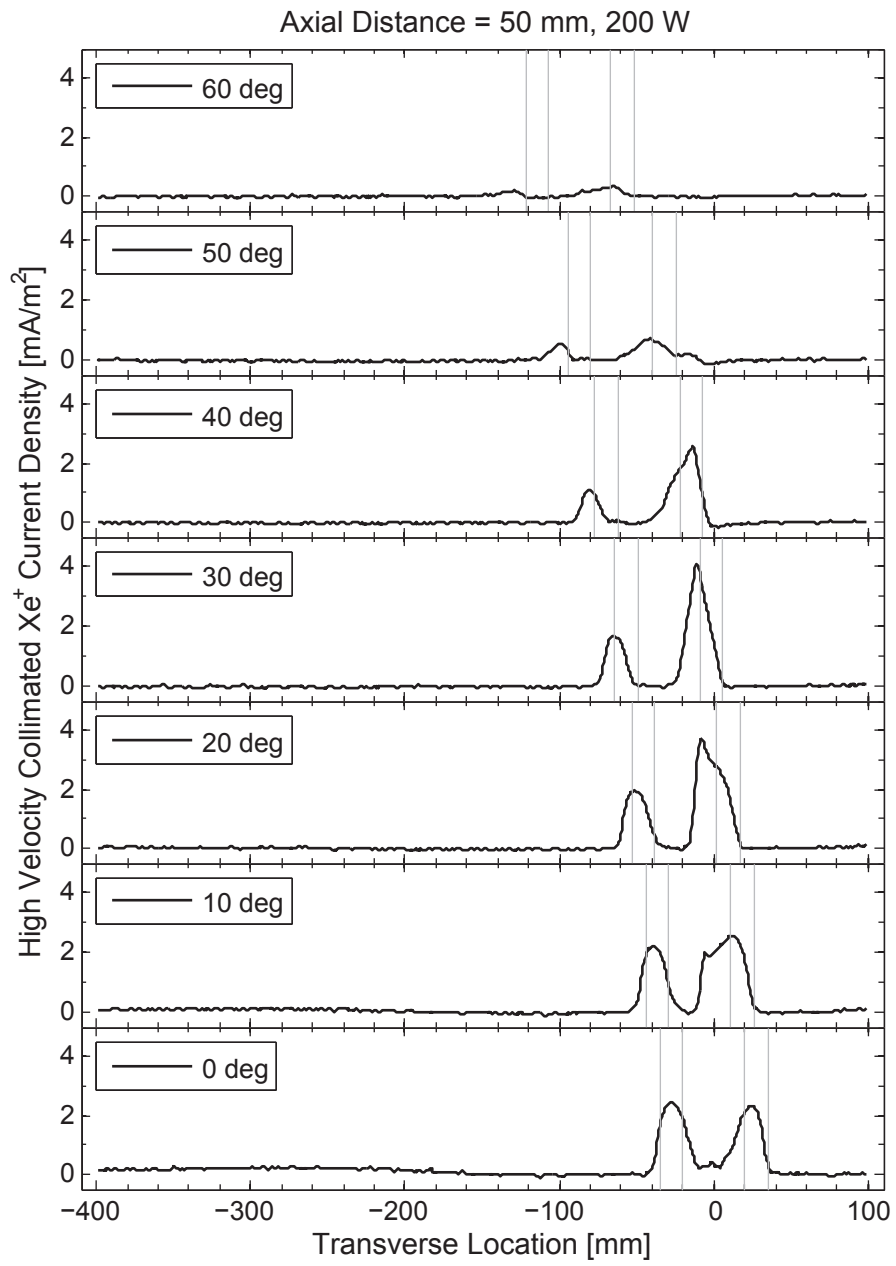


Figure 5.6: ExB results, 200 W case, at 50 mm.

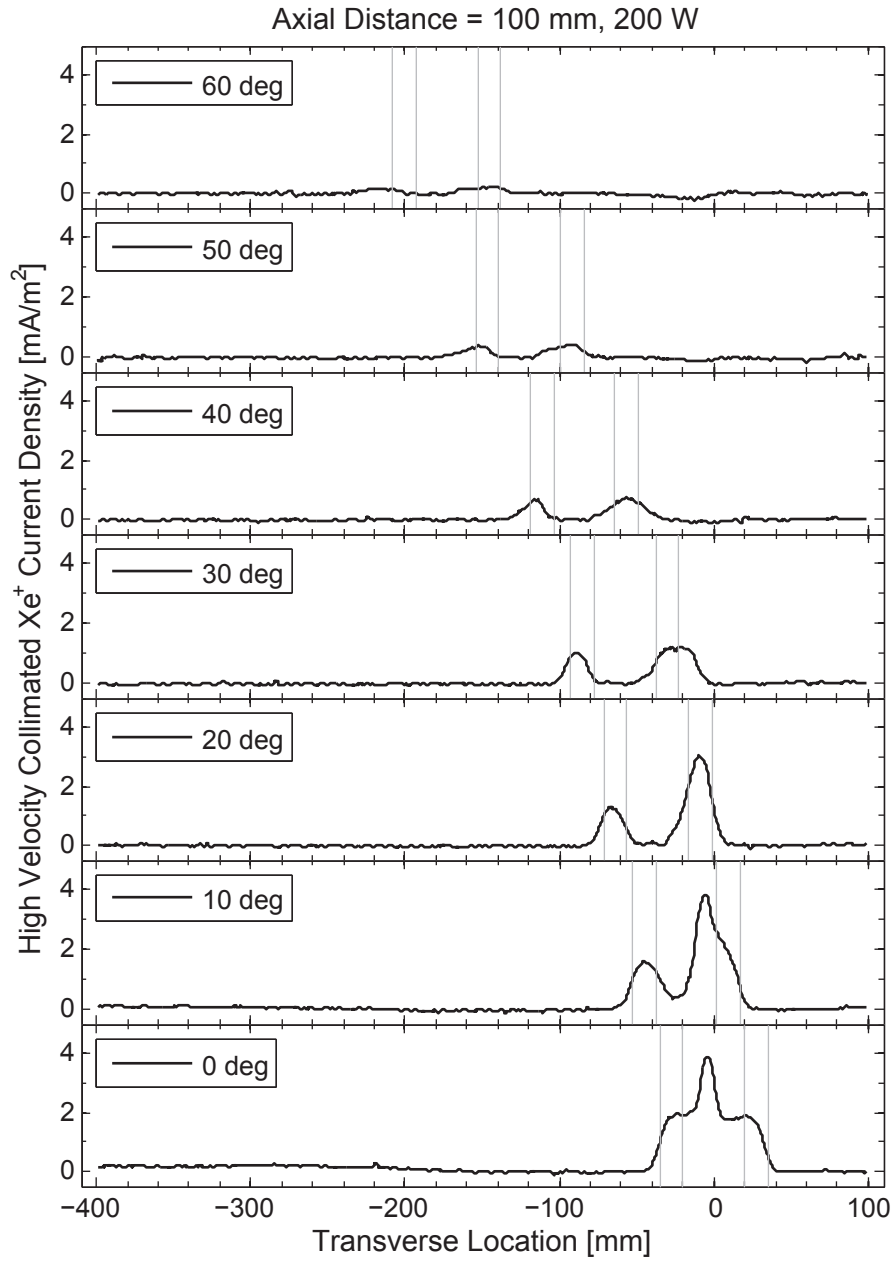


Figure 5.7: ExB results, 200 W case, at 100 mm.

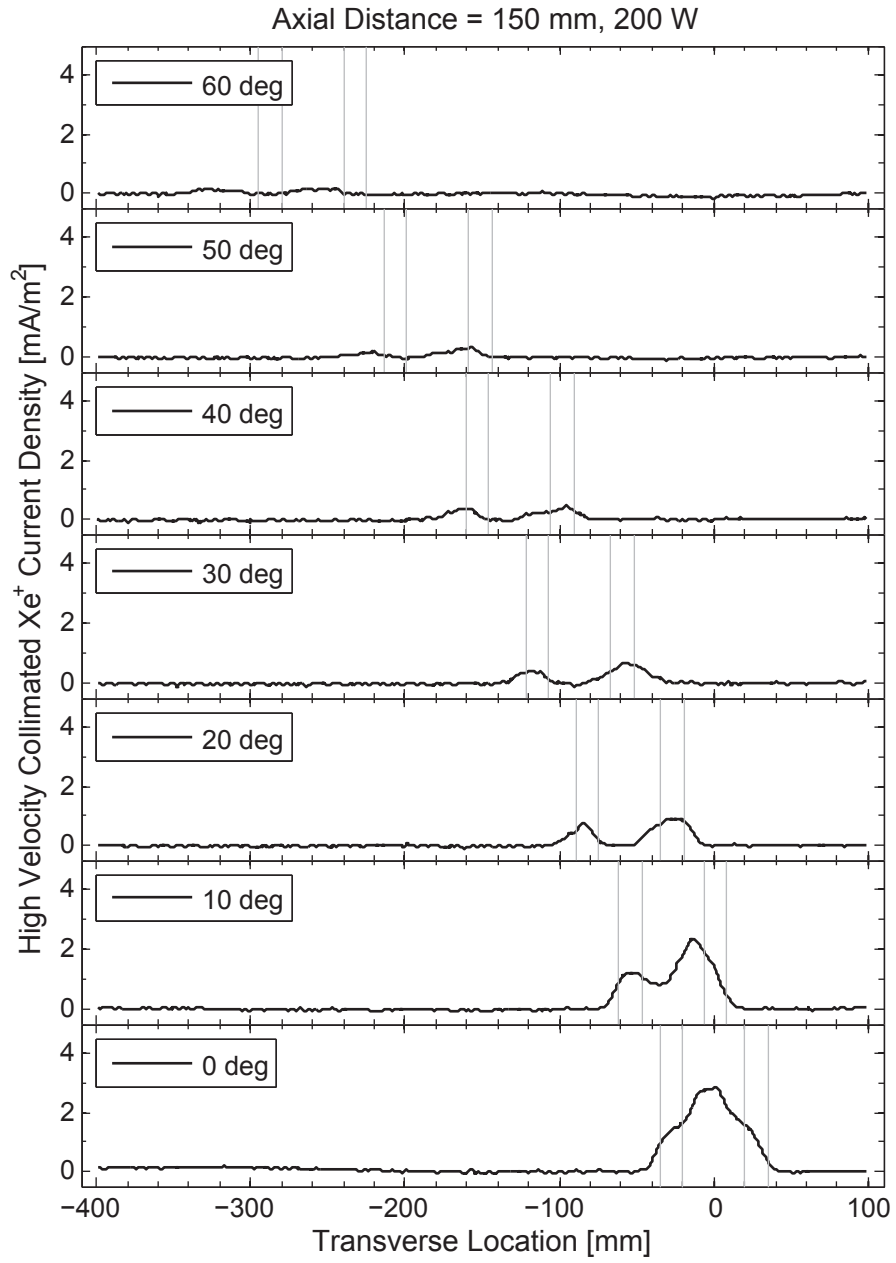


Figure 5.8: ExB results, 200 W case, at 150 mm.

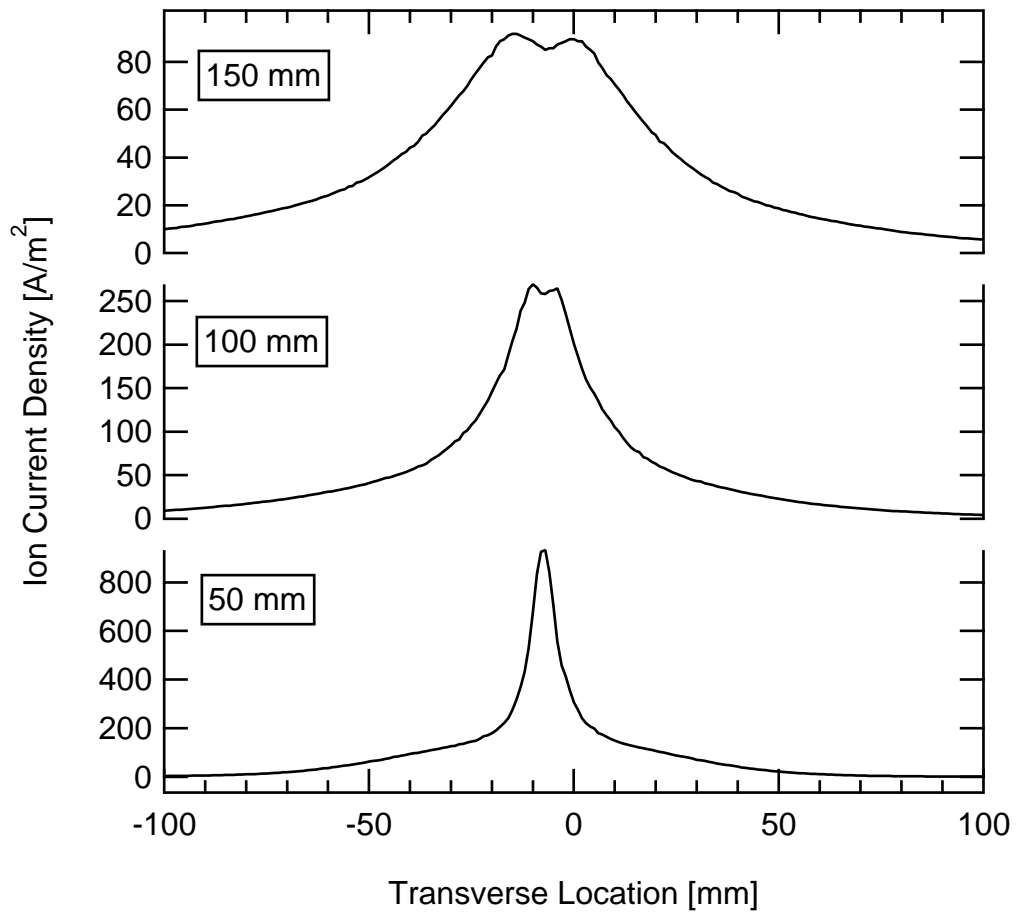


Figure 5.9: Faraday probe results, 200 W case.

### 5.1.1.2 650 W Results

Figure 5.10 shows the results of transverse scans at 650 W, at different angles relative to the centerline, for the 50 mm case. This shows roughly the same trends as the 200 W case: larger inward-radial current density, and substantial deviation from straight line trajectories as the angle increases. Figure 5.13 shows the corresponding Faraday probe trace at 50 mm and with zero angle relative to the centerline. In this trace, there is a large peak at the center, with “shoulders” on the distribution that appears to correspond to the channel, and which are not present in the 200 W case. This suggests that at 650 W, at 50 mm the annular ring makes a proportionally greater contribution to the total ion current density than it does in the 200 W case. Thus, it appears that the beam takes a longer distance to transition from ring to jet as the power is increased.

Figure 5.11 shows the results of transverse scans for the 650 W condition, at different angles relative to the centerline, for the 100 mm case. Again, this shows roughly the same trends as were seen at the 200 W condition. Figure 5.13 shows the corresponding Faraday probe trace at 100 mm and with zero angle relative to the centerline. Unlike the 50 mm case, there are no shoulders in the trace; rather there is a single peak at the center of the distribution. This peak is higher in magnitude than the central peak in the 50 mm case, so the central jet has a greater total current density at 100 mm than at 50 mm.

Figure 5.12 shows the results of transverse scans for the 650 W condition, at different angles relative to the centerline, for the 150 mm case. In this case, the beam appears to be fully transitioned to the central jet, since the contributions from the two sides of the channel appear to have merged, even at higher angles off of the centerline. Figure 5.13 shows the corresponding Faraday probe trace at 150 mm and with zero angle relative to the centerline. In contrast to the 200 W case at 150 mm, the Faraday probe trace appears to have less spread, and thus it appears that the beam is more tightly collimated.

### 5.1.2 Axial Scans

Figure 5.14 and 5.15 shows the results of the axial scans for the 200 W and 650 W cases. Along the channel center, the  $\text{Xe}^+$  angle-resolved high velocity ion current density drops off monotonically. However, along the thruster center, the current density peaks at roughly 125 mm downstream of the exit plane, and has a precipitous drop at roughly 330 mm. This is

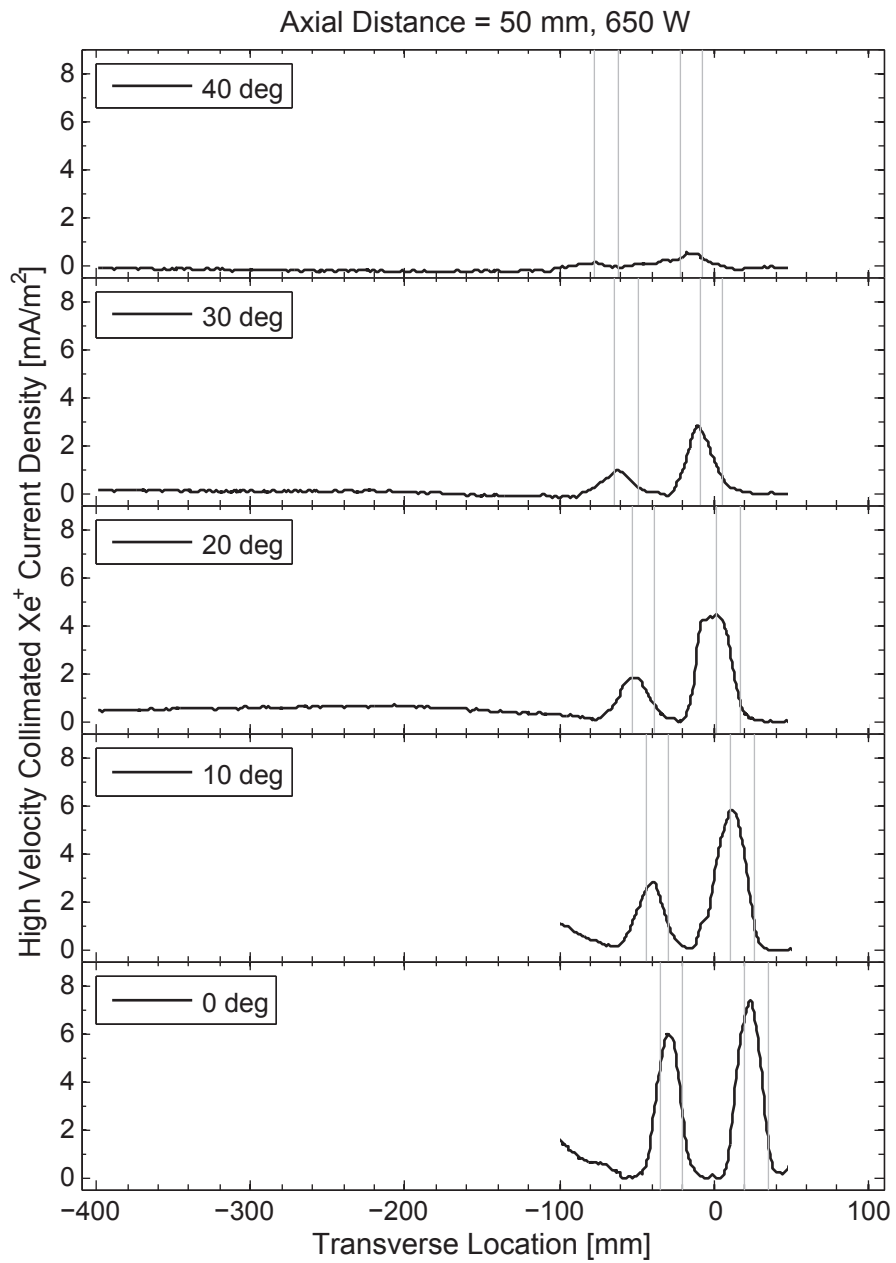


Figure 5.10: ExB results, 650 W case, at 50 mm.

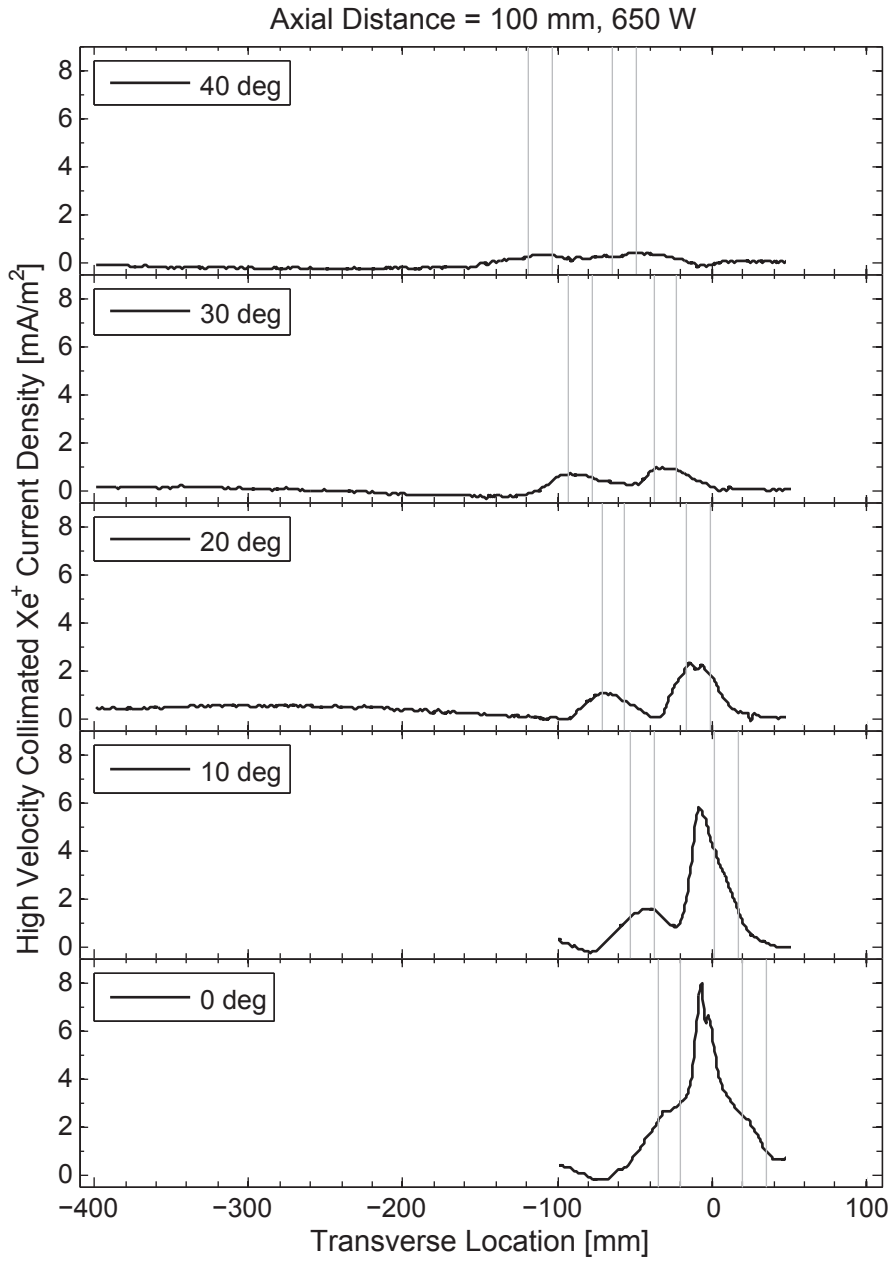


Figure 5.11: ExB results, 650 W case, at 100 mm.

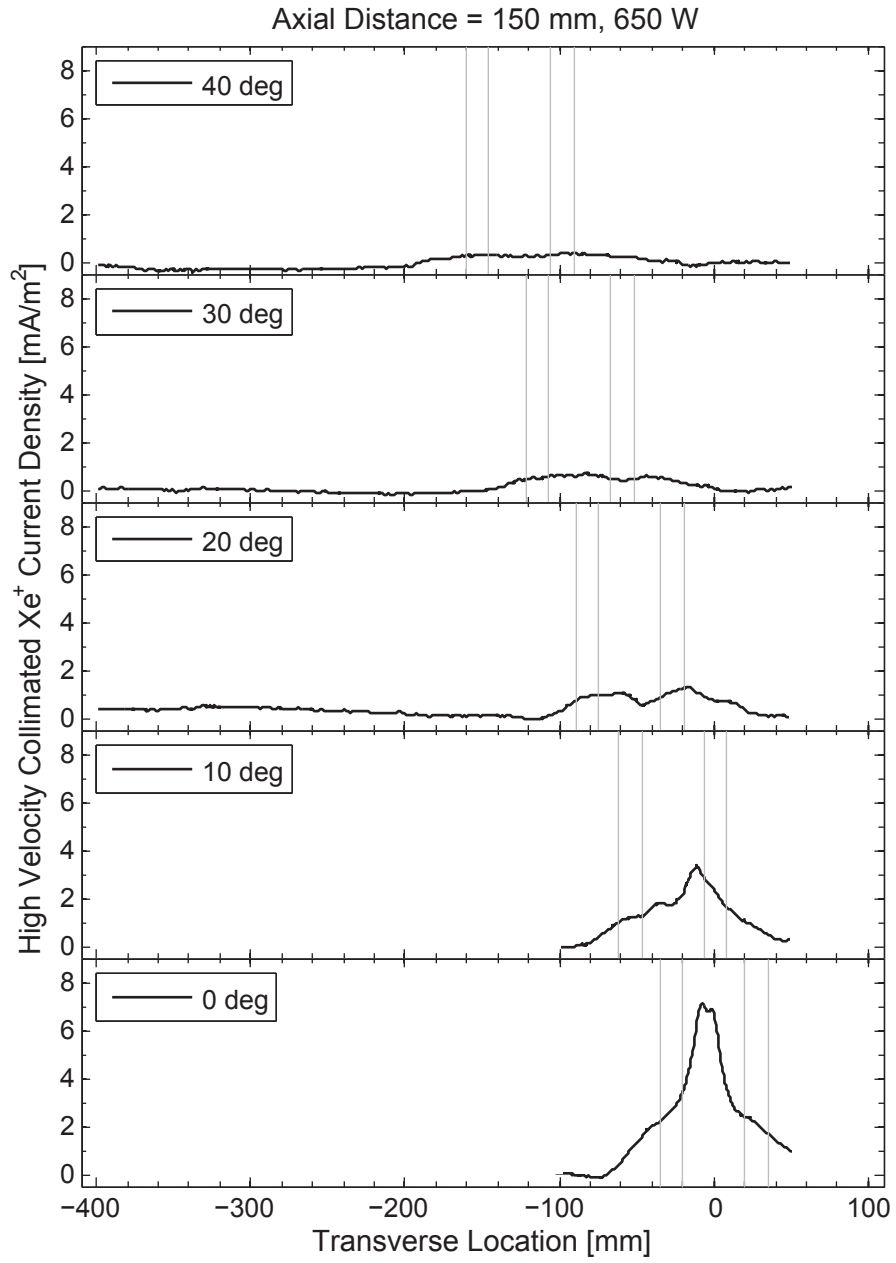


Figure 5.12: ExB results, 650 W case, at 150 mm.

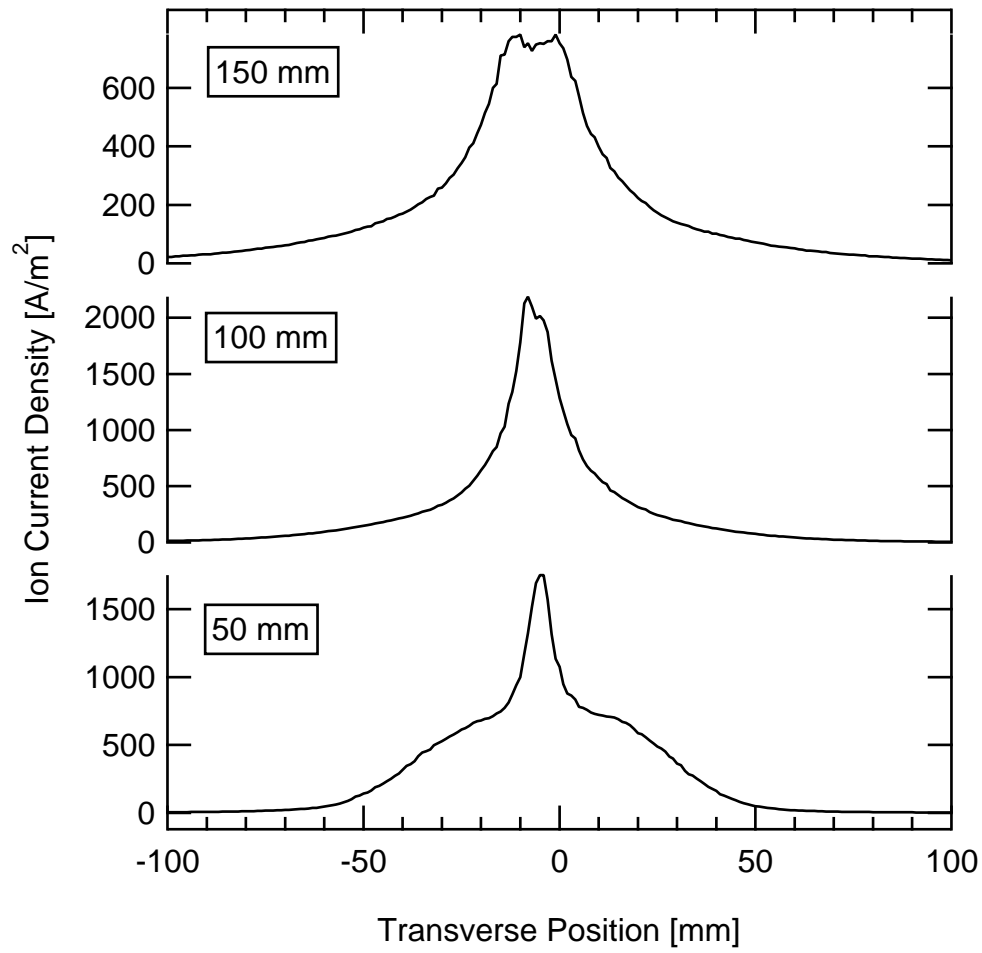


Figure 5.13: Faraday probe results, 650 W case.

strong evidence for an axially directed central jet that is made up of high-velocity  $\text{Xe}^+$  ions, as discussed previously.

It is also worth noting that along the channel centerline, the 650 W case behaves quite differently than the 200 W case. This can be seen by comparing Figure 5.14 to Figure 5.15. In the 200 W case, the ion current along the centerline is maximum at the exit plane, while in the 650 W case, the maximum is at 75 mm. One likely cause of this anomaly is that during an axial scan, the probe spends the duration of the scan directly in front of the thruster channel. This could lead to neutrals building up in front of the device, blocking a portion of the ion current. (In contrast, during a transverse scan the probe only spends a small fraction of the scan directly in front of the thruster channel). In the 200 W case, this discrepancy was not seen, most likely due to the lower ion and neutral densities.

Along the thruster centerline, the results at 650 W are similar to those at 200 W. Although the shape of the distribution is different, it still peaks at about 125 mm downstream, then decreases as axial position increases. Again, this indicates the presence of an axially directed jet. It is important to note that in both the 200 and 650 W cases, the largest high velocity ion current density that is axially directed is in a location that cannot have come directly from the channel. Therefore, there must be a mechanism within the near field that is changing ion trajectories as they leave the channel. As mentioned in the analysis of the transverse data, potential gradients caused by the residual electric field or non-uniform plasma density might influence ion motion in the near field.

## 5.2 Uncertainty in the ExB Data

As mentioned in Section 2.4.3, there are quantifiable uncertainties in the velocity measurement and the angle of acceptance of the ExB measurements. The velocity of accepted ions was found to be within one percent of the velocity that the ExB filter was set to accept ( $v_{acc} = E/B$ ). This means that the measured ions were within  $\pm 1$  percent of the primary energy ion velocity. Also, the acceptance angle was  $0.8^\circ$ , meaning that the ion trajectories were within  $\pm 0.8^\circ$  of the set angle of the probe. Finally, the measured position values are within  $\pm 1$  mm, which is the precision of the translation stage.

In addition to these quantifiable uncertainty values, there is a possible systematic uncertainty in the ion current density measured by the device. This is introduced by some of

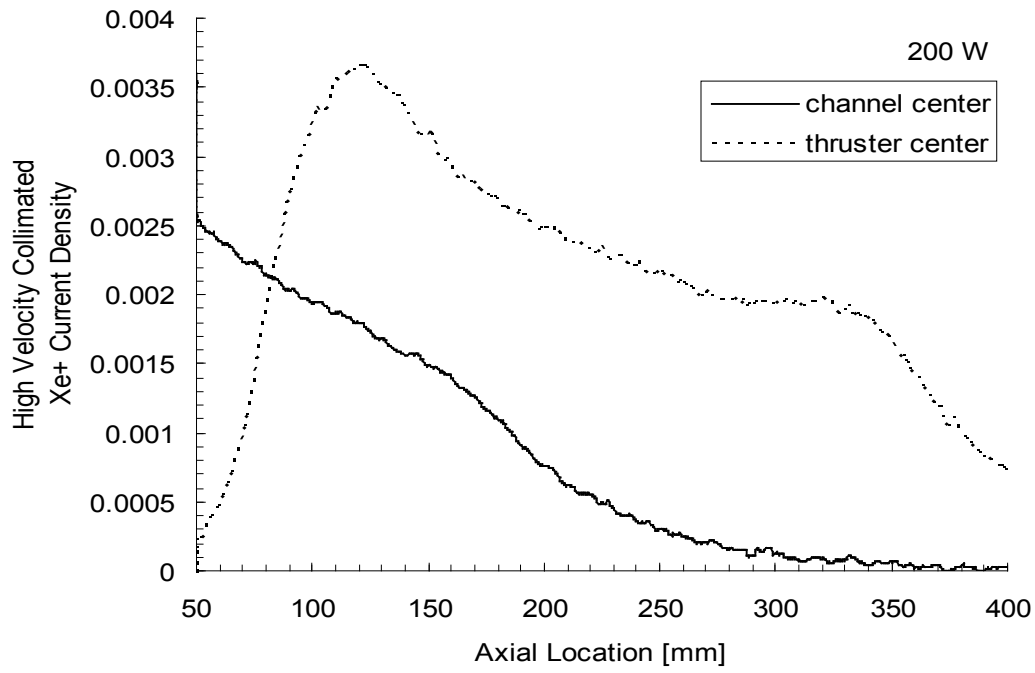


Figure 5.14: ExB axial results, 200 W.

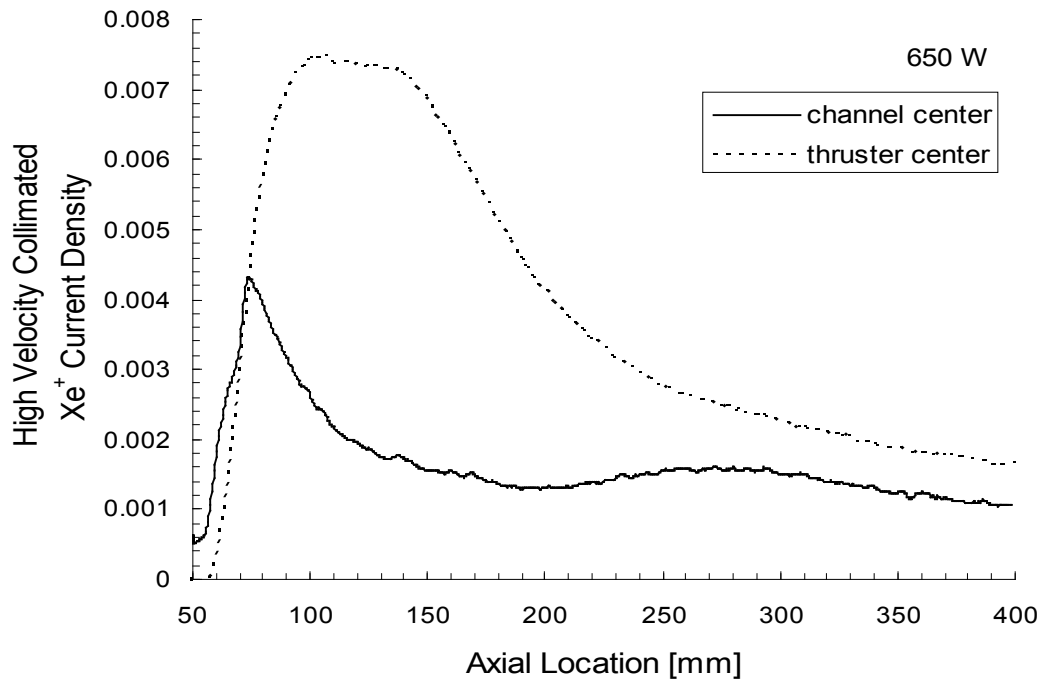


Figure 5.15: ExB axial results, 650 W.

the other possible sources of error that were discussed in Section 2.4.3 (such as the neutral density inside the device). The ideal way to quantify this systematic uncertainty is to calibrate the ExB filter on an ion source with a known current flux and velocity distribution. However, since this was not available in this case, there is a considerable uncertainty in the ion current density values measured by the device (the author's opinion is that it could be as large as a factor of two). Nonetheless, because the uncertainty is systematic (i.e., constant for a given thruster operating condition), it is acceptable to compare two traces taken at the same operating condition, as was done in the preceding sections. It should also be noted that this type of uncertainty should not have an impact on the x-axes of the ExB plots in the previous sections (the transverse or axial location of the probe), nor should it have an influence on the trajectory angles of the ions, since these values are set by the positioning system and the angle of acceptance, respectively.

### 5.3 RPA Analysis

As discussed in Section 2.5, the RPA raw data represents the "integrated" ion current, i.e., the current corresponding to ions above a certain energy. To obtain the ion energy distribution, the derivative of the raw data must be taken. (The differentiation method is described in Section 2.5, as well as the uncertainty introduced to the data through this process.) In this chapter, just the differentiated data will be presented. The raw data can be found in Appendix B so that the reader can clearly compare the total ion current between scans if desired.

The individual RPA scans were taken at a fixed distance from the thruster center, at different angles off the thruster centerline (see Section 2.6). In the 200 W case, scans from 0 to 30° were taken at a radial distance of 600 mm, while scans from 40 to 90° were taken at a distance of 400 mm. The same was done for the 650 W case, except for the scan at 0°, for which the radial distance was 1000 mm. The distance from the thruster was not the same for all scans due to facility constraints (at high angles the radius of the chamber limited the radius at which the RPA could be positioned), and due to device constraints (if the RPA was too close to the thruster, the high ion density inside the device led to electrical arcing between grids).

Energy distributions were calculated by taking the derivatives of the integrated cur-

rent plots. After the derivatives were taken, the energy distributions were normalized by the total ion current, so that the integral over all energies equals one for each plot. Therefore, the plots in Figures 5.16 to 5.21 show the proportion of ion current versus ion energy, rather than the value of the current itself. This normalization was done so that different scans could be compared on the same scale, even if the scans were taken at different distances from the thruster. The alternative was to adjust the data by using a certain scaling factor that corresponded to the distance at which the data was taken. For example, the total ion current could have been scaled by  $1/R^2$ . However, because of the uncertainty that this scaling would introduce, it was decided that the plots presented in this chapter would be normalized rather than scaled. For reference, the non-normalized plots can be found in Appendix B.

Figure 5.16 shows that, at the 200 W condition, as the angle increases the proportion of ion current due to primary beam ions decreases, and a greater proportion of ion current at lower energies is present. Note that at 200 W, the thruster acceleration potential was 250 V, and the measured extraction potential of the cathode was approximately 20 V, so one would expect to see primary beam ions at 230 eV/q, which is what is seen in Figures 5.16 to 5.18. At 20°, ions with energies as low as 100 eV/q are seen, while at 40°, ions with energies as low as 20 eV/q are observed. However, even at 40°, there is still a substantial proportion of ion current at the primary beam energy. This suggests that at 200 W, the plume is not particularly well-collimated.

From 45 to 65°, as shown in Figure 5.17, the peak corresponding to the high velocity ions continues to decrease in height, while a peak centered at roughly 30 to 40 eV emerges. Previous research has suggested that this low energy peak can be explained by the effect of charge exchange (CEX) collisions in which a fast moving  $\text{Xe}^+$  ion trades momentum with a slow moving neutral Xe atom. Additionally, the mid-range energy ions (at roughly 50 to 200 eV) have been attributed to elastic scattering collisions [48]. For this angle range, there is a substantial proportion of mid-range energy ions, the proportion of which remains approximately constant as the angle is increased from 45 to 65°. Looking at the 65° trace, one can see that the peak corresponding to the low energy CEX ions is larger than that due to the primary beam energy ions. From 70 to 90°, as shown in Figure 5.18, the high velocity ion peak continues to decrease in height, while the low energy CEX peak increases in height, and the distribution of the elastically scattered ion energies shift toward lower

values. However, it should be noted that even at  $80^\circ$ , a noticeable peak corresponding to the primary beam energy is still present, and even at  $85^\circ$ , some high velocity ions can still be seen.

For the 650 W case, from  $0$  to  $40^\circ$  (Figure 5.19), a high velocity ion peak is seen, centered roughly at  $270$  eV/q. (Note that the acceleration potential for this case was  $300$  V, while the cathode extraction potential was roughly  $25$  V, so one would expect to see the primary beam peak at roughly  $275$  eV/q) From  $0$  to  $10^\circ$ , the primary energy ion peak decreases in height as angle is increased, and the proportion of elastically scattered ions increases. At  $0$  and  $10^\circ$ , one can also see a “tail” off the primary beam energy peak, extending to energies roughly  $400$  eV/q, which is substantially greater than the applied acceleration potential of  $300$  V. As discussed in Section 2.5, an explanation for ions with an energy per charge greater than the acceleration potential of the thruster is that these ions have gone from  $\text{Xe}^{2+}$  to  $\text{Xe}^+$  in a CEX collision.

Looking at Figure 5.19, between  $10^\circ$  to  $20^\circ$  the high energy peak actually increases in height. This may be due to the CEX phenomena mentioned in the previous paragraph;  $\text{Xe}^{2+}$  ions that would have contributed to the peak height have been converted to  $\text{Xe}^+$  and their energies have spread out in the high energy tail portion of the distribution. As the angle is increased further from  $20$  to  $40^\circ$ , the primary beam energy peak decreases in height, and the proportion of elastically scattered and CEX ions increases. At  $40^\circ$ , the energies corresponding to elastic scattering dominate the distribution.

As in the 200 W case, as the angle is increased from  $45$  to  $65^\circ$  (Figure 5.20), the low energy CEX peak increases in height while the primary beam energy peak decreases in height. At  $65^\circ$ , there is no ion current due to the ions with the primary beam energy. As the angle is further increased from  $70$  to  $90^\circ$ , the proportion of ions corresponding to elastic scattering decreases, while the low energy CEX peak increases slightly in height. No high velocity ions are present at these angles either.

Comparing the 200 W case to the 650 W case suggests that the 200 W case is significantly less collimated than the 650 W case, since a larger proportion of ions with the primary energy are seen at higher angles off of the thruster centerline in the 200 W case. This can be seen clearly by comparing Figure 5.16 to 5.19, Figure 5.17 to 5.20, and Figure 5.18 to 5.21. For example, by comparing the two cases at  $45^\circ$ , it is clear that in the 200 W case, the high velocity ions make up a major proportion of the ion current, whereas

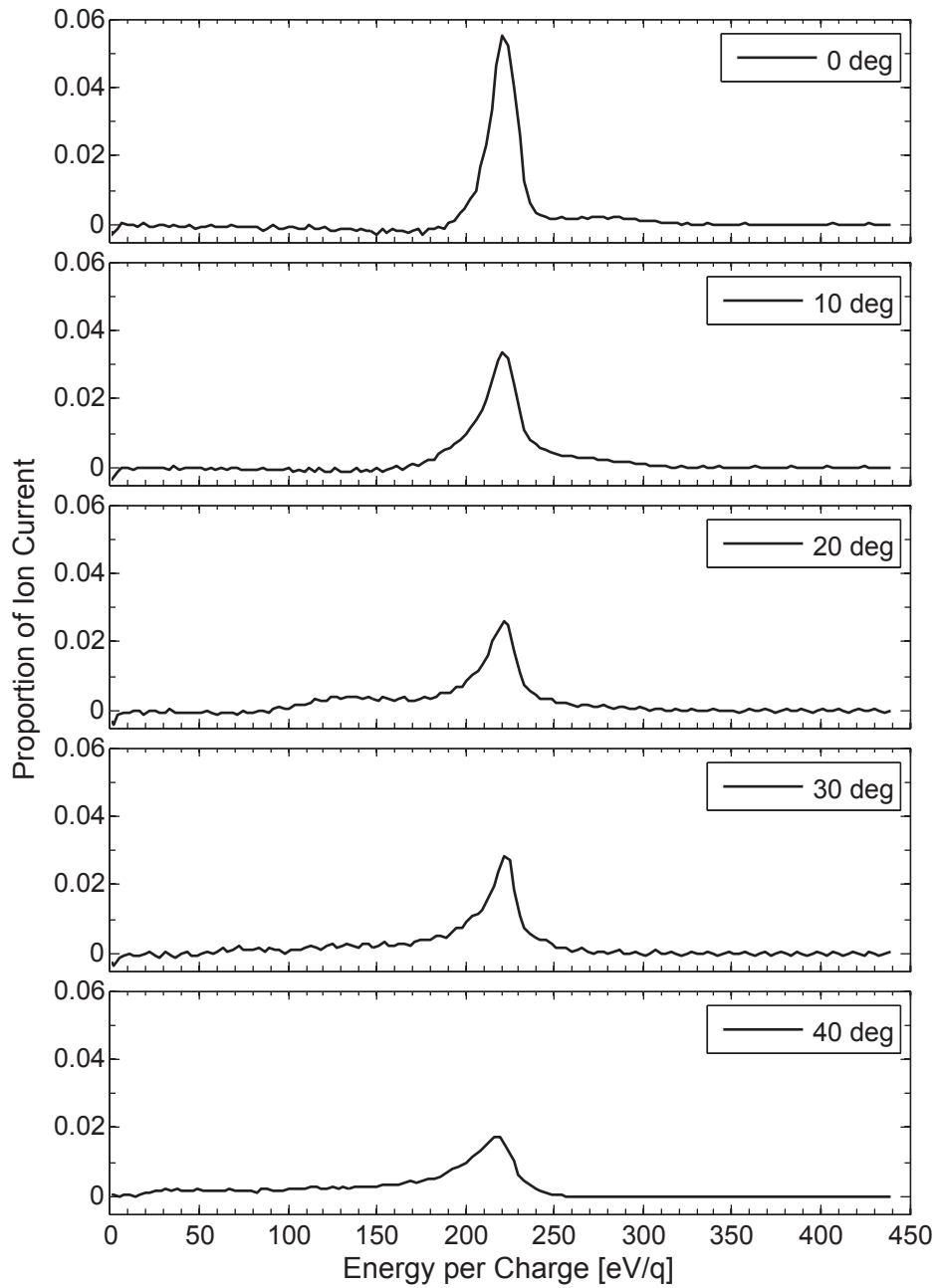


Figure 5.16: Differentiated RPA data at 200 W, 0 to 40° from centerline.

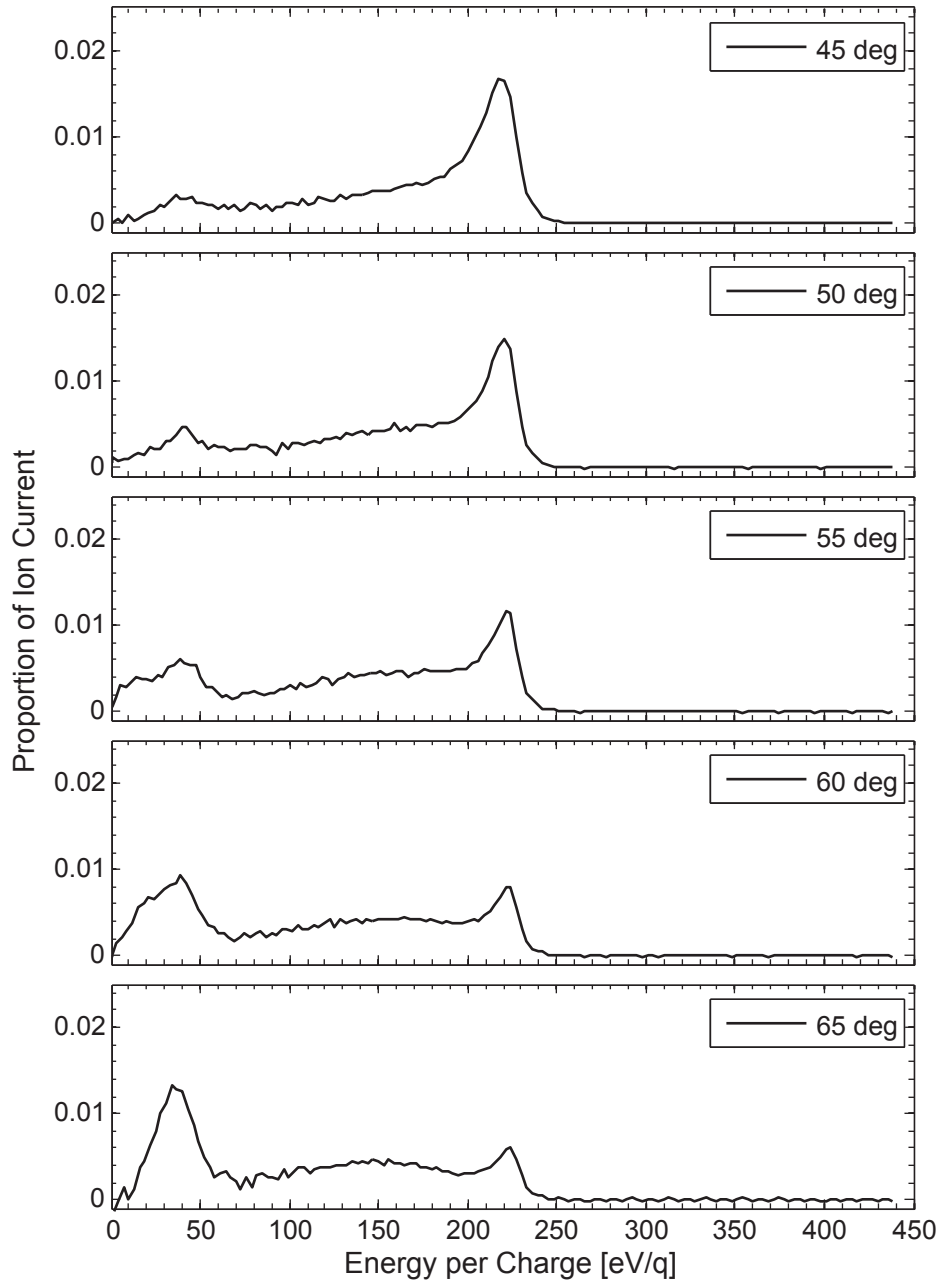


Figure 5.17: Differentiated RPA data at 200 W, 45 to 65° from centerline.

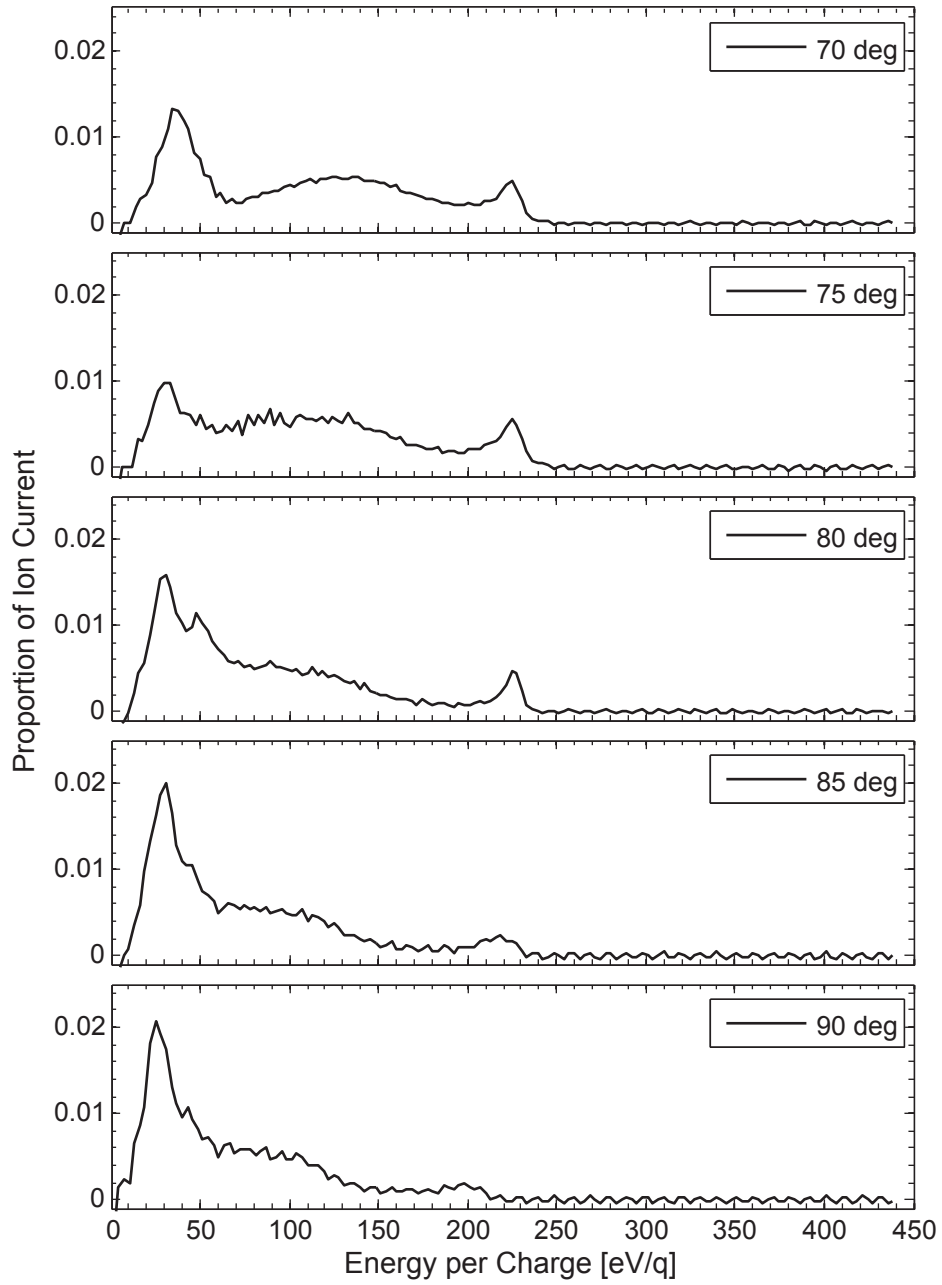


Figure 5.18: Differentiated RPA data at 200 W, 70 to 90° from centerline.

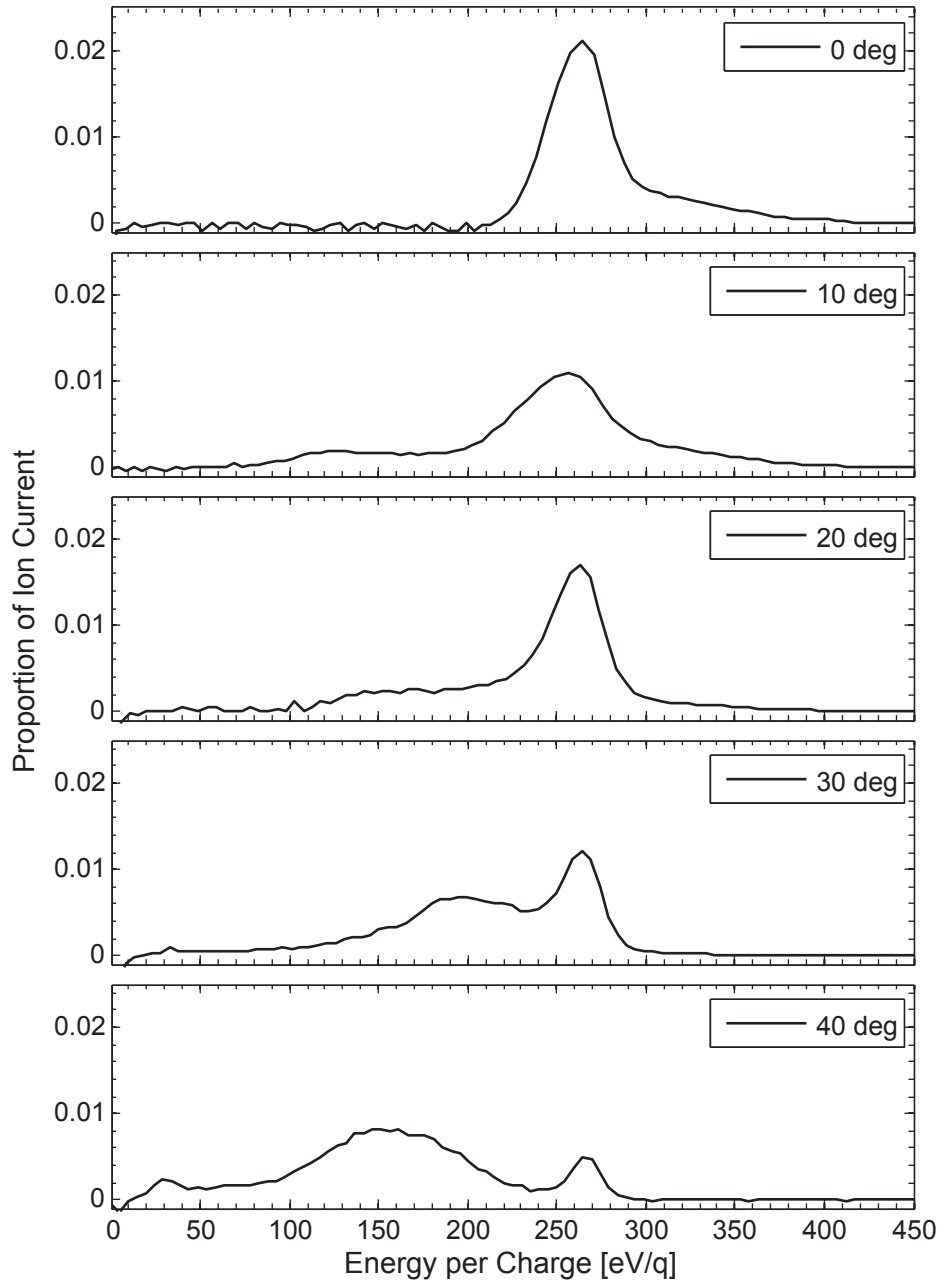


Figure 5.19: Differentiated RPA data at 650 W, 0 to 40° from centerline.

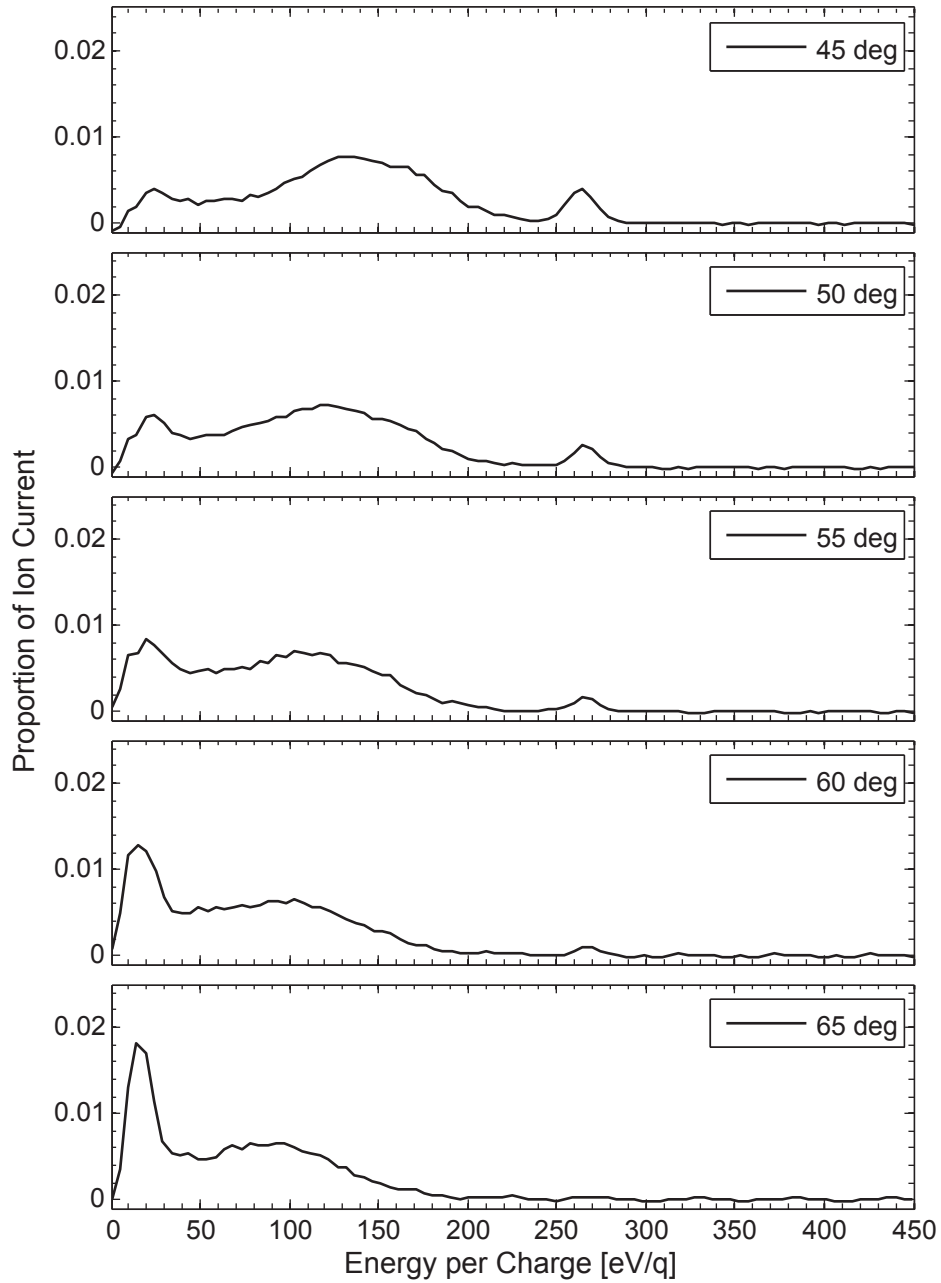


Figure 5.20: Differentiated RPA data at 650 W, 45 to 65° from centerline.

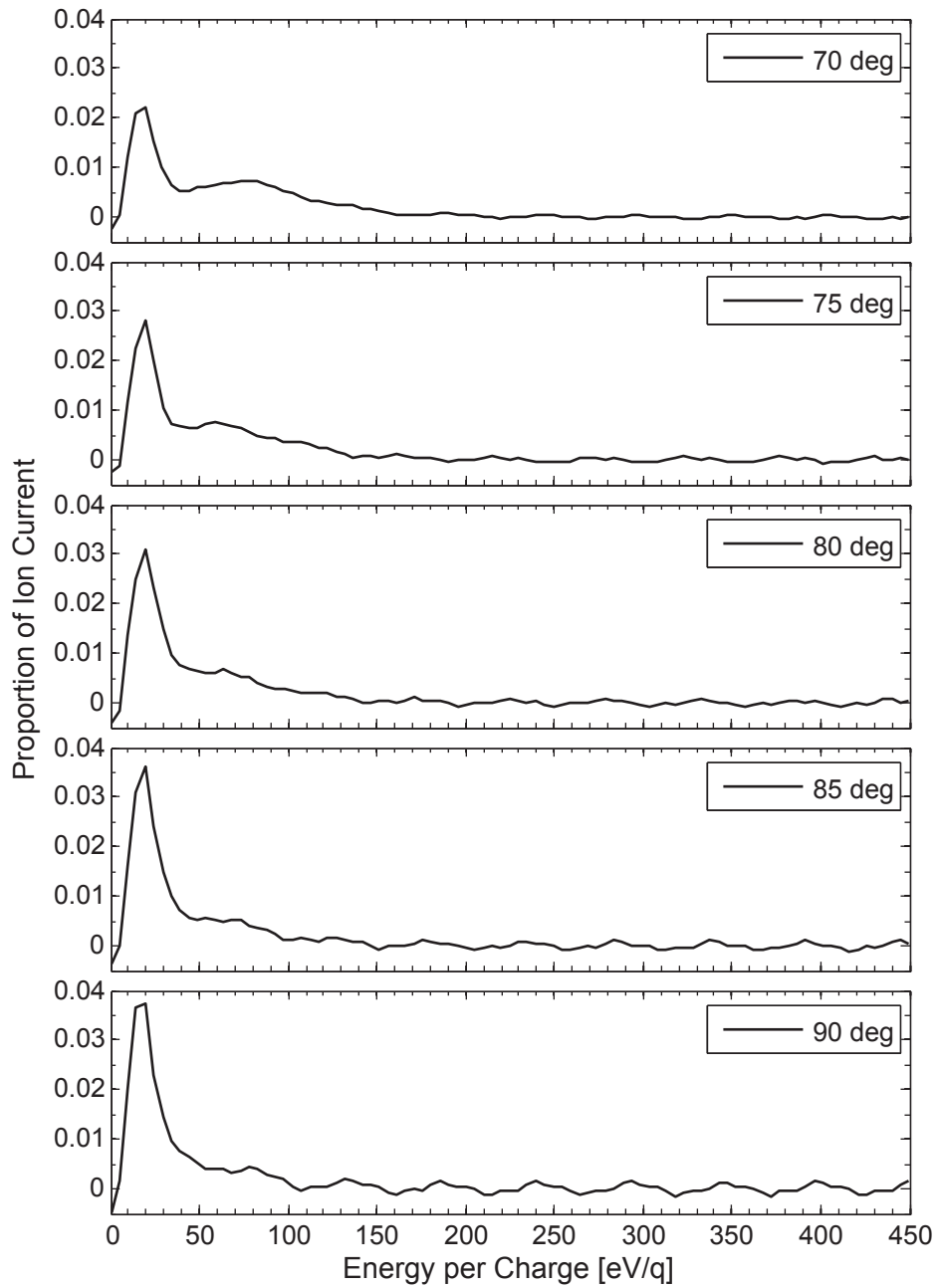


Figure 5.21: Differentiated RPA data at 650 W, 70 to 90° from centerline.

in the 650 W case, the mid-range elastic scattering energies dominate the distribution.

In terms of high angle ions with the primary beam energy, in the 200 W case, these ions can be seen out to  $85^\circ$ , while in the 650 W case these ions can be seen out to  $60^\circ$  from centerline. This begs the question: if the thruster is designed such that the electric field is primarily axial, then how are initially axial ions being accelerated out to high angles off the centerline? The answer to this question will be addressed in Chapter 6, and is an important issue to arise from the experimental investigation, primarily because it has repercussions for thruster integration onto spacecraft.

## 5.4 Uncertainty in the RPA Data

As mentioned in Section 2.5.3, there is a quantifiable uncertainty in the energy per charge values in the RPA traces, due to the way in which the raw data was differentiated. The bound on the energy per charge values was found to be  $\pm 3$  V for the 200 W condition, and  $\pm 5$  V for the 650 W condition. Again, as with the ExB probe, because the RPA was not calibrated on an ion source with a known current flux/energy distribution, there was a systematic uncertainty in the ion current measured by the RPA which could be as high as a factor of two. However, since each RPA trace shown in this section was normalized by the total current for the trace, this eliminates the effect of the uncertainty in the ion current measurement. Nonetheless, one should keep in mind this uncertainty if one looks at the raw and non-normalized data in Appendix B.

## 5.5 Sputter Yield Analysis

From a thruster integration standpoint, an important metric is the total sputter yield. Sputter yield is a measure of the number of atoms that are liberated due to a collision between an ion and a material surface. The higher the total sputter yield, the more damage done by an ion of a given energy. By multiplying the RPA ion energy distributions (Figures B.7 to B.12 in Appendix B) by sputter yield distributions as a function of energy (Figures B.13 to B.16 in Appendix B), one can obtain a distribution of the total number of atoms of sputtered material as a function of energy, as illustrated in Figure 5.22. This is what was done in Figures 5.23 to 5.30, for several different elements likely to be found in materials used to

make spacecraft. Note that because all of the data plotted here were based on measurements taken at 400 mm from the centerline of the thruster, there was no need to normalize these plots so that they can be compared on the same set of axes. Therefore, the plots represent the total sputter yield, in atoms/s/cm<sup>2</sup>. The sputter yield distributions were taken from Matsunami [49] and Doerner [50], and are shown in Appendix B.

Figures 5.23 to 5.26 are the total sputter yield for carbon, silicon, aluminum, and titanium, for the 200 W case at angles between 40 and 80°. In general, these figures all follow the same trend, i.e., the high energy peak makes the greatest contribution to the total sputter yield. Additionally, there is some contribution from the mid-range energies, as can be seen by the tail extending off the main peak to lower energies. Carbon has the lowest total yield, while aluminum has the highest sputter yield. These figures show that even though the primary energy peak may be smaller in height than the low energy CEX peak in the energy distributions (as seen in Figures 5.16 through 5.18), in regards to total sputter yield the primary energy peak is a much greater concern.

Figures 5.27 to 5.30 are the total sputter yield for carbon, silicon, aluminum, and titanium, for the 650 W case at angles between 40 and 80°. In contrast to the 200 W case, in the 650 W case the carbon graphs show that the height of the high energy peak is comparable to the height of the structure corresponding to the mid-range energy ions. Additionally, because the high energy peak is narrower than the mid-range energy structure, it contributes less to the total sputter yield. In the case of the other materials, the high energy peak is taller than the mid-range structure, although if one were to take the integral of the curve, the contribution of the two structures would be comparable. Therefore, the data show that at 650 W, although the high energy peak is still a significant contributor to the total sputter yield, it is not necessarily the dominant contributor. In the 650 W case, elastically scattered ions appear to be of equal concern.

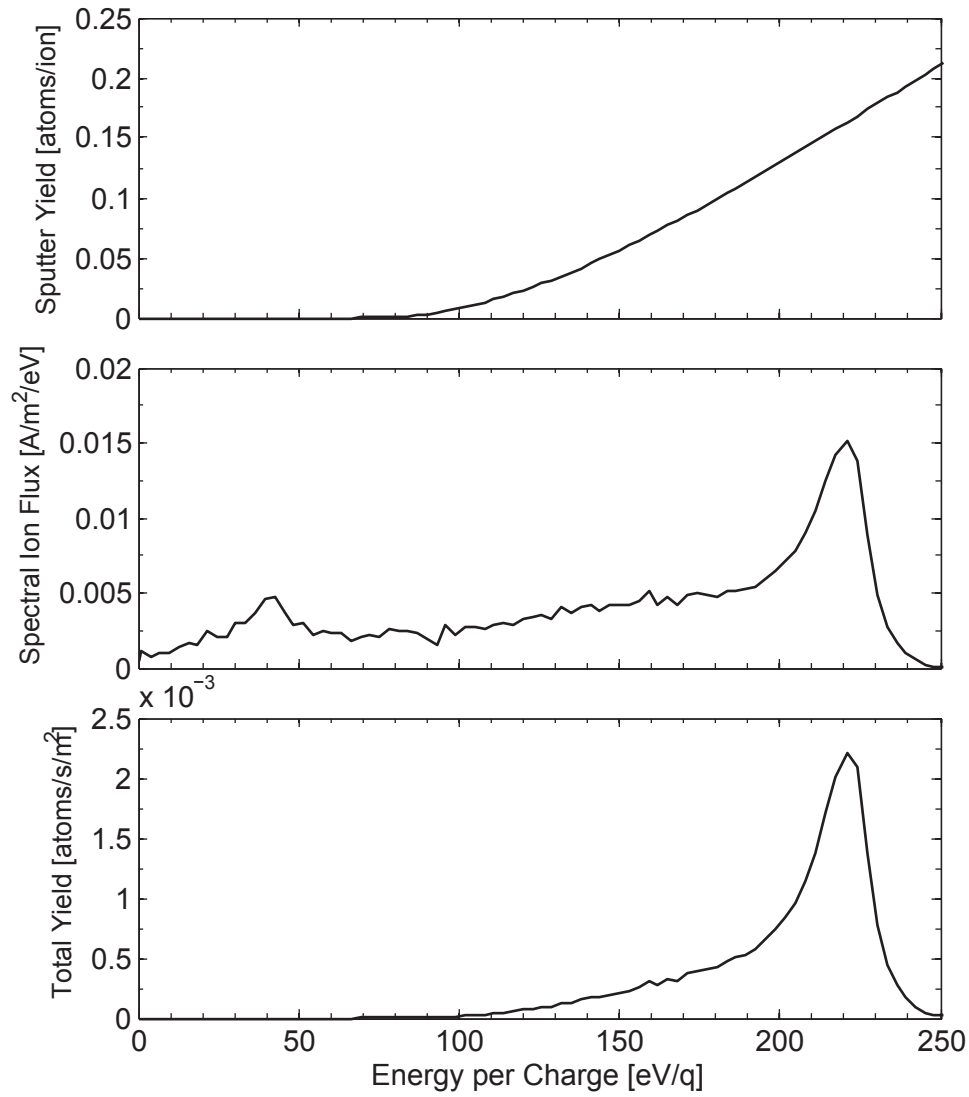


Figure 5.22: Example of sputter yield calculation. The top plot is the sputter yield from [49] or [50], the middle plot is an RPA trace from the experiment, and the bottom plot is created by multiplying the top two together.

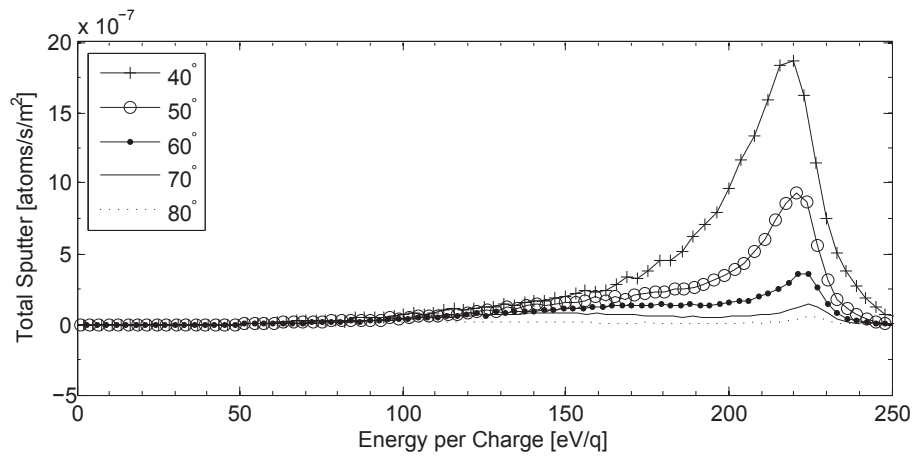


Figure 5.23: Carbon sputter yield estimate as a function of energy per charge, 200 W.

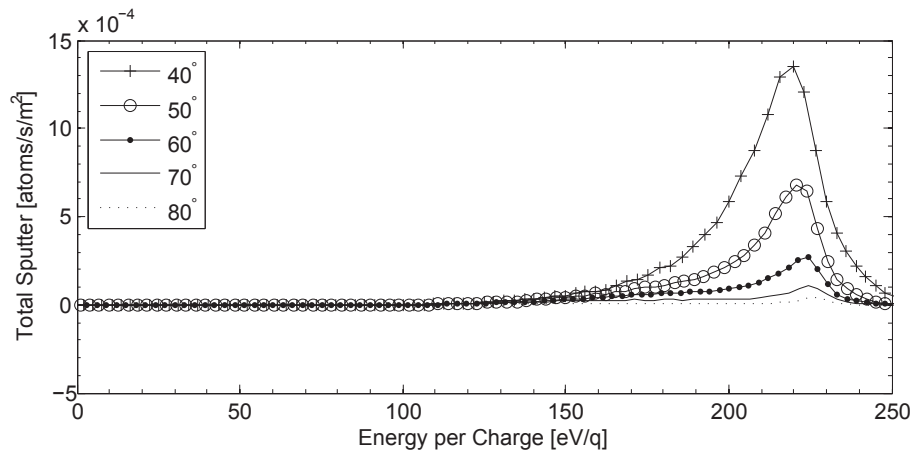


Figure 5.24: Silicon sputter yield estimate as a function of energy per charge, 200 W.

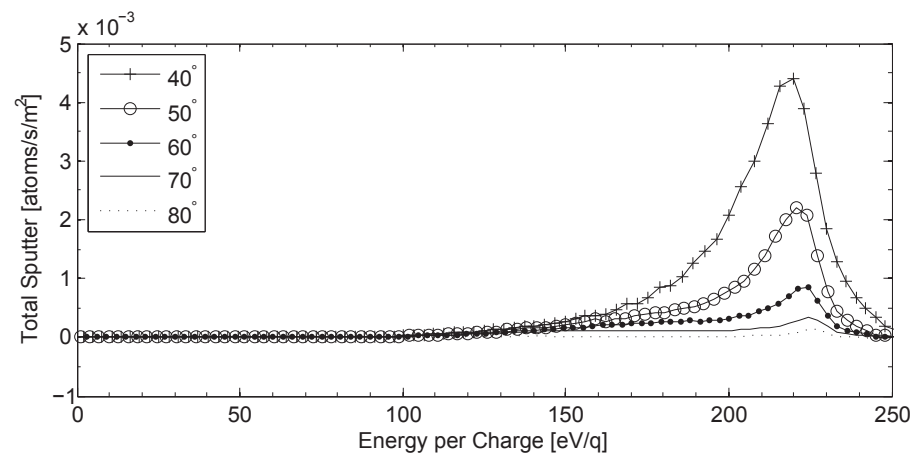


Figure 5.25: Aluminum sputter yield estimate as a function of energy per charge, 200 W.

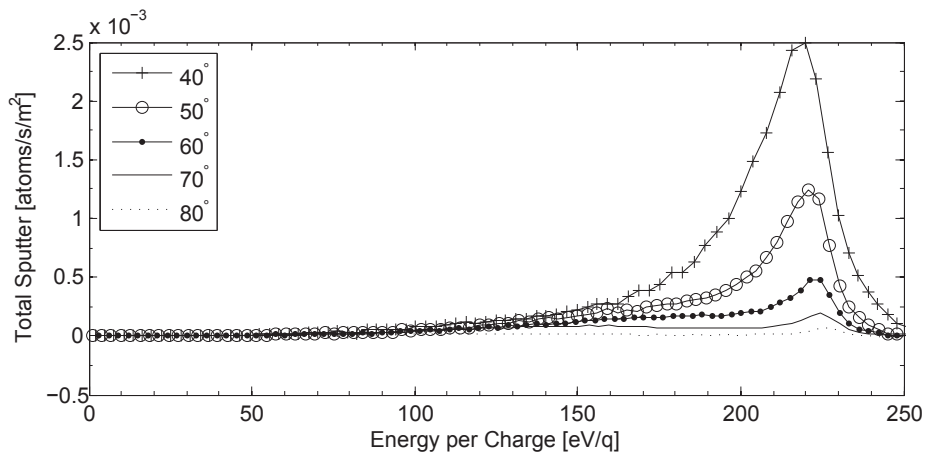


Figure 5.26: Titanium sputter yield estimate as a function of energy per charge, 200 W.

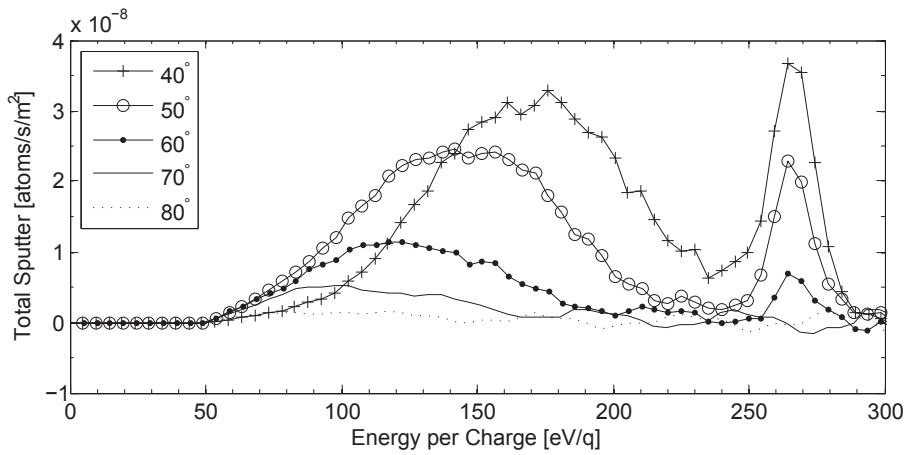


Figure 5.27: Carbon sputter yield estimate as a function of energy per charge, 650 W.

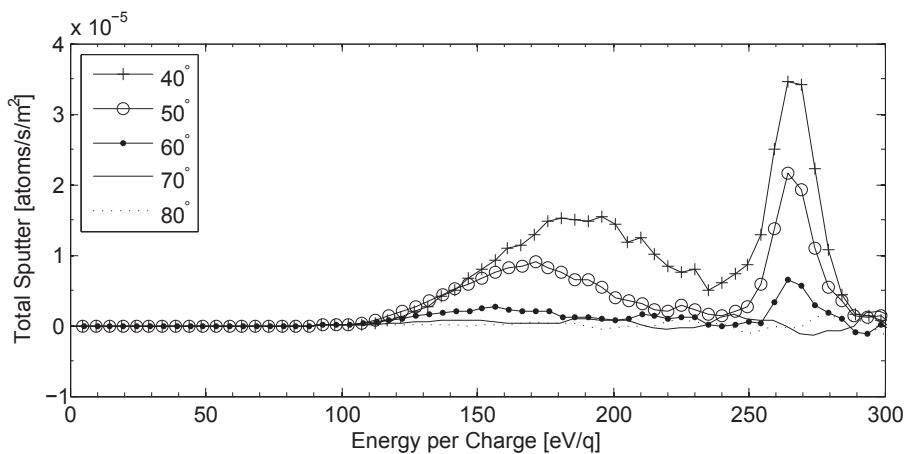


Figure 5.28: Silicon sputter yield estimate as a function of energy per charge, 650 W.

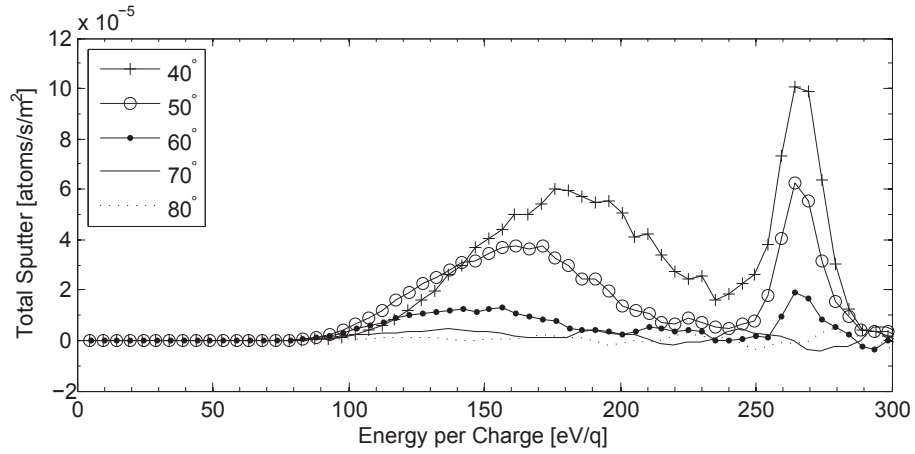


Figure 5.29: Aluminum sputter yield estimate as a function of energy per charge, 650 W.

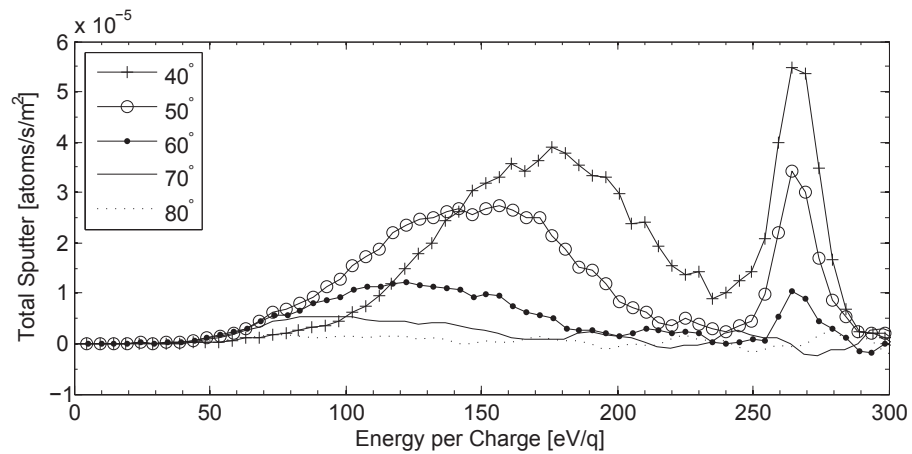


Figure 5.30: Titanium sputter yield estimate as a function of energy per charge, 650 W.

## Chapter 6

# HPHall Results and Discussion

This chapter details the results from the HPHall simulations. As described in Section 3.3.2, four different HPHall runs were selected: (1) a 650 W power level in which most of the acceleration region was upstream of the exit plane, (2) a 650 W power level in which a substantial proportion of the acceleration region was downstream of the exit plane, and (3) 200 W “upstream” and (4) 200 W “downstream” conditions. For each of these runs, averaged plasma parameters particle trajectories were tracked. The purpose of the HPHall simulations was to investigate the formation of the central jet, as well as determine whether certain configurations in HPHall could come close to reproducing the high angle, high energy ion populations seen in the experiment.

Simulated Faraday probe, ExB, and RPA traces were created from the HPHall outputs. Uncertainty values for these data were also calculated and are presented in this chapter. Although it was not expected that these simulated traces would exactly match those presented in Chapter 5, they do provide some insight into the physical mechanisms that determine the characteristics of the thruster plume. For instance, the simulated ExB results show that the central jet is not just the result of a symmetrically expanding ion beam, but that it also is influenced by asymmetry in the internal plasma potential profile. Additionally, although none of the four runs exactly reproduce the RPA results seen in the experiment, the simulated RPA results are clearly signatures of the internal electric field and ion density of the thruster.

Table 6.1: Description of the four runs modeled in HPHall.

Run Name	$V_D$ [V]	$\dot{m}$ [mg/s]	Transition Locations [m]	Mobility Coefficients	$T_{e\parallel}/T_{e\perp}$
650 W upstream	300	1.7	$z_c=0.025,$ $z_{e1}=0.027,$ $z_{e2}=0.029,$ $z_p=0.031$	$\alpha_c=0.055,$ $\alpha_e=0.5, \alpha_p=1$	0.5
650 W down-stream	300	1.7	$z_c=0.034,$ $z_{e1}=0.036,$ $z_{e2}=0.036,$ $z_p=0.036$	$\alpha_c=0.125,$ $\alpha_e=1.1,$ $\alpha_p=1.1$	0.3
200 W upstream	250	0.8	$z_c=0.025,$ $z_{e1}=0.027,$ $z_{e2}=0.029,$ $z_p=0.031$	$\alpha_c=0.03,$ $\alpha_e=0.3, \alpha_p=1$	0.5
200 W down-stream	250	0.8	$z_c=0.034,$ $z_{e1}=0.036,$ $z_{e2}=0.036,$ $z_p=0.036$	$\alpha_c=0.13,$ $\alpha_e=1, \alpha_p=1$	0.3

## 6.1 HPHall Run Conditions

As discussed in Section 3.3.2, two different runs per operating condition were modeled in HPHall. In one run the acceleration region was upstream of the exit plane, while in the other a significant portion of the acceleration occurred downstream of the exit plane. These runs were labeled as described in Table 6.1: (1) 650 W upstream, (2) 650 W downstream, (3) 200 W upstream, and (4) 200 W downstream.

## 6.2 Time Averaged Results from HPHall

### 6.2.1 650 W Results

Figures 6.1 to 6.5 show time-averaged plots of the plasma potential, electron temperature, ion density, ionization rate, radial and axial electric field, respectively, for the 650 W upstream run. As can be seen in Figure 6.1, most of the potential drop occurs between  $z = 0.0200$  and  $z = 0.0290$  m (the exit plane). At the exit plane, the potential is about 100 V. Looking at the axial electric field plot (Figure 6.2), it is clear that most of the acceleration occurs between these two axial locations.

The radial electric field plot (Figure 6.3) shows that the radial component is approx-

imately zero, except near the corners of the channel, where it is large. Near the corners, it is comparable in magnitude to the maximum axial electric field at approximately  $4$  to  $5 \times 10^4$  V/m. However, the extent of this region of high radial electric field is only several millimeters from the corners, so for ions to be accelerated out to high angles, they would have to pass within a millimeter or so of the corner. The electric field configuration thus suggests that in the 650 W upstream run, few ions will be accelerated out to high angles.

Figure 6.4 shows a peak in electron temperature that occurs at roughly  $z = 0.025$  m, with a maximum of about 35 eV. Figure 6.5 shows that the peak in ion density occurs upstream of the peak in electron temperature, and is centered at about  $z = 0.015$  m, with a maximum of  $12 \times 10^{17}$  m<sup>-3</sup>. The ion density distribution is not symmetric about the peak in the  $z$ -direction, rather it drops off more rapidly on the downstream side.

It is important to note that the ion density distribution is not symmetric about the center of the channel ( $r = 0.0275$  m) outside the exit plane of the thruster. There is a greater ion density at smaller radial distances from the centerline. This can possibly be explained by the slight asymmetry in the plasma potential plot, although the radial electric field plot does not suggest that there is significantly greater acceleration inward versus outward.

Figures 6.6 to 6.10 show the time-averaged quantities for the 650 W downstream run. In contrast to Figure 6.1, Figure 6.6 shows that for this run, most of the potential drop occurs between  $z = 0.020$  and  $z = 0.040$  m. The axial electric field, plotted in Figure 6.7 also shows that most of the axial acceleration occurs between these two locations, and shows the maximum axial field strength is significantly less than that of the 650 W upstream condition, since the potential drop is spread out over a larger axial distance.

Figure 6.8 shows that overall the radial electric field is greater in magnitude than in the 650 W upstream condition. Also, near the exit plane, the magnitude of the radial component is comparable to the axial component, with a value of approximately  $1$  to  $1.5 \times 10^4$  V/m. Near the corners, the radial electric field is roughly an order of magnitude higher than the axial electric field. This stronger radial electric field component suggests that more ions will be accelerated out to high angles in this run than in the 650 W upstream run.

Figure 6.8 shows a broad peak in electron temperature that extends from about  $z = 0.029$  to  $z = 0.035$  m, with a value of 30 eV, which is less than the maximum of 35 eV seen in the upstream run. The peak in ion density is farther downstream than in the previous run, occurring at about  $z = 0.0175$  m, with a maximum value of  $11.5 \times 10^{17}$  m<sup>-3</sup>. As in the

upstream run, the density is not symmetric about the channel center outside the exit plane.

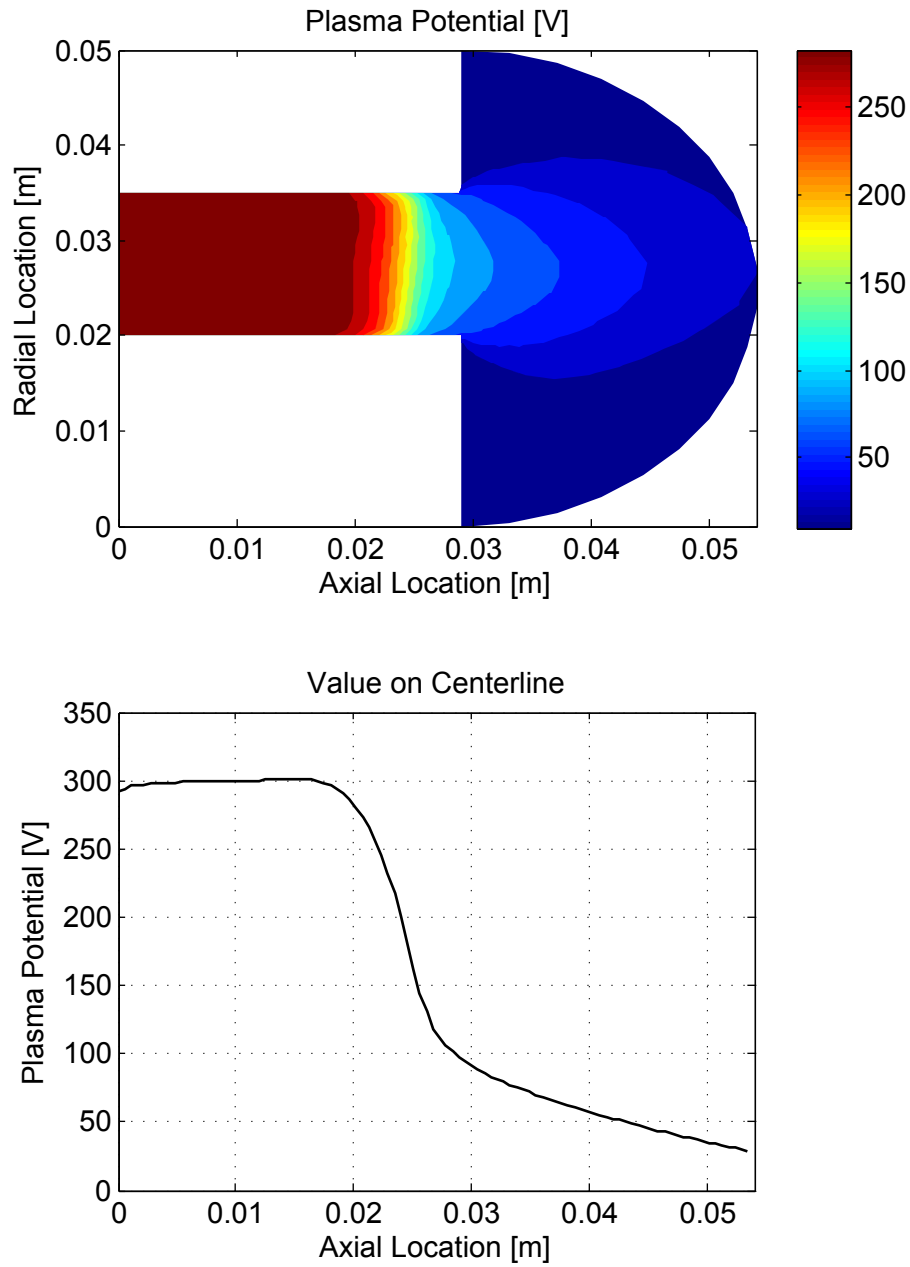


Figure 6.1: Averaged plasma potential distribution for the simulated 650 W upstream run.

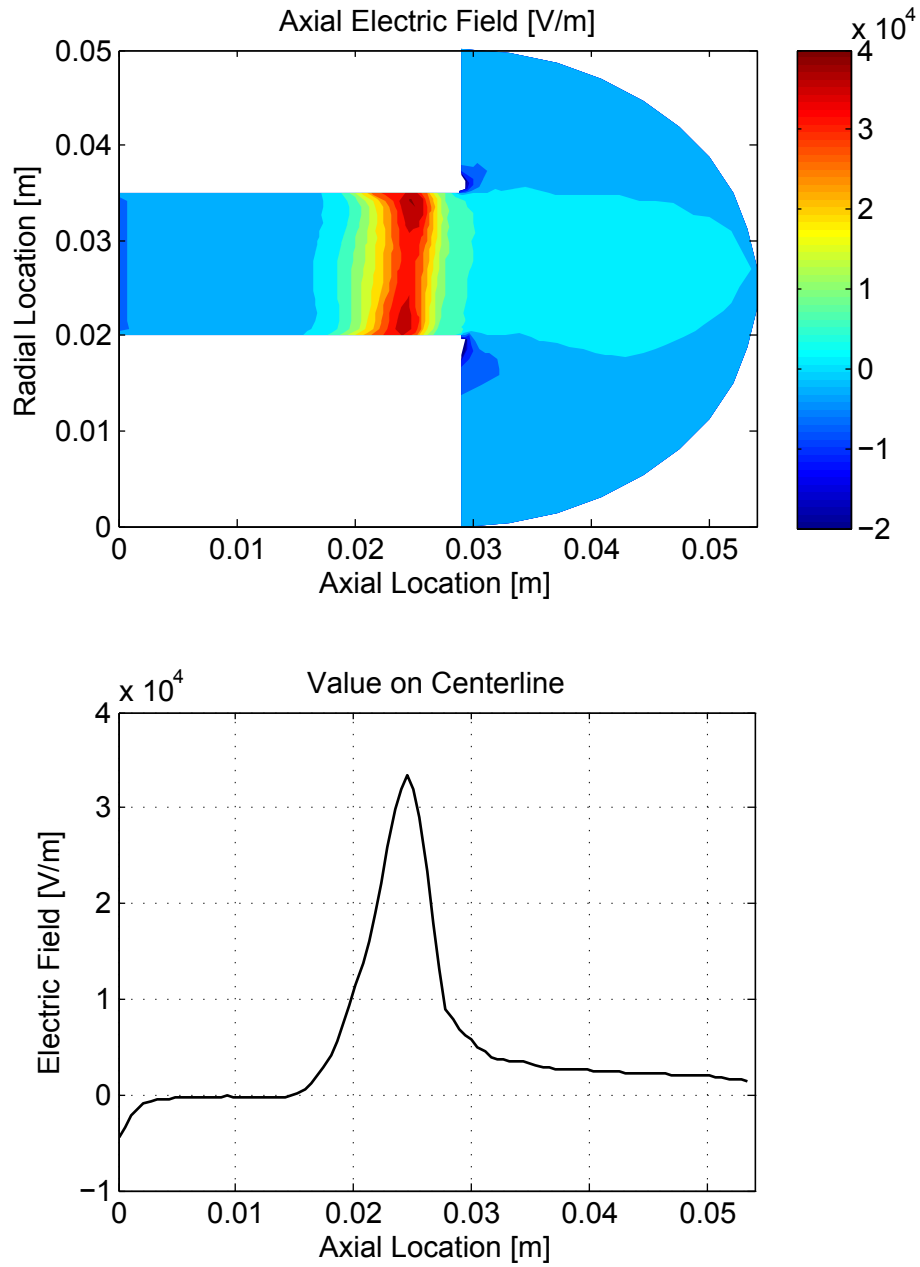


Figure 6.2: Averaged axial electric field distribution for the simulated 650 W upstream run.

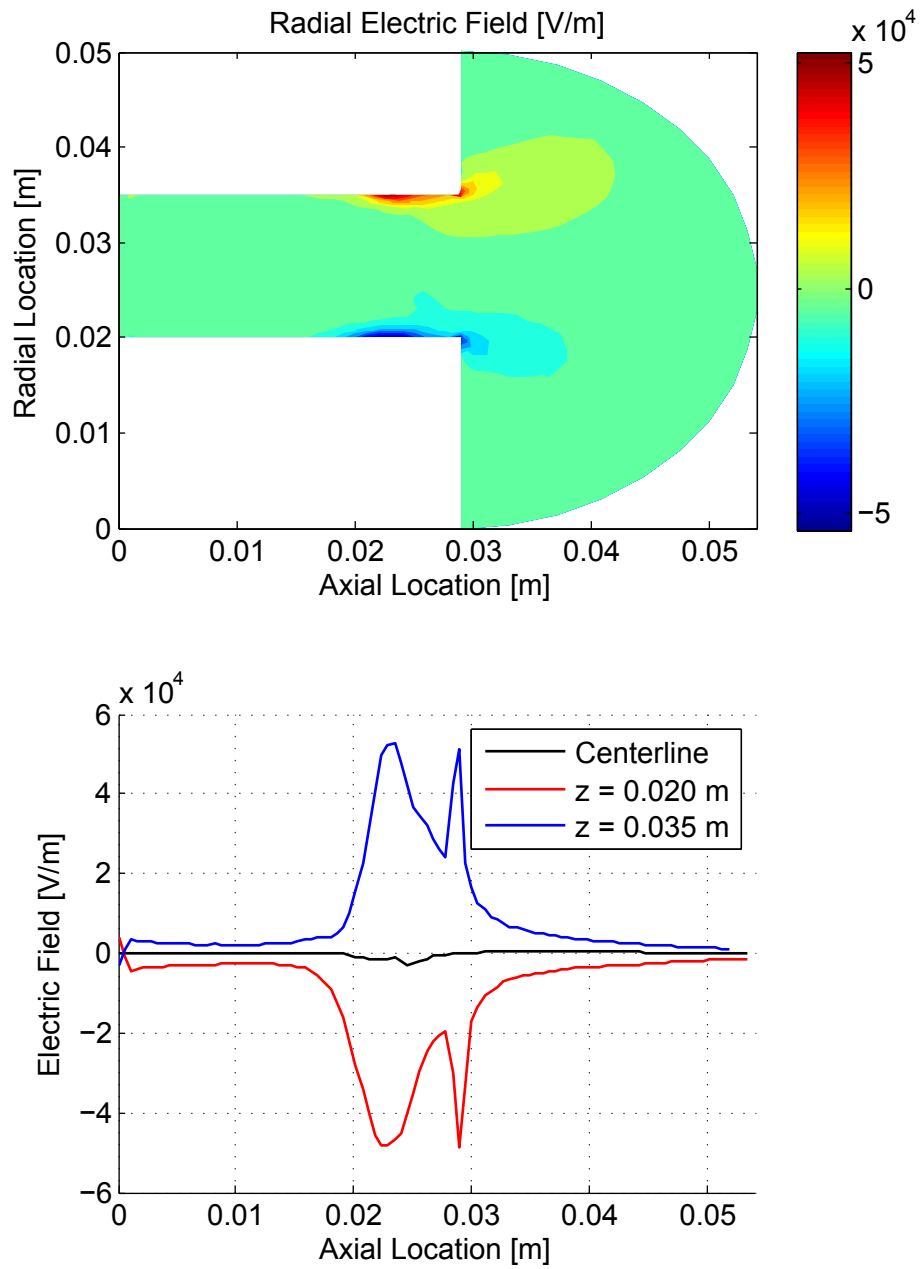


Figure 6.3: Averaged radial electric field distribution for the simulated 650 W upstream run.

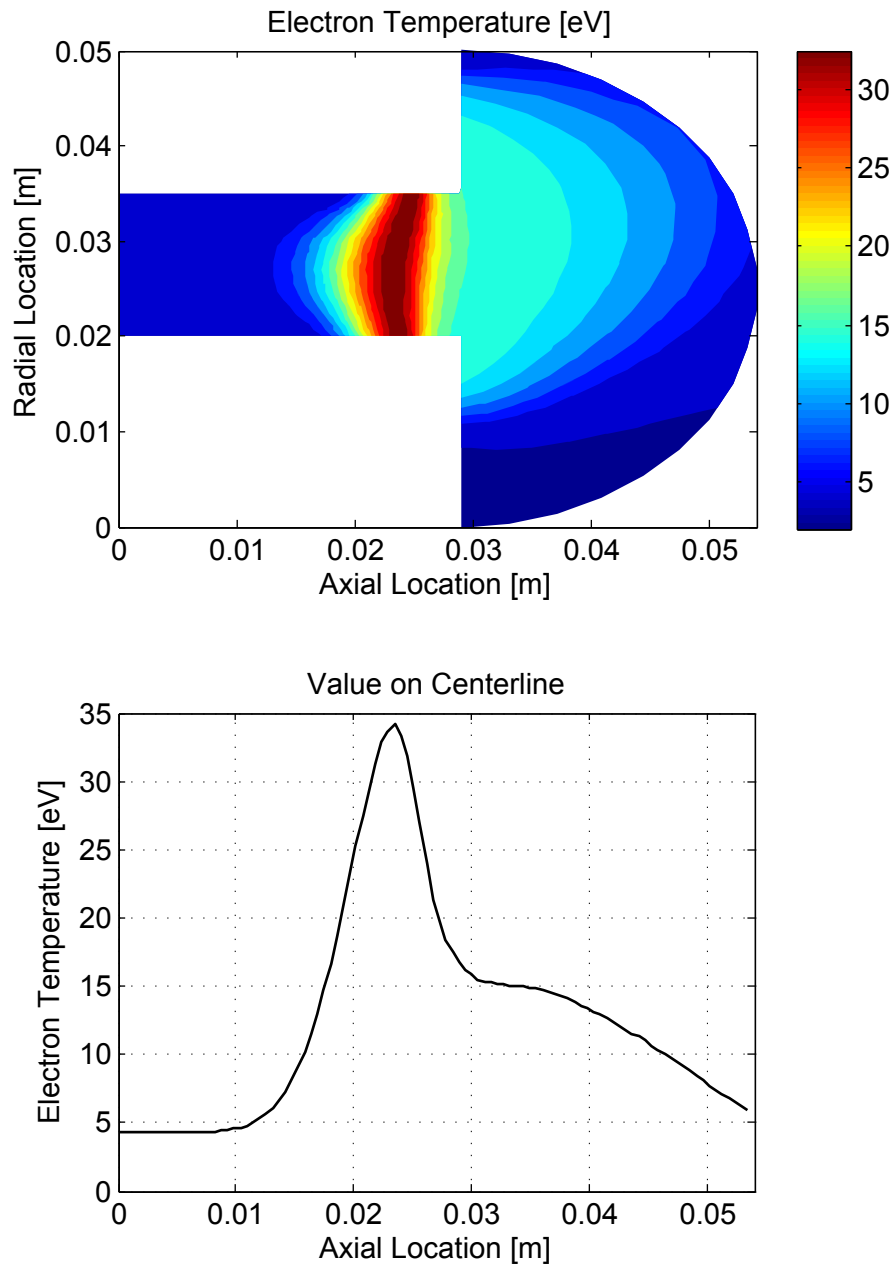


Figure 6.4: Averaged electron temperature distribution for the simulated 650 W upstream run.

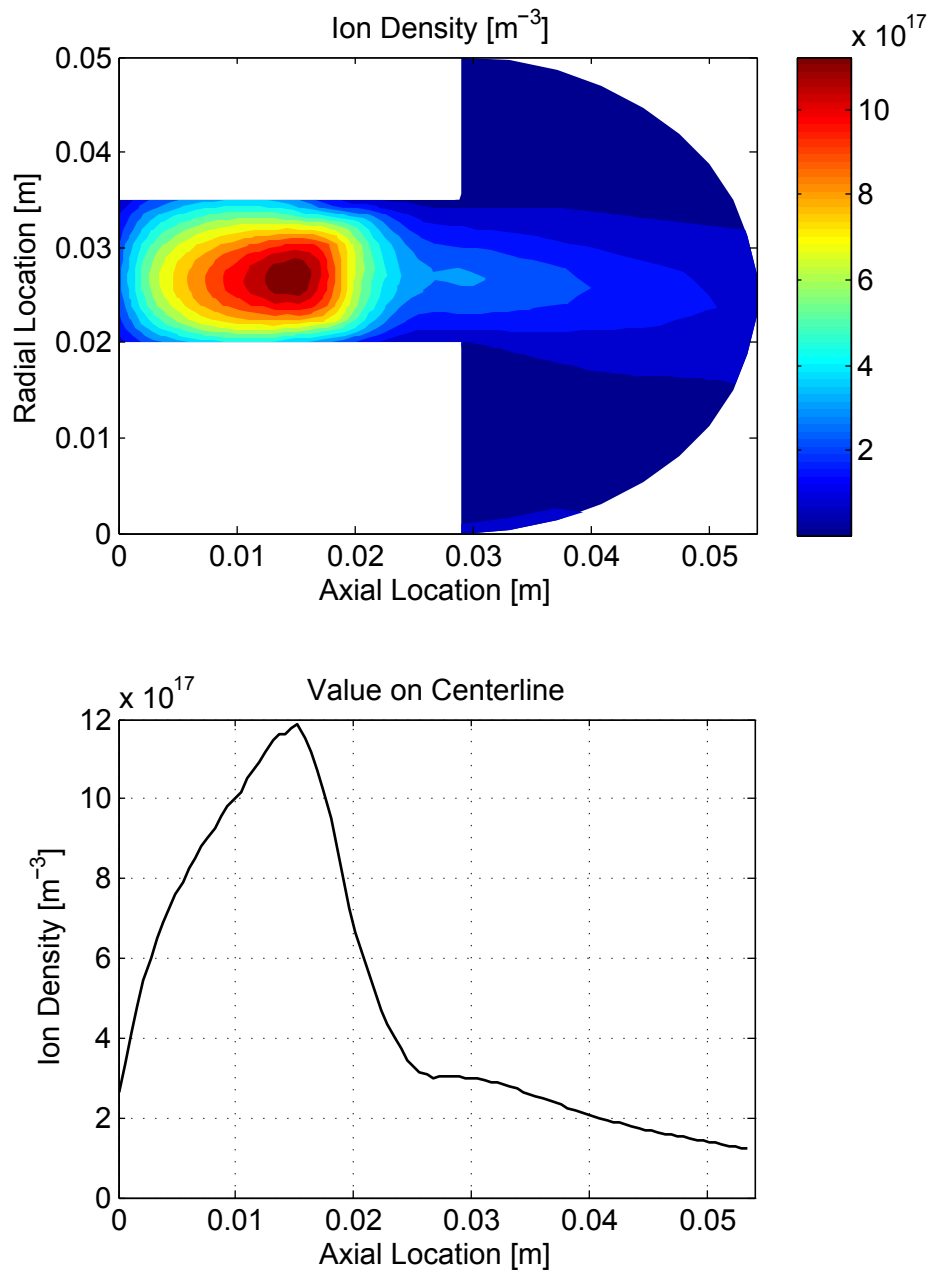


Figure 6.5: Averaged ion density distribution for the simulated 650 W upstream run.

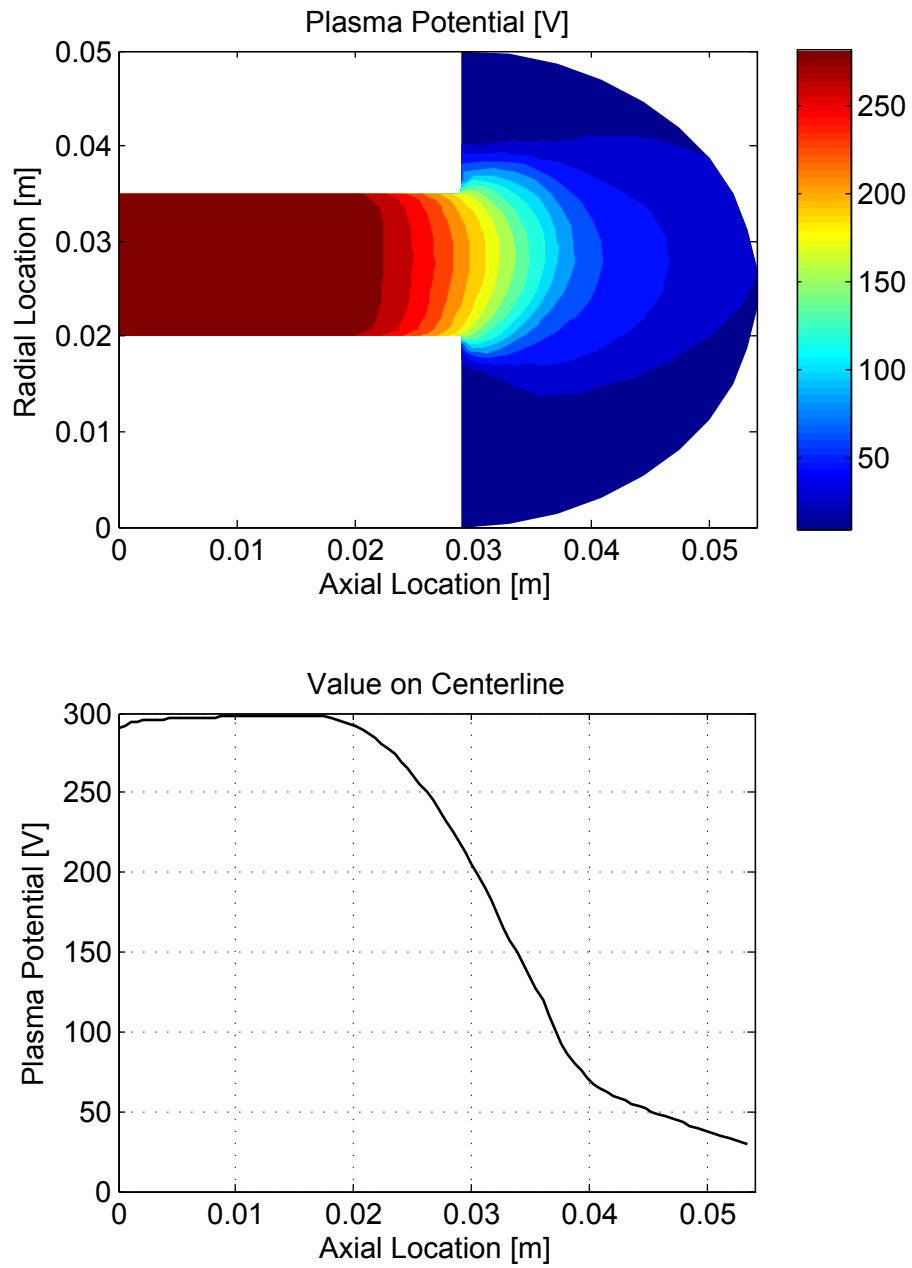


Figure 6.6: Averaged plasma potential distribution for the simulated 650 W downstream run.

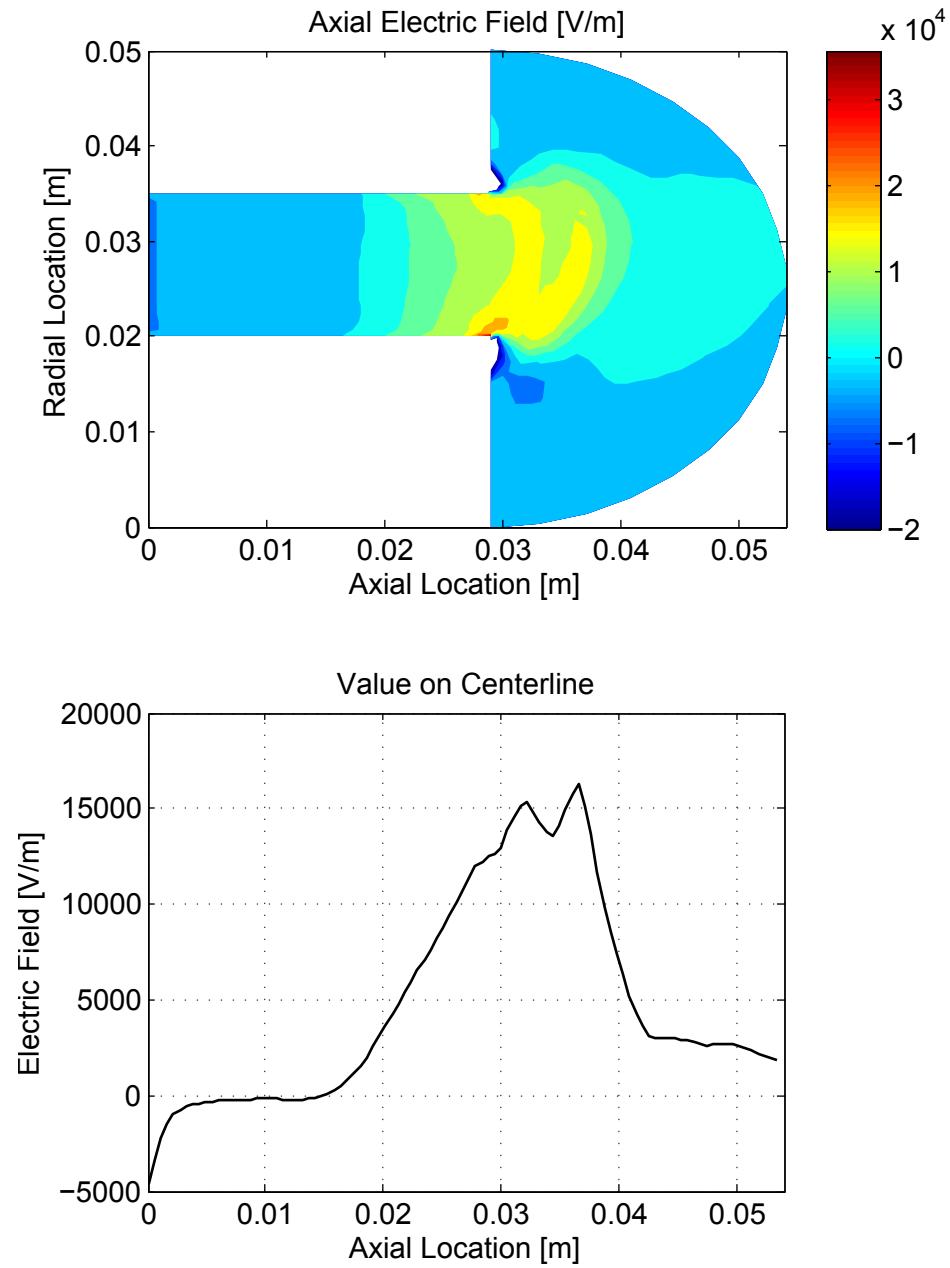


Figure 6.7: Averaged axial electric field distribution for the simulated 650 W downstream run.

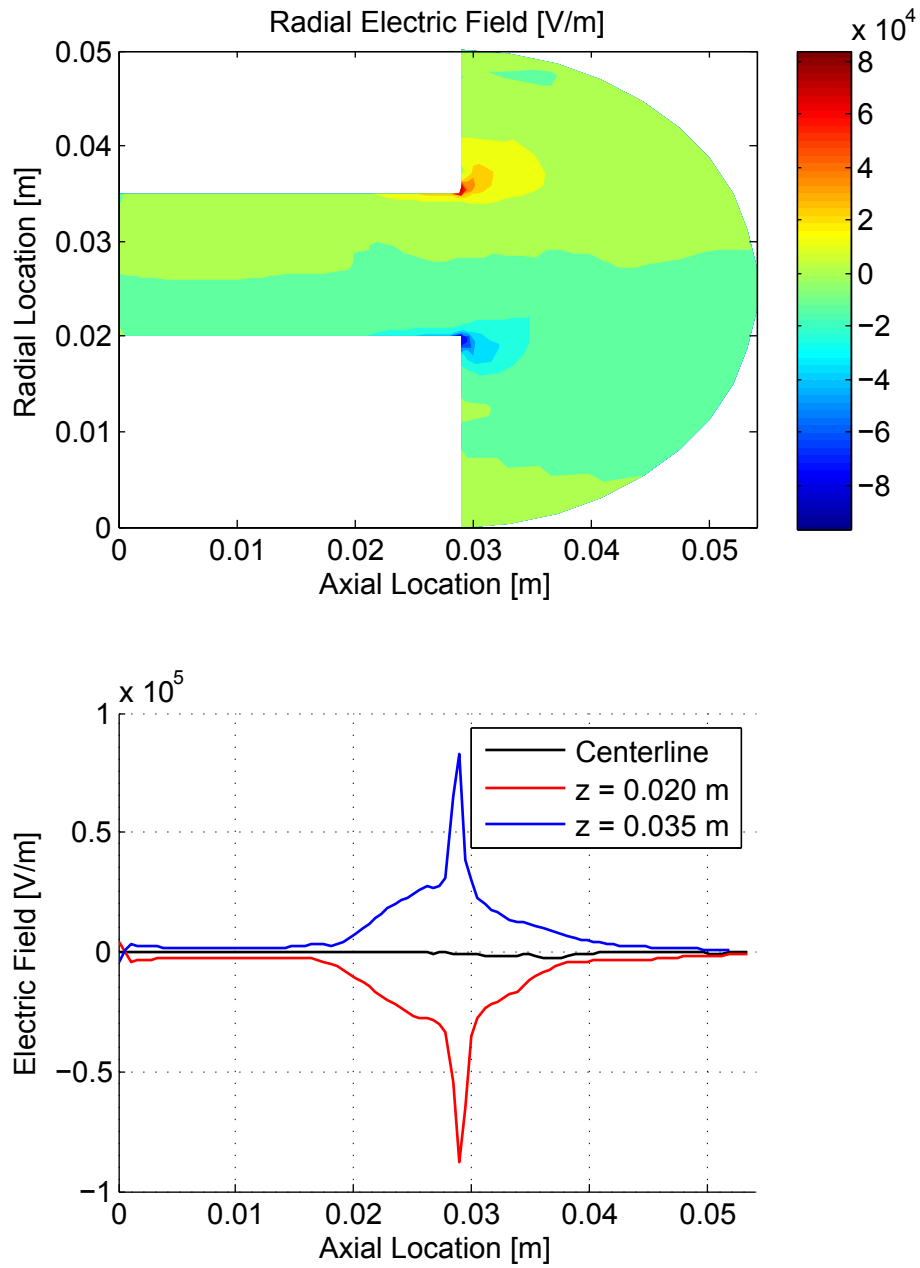


Figure 6.8: Averaged radial electric field distribution for the simulated 650 W downstream run.

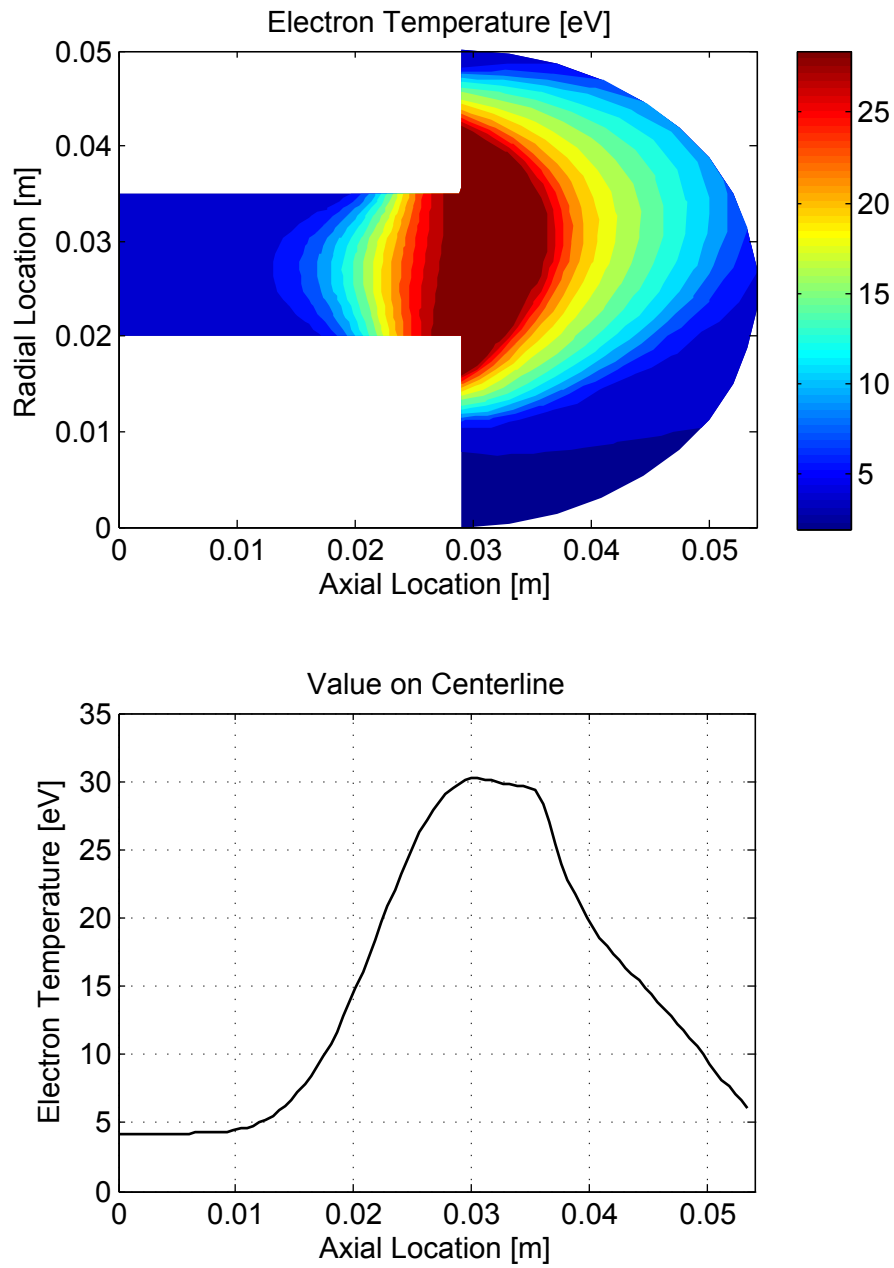


Figure 6.9: Averaged electron temperature distribution for the simulated 650 W downstream run.

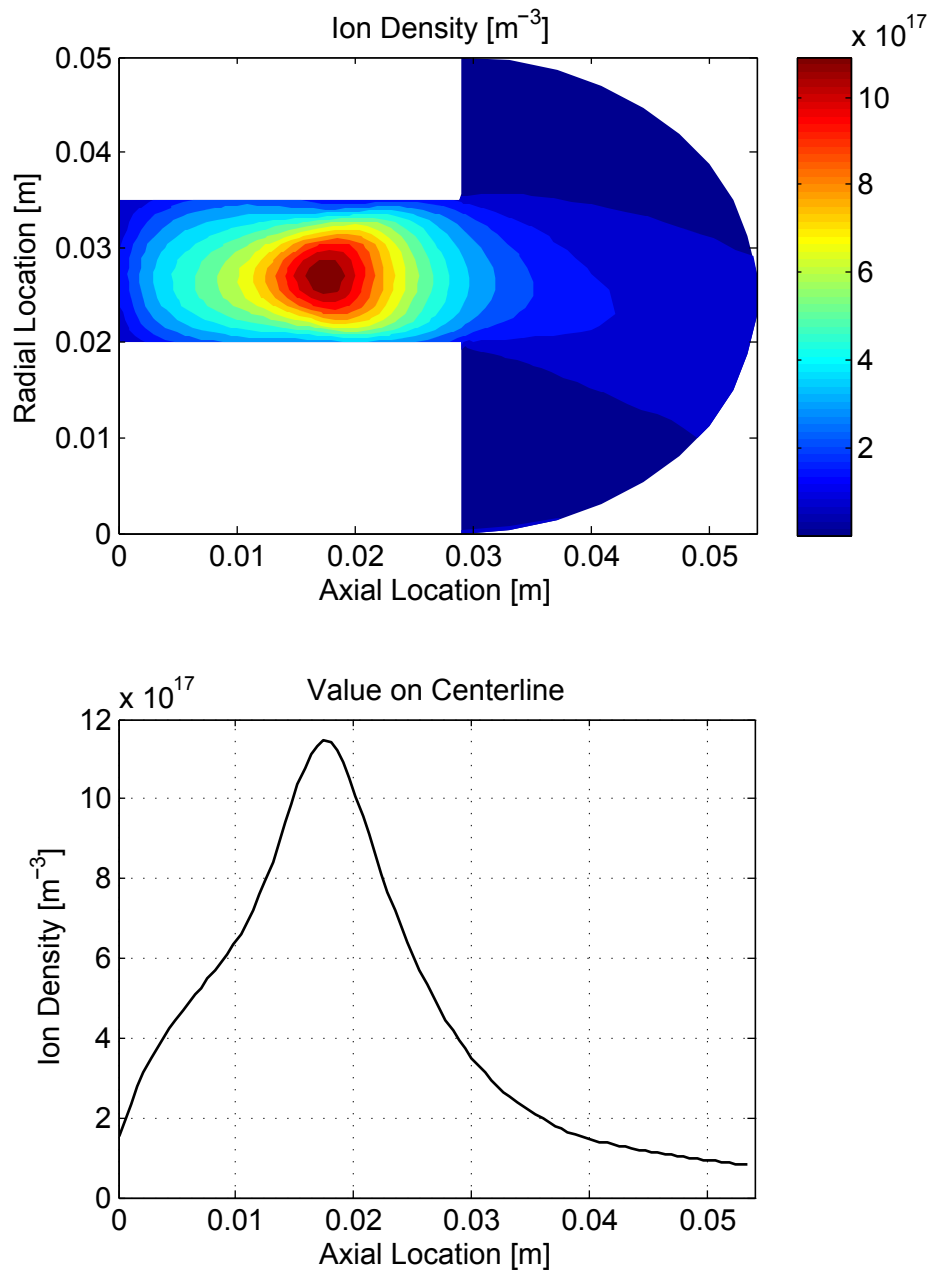


Figure 6.10: Averaged ion density distribution for the simulated 650 W downstream run.

### 6.2.2 200 W Results

Figures 6.11 to 6.15 show the time-averaged quantities for the 200 W upstream run. Figure 6.11 shows that most of the potential drop occurs between  $z = 0.020$  and  $z = 0.040$  m. Figure 6.12 shows that the axial electric field has a peak of about  $1.75 \times 10^4$  V/m between  $z = 0.0225$  and  $0.025$  m, with a tail extending out to  $0.040$  m. This suggests, as in the 650 W upstream, that most of the axial acceleration is occurring upstream of the exit plane.

Looking at Figure 6.13, as in the 650 W upstream run, the region of high radial electric field is confined to within several centimeters of the corner. Away from the corner, its magnitude is less than  $1 \times 10^4$  V/m, compared to the maximum value of the axial electric field of about  $1.75 \times 10^4$  V/m. This electric field configuration suggests that more ions may be accelerated out to mid-range angles ( $40$  to  $60^\circ$ ) than in the 650 W upstream run, but that ions still must pass within several millimeters of the corner to be accelerated out to higher angles.

Figure 6.14 shows that the peak in electron temperature occurs at about  $0.0225$  m, with a maximum value of 23 eV, which is lower than the value in both of the 650 W runs, as is to be expected due to the lower power level. Figure 6.15 shows that the ion density peak is considerably farther back in the channel than in either of the 650 W runs, and is centered approximately at  $z = 0.0100$ . A "tail" on this peak extends out towards the exit plane, so that even at  $z = 0.0290$  m, there is still a significant density of ions, and downstream of the exit plane. The distribution is again asymmetric about the channel centerline outside of the exit plane.

Figure 6.16 to 6.20 show the time-averaged quantities for the 200 W downstream run. As shown in Figure 6.16, most of the potential drop occurs from  $z = 0.0200$  to  $z = 0.050$  mm, resulting in an axial electric field component that is weaker than in the 200 W upstream run (a maximum of  $1 \times 10^4$  versus  $1.75 \times 10^4$  V/m), as shown in Figure 6.17.

Figure 6.18 shows that the radial electric field is comparable in magnitude to that of the 200 W upstream run, with a maximum of roughly  $6 \times 10^4$  V/m near the corners of the channel. As in the upstream run, near the exit plane (away from the corners) the radial electric field is about as strong as the axial electric field, with a magnitude of about  $0.5 \times 10^4$  V/m. Although the radial electric field profile looks similar in both the upstream and downstream 200 W runs, the weaker axial electric field in the downstream run suggests

acceleration of ions out to higher angles off of the thruster centerline.

Figure 6.19 shows a broad peak in electron temperature that extends from  $z = 0.0225$  to  $z = 0.0275$  m, with a maximum value of 17.5 eV, which is considerably lower than in the upstream run. Again, the ion density peak is farther upstream than in either of the 650 W runs, and is centered at about  $z = 0.0125$  m with a magnitude of  $3 \times 10^{17} \text{ m}^{-3}$ , as seen in Figure 6.20. There is also a large tail on the ion density peak that extends beyond the exit plane.

Overall, the plots in this section suggest that for the two downstream runs, the radial component of the electric field is greater in magnitude than in the upstream runs. Also, the ion density near the exit plane is greater in the downstream runs, meaning that more ions are created where the radial electric field is high. This suggests that there should be more high velocity, high angle ions in the downstream runs than in the upstream runs. Additionally, the ion density plot in all runs is asymmetric about the channel centerline ( $r = 0.0275$  m) downstream of the exit plane. This asymmetry in the ion density suggests that more ions are accelerated inwards than outward. The reason for this asymmetry will be discussed in Section 6.2.3. Whether the data from these simulated runs match those seen in the experiment will be discussed in the Chapter 8.

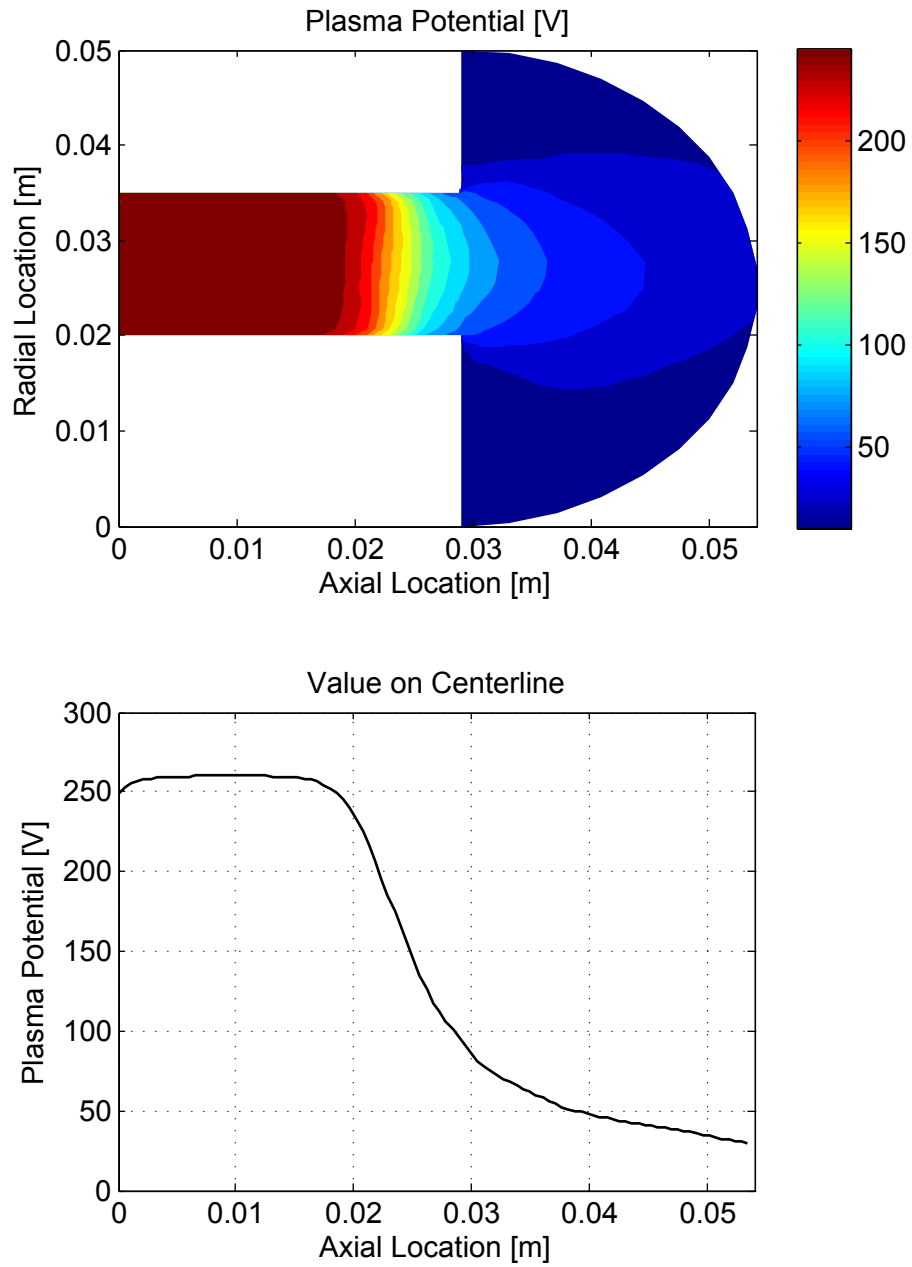


Figure 6.11: Averaged plasma potential distribution for the simulated 200 W upstream run.

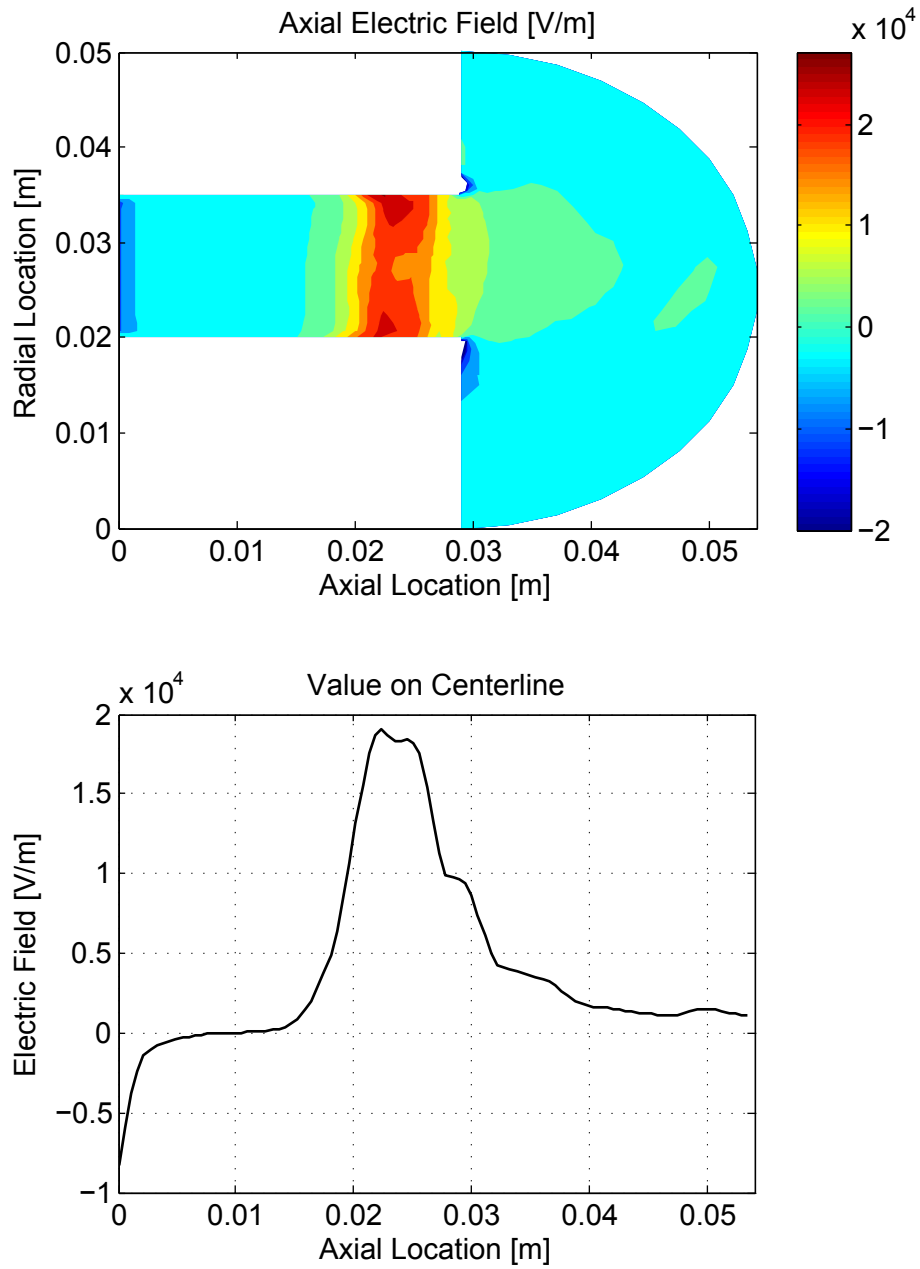


Figure 6.12: Averaged axial electric field distribution for the simulated 200 W upstream run.

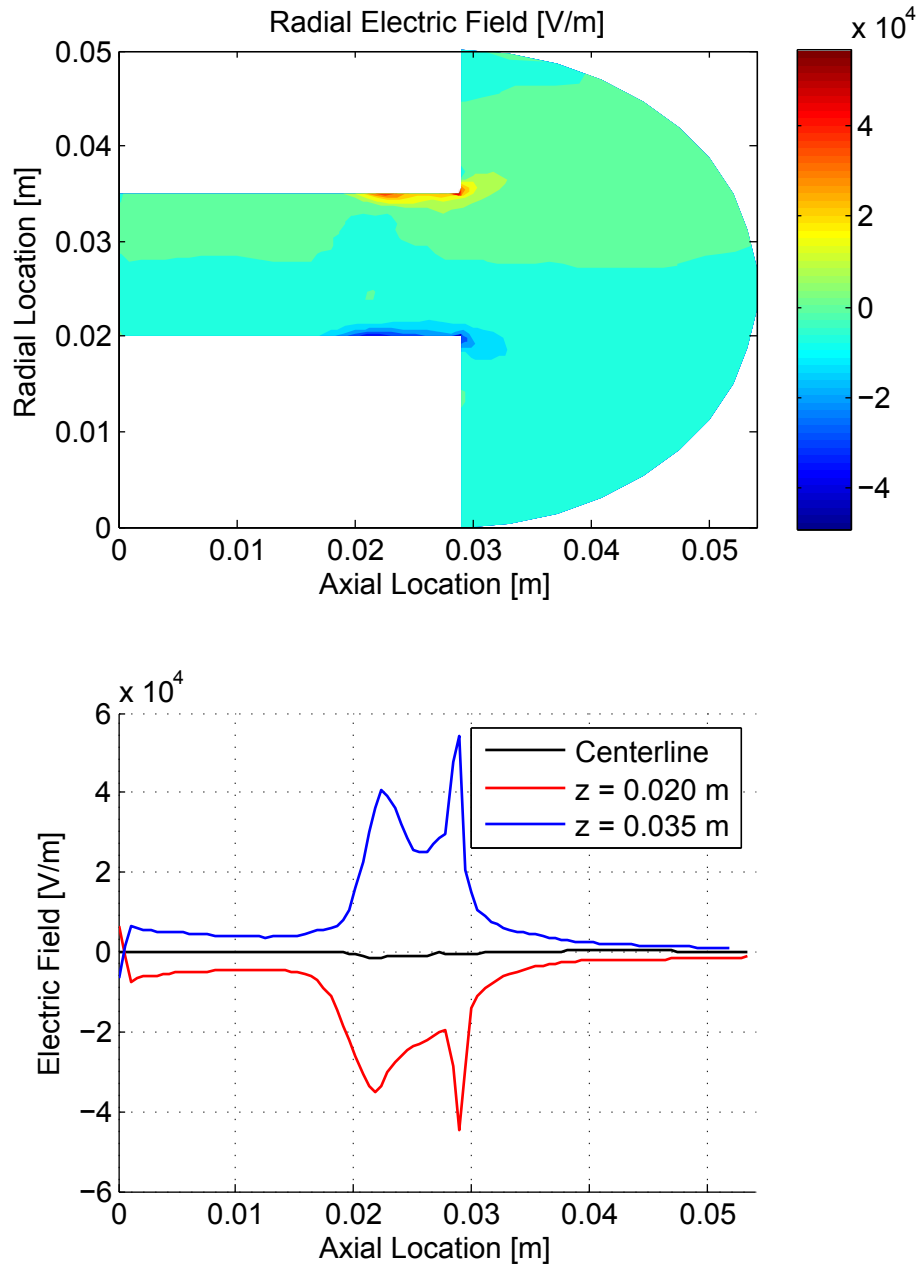


Figure 6.13: Averaged radial electric field distribution for the simulated 200 W upstream run.

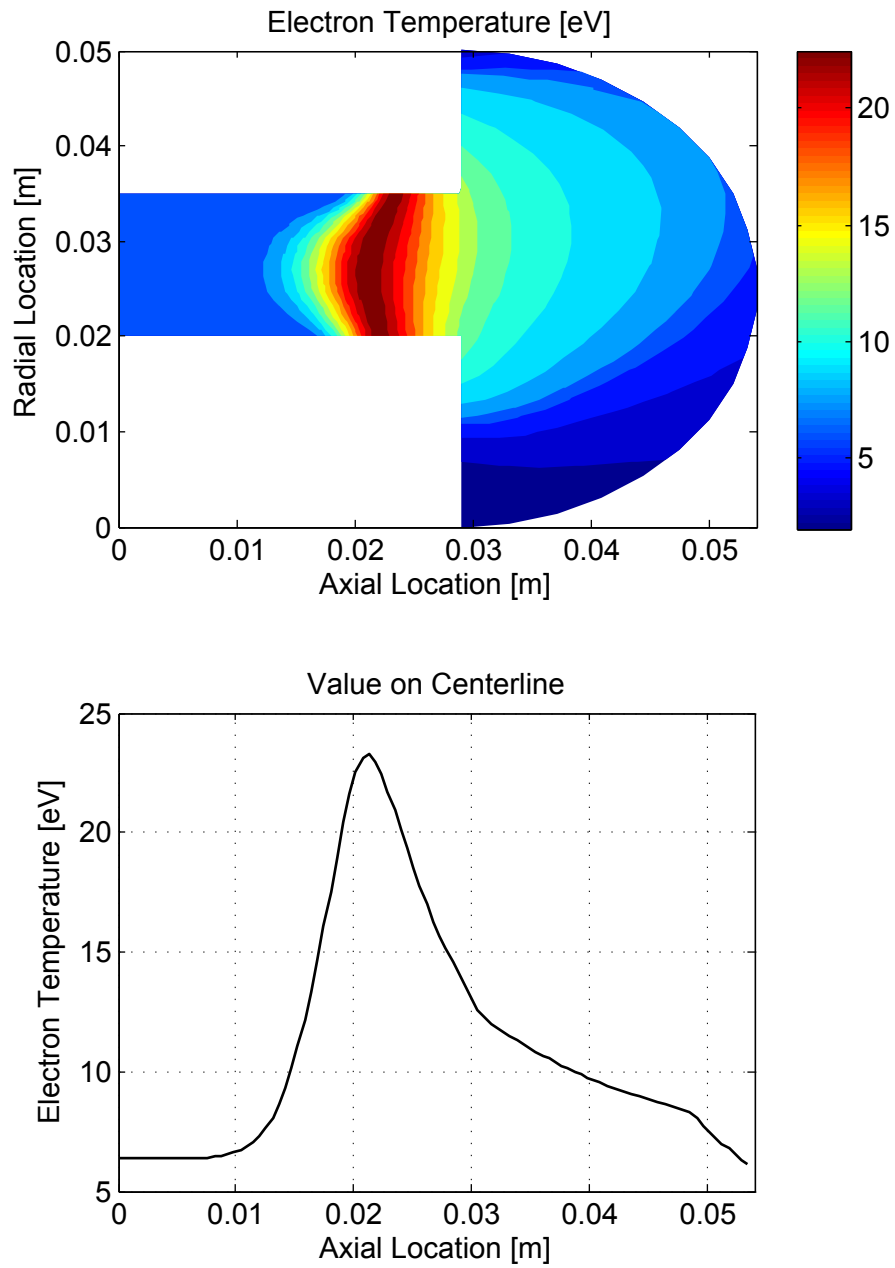


Figure 6.14: Averaged electron temperature distribution for the simulated 200 W upstream run.

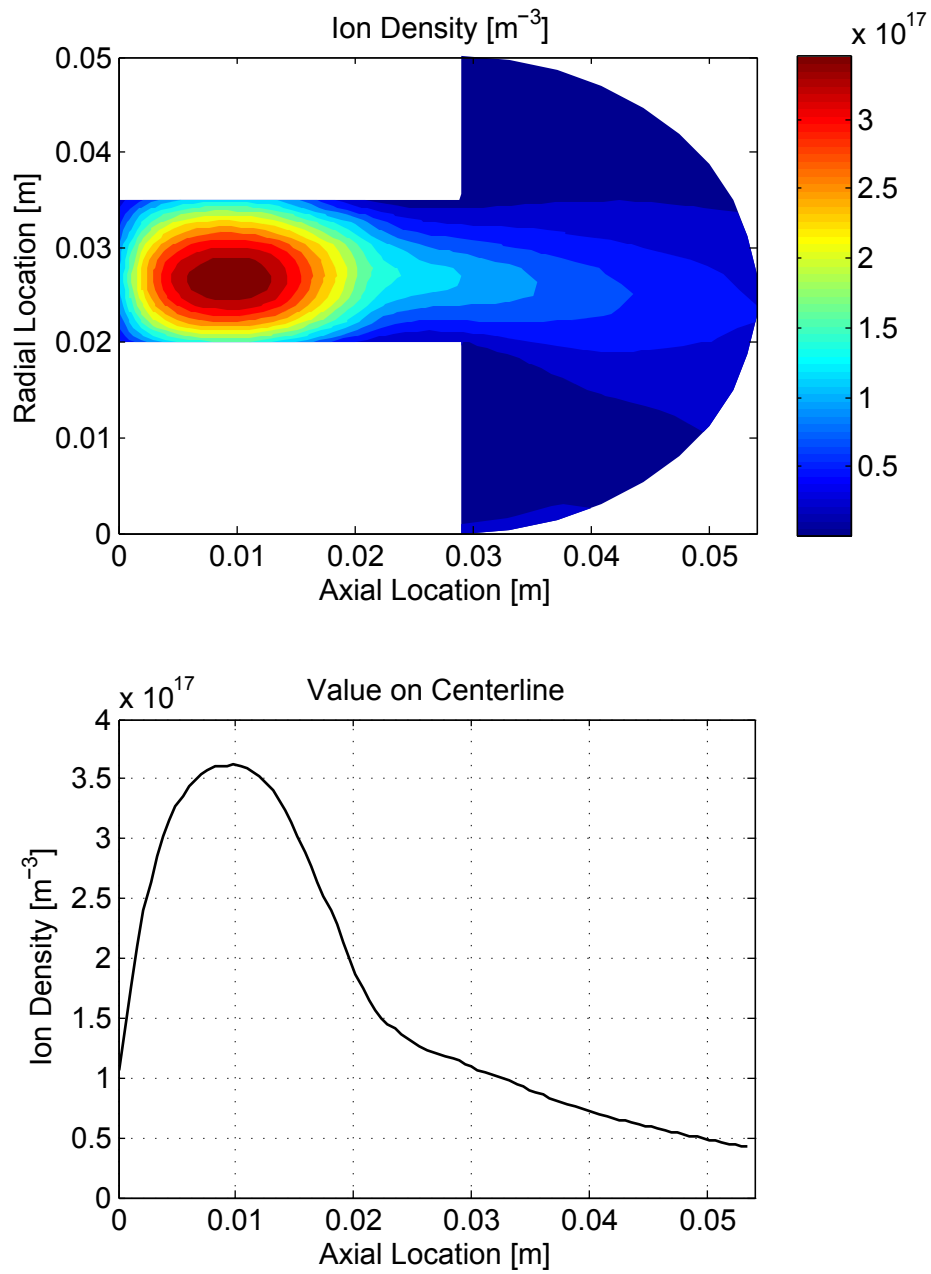


Figure 6.15: Averaged ion density distribution for the simulated 200 W upstream run.

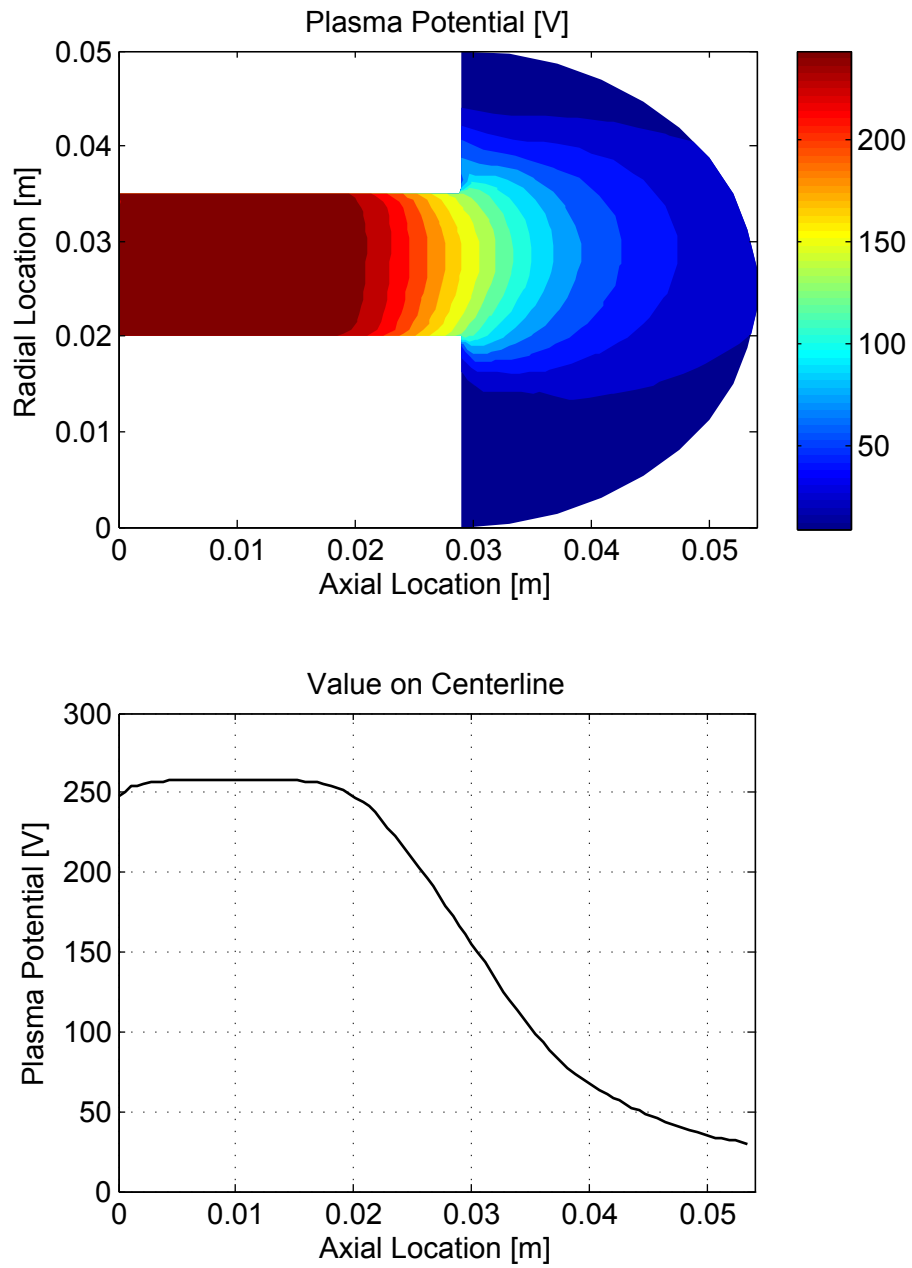


Figure 6.16: Averaged plasma potential distribution for the simulated 200 W downstream run.

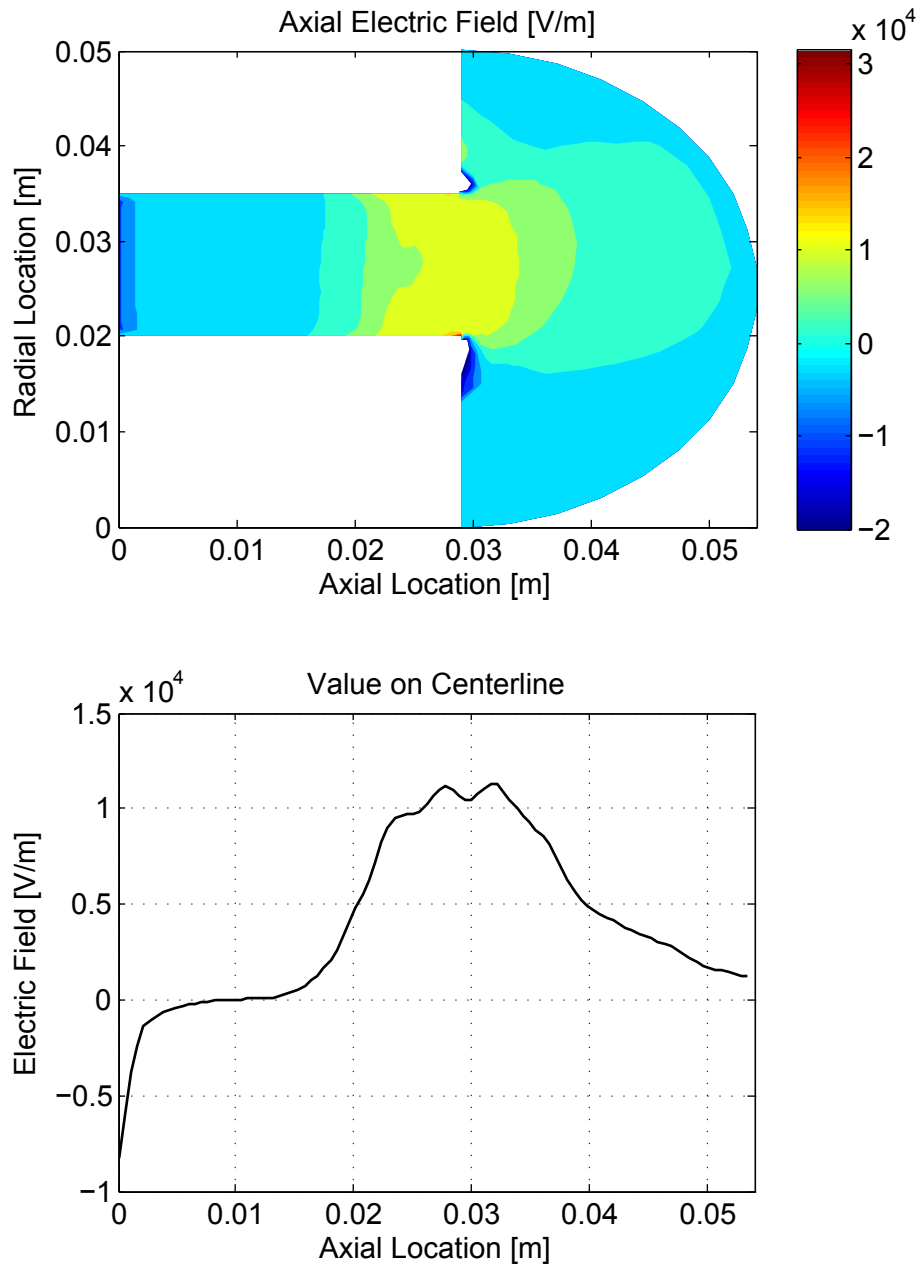


Figure 6.17: Averaged axial electric field distribution for the simulated 200 W downstream run.

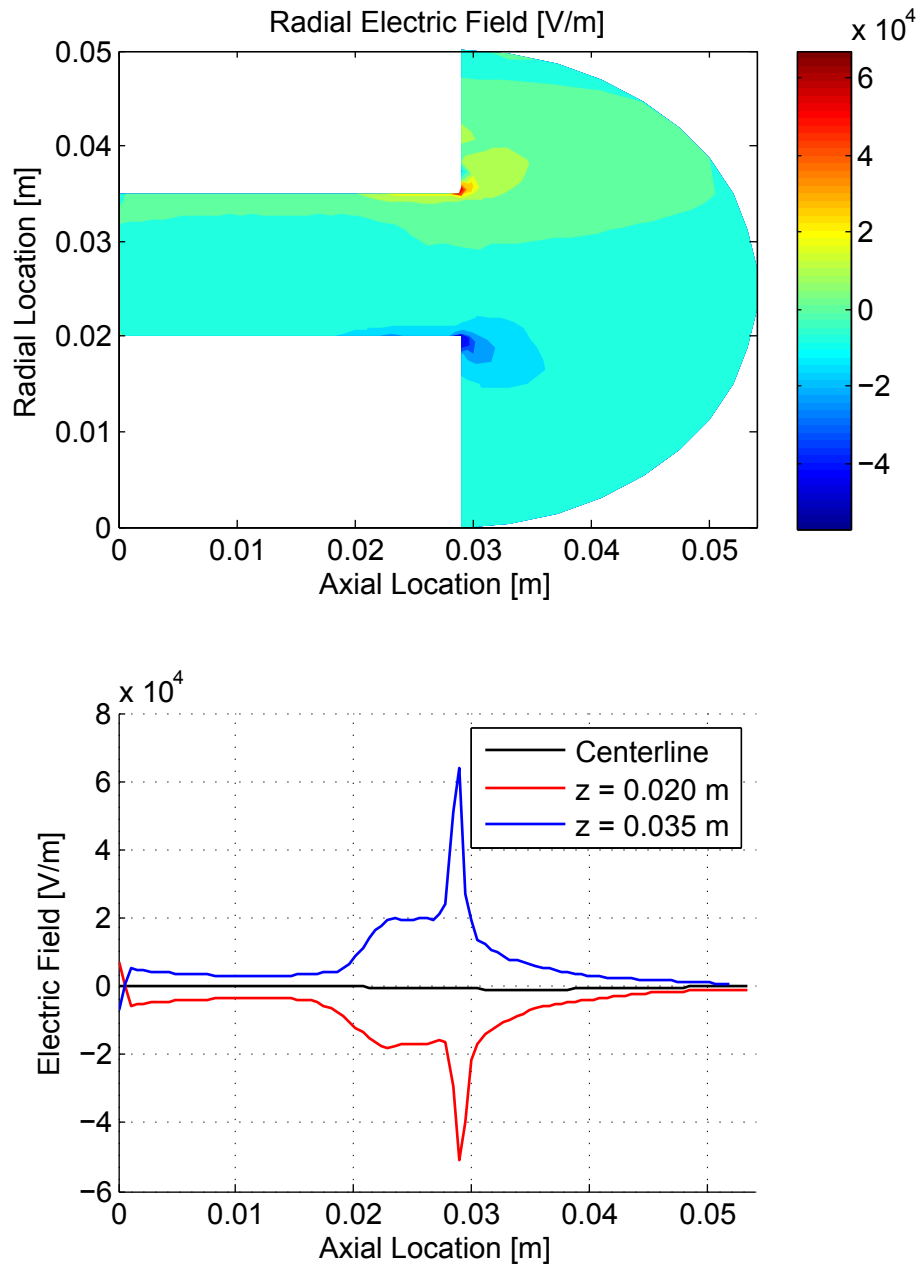


Figure 6.18: Averaged radial electric field distribution for the simulated 200 W downstream run.

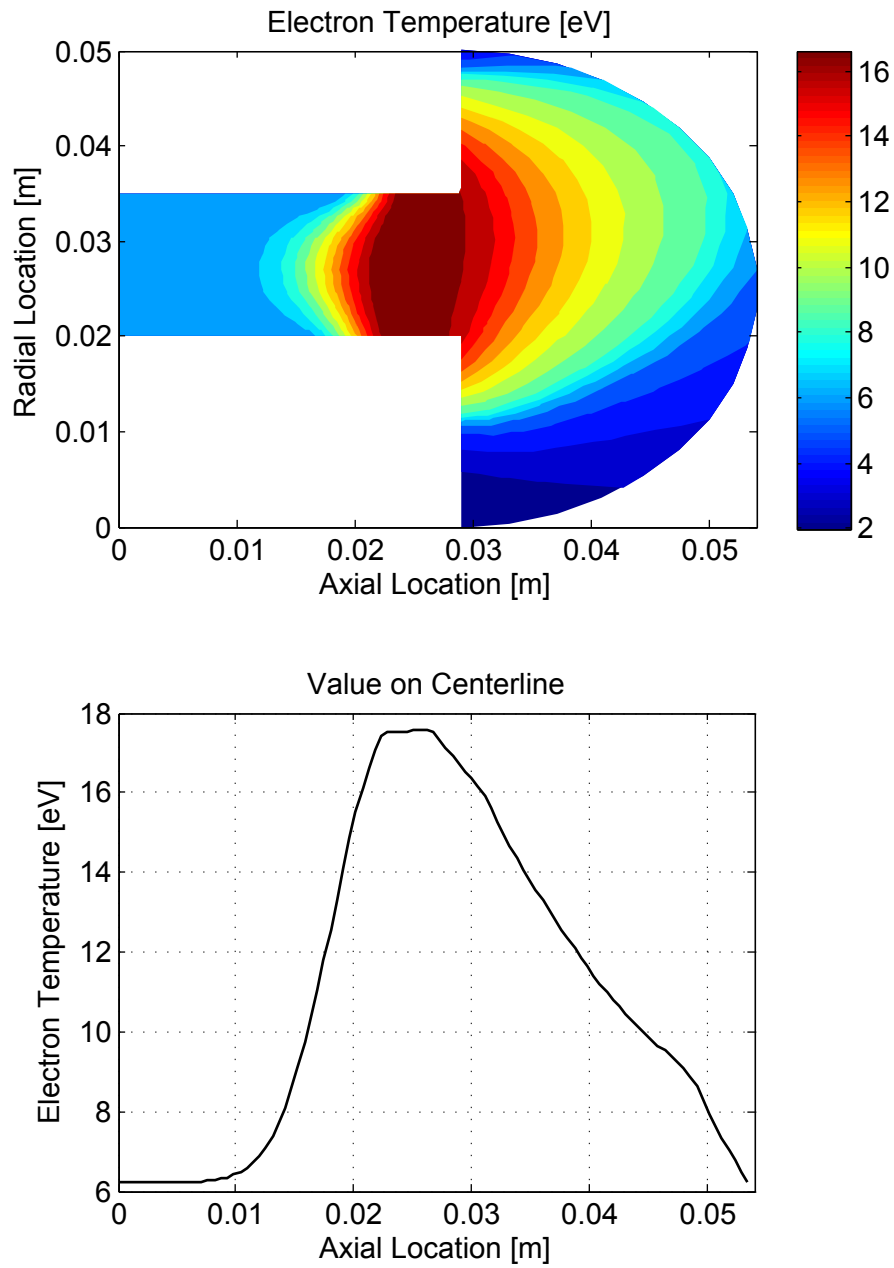


Figure 6.19: Averaged electron temperature distribution for the simulated 200 W downstream run.

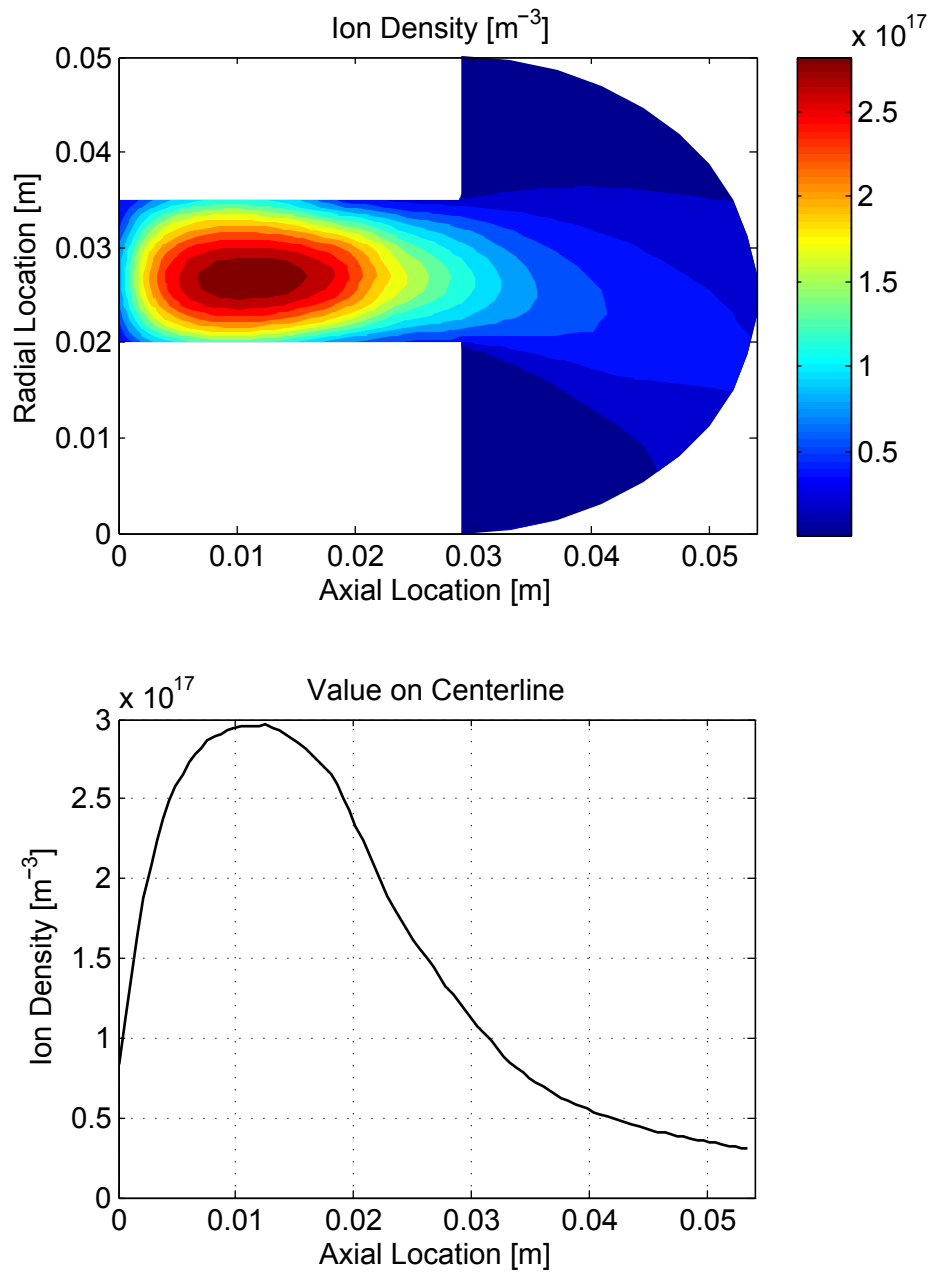


Figure 6.20: Averaged ion density distribution for the simulated 200 W downstream run.

### 6.2.3 Asymmetry of Ion Density Plots

The ion density plots show that for all runs, the ion density is not symmetric about the channel centerline downstream of the exit plane. By plotting the potential as a function of radial location, at different axial locations, one can determine whether there is asymmetry in the potential that causes a greater number of ions to be accelerated inwards. This is what has been done in Figures 6.21 to 6.24 for the 4 different runs.

In the 650 W upstream run, Figure 6.21 shows that there is slight asymmetry in the plasma potential at  $z = 0.020$  m, with the potential increasing slightly as the radial location is increased. At  $z = 0.025$  m, the potential is even more asymmetric, increasing about 20 V from one side of the channel to the other. At the exit plane, the potential is fairly symmetric, and as the axial location is increased, it remains symmetric. Figure 6.21 thus suggests that in this run, the asymmetry in the ion density arises from ions that are being accelerated upstream of the exit plane, between  $z = 0.020$  and  $z = 0.029$  m.

In the 650 W downstream run (Figure 6.22), the potential appears to be fairly symmetric upstream of the exit plane, but as the axial position is increased, the potential becomes less symmetric. At  $z = 0.035$  m, for instance, the peak in the potential is shifted by about a millimeter, and if one compares the potential at  $r = 0.020$  to  $r = 0.035$  m, one sees a difference of about 25 V (75V versus 100V). This is similar to the degree of asymmetry seen in the 650 W upstream data. Therefore, in the 650 W downstream run, the asymmetry in the ion density appears to arise downstream of the exit plane, between  $z = 0.030$  and  $0.040$  m.

The 200 W runs show similar trends as the 650 W runs, i.e., in the 200 W upstream run the asymmetry in the potential occurs between  $z = 0.020$  and  $0.029$  m, while in the downstream run it occurs between  $z = 0.030$  and  $0.040$  m. In all runs, the asymmetric potential ( $r = 0.0275$  m) leads to ions being accelerated towards the thruster centerline. In Section 6.2.3, this inward radial motion was proposed as a mechanism for the formation of the central jet. This mechanism for central jet formation will be further discussed in Chapter 8.

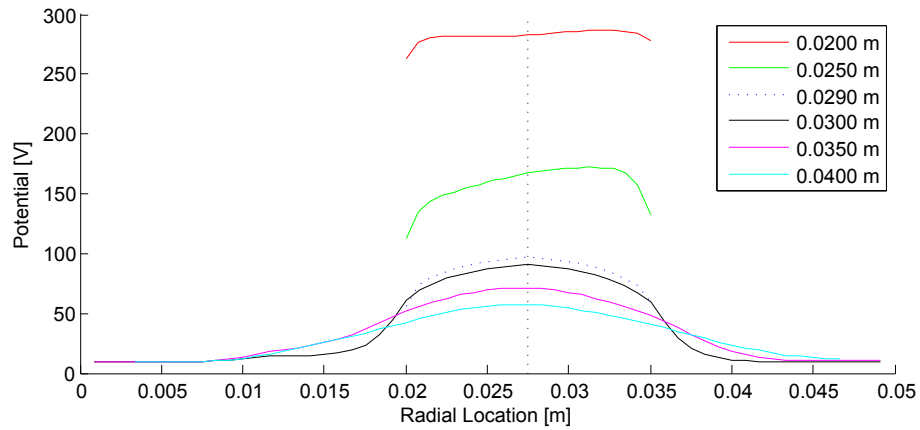


Figure 6.21: Plasma potential from HPHall at different axial locations for the 650 W up-stream run.

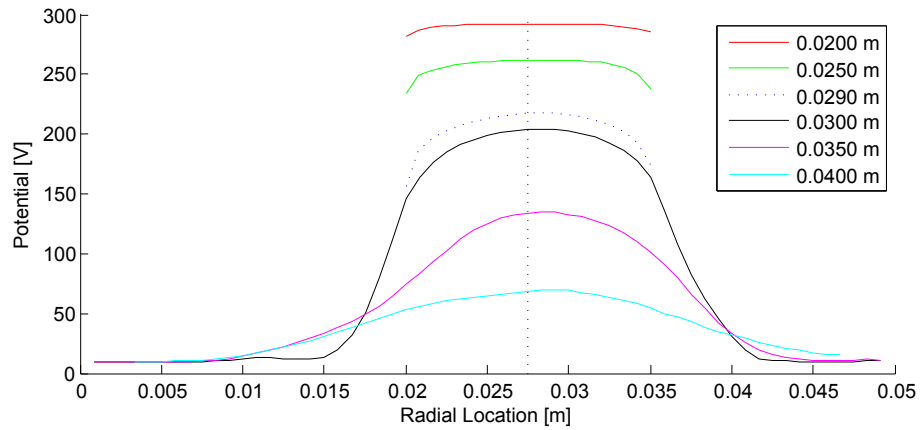


Figure 6.22: Plasma potential from HPHall at different axial locations for the 650 W down-stream run.

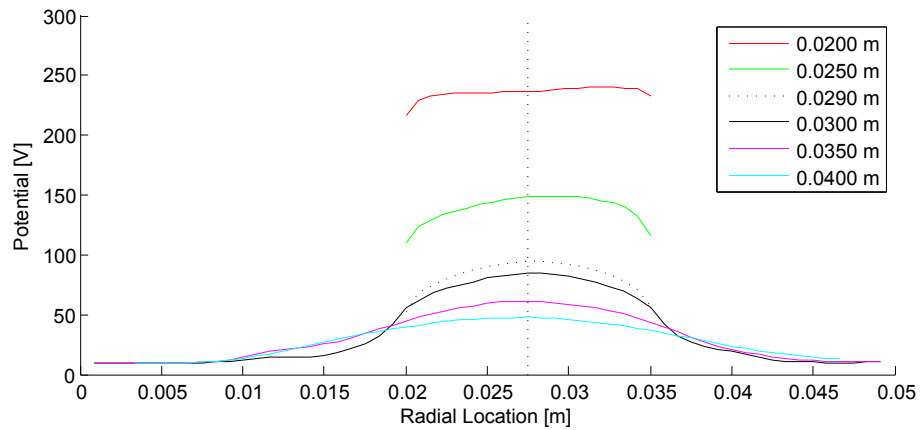


Figure 6.23: Plasma potential from HPHall at different axial locations for the 200 W up-stream run.

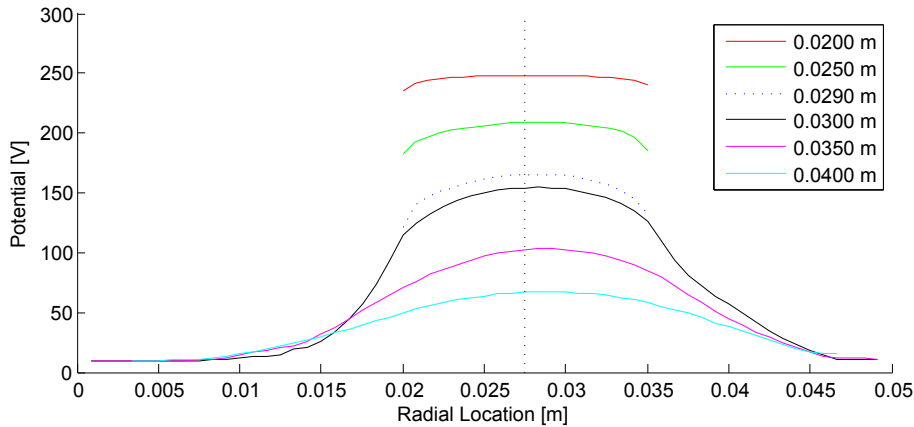


Figure 6.24: Plasma potential from HPHall at different axial locations for the 200 W downstream run.

#### 6.2.4 Comparison of averaged data to existing studies

In terms of comparisons to previous research, it makes sense to look at two different studies: (1) Fife's initial HPHall model, which does not include the more recent updates to the code but is a reference for running a SPT-70 model in HPHall [14], and (2) the JPL model of a 6 kW laboratory Hall thruster, which uses the same version of the code used in this study on a different thruster [35]. Fife's thesis includes data for two runs, one in which the cathode was set at 0.03 m downstream of the exit plane, and one in which the cathode was 0.005 m downstream of the exit plane. The JPL study attempted to match the code to experimental data for a 6kW Hall thruster, and found that the best agreement occurred using a 3 region mobility model with anisotropic electrons. Fife's results and the JPL results are summarized in Table 6.2, while the results from Section 6.2 are presented in Table 6.3. Note that the axial ( $z$ ) locations have been normalized by the thruster channel length in order to compare the 6kW and SPT-70 data sets. Also, all of the  $\phi$ ,  $T_e$ , and  $n_e$  refer to values on the channel centerline. Additionally, note that  $\phi_1$  and  $\phi_2$  were arbitrarily selected values of  $\phi$  that are shown so that the length of the acceleration region could be gauged, i.e., the quantity  $z_2 - z_1$  is a quantity that can be used to judge the length of this region.

The most notable discrepancy between the results in Table 6.2 and Table 6.3 is the maximum electron temperature. In Fife's case, it was from between about 20 and 23 eV, in the JPL "best-match" case it was 25 eV, and in the current study it ranged from 30 to 35 eV for the 650 W run, and 17.5 to 23 eV for the 200 W run. However, it was

Table 6.2: Averaged data from previous HPHall studies.

Parameter	Fife CASE 1	Fife CASE 2	JPL "Best Match"
$\dot{m}$ [mg/s]	2.34	2.34	20.98
$V_D$ [V]	300	300	300
$I_A$ [A]	1.98	2.47	20
$\phi_1$ [V] at $z_1/L$	280 at 0.7	280 at 0.7	280 at 0.7
$\phi_2$ [V] at $z_2/L$	100 at 1.4	100 at 1.1	100 at 1.0
$T_{e,max}$ [eV] at $z_{T_{e,max}}/L$	23 at 1.30	20 at 1.00	25 at 0.95
$n_{e,max}$ [ $m^{-3}$ ] at $z_{n_{e,max}}/L$	7e17 at 0.6	9e17 at 0.5	N/A

Table 6.3: Averaged data from current HPHall study.

Parameter	650 W upstream	650 W downstream	200 W upstream	200 W downstream
$\dot{m}$ [mg/s]	1.7	1.7	0.8	0.8
$V_D$ [V]	300	300	250	250
$I_A$ [A]	2.2	2.2	0.8	0.8
$\phi_1$ [V] at $z_1/L$	280 at 0.7	280 at 0.7	250 at 0.7	250 at 0.7
$\phi_2$ [V] at $z_2/L$	100 at 1.0	100 at 1.3	100 at 1.0	100 at 1.2
$T_{e,max}$ [eV] at $z_{T_{e,max}}/L$	35 at 0.85	30 at 1.1	23 at 0.80	17.5 at 0.85
$n_{e,max}$ [ $m^{-3}$ ] at $z_{n_{e,max}}/L$	12e17 at 0.5	11.5e17 at 0.6	3.6e17 at 0.3	3.0e17 at 0.4

found in the JPL study that the code underpredicted the experimentally measured electron temperature by about 10 eV, while in Fife's study one of the cases overpredicted SPT-70 measured values by about 10 eV. This suggests that it is difficult to assess the accuracy of the electron temperature predicted by HPHall. Therefore, a discrepancy of about 10eV between the current study and the previous studies is not necessarily cause for alarm.

## 6.3 Faraday Probe and ExB Plots from HPHall

As described in Section 3.3.3, Faraday probe and ExB traces were built up from the HPHall data by projecting the paths of the simulated ions out to planes parallel to the thruster exit plane, at different axial distances. There are two important aspects of these simulated traces worth noting. First, to obtain an estimate of ion current density, the ion current into a certain radial “bin” with bounds  $r_1$  and  $r_2$  had to be divided by the area of that bin, i.e.,  $\pi (r_2^2 - r_1^2)$ . This means that the simulated ion current density near the centerline of the thruster is very large simply due to the fact that the area corresponding to those bins is very small. Second, because the simulated Faraday probe and ExB traces represent projections of the particle data from the edge of the HPHall domain, features that cause the spreading of the beam (e.g., collisions) are not present.

### 6.3.1 Faraday Probe Results

Figure 6.25 to 6.26 show the simulated Faraday probe traces at three axial locations (50, 100, 150 mm) for the four different runs. In all four runs, at all three distances, the contributions of the two sides of the channel have merged, and there is simply a single peak in the center. The width of this peak is about the same for all runs/distances, and is zero at transverse locations beyond +/- 50 mm. The height of this peak changes depending on the condition and axial distance, as does the shape of the “shoulders” extending out to the sides.

Figure 6.25 shows that for the 650 W upstream run, the peak has a magnitude of roughly 2000 A/m<sup>2</sup> at 50 mm, increasing to about 3000 A/m<sup>2</sup> at 100 mm, and staying relatively constant from 100 to 150 mm. In the 650 W downstream run, rather than increasing with axial distance, the peak height decreases from about 3000 A/m<sup>2</sup> at 50 mm, to 2500 A/m<sup>2</sup> at 100 mm, to a little under 2000 A/m<sup>2</sup> at 150 mm. So the maximum ion current density of about 3000 A/m<sup>2</sup> occurs at a shorter axial distance in the downstream

run.

The 200 W runs also show a similar trend (Figure 6.26). In the 200 W upstream run, the height of the peak increases from about 700 A/m<sup>2</sup> at 50 mm, to 950 A/m<sup>2</sup> at 100 mm, and then decreases slightly to 850 A/m<sup>2</sup> at 150 mm. In the 200 W downstream run, the peak height decreases from about 1000 A/m<sup>2</sup> at 50 mm to 800 A/m<sup>2</sup> at 100 mm, and then to 600 A/m<sup>2</sup> at 150 mm. As in the 650 W runs, the maximum ion current density occurs at a shorter axial distance in the downstream run.

Just by examining the data in Figures 6.25 to 6.26, it isn't possible to see the transition from ring to jet, since all of the plots simply show a sharp peak at the center of the distribution. However, if the Faraday probe data at 25 mm is also plotted, one can see this transition in some of the runs. Figure 6.27 shows a comparison between the Faraday probe traces at 25 mm for the four different runs. The top plot shows the 650 W runs, while the bottom plots show the 200 W runs. It is clear from these plots that for both upstream runs, the central peak is much shorter, and there are short secondary peaks corresponding to the two sides of the channel. This suggests that the transition from ring to jet is definitely occurring at a farther axial distance in the downstream runs than in the upstream runs.

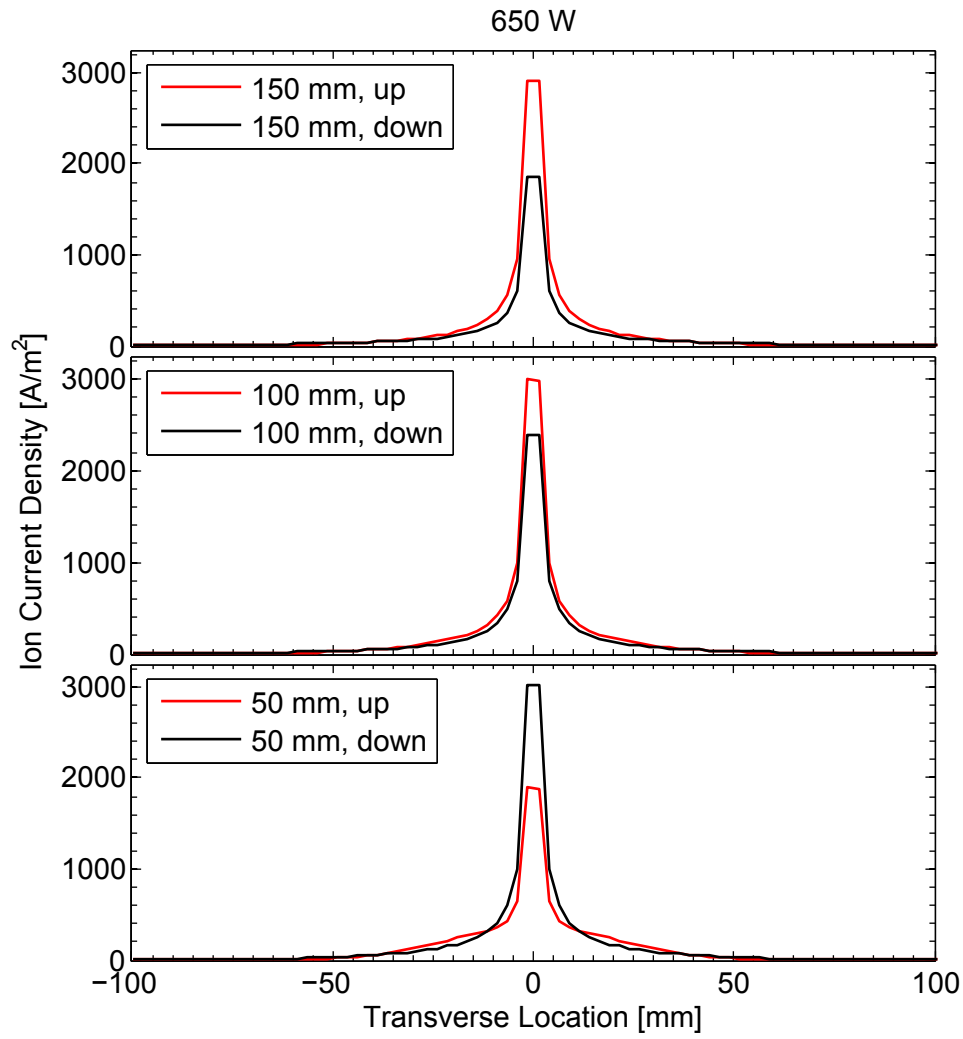


Figure 6.25: Faraday probe traces created from HPHall data, 650 W upstream and downstream runs.

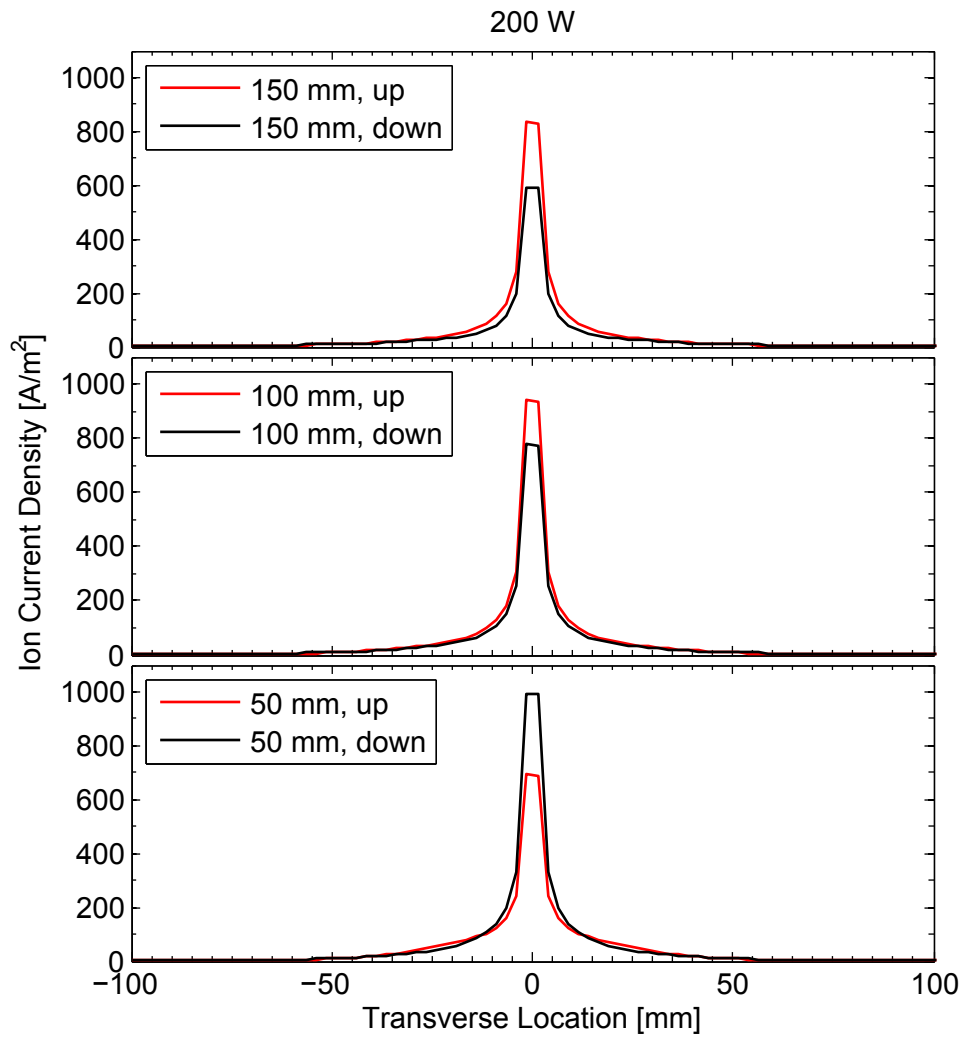


Figure 6.26: Faraday probe traces created from HPHall data, 200 W upstream and downstream runs.

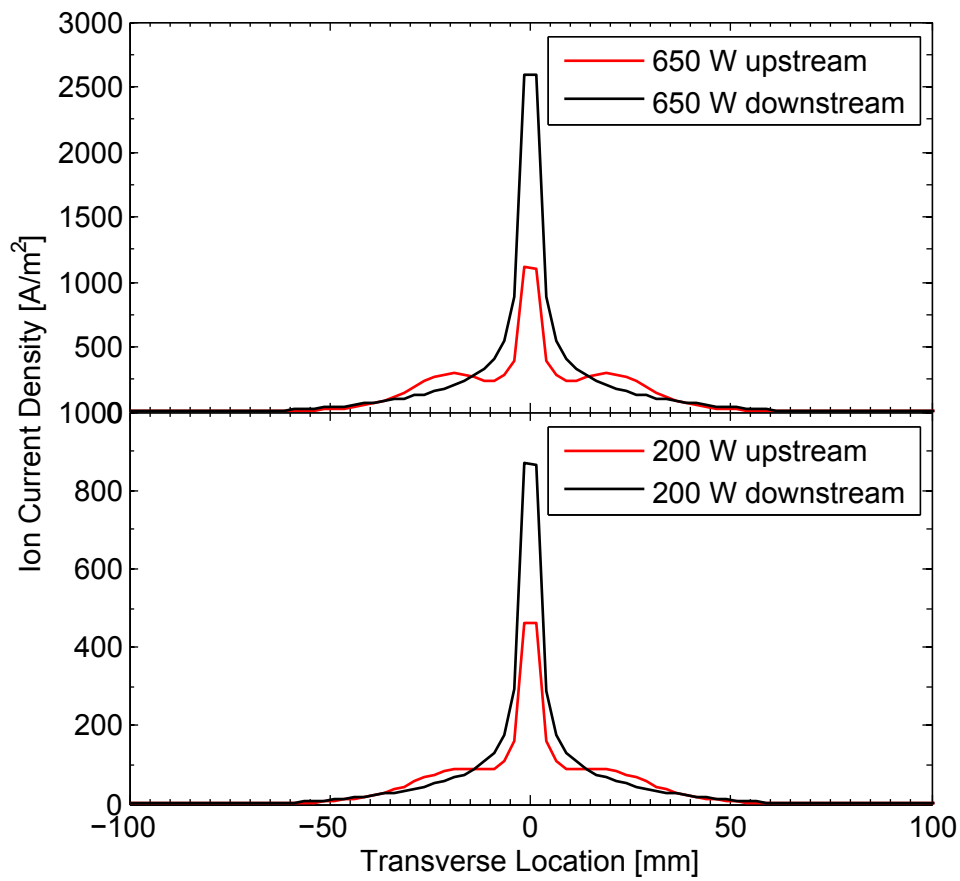


Figure 6.27: Faraday probe traces created from HPHall data, all runs at an axial distance of 25 mm.

### 6.3.2 ExB Probe Results

Figures 6.28 to 6.31 show the simulated ExB data for the 650 W runs, at the three axial distances of 50, 100, and 150 mm. Each of the plots represents ions at a different angle, and the plots have been constructed so that they can be directly compared to the experimental scans (see Chapter 5). Figure 6.28 shows that at 50 mm, in the upstream run the current density is largest at 10 to 20° (the maxima of these two traces are both about 25 A/m<sup>2</sup>). In the downstream run, the largest ion current density is due to ions traveling at 20° relative to the centerline, and the total ion current density at 20° is much larger in the downstream case than in the upstream run.

At angles of 20° and above, the current density in the downstream run is much larger than in the upstream run, whereas at 0° the current density in the upstream run is significantly greater. At 10° the two runs show approximately equal values. This shows that the ion beam is significantly less collimated in the downstream case than in the upstream case. It is also worth noting that, for both the upstream and downstream runs, as the angle is increased above zero degrees, the peak corresponding to inward moving ions (the right peak) is considerably larger than that corresponding to the outward moving ions (the left peak). This is seen at angles from 10 to 20° in the upstream run and 10 to 60° in the downstream run.

As discussed earlier, one of the reasons for the large peaks in the ion current density near the thruster centerline is because the simulated ion current must be divided by the area, which is smaller near the centerline. Looking at the ion current data itself in Figure D.1, one can see that for angles from 10 to 20° the contribution due to inward moving ions is larger in both runs. At 30° the contribution from outward moving ions is larger in the upstream run, although inward ions still dominate the 30° traces in the downstream run. This shows that, from 10 to 20° in the upstream run, and 10 to 30° in the downstream run, inward moving ions account for a significantly larger amount of the ion current.

Since the ion current is largest from 0 to 30° in both runs, and falls off significantly as the angle is increased beyond 30°, this shows clearly that inward moving ions are responsible for a much greater proportion of the *total* ion current in both the 650 W upstream and downstream runs. Similar trends are seen at the other distances (100 and 150 mm), and in the 200 W runs. This is strong evidence that within the ion beam, there is a greater

number of inward moving versus outward moving ions, and that the greater ion current *density* seen in both the experimental and simulated data is not merely due to geometry (i.e., ions moving into a smaller area).

Rather than present both the ion current density data *and* the ion current data for all of the runs in this chapter (which would result in a very large number of graphs), the ion current data for the rest of the runs has been put in Appendix D for reference. Ion current density data is used as the standard in this chapter because it can be directly compared to the experimental data in Chapter 5, while the ion current data cannot.

At 100 mm (Figure 6.30), the largest current density contribution is made by ions traveling at  $10^\circ$  in both the 650 W upstream and downstream run. At this distance, for both runs, the inward moving ions make a larger contribution to the current density at  $10$  to  $30^\circ$ . As the angle is further increased, the inward and outward moving ion contributions are about the same in the upstream run, while the inward moving ion peak is larger at  $40$  and  $50^\circ$  in the downstream run.

At 150 mm (Figure 6.31), the largest current density contribution is made by ions traveling at  $10^\circ$  in both 650 W runs. At this distance, for both runs, the inward moving ions make a larger contribution to the current density at  $10$  to  $30^\circ$ . As the angle is further increased, the inward and outward moving ion contributions are about the same in the upstream run, while the inward moving ion peak is larger at  $40^\circ$  in the downstream run.

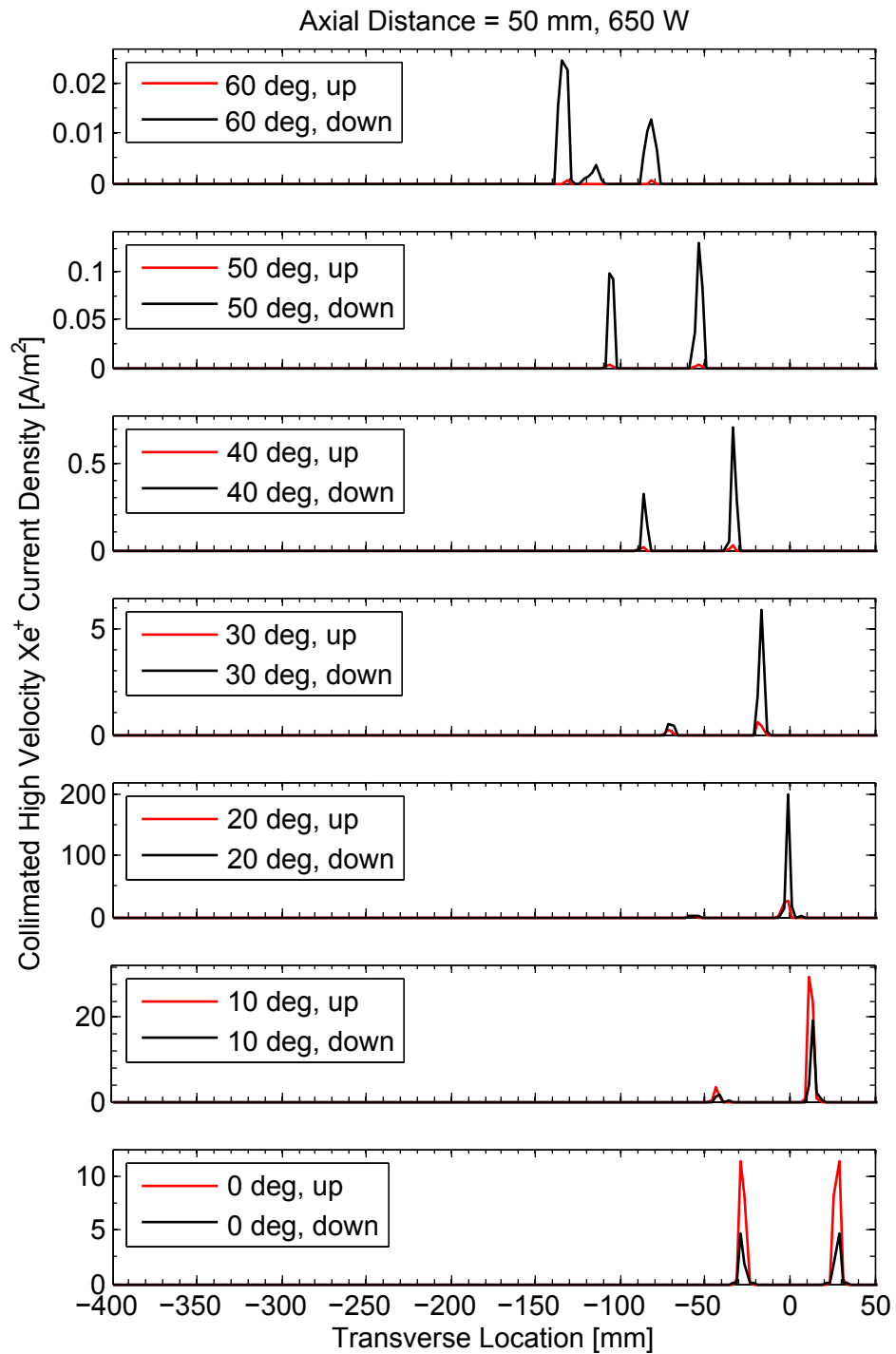


Figure 6.28: ExB probe traces created from HPHall data at 50 mm, 650 W upstream and downstream runs.

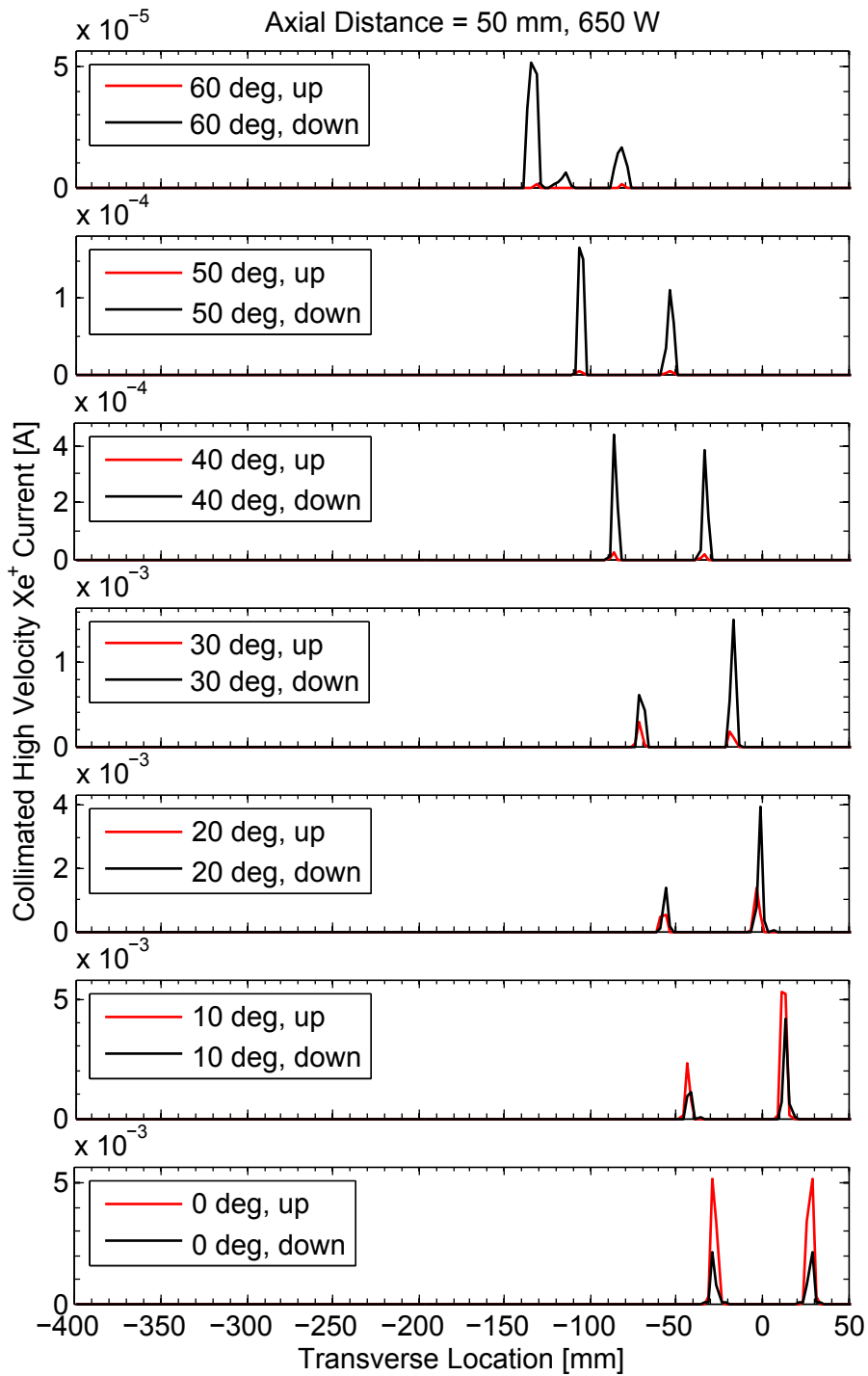


Figure 6.29: ExB probe traces created from HPHall data at 50 mm, 650 W upstream and downstream runs. *Ion current*, not ion current density (i.e., not divided by area).

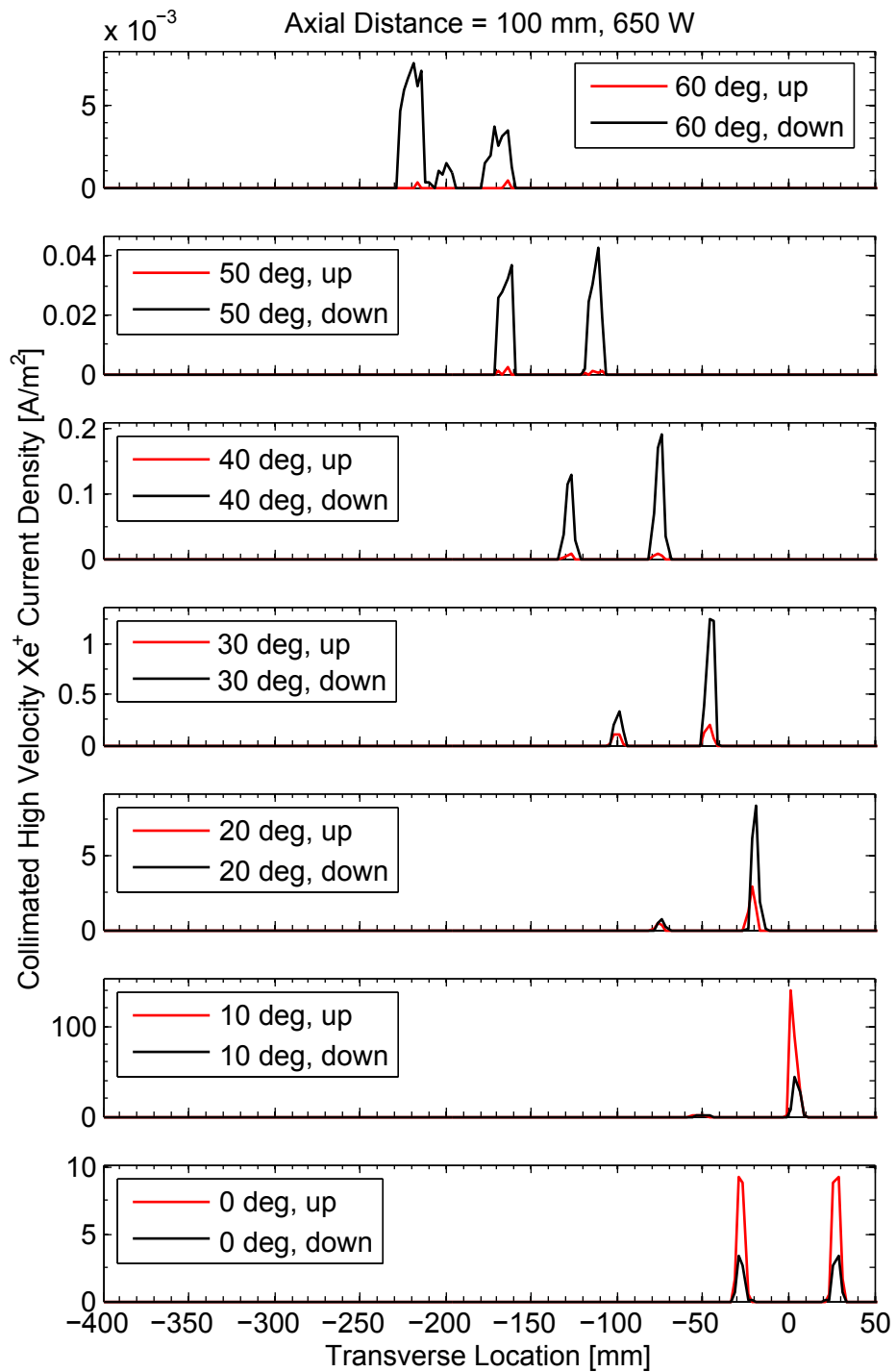


Figure 6.30: ExB probe traces created from HPHall data at 100 mm, 650 W upstream and downstream runs.

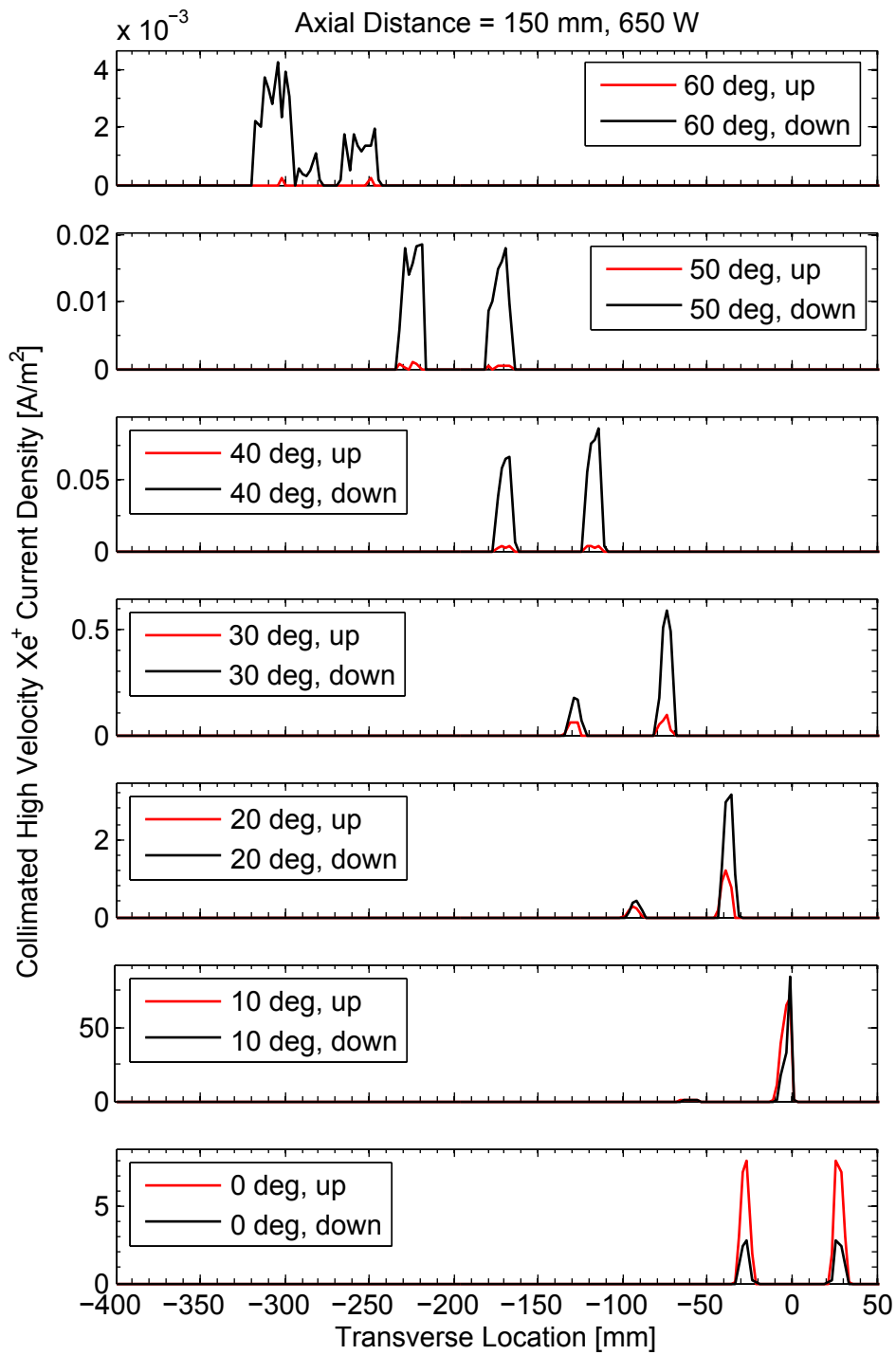


Figure 6.31: ExB probe traces created from HPHall data at 150 mm, 650 W upstream and downstream runs.

Figures 6.32 to 6.34 show the simulated ExB data for the 200 W upstream and downstream runs, at the three axial distances. In the 200 W upstream run, the total ion density is roughly constant from 0 to 20° (if you add up the two peaks, the total is roughly 10 A/m<sup>2</sup>). In the 200 W downstream run, the maximum in total ion density is at 20°. Additionally, it can be seen in both runs that from 10 to 30° the contribution to the current density due to the inward moving ions is greater than the outward moving ions. In the downstream case, the peak corresponding to the inward moving ions also is larger in the 40° trace.

One also sees that, as in the 650 W runs, at 0°, the current density in the 200 W downstream run is about half of the 200 W upstream run. At 10° they are about even, but at angles higher than 20° the current density is about an order of magnitude higher in the downstream run. This suggests a less-collimated beam for the downstream run. At 100 mm away from the thruster exit plane (Figure 6.33) one can see that in both runs, the maximum current density is seen at 10°, and that the inward moving ions make a greater contribution at angles from 10 to 30°. At 150 mm (Figure 6.34), the same trends are seen.

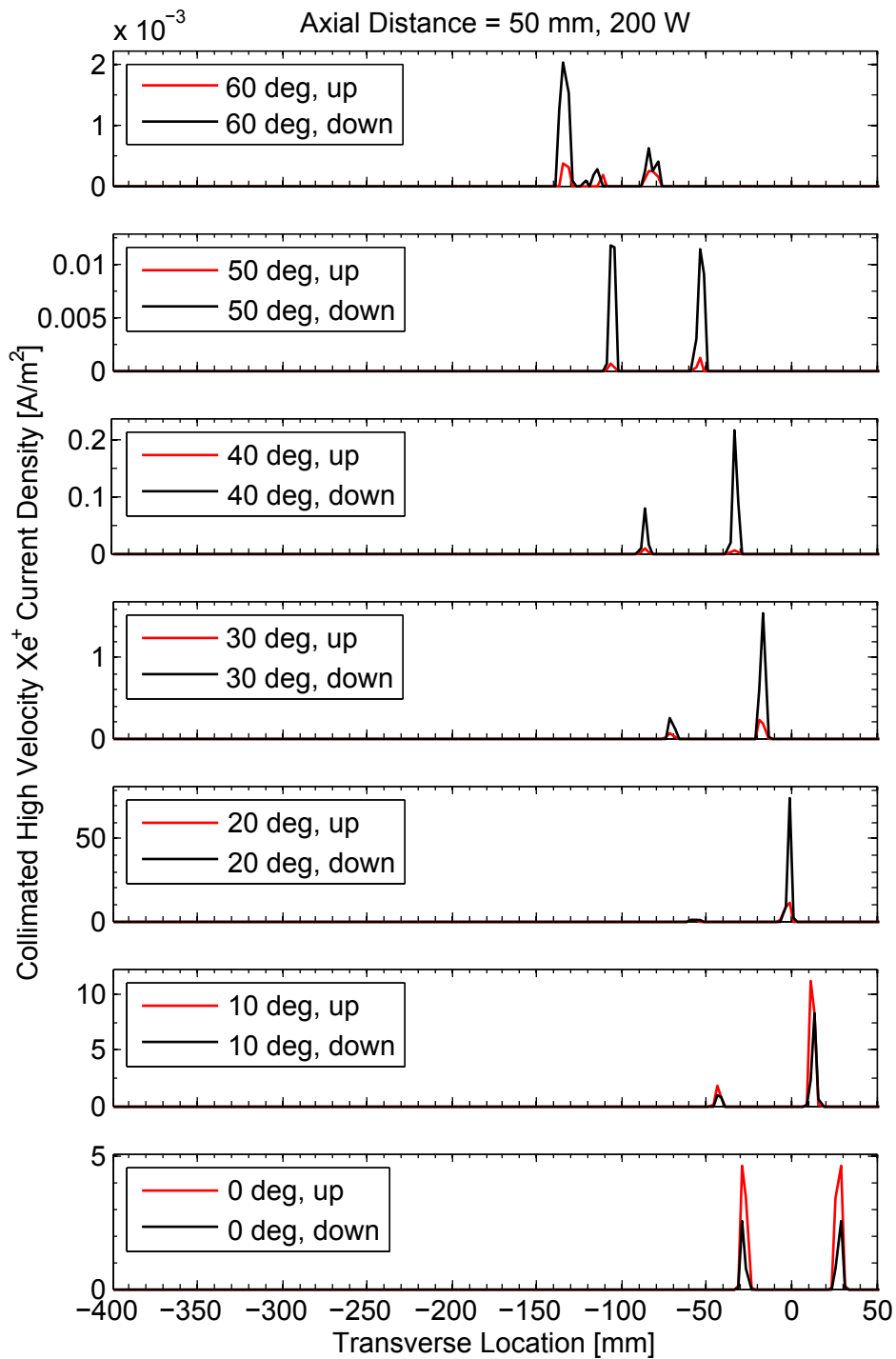


Figure 6.32: ExB probe traces created from HPHall data at 50 mm, 200 W upstream and downstream run.

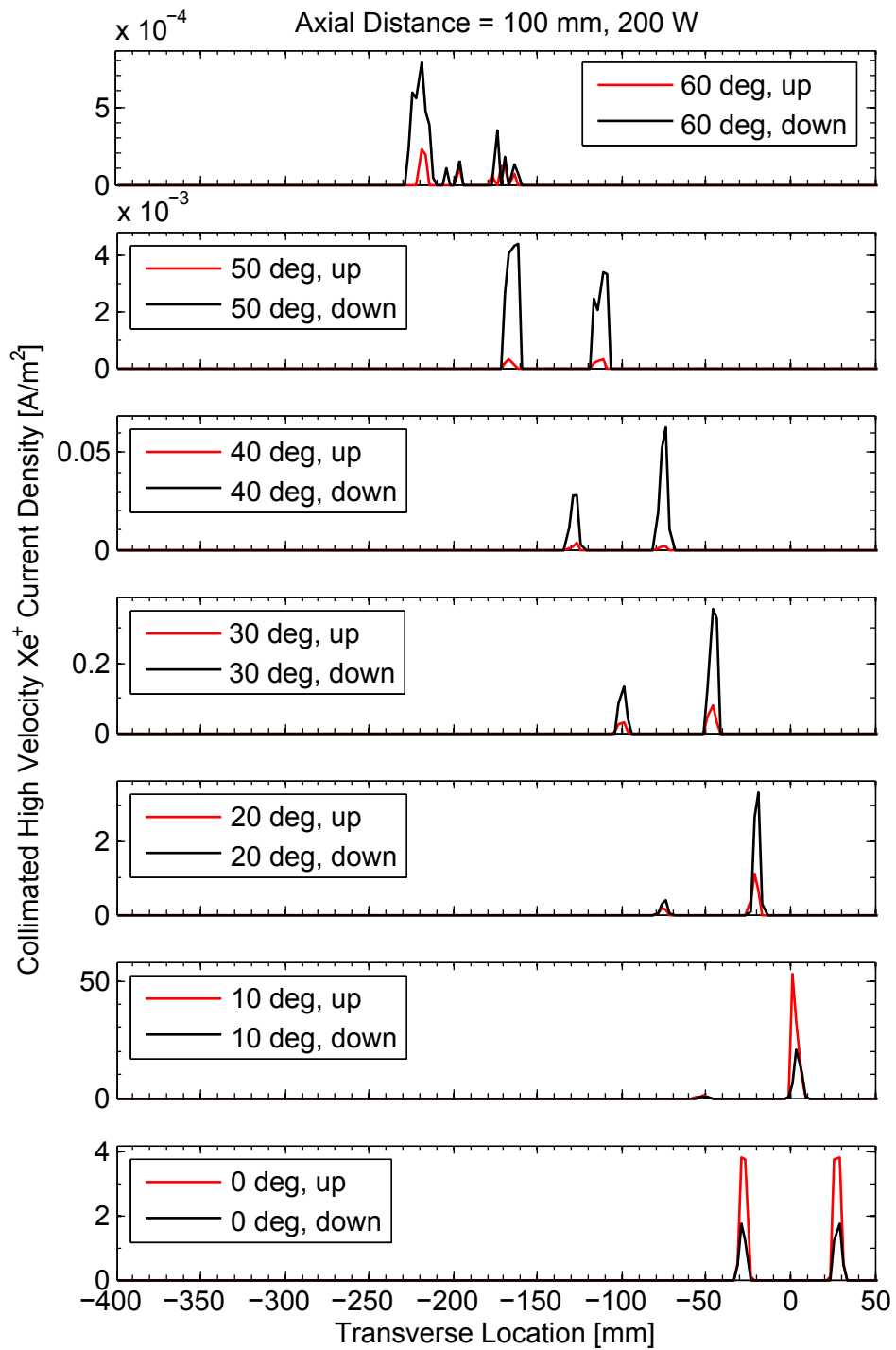


Figure 6.33: ExB probe traces created from HPHall data at 100 mm, 200 W runs.

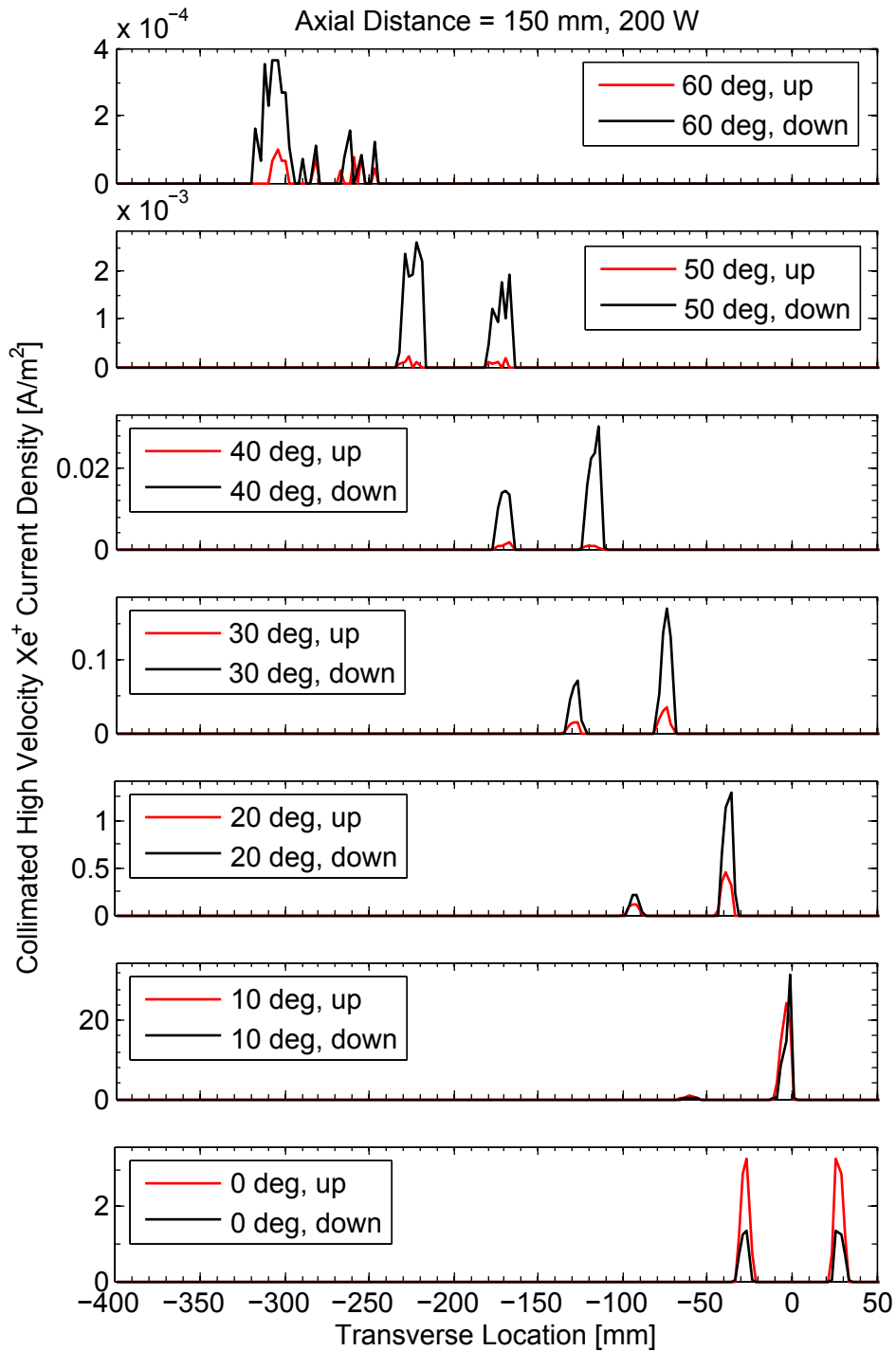


Figure 6.34: ExB probe traces created from HPHall data at 150 mm, 200 W upstream and downstream runs.

To summarize the results, for all runs, at 50 mm, the maximum ion current density was seen at 10 to 20°. At 100 mm and 150 mm, the maxima were seen at 10°. The relative contributions of inward versus outward moving ions varied on a case to case basis, as described above. However, for all runs the peak corresponding to the inward moving ions was larger than that of the outward ions for angles from 10 to 30°. Also, in all runs except the 650 W upstream run, the outward moving ions made a greater contribution at 60°. This suggests that the simulated run produces a central jet which is made up primarily of inward moving ions.

When the upstream runs were compared to the downstream runs, the data showed that the beam was more collimated in the upstream runs. This is in line with the data shown in Section 6.2, since the averaged electric field plots suggest that more radial acceleration occurs in the downstream runs, which would lead to a more divergent beam in the downstream runs.

## 6.4 RPA Results from HPHall

In a similar fashion to the way the ExB plots were constructed, RPA plots were also made using the particle tracking data from HPHall. These plots have been normalized by the total ion current at each angle, for comparison with the experimental data.

### 6.4.1 650 W results

Figure 6.35 shows the simulated RPA trace for the 650 W upstream and downstream runs, for angles from 0 to 40° off the thruster centerline. As can be seen from this figure, from 0 to 30°, there is a peak centered at roughly 270 eV/q in the 650 W upstream run, corresponding to the acceleration potential of the thruster (which was set at 300 V). In the 650 W downstream run, there is still a high energy peak, but its energy decreases as the angle is increased. Additionally, as the angle is increased in both runs, the high energy peak gets shorter and broader, and a greater proportion of ions are found at lower energies. At 40°, the 650 W upstream run shows a broad peak centered at roughly 70 eV/q, while in the 650 W downstream run, there is no low energy peak, and the high energy peak is still present.

Looking at Figure 6.36, one sees that as the angle is increased further in the 650

W upstream run, from 45 to 65°, the primary energy ion population is very small, and the distribution is dominated by a low energy peak centered at roughly 50 eV/q. This feature is sharpest at 50° off the channel centerline. Further increasing the angle from 70 to 80° (Figure 6.37) in the upstream run, continues to show a low energy peak, with negligible proportion of ions with energies above 150 eV/q. Charge exchange collisions could explain the presence of ions with low energies; however, as mentioned in Section 3.1.2, in the version of HPHall used here CEX collisions were not enabled. Therefore, the low energy peak seen at high angles is merely due to the acceleration of ions through the electric field.

The analysis of the potential and electric field plots in Section 6.2 suggested that there should be more ions with higher angle trajectories in the 650 W downstream run. This is indeed true, and can be seen in Figures 6.35 to 6.37. At angles from 45 to 55° off the thruster centerline, as shown in Figure 6.36, there is a broad population of ions centered roughly at the primary beam energy. The traces corresponding to angles greater than 55° show a broad structure extending from roughly 150 eV/q to 300 eV/q, rather than showing a sharper peak centered at about 50 eV/q, as was seen in the upstream run.

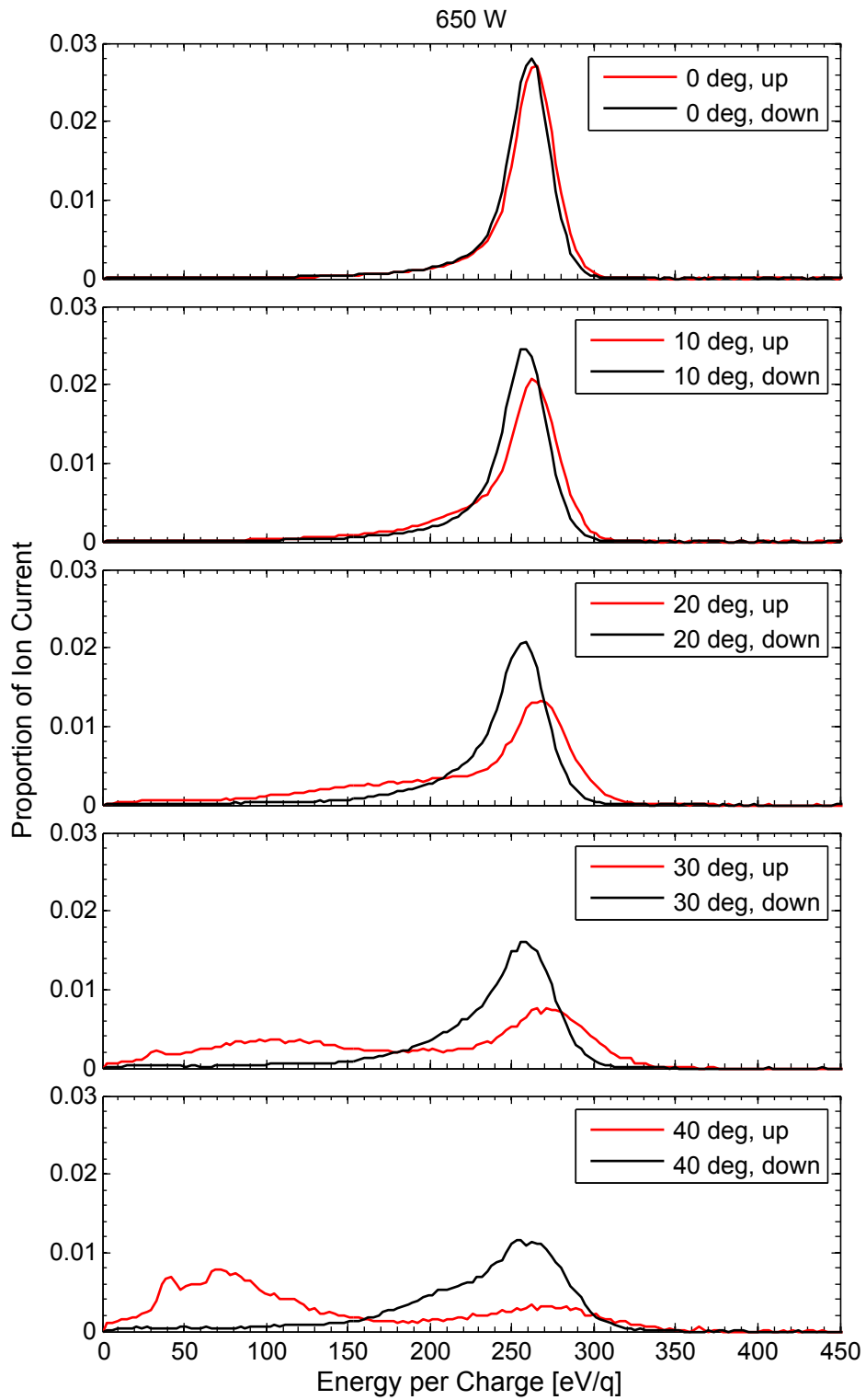


Figure 6.35: RPA traces created from HPHall data, 650 W upstream and downstream runs, 0 to 40°

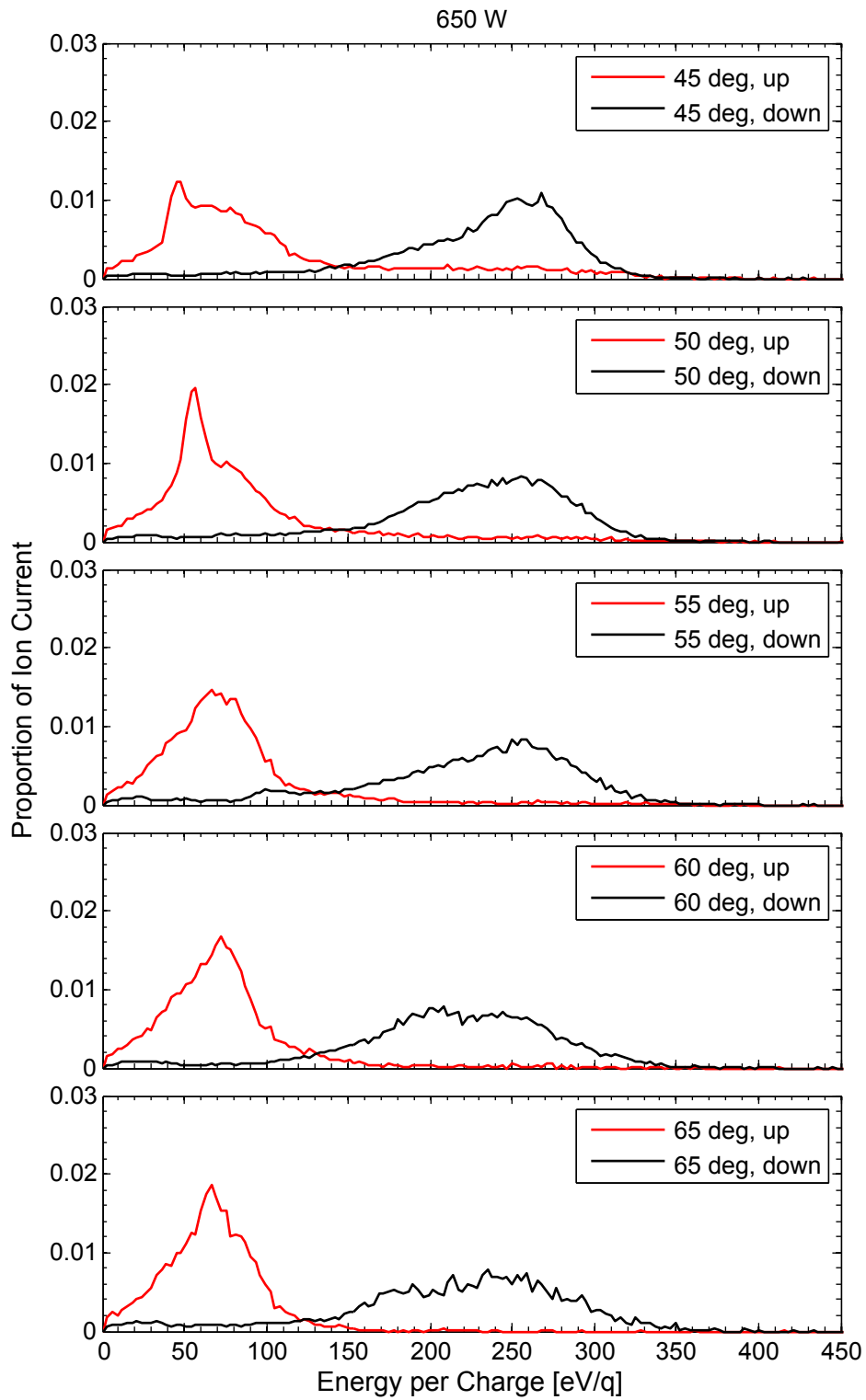


Figure 6.36: RPA traces created from HPHall data, 650 W upstream and downstream runs, 45 to 65°

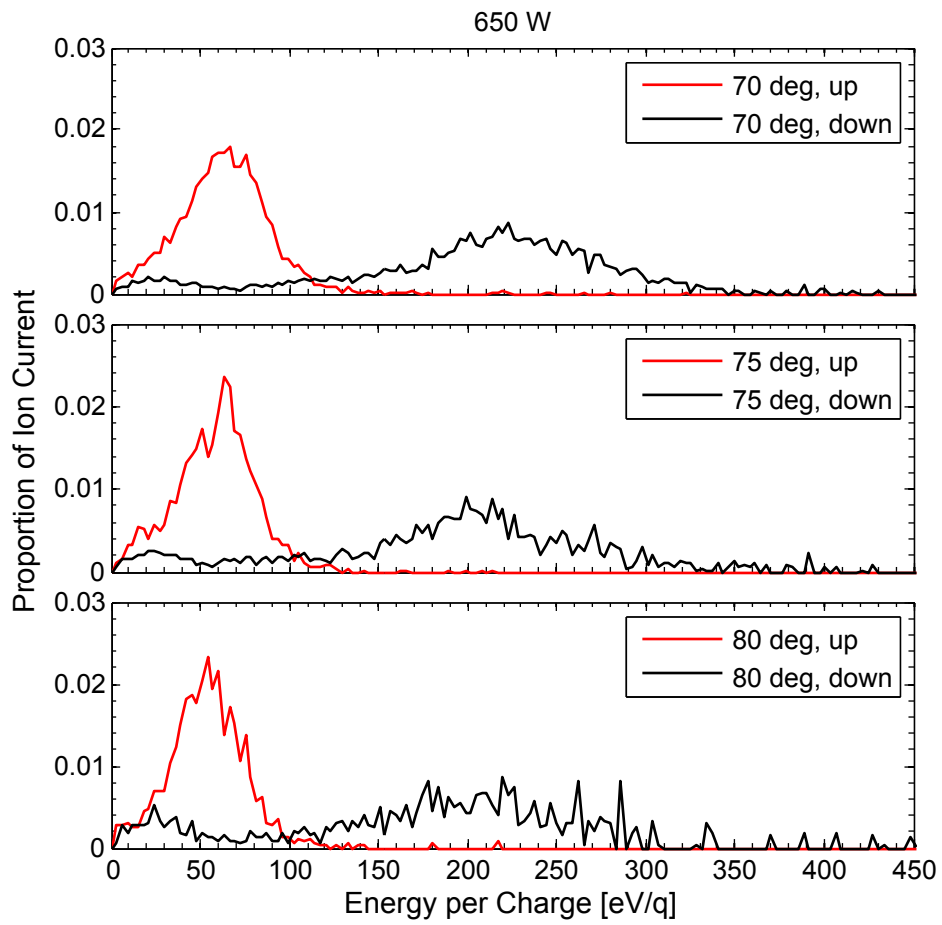


Figure 6.37: RPA traces created from HPHall data, 650 W upstream and downstream runs, 70 to 80°

### 6.4.2 200 W results

Figures 6.38 to 6.40 show the simulated RPA traces for the 200 W run. The 200 W upstream traces follow similar trends to the 650 W upstream run, i.e., a primary ion peak that decreases in magnitude with increasing angle, which is no longer seen at angles above  $40^\circ$ , and a low energy peak that begins to form at  $40^\circ$  and dominates the distribution for angles above  $40^\circ$ . In this run, the low energy peak is shorter and broader than in the 650 W run, although it is still centered at roughly 50 eV/q.

In the 200 W downstream run, one can see primary beam ions out at higher angles. For example, there is still a substantial proportion of these ions at  $50^\circ$ . As the angle is increased above  $55^\circ$ , there is no clear peak in the data; instead, there is a broad population of ions with energies from 0 to about 250 eV/q. At  $60^\circ$  there is a peak within the data at approximately 130 eV/q, which corresponds roughly to the potential at  $z = 0.030$  (as shown in Figure 6.16), so these ions could be the result of ions that are created just outside the exit plane of the thruster.

To summarize the simulated RPA results, in both of the upstream runs, primary energy, high angle ions are not seen at high angles off of the thruster centerline. In the downstream runs, ions with the primary energy are seen at high angles (up to  $80^\circ$ ), but as part of a broad distribution of ions with various energies, rather than being seen as a separate, narrow peak in the data centered at the primary beam energy.

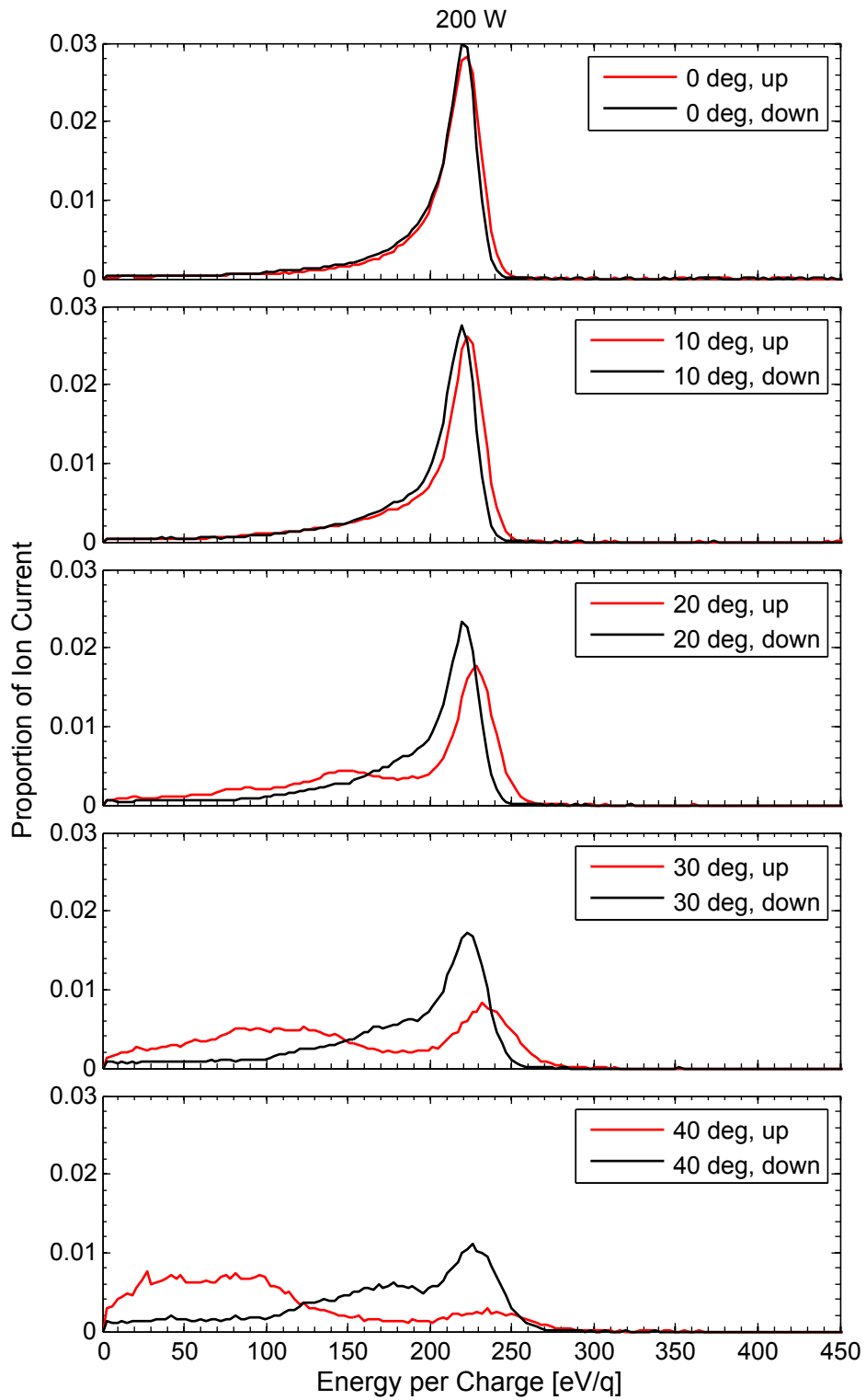


Figure 6.38: RPA traces created from HPHall data, 200 W upstream and downstream runs, 0 to 40°

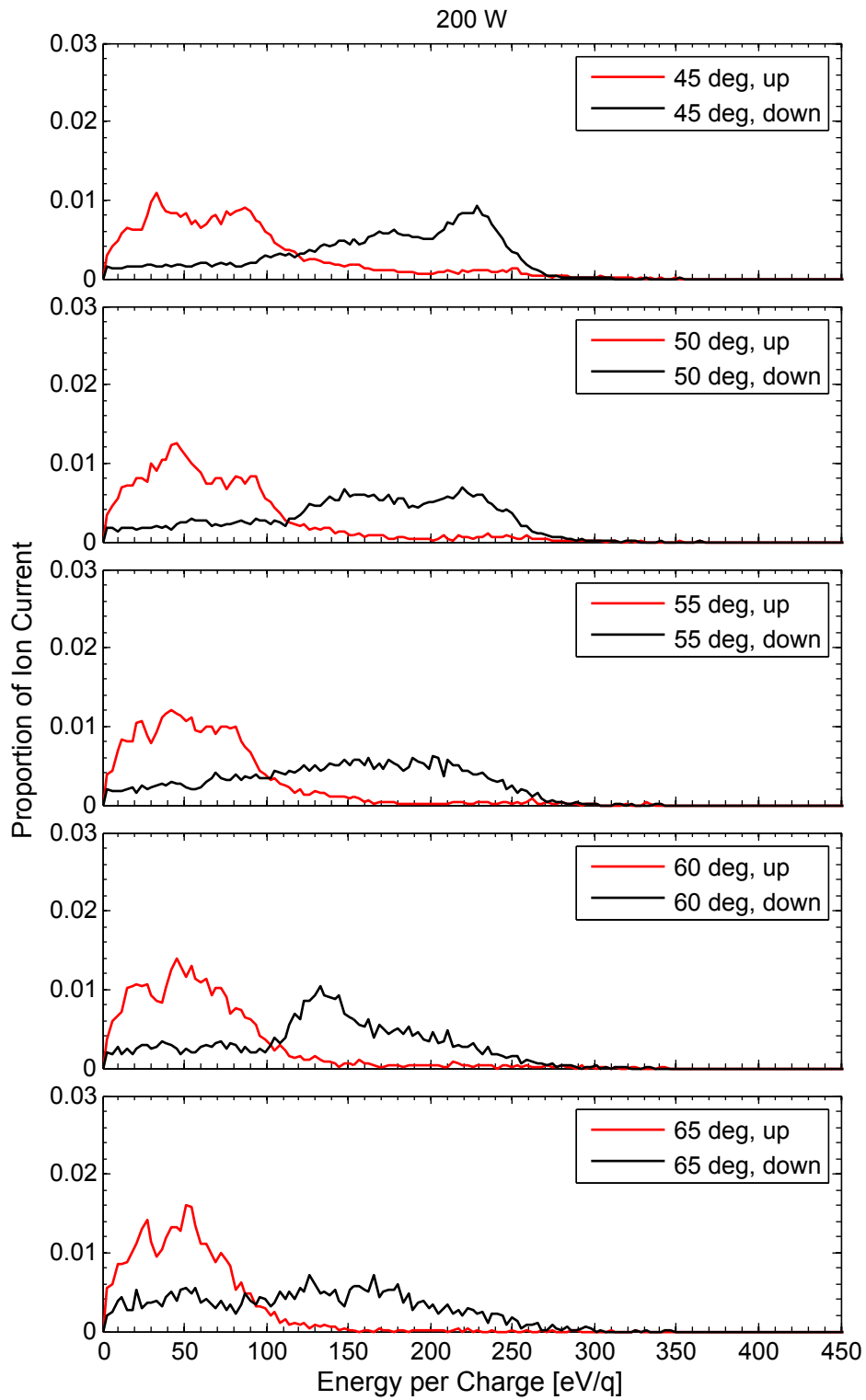


Figure 6.39: RPA traces created from HPHall data, 200 W upstream and downstream runs, 45 to 65°

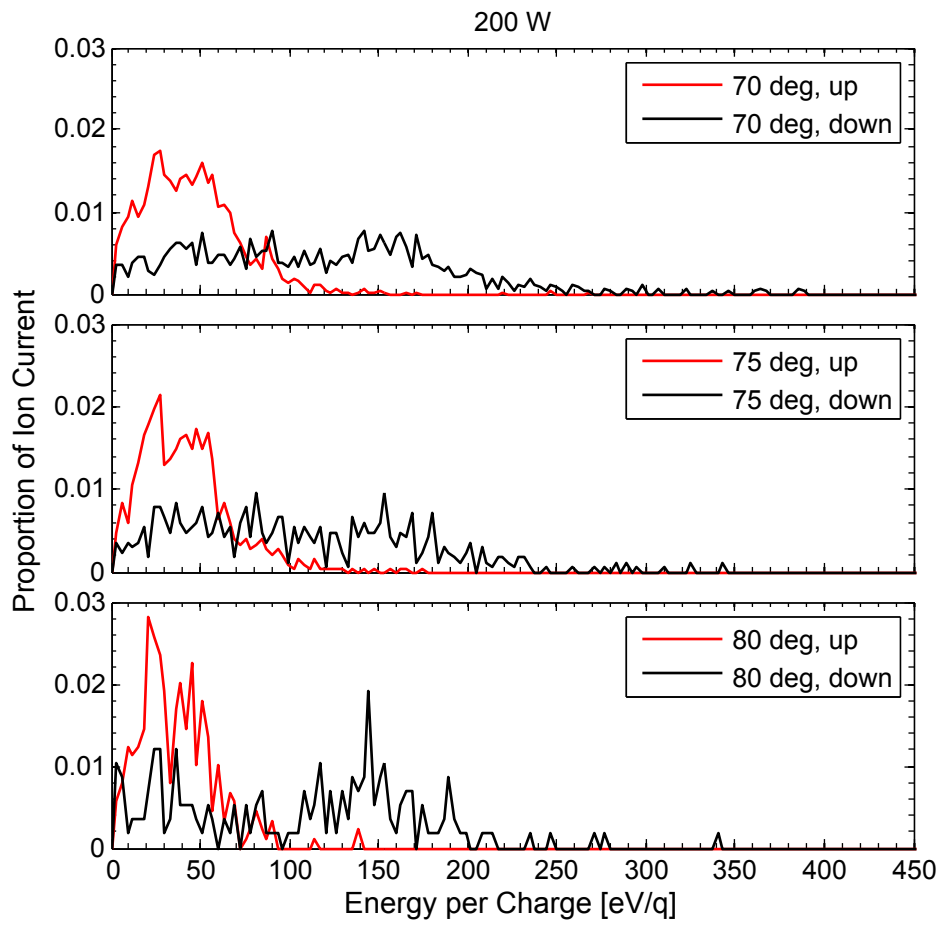


Figure 6.40: RPA traces created from HPHall data, 200 W upstream and downstream runs, 70 to 80°

Table 6.4: Maximum error in the simulated Faraday probe data.

Distance [mm]	650 W upstream [A/m <sup>2</sup> ]	650 W downstream [A/m <sup>2</sup> ]	200 W upstream [A/m <sup>2</sup> ]	200 W downstream [A/m <sup>2</sup> ]
50	11.46	40.67	16.50	12.92
100	47.60	18.37	6.595	10.39
150	28.56	15.24	7.326	9.229

## 6.5 Repeatability of the Simulated Results

When discussing uncertainties in the simulated data, there are two different questions that one should ask. First, how well does the simulated data predict the actual results, i.e., how accurate is it? The accuracy of the simulation depends on the approach used, for example the assumptions, simplifications, numerical methods, etc. that go into the calculations. These topics have been discussed in depth in Chapters 3 and 4, and will be discussed further in Chapter 8. The second question is how repeatable is the data from one run to the next, i.e., how precise is the simulation? This section will discuss the question of repeatability in the simulated Faraday probe, ExB, and RPA traces.

To gauge the repeatability of the data, three different runs of 10,000 time steps each were conducted for each of the four HPHall conditions (650 W upstream, 650 W downstream, 200 W upstream, and 200 W downstream). For each condition, Faraday probe, ExB, and RPA traces were calculated for each of these three runs, and the average of each trace was calculated (this was done for each of the different angles and distances shown in the plots in Sections 6.3 and 6.4.) Then, the maximum deviation from the mean was calculated for all of the traces. The maximum deviation, rather than the standard deviation, was used because of the small sample size ( $n = 3$  runs), and the small sample size was due to time constraints. The maximum deviation for each of the traces in Sections 6.3 and 6.4 are shown in Tables 6.4 to 6.6.

Figure 6.41 is an example of the bound on the simulated data, found by adding and subtracting the maximum deviation from the mean. For all of the Faraday probe and ExB traces, the deviation was small enough relative to the mean of the traces that the bounds are not discernable from the trace itself. However, in the case of the RPA data, for angles greater than about 70°, the maximum deviation is roughly as large as the mean value of the trace.

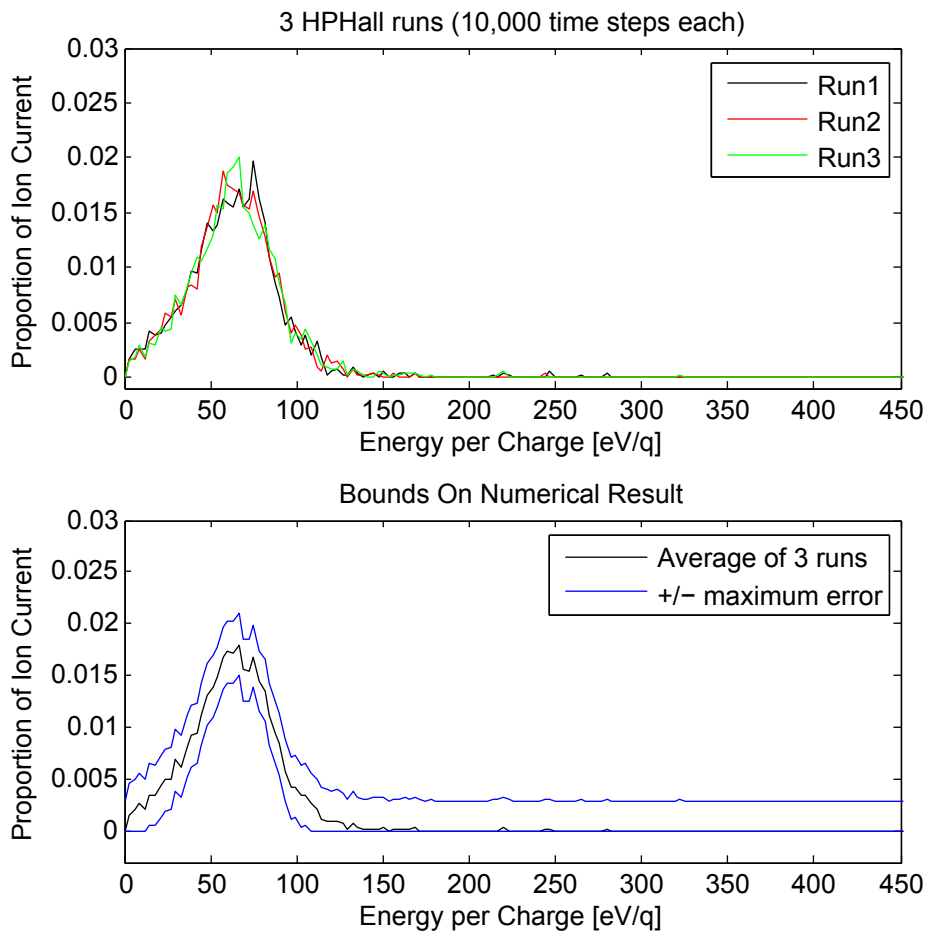


Figure 6.41: Bound on the simulated RPA data for the 70°, 650W upstream run.

Table 6.5: Maximum error in the simulated ExB data.

Distance [mm]	Angle [°]	650 W upstream [A/m <sup>2</sup> ]	650 W downstream [A/m <sup>2</sup> ]	200 W upstream [A/m <sup>2</sup> ]	200 W downstream [A/m <sup>2</sup> ]
50	0	0.38	0.31	0.20	0.043
50	10	0.20	0.57	0.13	0.15
50	20	1.43	7.38	1.15	2.13
50	30	0.081	0.26	0.015	0.047
50	40	0.010	0.038	0.0013	0.0057
50	50	0.0023	0.015	0.0008	0.0022
50	60	0.0009	0.0045	0.0003	0.0006
100	0	0.34	0.24	0.18	0.049
100	10	1.45	1.70	0.43	0.41
100	20	0.16	0.29	0.076	0.084
100	30	0.023	0.075	0.0058	0.012
100	40	0.0033	0.015	0.0008	0.0041
100	50	0.0010	0.0055	0.0004	0.0012
100	60	0.0005	0.0025	0.0002	0.0004
150	0	0.28	0.15	0.16	0.041
150	10	2.02	4.67	0.45	0.39
150	20	0.065	0.17	0.037	0.038
150	30	0.014	0.031	0.0031	0.0071
150	40	0.0025	0.0059	0.0007	0.0020
150	50	0.0009	0.0032	0.0002	0.0001
150	60	0.0002	0.0017	0.0001	0.0001

Table 6.6: Maximum error in the simulated RPA data.

Angle [°]	650 W upstream	650 W downstream	200 W upstream	200 W downstream
0	0.0005	0.0009	0.0007	0.0007
10	0.0007	0.0008	0.0007	0.0007
20	0.0009	0.0008	0.0008	0.0011
30	0.0009	0.0010	0.0009	0.0010
40	0.0012	0.0013	0.0011	0.0013
45	0.0009	0.0013	0.0013	0.0014
50	0.0011	0.0017	0.0025	0.0014
55	0.0015	0.0022	0.0021	0.0016
60	0.0019	0.0016	0.0029	0.0021
65	0.0018	0.0027	0.0036	0.0028
70	0.0030	0.0033	0.0070	0.0046
75	0.0070	0.0043	0.0068	0.0098
80	0.0089	0.0075	0.0167	0.0214

## 6.6 Effect of Oscillations

As discussed in Section 3.3.4, oscillations were tracked in HPHall to help determine their impact on ion trajectories. To assess the magnitude of the oscillation effects, the value of several plasma parameters, including potential, electron temperature, and ion density were recorded as a function of time. Figure 6.42 shows the values of these three parameters over 10,000 time steps ( $5 \times 10^{-4}$  s of simulation time) at the point  $z = 0.0290$  m,  $r = 0.0275$  m in the simulation domain (i.e., the center of the channel at the exit plane), for the 650 W upstream HPHall run. Ion current was also recorded and is plotted in this figure as well. The black curve in the plots represents the data taken directly from HPHall, while the red curve is the average over ten data points.

As can be seen in Figure 6.42, the ion current has a fairly regular oscillation that occurs with a period of approximately  $4 \times 10^{-4}$  s. The amplitude of the oscillation is approximately 0.4 A. The ion density seems to follow the ion current fairly well, with the same oscillation period, albeit with a bit more noise. The amplitude of the ion density oscillation is about  $7.5 \times 10^{16} \text{ m}^{-3}$ , with a mean density of  $3 \times 10^{17} \text{ m}^{-3}$ . The potential and the electron temperature do not seem to follow the current oscillation.

To make sure that the potential and temperature indeed do not follow the current oscillation, the parameters in Figure 6.42 were plotted on a shorter time scale, which is shown in Figure 6.43. From these plots, it appears that the potential data does in fact contain a oscillation with approximately the same period as the current oscillation, although the peaks and troughs of the two do not line up. This suggests that the potential either leads or lags the current. From Figure 6.43, it is difficult to tell the relationship between the electron temperature oscillation and the other parameters, due to the amount of variation in the signal. For reference, the amplitude of the potential oscillations is about 15 V, centered at a mean of 95 V, while the amplitude of the electron temperature oscillations is about 1 eV, centered at a mean of 11.5 eV.

In addition to plotting the parameters as a function of time, the Fourier transform of the data were also taken, and the normalized magnitude versus frequency can be found in Figure 6.44. For the ion current, the graph has a maximum at about 25 kHz, and oscillations at frequencies above 100 kHz are negligible. The potential has a maximum at about 30 kHz, but also has a significant amount of content at frequencies from 100 to 500 kHz, in

contrast to the ion current. The electron temperature possibly has a maximum at around 20 kHz, although this is difficult to determine. As suggested by the time-dependent plots, the ion density has a frequency spectrum that is very similar to the ion current.

The corresponding plots for the other HPHall runs (650 W downstream, 200 W upstream, 200 W upstream) are shown in Appendix C. Rather than discuss each of these plots individually as was done for the 650 W upstream run, Table 6.7 summarizes these results, providing information on the oscillation amplitude, mean, and local maxima in the frequency spectra for the different runs. One observation from Table 6.7 worth mentioning is that while all of the potential frequency spectra show evidence of content above 100 kHz, the only one to have a clear local maximum above 100 kHz is the 650 W downstream run. This run has a peak at about 110 kHz. This appears to be the “transit time” oscillation described by Fife and others [14, 37].

Overall, the data clearly show evidence of a “breathing mode” oscillation in the ion current and density data, with a frequency of 10 to 25 kHz, depending on the conditions. The 200 W runs have breathing mode oscillation frequencies that are smaller than the 650 W runs. In all of the runs, the potential oscillations also show a peak in frequency corresponding to the breathing mode, although there is significant frequency content above 100 kHz which is not present in the ion current/density data.

In terms of the effect on ion trajectories, what is important is the ion density (determines number of ions) and the potential (determines energies). Looking at the potential variations, in the 650 W upstream and 200 W upstream runs, the potential varies by 15 V about a mean of 95 V at the thruster exit plane. This suggests that energies of ions created at the exit plane could vary by as much as 30 eV/q, as ions created at a peak in the potential oscillation would start off with 110 V, while those created at a trough would start off with 80 V. Additionally, since the data show that the peaks and troughs in the potential oscillation do not line up with those of the ion density oscillation, there should not be a substantially larger number of 110 eV/q ions versus 80 eV/q ions produced.

What one would expect to see, as a consequence of these observations, is that there would be a spread of roughly 30 eV/q in the energy spectra data for the 200 and 650 W upstream runs. In the 650 W downstream run, this spread in energy due to oscillations would be about 24 eV/q, while in the 200 W downstream run it would be about 14 eV/q. What is definitely not suggested by the oscillation data is that ions with potentials corresponding

Table 6.7: Summary of oscillation data from HPHall.

Parameter	650 W upstream	650 W downstream	200 W upstream	200 W downstream
$I_A$ mean [A]	2.2	2.2	0.8	0.8
$I_A$ amplitude [A]	0.4	0.3	0.2	0.25
$I_A$ freq. peaks [kHz]	24	20	10	10
$n_i$ mean [m <sup>-3</sup> ]	3.0e17	4.0e17	1.2e17	1.3e17
$n_i$ amplitude [m <sup>-3</sup> ]	7.5e16	1.0e17	3.5e16	3.0e16
$n_i$ freq. peaks [kHz]	30	20	10	10
$\phi_i$ mean [V]	95	215	95	163
$\phi_i$ amplitude [V]	15	12	15	7
$\phi_i$ freq. peaks [kHz]	30	20 and 110	10	10
$T_e$ mean [eV]	11.5	17	10	11.5
$T_e$ amplitude [eV]	1.0	2.0	1.0	0.5
$T_e$ freq. peaks [kHz]	15	15	N/A	10

to the primary beam energy could be produced solely by oscillation effects, so high angle, high energy ions are unlikely to be created by this mechanism. However, oscillations in the potential could explain the spread in velocities peak in the data, if one exists.

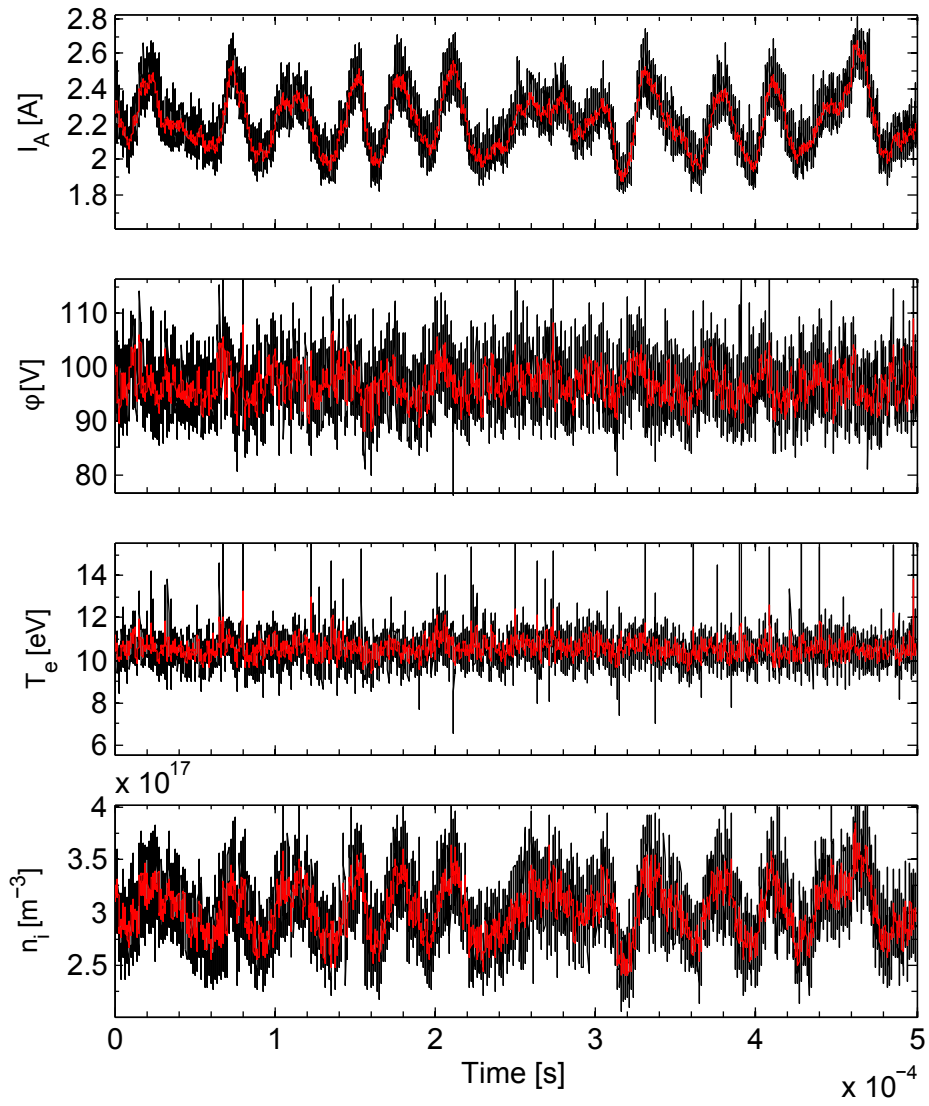


Figure 6.42: Oscillation tracking in HPHall for the 650 W upstream run.

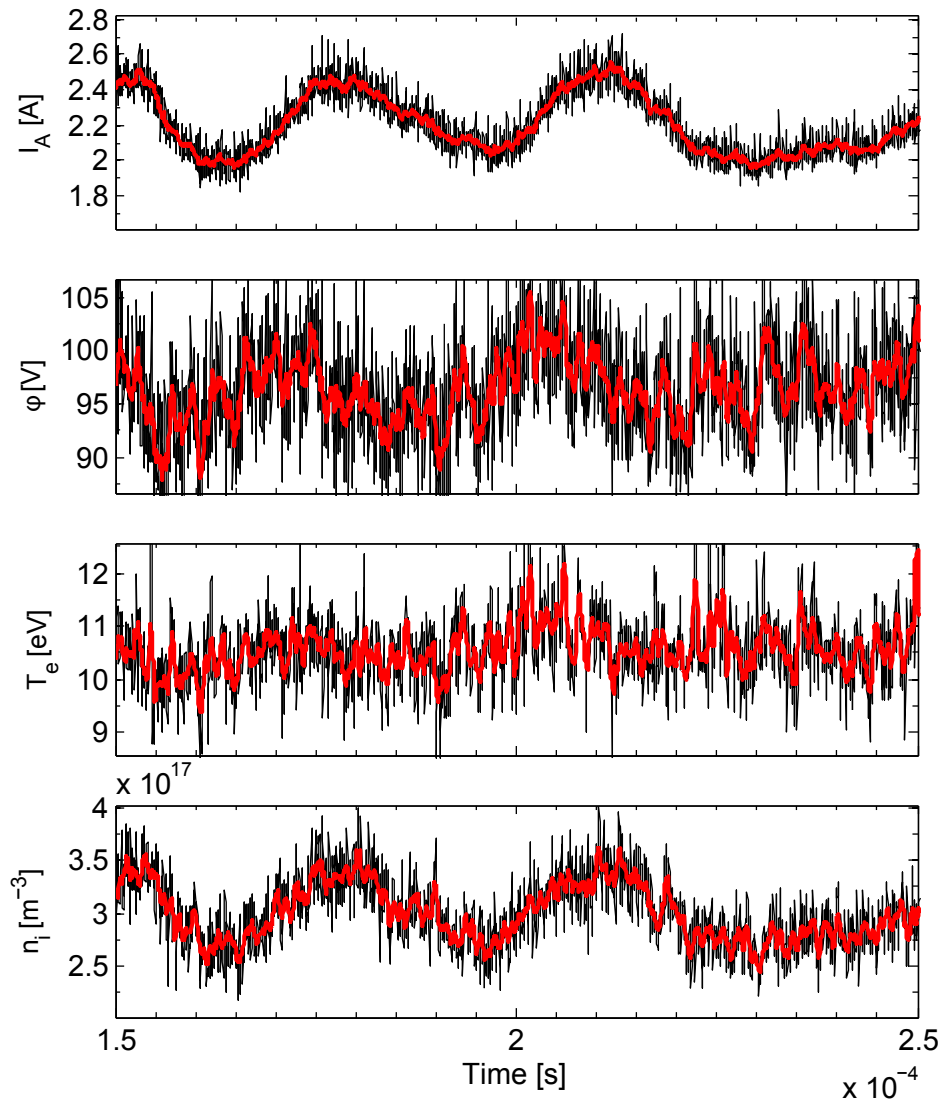


Figure 6.43: Oscillation tracking in HPHall, on a shorter time scale, for the 650 W upstream run.

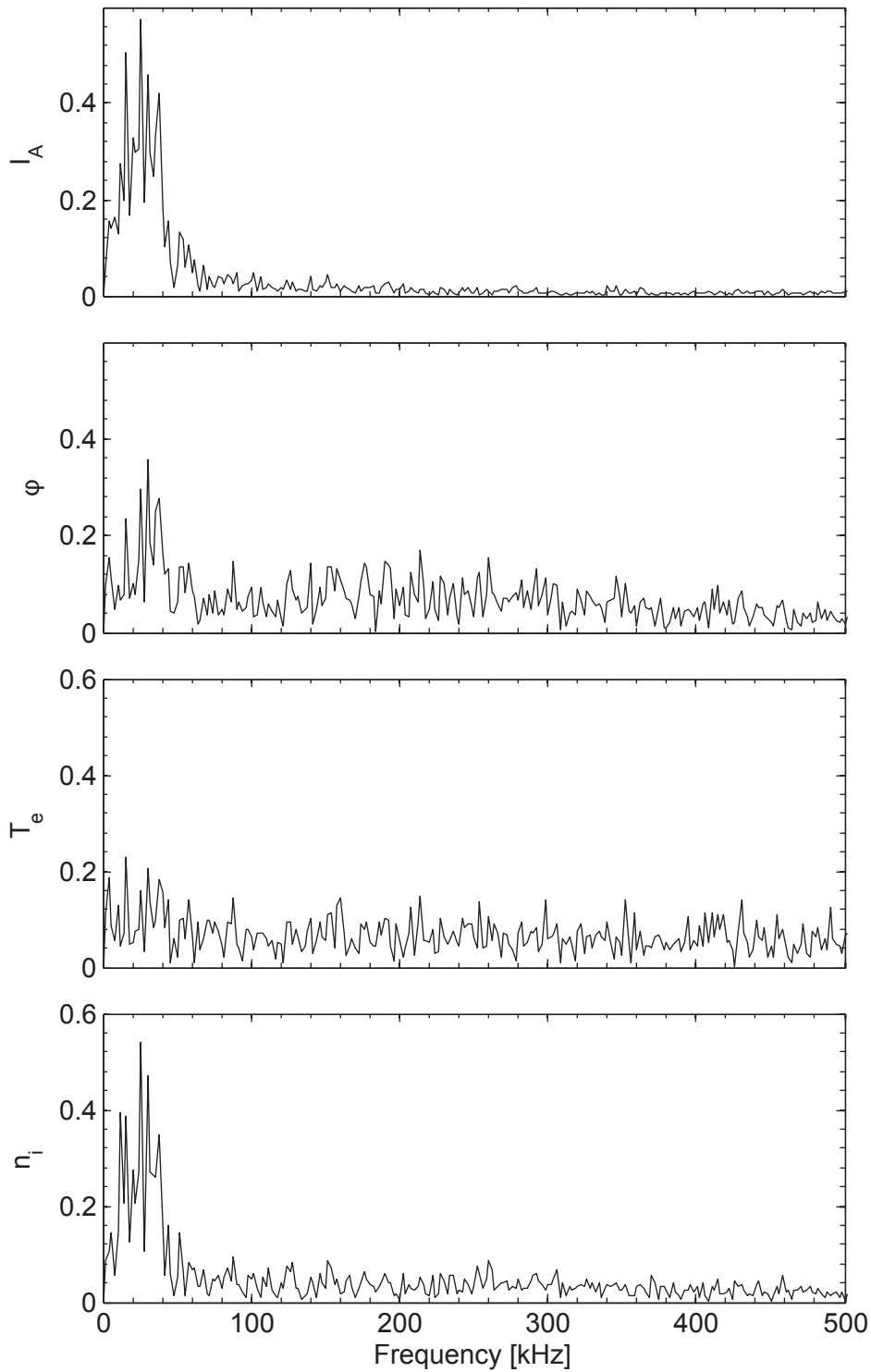


Figure 6.44: Frequency spectrum for the 650 W upstream run.

## Chapter 7

# Corner Sheath Model Results and Discussion

This chapter details the results from applying the corner sheath model to the outputs from the four different HPHall runs. As was discussed in Section 4.1, values from HPHall were required to define the boundary conditions for the sheath model. For each run, the sheath thickness and potential profile were determined using the model and plotted as a function of radial and axial location. Simulated ion trajectories were then calculated by introducing test particles with different initial velocities at the sheath boundary, and then tracking their paths as they moved through the sheath. Overall, the results showed that the sheath could change an ion's trajectory by roughly 10 to 20°. Although this represents a significant change in angle, it is not enough to be the sole explanation for the high velocity, high angle ion trajectories.

### 7.1 Boundary Conditions

The corner sheath model was applied to the four runs (650 W upstream, 650 W downstream, 200 W upstream, and 200 W downstream) that were run in HPHall. As discussed in Section 4.1, the only outside input that is needed is the electron temperature at the sheath boundary. By applying a secondary electron emission yield model, one can then calculate  $\Gamma_{SEE}$ , and from that can solve for the potential and electric field at the wall, using the Hobbs and Wesson approach (Eqn. 4.12 to 4.14). These conditions, along with the fact that the non-dimensional potential,  $\chi$ , at the pre-sheath boundary is  $-1/2$  relative to the reference potential far from the wall, allow the sheath equations to be solved for the sheath

thickness and potential profile. Figures 7.1 to 7.4 show the boundary conditions for the four different HPHall cases, where  $\Gamma_{SEE}$  has been found using the power fit of Dunaevsky [43].

## 7.2 Potential Profile

Figures 7.5 to 7.8 show the potential profiles generated by the sheath model for the four runs, as a function of non-dimensional axial ( $\zeta$ ) and radial ( $\rho$ ) locations. The sheath edge in each run is marked in black. For the 650 W upstream run, the sheath contracts in size as the distance from the exit plane is decreased, with its minimum thickness at roughly  $\zeta = -65$ . As  $\zeta$  is further increased, the sheath expands. In contrast, in the 650 W downstream run, the sheath does not expand and contract, rather it simply decreases in thickness as  $\zeta$  is increased. The 200 W upstream run follows a trend similar to the 650 W upstream run, although the contraction in sheath thickness is not as large. The 200 W downstream follows a trend similar to the 650 W downstream run.

The primary driving factor in the determination of the sheath thickness is the electron temperature, since it determines the boundary conditions. In general, the higher the electron temperature, the thinner the sheath will be. In both of the upstream cases, as shown in Figures 7.5 and 7.7, the electron temperature peak is upstream of the exit plane, whereas in the downstream cases the maximum temperature is found downstream (Figures 7.6 and 7.8). This is why there is a local minimum in sheath thickness upstream of the exit plane in both of the upstream cases.

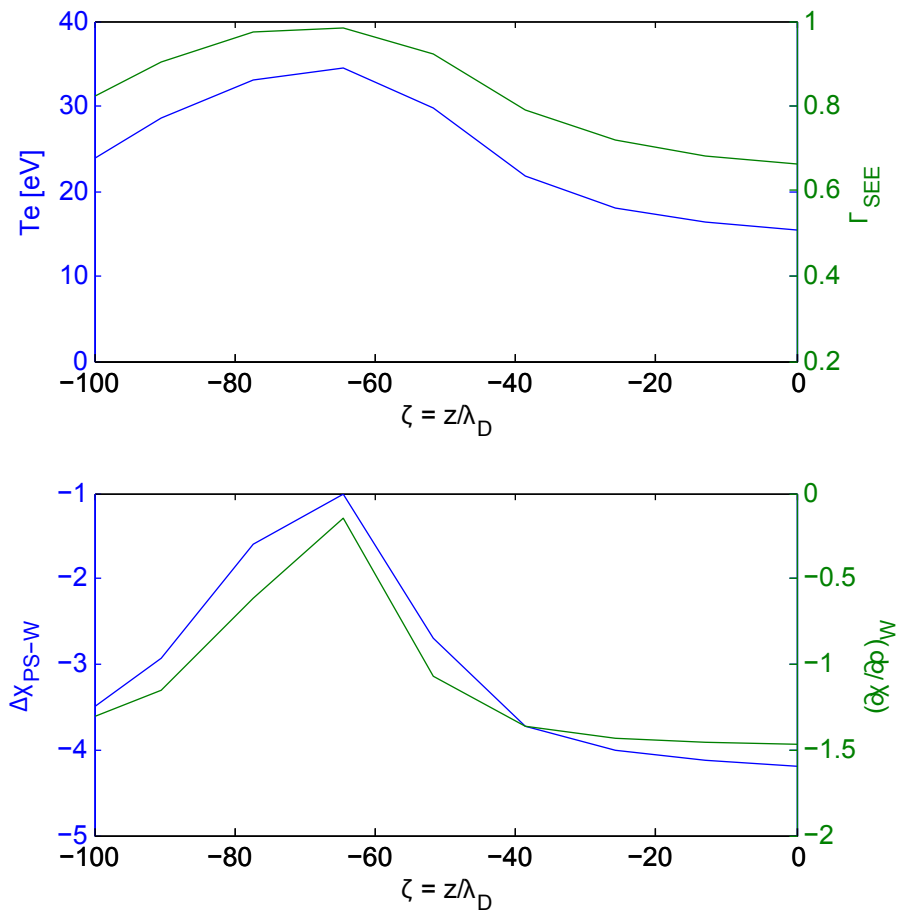


Figure 7.1: Boundary conditions for the corner sheath model, 650 W upstream run.

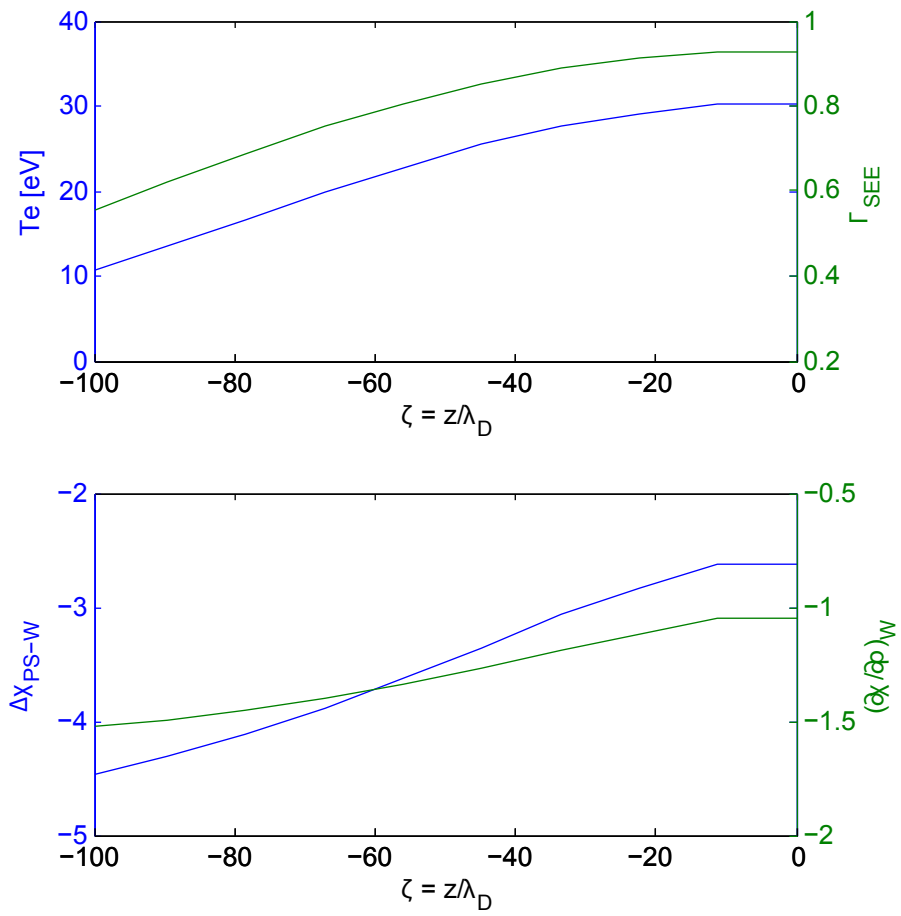


Figure 7.2: Boundary conditions for the corner sheath model, 650 W downstream run.

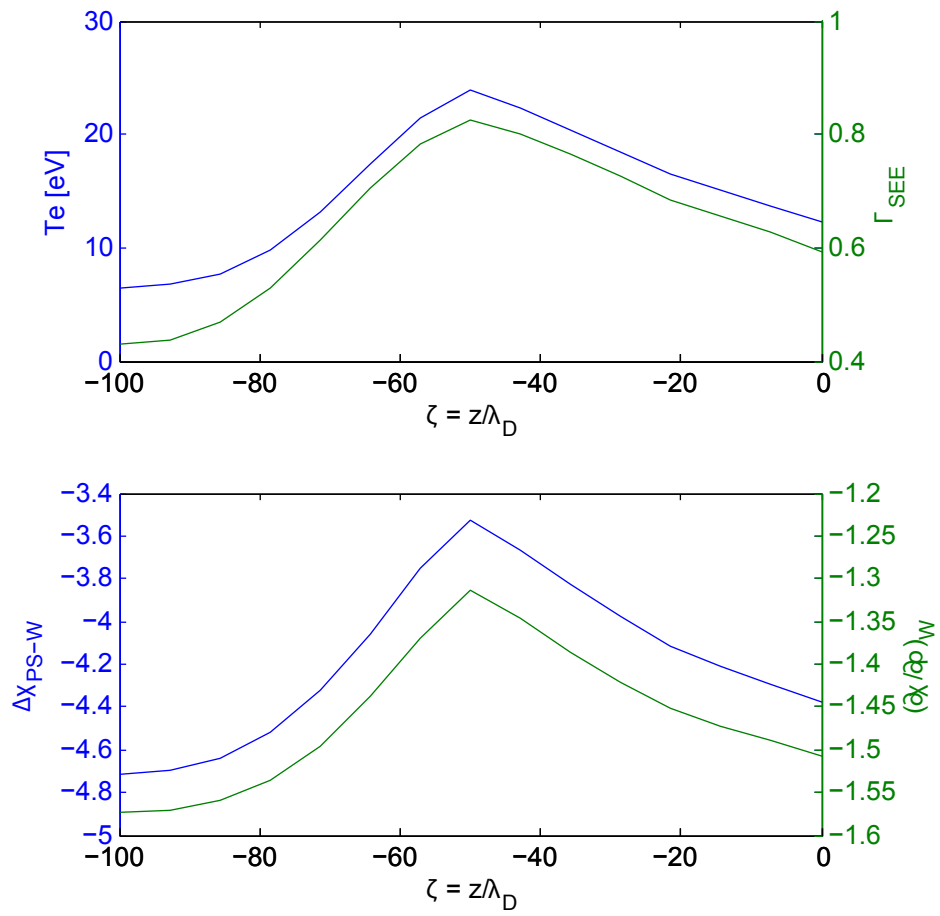


Figure 7.3: Boundary conditions for the corner sheath model, 200 W upstream run.

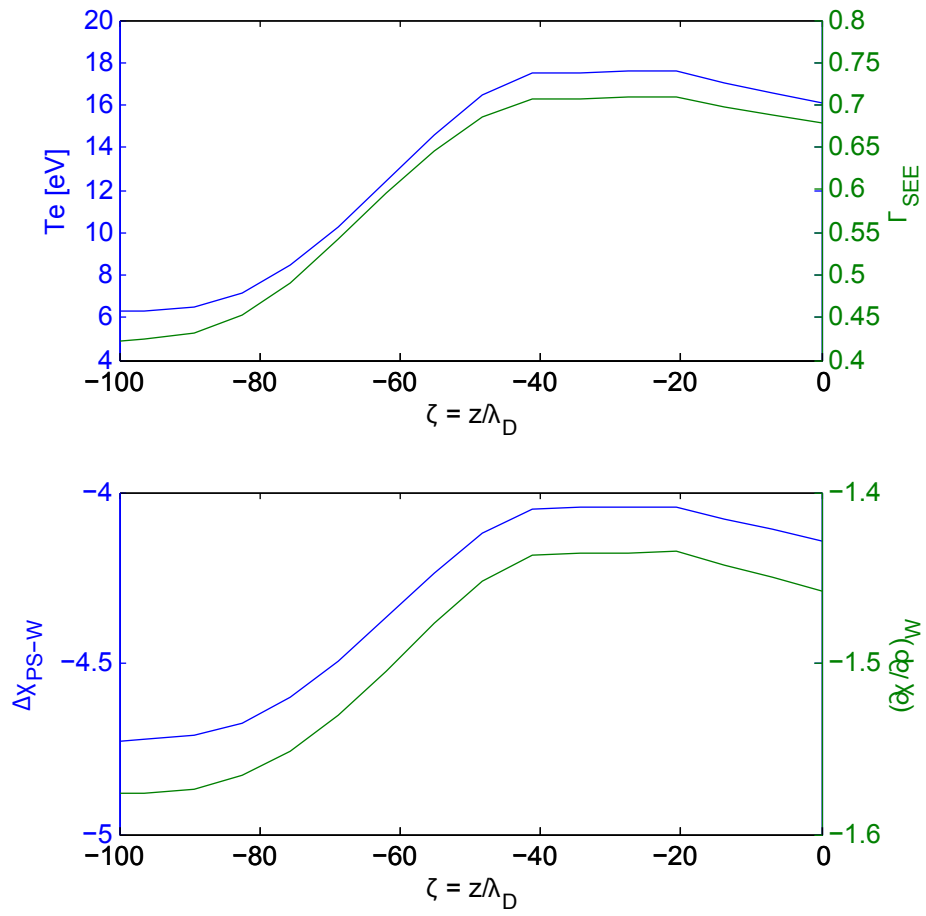


Figure 7.4: Boundary conditions for the corner sheath model, 200 W downstream run.

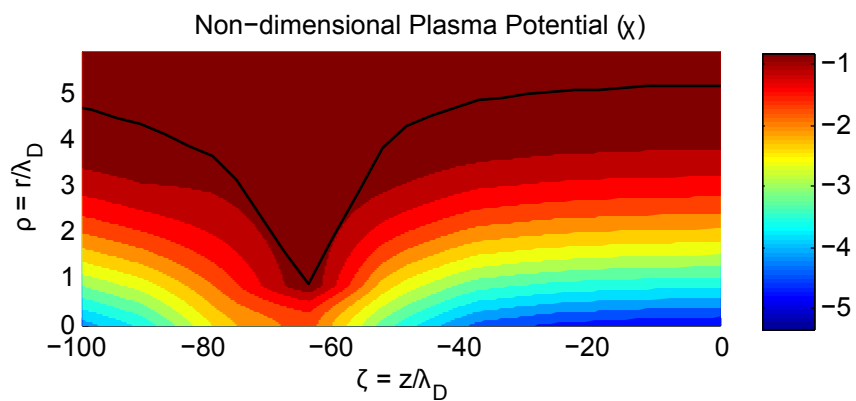


Figure 7.5: Plasma potential from the corner sheath model, 650 W upstream run.

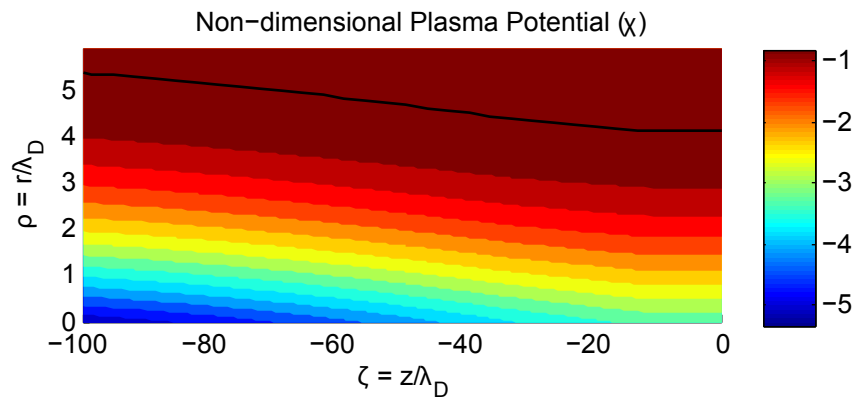


Figure 7.6: Plasma potential from the corner sheath model, 650 W downstream run.

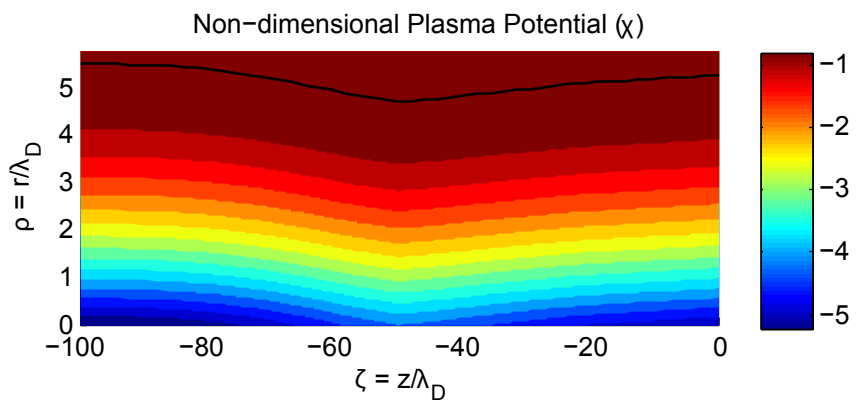


Figure 7.7: Plasma potential from the corner sheath model, 200 W upstream run.

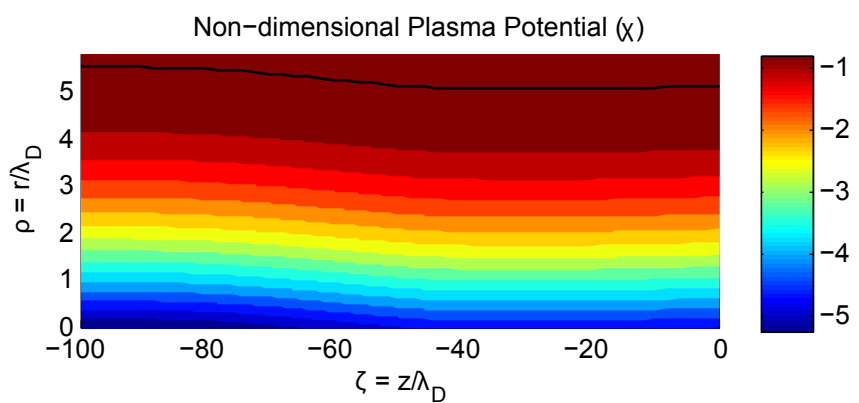


Figure 7.8: Plasma potential from the corner sheath model, 200 W downstream run.

### 7.3 Ion Trajectories Through the Sheath

As discussed in Section 4.1, after the potential field was calculated, its effect on particle trajectories was determined. Figures 7.9 to 7.10 show the paths of ten ion trajectories for the 650 W upstream run, for two different initial non-dimensional axial velocities,  $U_0 = 2.5$ , 5.0, respectively. Note that the initial radial velocity is always  $V_0 = -1$ , corresponding to the ions entering the sheath with the Bohm velocity. Tables 7.1 to 7.2 summarize these ion paths, with starting position, initial trajectory angle, final angle, and total change in angle catalogued for each one. From the figures, one can see that not all ions pass by the corner unimpeded; a large number of the paths collide with the wall. In Tables 7.1 to 7.2 the trajectories that impact the corner are shown in black text, while those that clear the corner are shown in red. Additional plots and tables were created for  $U_0 = 7.5$  and 10.0; these plots can be found in Appendix E.

From Tables 7.1 to 7.2, one sees that for the 650 W upstream run, the maximum angle change for a particle that does not impact the wall is  $-22.6^\circ$ . This change in angle occurs for  $U_0 = 2.5$ ,  $\zeta_0 = -5$ . At  $U_0 = 5.0$ , the maximum angle change for an ion that clears the corner is  $-20.1^\circ$ . In the 650 W downstream run, (Figures 7.11 to 7.12 and Tables 7.3 to 7.4)) the maximum angle changes are  $-22.0$  and  $-11.1^\circ$  at  $U_0 = 2.5$  and 5.0, respectively. In the 200 W upstream run (Figures 7.13 to 7.14 and Tables 7.5 to 7.6), the maximum angle changes for the two starting axial velocities are  $-17.4$  and  $-20.4^\circ$ , while in the 200 W downstream run (Figures 7.13 to 7.14 and Tables 7.7 to 7.8) they are  $-17.9$  and  $-9.4^\circ$ .

Several conclusions can be drawn from these results. First, the higher the initial axial velocity, the farther upstream the ion can start without colliding with the wall. This suggests that a greater number of ions will be turned to higher angles by the sheath if the velocity is higher, since the “window” in which they can enter the sheath is larger. Second, the results show that higher velocities generally result in smaller changes in angle, since the particle spends less time being accelerated by the sheath. Therefore, there is a tradeoff between the *number* of ions that are accelerated by the sheath and the *total angle* change imparted to the ions.

Bounds on the initial axial position at which a particle can start and not impact the wall, as well as bounds on the angle change, can be estimated from the data in Figures 7.9 to 7.16 and Tables 7.1 to 7.8. For an SPT-70 operating at either 650 W or 200 W (with

a discharge voltage of 300 V or 250 V, respectively), the nominal velocity is between  $U_0 = 2.5$  and  $U_0 = 5.0$ . Looking across all four runs, for  $U_0 = 2.5$ , the initial starting point must be between  $\zeta = -5$  and  $-10$  for the particle to clear the corner, with a maximum angle change of about  $-20^\circ$ . For  $U_0 = 5.0$ , the initial starting point must be between  $\zeta = -10$  and  $-20$ , with a maximum angle change of between  $-10$  and  $-20^\circ$ .

Clearly, these maximum angle changes are not sufficient to explain the high velocity ions seen at angles greater than  $60^\circ$  in the experiment. Nonetheless, an angle change of  $10$  to  $20^\circ$  is not insignificant, and may have an impact on the evolution of the thruster plume. However, it should be noted that the “window” in axial location through which ions must enter the sheath is small. For the SPT-70, which has a Debye length on the order of  $10^{-4}$  m near the exit plane, the ions must pass within about  $1 \times 10^{-3}$  m (1 mm) of the corner. This corresponds to a surface area on the order of  $1 \times 10^{-4}$  m<sup>2</sup> (i.e., the cylindrical surface extending  $1 \times 10^{-3}$  m upstream of the exit plane, with a radius of 0.020 to 0.035 m, depending on whether one considers the inner or outer wall of the channel).

A quick estimation of the ion current density at the exit plane can be found by dividing the total current by the exit area of the thruster. This gives a density of 850 A/m<sup>2</sup> for the 650 W run, and a density of 310 A/m<sup>2</sup> for the 200 W run. Multiplying this by the surface area of the “window,” the total current that can be accelerated by the sheath to angles from  $10$  to  $20^\circ$ , is on the order of  $1 \times 10^{-1}$  A in the 650 W run, and  $1 \times 10^{-2}$  A in the 200 W run, which is about five percent of the current in the 650 W run, and one percent of the current in the 200 W run.

Although this estimate suggests that the percentage of ions that are influenced by the sheath is small, it should be kept in mind that the total percentage of ion current seen at high angles is also small. This was seen in both the experiments and in the simulation. Therefore, it is possible that the sheath acceleration could have an impact on the high angle ion trajectories. However, since the change in angle would only be on the order of  $10$  to  $20^\circ$ , another mechanism must exist to provide the additional  $40$  to  $50^\circ$  needed to see ions at  $60$  to  $70^\circ$ .

Table 7.1: Trajectories through sheath,  $U_0 = 2.5$ , 650 W upstream run.

$\zeta_0$	$\rho_0$	$\theta_0$ [°]	$\theta_f$ [°]	$\Delta\theta$ [°]
-50	4.2	-21.8	-46.1	-24.3
-45	4.5	-21.8	-47.9	-26.1
-40	4.8	-21.8	-49.1	-27.3
-35	4.9	-21.8	-49.6	-27.8
-30	5.0	-21.8	-50.0	-28.2
-25	5.0	-21.8	-50.2	-28.4
-20	5.1	-21.8	-50.3	-28.5
-15	5.1	-21.8	-50.5	-28.7
-10	5.1	-21.8	-50.6	-28.8
-5	5.2	-21.8	-44.4	-22.6

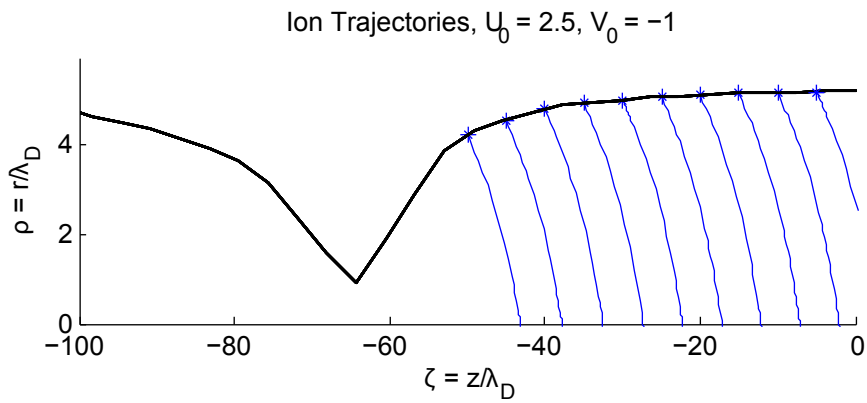
Figure 7.9: Trajectories from the corner sheath model,  $U_0 = 2.5$ , 650 W upstream run.

Table 7.2: Trajectories through sheath,  $U_0 = 5.0$ , 650 W upstream run.

$\zeta_0$	$\rho_0$	$\theta_0$ [°]	$\theta_f$ [°]	$\Delta\theta$ [°]
-50	4.2	-11.3	-28.8	-17.5
-45	4.5	-11.3	-29.9	-18.6
-40	4.8	-11.3	-30.4	-19.1
-35	4.9	-11.3	-30.7	-19.4
-30	5.0	-11.3	-31.1	-19.8
-25	5.0	-11.3	-31.1	-19.8
-20	5.1	-11.3	-31.3	-20.0
-15	5.1	-11.3	-31.4	-20.1
-10	5.1	-11.3	-22.2	-10.9
-5	5.2	-11.3	-14.8	-3.4

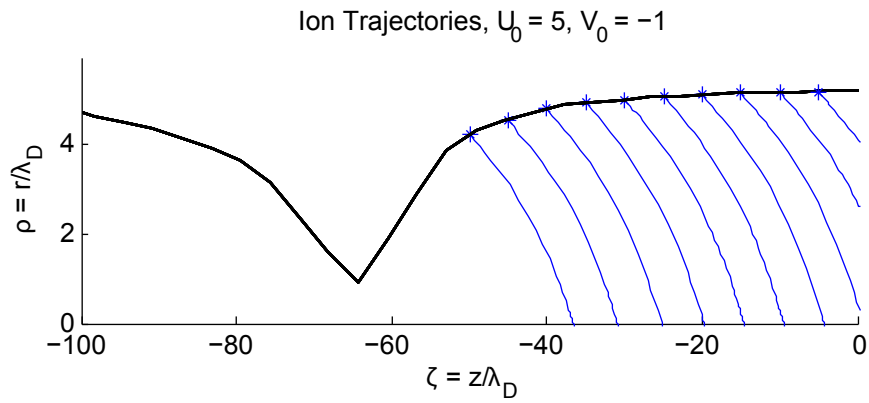
Figure 7.10: Trajectories from the corner sheath model,  $U_0 = 5.0$ , 650 W upstream run.

Table 7.3: Trajectories through sheath,  $U_0 = 2.5$ , 650 W downstream run.

$\zeta_0$	$\rho_0$	$\theta_0$ [°]	$\theta_f$ [°]	$\Delta\theta$ [°]
-50	4.7	-21.8	-48.3	-26.5
-45	4.6	-21.8	-47.8	-26.0
-40	4.5	-21.8	-47.3	-25.5
-35	4.4	-21.8	-46.7	-24.9
-30	4.4	-21.8	-46.2	-24.4
-25	4.3	-21.8	-45.7	-23.9
-20	4.2	-21.8	-45.2	-23.5
-15	4.2	-21.8	-44.9	-23.1
-10	4.1	-21.8	-44.9	-23.1
-5	4.1	-21.8	-43.8	-22.0

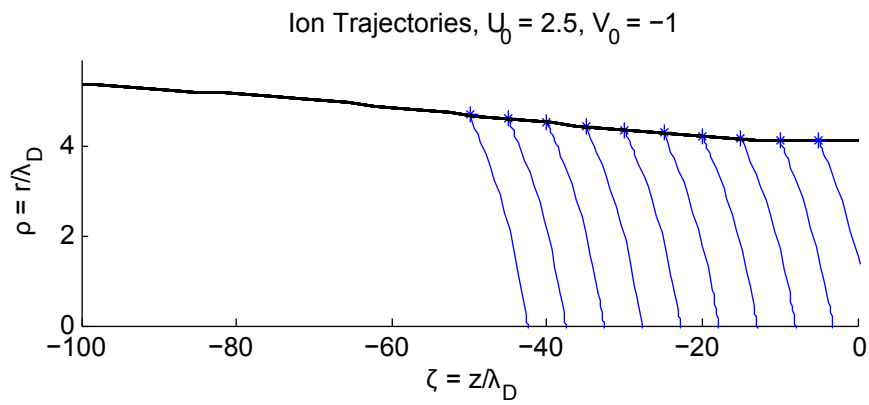
Figure 7.11: Trajectories from the corner sheath model,  $U_0 = 2.5$ , 650 W downstream run.

Table 7.4: Trajectories through sheath,  $U_0 = 5.0$ , 650 W downstream run.

$\zeta_0$	$\rho_0$	$\theta_0$ [°]	$\theta_f$ [°]	$\Delta\theta$ [°]
-50	4.7	-11.3	-28.7	-17.4
-45	4.6	-11.3	-28.4	-17.1
-40	4.5	-11.3	-27.8	-16.5
-35	4.4	-11.3	-27.5	-16.2
-30	4.4	-11.3	-27.1	-15.8
-25	4.3	-11.3	-26.8	-15.5
-20	4.2	-11.3	-26.4	-15.1
-15	4.2	-11.3	-26.4	-15.1
-10	4.1	-11.3	-22.4	-11.1
-5	4.1	-11.3	-15.2	-3.9

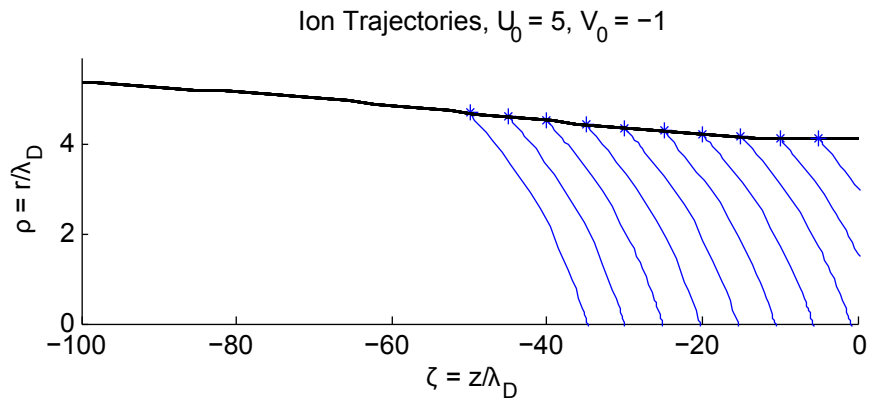
Figure 7.12: Trajectories from the corner sheath model,  $U_0 = 5.0$ , 650 W downstream run.

Table 7.5: Trajectories through sheath,  $U_0 = 2.5$ , 200 W upstream run.

$\zeta_0$	$\rho_0$	$\theta_0$ [°]	$\theta_f$ [°]	$\Delta\theta$ [°]
-50	4.7	-21.8	-48.7	-26.9
-45	4.8	-21.8	-48.9	-27.1
-40	4.9	-21.8	-49.4	-27.6
-35	4.9	-21.8	-49.7	-27.9
-30	5.0	-21.8	-50.0	-28.2
-25	5.1	-21.8	-50.4	-28.6
-20	5.1	-21.8	-50.6	-28.8
-15	5.2	-21.8	-50.8	-29.0
-10	5.2	-21.8	-51.0	-29.1
-5	5.3	-21.8	-39.2	-17.4

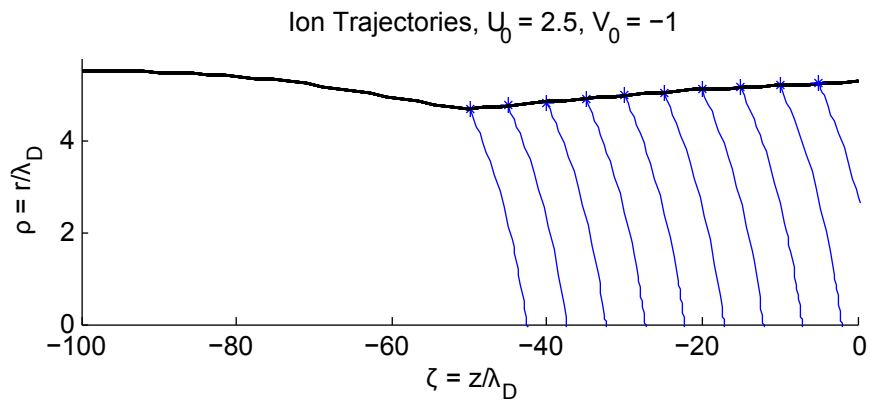
Figure 7.13: Trajectories from the corner sheath model,  $U_0 = 2.5$ , 200 W upstream run.

Table 7.6: Trajectories through sheath,  $U_0 = 5.0$ , 200 W upstream run.

$\zeta_0$	$\rho_0$	$\theta_0$ [°]	$\theta_f$ [°]	$\Delta\theta$ [°]
-50	4.7	-11.3	-30.1	-18.8
-45	4.8	-11.3	-30.4	-19.0
-40	4.9	-11.3	-30.5	-19.2
-35	4.9	-11.3	-30.9	-19.6
-30	5.0	-11.3	-31.2	-19.9
-25	5.1	-11.3	-31.4	-20.0
-20	5.1	-11.3	-31.6	-20.3
-15	5.2	-11.3	-31.7	-20.4
-10	5.2	-11.3	-20.6	-9.3
-5	5.3	-11.3	-13.9	-2.6

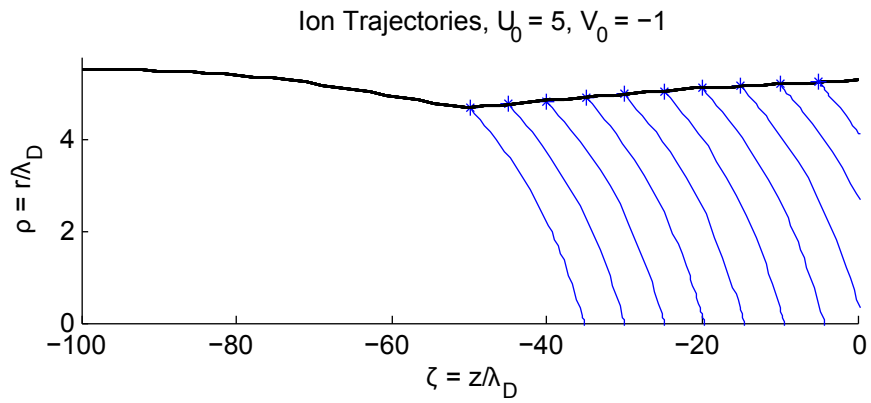
Figure 7.14: Trajectories from the corner sheath model,  $U_0 = 5.0$ , 200 W upstream run.

Table 7.7: Trajectories through sheath,  $U_0 = 2.5$ , 200 W downstream run.

$\zeta_0$	$\rho_0$	$\theta_0$ [°]	$\theta_f$ [°]	$\Delta\theta$ [°]
-50	5.15	-21.8	-50.6	-28.9
-45	5.10	-21.8	-50.4	-28.6
-40	5.08	-21.8	-50.4	-28.6
-35	5.08	-21.8	-50.3	-28.5
-30	5.08	-21.8	-50.3	-28.5
-25	5.08	-21.8	-50.3	-28.5
-20	5.08	-21.8	-50.3	-28.5
-15	5.09	-21.8	-50.4	-28.6
-10	5.11	-21.8	-51.5	-28.7
-5	5.12	-21.8	-39.7	-17.9

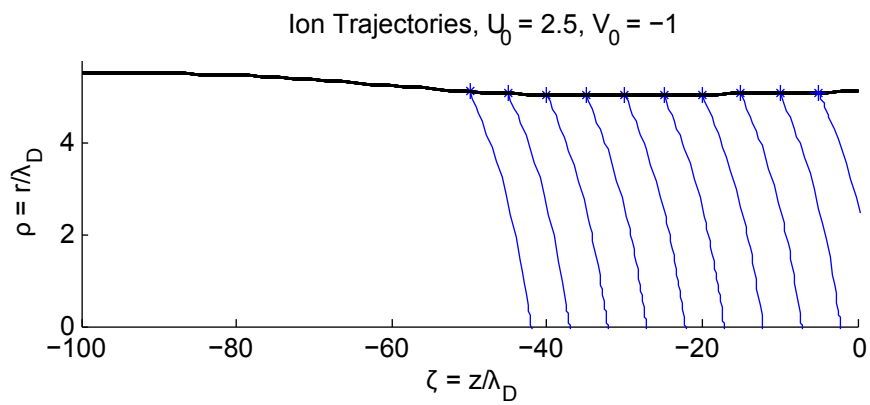
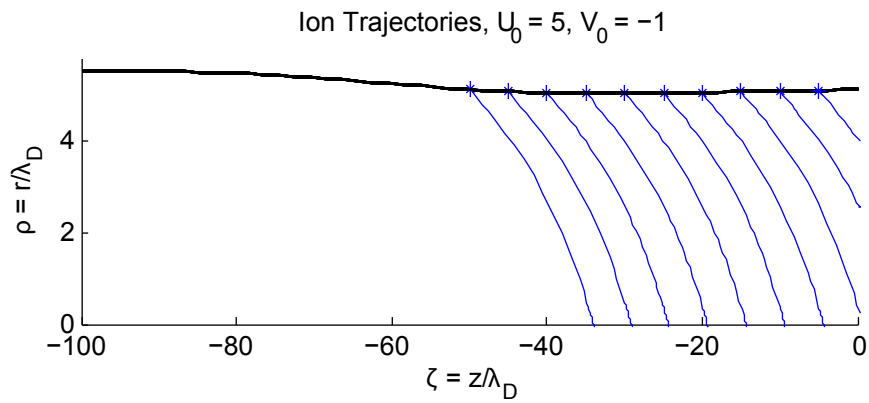
Figure 7.15: Trajectories from the corner sheath model,  $U_0 = 2.5$ , 200 W downstream run.

Table 7.8: Trajectories through sheath,  $U_0 = 5.0$ , 200 W downstream run.

$\zeta_0$	$\rho_0$	$\theta_0$ [°]	$\theta_f$ [°]	$\Delta\theta$ [°]
-50	5.15	-11.3	-31.2	-19.9
-45	5.10	-11.3	-31.1	-19.8
-40	5.08	-11.3	-31.2	-19.9
-35	5.08	-11.3	-31.0	-19.7
-30	5.08	-11.3	-31.1	-19.8
-25	5.08	-11.3	-31.1	-19.8
-20	5.08	-11.3	-31.3	-20.0
-15	5.09	-11.3	-31.2	-19.9
-10	5.11	-11.3	-20.7	-9.4
-5	5.12	-11.3	-14.0	-2.7

Figure 7.16: Trajectories from the corner sheath model,  $U_0 = 5.0$ , 200 W downstream run.

## Chapter 8

# Comparison of Experimental and Simulated Results

As discussed in Chapters 3 and 4, the purpose of running the simulations was to gain insight into the physical phenomena leading to the results seen in the experiments, in particular the formation of the central ion jet and the generation of high energy, high angle ions. In this section, the experimental and simulated data will be compared, an assessment of the simulations' ability to match the observations will be made, and conclusions regarding the ion trajectory physics will be drawn.

Before discussing the data in-depth, a few general comments about data sets will be made. As previously discussed, it is important to recall that for the simulated probe traces, the simulated ion trajectories from HPHall are projected along straight line paths from the exit plane to a given axial location. No physical interactions between particles, such as charge exchange or elastic scattering collisions, are modeled. Additionally, plasma effects are not included in the simulated probe data. For instance, a deficit of ion density near the thruster center, as well as a buildup of ions along the thruster centerline (as is the case during jet formation), could alter the potential profile.

The effects of not modeling the collisions and plasma effects are apparent, for example, in the simulated Faraday and ExB probe results. In the simulated Faraday probe data, there is a narrow peak in the center of the trace that has a transverse extent that stays approximately constant as the axial distance is increased. However, in the experimental data, the central peak is tall and narrow near the thruster, but becomes considerably shorter and wider at larger axial distances. If one compares the experimental ion current density on centerline for the 200 W experimental case to the simulated 200 W upstream case and the

200 W downstream case, one finds fairly good agreement at an axial distance of 50 mm. At 50 mm, the values of ion current density for these three cases are 900, 700, and 1000 A/m<sup>2</sup>, respectively. However, at 100 mm, the simulated cases both show a value of about 1000 A/m<sup>2</sup>, while the experimental value is about 250 A/m<sup>2</sup>. The reason for this discrepancy is that in the simulation, there is no mechanism that causes the ions to disperse.

Similarly, in the simulated ExB data, the peaks are very narrow, and match up almost exactly with the channel projection. In contrast, the actual experimental peaks are considerably wider, often with considerable current density due to ions that cannot have traveled in straight line paths to the probe. Collisions, external fields, and other effects that are not accounted for in the simulated probe traces could explain some of the spreading of the current density peaks in the experimental results, since these effects could produce ions with slightly different trajectory angles than they started with.

## 8.1 Formation of the Central Jet

In Chapter 5, Faraday probe data was presented that showed that the ion ring to jet transition occurred at an axial distance between 15 to 30 mm in the 200 W case, and between 25 and 50 mm in the 650 W case. Looking at the simulated probe data presented in Figure 6.27, one sees that in the 650 W upstream model, the beam has not yet fully transitioned from ring to jet, while in the 650 W downstream model, it has. This suggests that the 650 W upstream model does a more accurate job of representing the actual transition from ring to jet, since in the experiment the transition occurred downstream of  $z = 25$  mm. In contrast, the 200 W downstream model, in which the beam has already converged on itself by 25 mm, seems to be a better match for the experimental data than the 200 W model.

As was discussed in Chapter 5, the experimental ExB data suggest that the transition occurs between 75 and 150 mm at 200 W, and between 75 and 100 mm at 650 W. Also, as was mentioned in Chapter 5, the discrepancy between the Faraday probe convergence distance and the ExB probe convergence distance in the experiment is likely due to the different angles of acceptance of the two devices. In the experimental data, when the beam had converged on itself to form the central jet, a peak centered at  $r = 0$  mm was present in the 0° ExB traces. In the simulated ExB probe data, no such central peak is seen. For example, in the 200 W upstream model at 100 mm, two distinct peaks are seen at 0°, while

one does see a large peak on centerline in the  $10^\circ$  trace. This shows that while the central jet seen in the experiment is made up primarily of axially moving ions (as was discussed in Section 5.1), the simulated central jet is made up of ions moving at higher angles. This difference will be discussed further in Section 8.2. One observation that can be made from comparing the actual and simulated probe data is that while the experimental ExB data clearly shows the region over which the beam transition is occurring, the location is not readily apparent in the simulated ExB data.

In Section 6.2, it was suggested that a small degree of asymmetry in the plasma potential could provide the radial acceleration necessary to facilitate the formation of the central jet. Figures 6.21 to 6.24 showed that the asymmetry in the potential was either upstream or downstream of the exit plane, depending on whether the case was an “upstream” or “downstream” case. Although it is difficult to tell about convergence from the simulated ExB data, the simulated Faraday probe data show that the experimental distances of convergence matched those of the 200 W downstream model and the 650 W upstream model. This shows that as far as convergence is concerned, the asymmetry in the potential profiles is sufficient to generate the same results as the experiment.

## 8.2 Angles of Ion Trajectories within the Near Field Plume

The central jet is made up of ions with a range of trajectory angles. In both the 200 W and 650 W ExB measurements, the central jet has started to form by  $z = 100$  mm. For the 200 W, 100 mm measurements, most of the ion current density near the thruster centerline ( $r = 0$  mm), is due to ions traveling at  $0$  to  $10^\circ$ . This is also true at 150 mm axial distance. In the 200 W upstream simulation, most of the ion current density at 100 mm on centerline is due to ions traveling at  $10^\circ$ , as is true at 150 mm. The 200 W downstream simulated probe data shows the same results. So at 200 W, the results seem to match fairly well (most of the centerline ions have trajectories between  $0$  and  $10^\circ$ ), although the simulated ExB results do not show any  $0^\circ$  ions on centerline. This is expected due to the fact that the simulated results are simply straight line projections from the outer boundary of the simulation domain.

At 650 W, 100 mm, most of the actual ion current density along the thruster centerline is due to ions with trajectory angles from  $0$  to  $10^\circ$ , while at 150 mm, most of it is

due to ions with purely axial trajectories. In the 650 W upstream model, most of the current density at 100 mm is due to ions traveling at  $10^\circ$ , and the same is true at 150 mm. The 650 W downstream model also shows that ions near the centerline have  $10^\circ$  trajectory angles at both 100 mm and 150 mm. The 650 W experimental results thus match the simulated results fairly well, except the simulated results show no purely axial ions within the central jet (as was true with the 200 W data).

It is not surprising that there are no  $0^\circ$  ions in the simulated central jet, namely that if an ion reaches the thruster centerline, it must be traveling at an angle, yet there is nothing in the simulation that can cause its radial velocity to decrease as it nears the centerline. So, in the simulation, the ion will retain the same angle as it left the HPHall domain. However, since the experiment shows that at both 200 W and 650 W there is a substantial ion current density associated with  $0^\circ$  ions, there must be a mechanism for decreasing an ion's trajectory angle as it nears the centerline. The buildup of ions near the centerline could definitely be a factor here, since as the ions move inward to form the jet, they form an area of relatively high ion density. Since electrons from the cathode can also easily reach this area (the magnetic field is low on the thruster centerline), this leads to a higher overall (quasi-neutral) plasma density on the centerline. A higher plasma density,  $n_i = n_e = n$ , would lead to a higher potential, according to the barometric law:  $\phi = (kT_e/e)\ln(n)$ . This high potential region could then decrease an ion's radial velocity as it nears the centerline.

In addition to ions that end up near the thruster centerline and form the jet, there are ions that form the more diffuse plume around the jet as well. One of the more intriguing conclusions from the experimental ExB results was that at angles above  $10^\circ$ , more ion current density was attributable to ions that had moved radially inward, crossing the thruster centerline in the process, than was attributable to ions that had an outward component of radial velocity. This was also seen in the simulated data for ions with trajectory angles between  $10$  and  $30^\circ$ . Naturally, the central jet was thought to be due to ions moving with an inward radial velocity component, but what was not necessarily expected was that most of the ion current density far from the central jet would be also be due to inward moving ions. Measurements taken by Fife on the SPT-70 [14] show that there is indeed an area of higher potential that forms along the centerline of the thruster.

One might be tempted to say that the higher current density due to inward moving ions is not due to the fact that there are more inward moving ions being produced, but

rather that these ions are moving into a smaller area. However, as was pointed out in Section 6.3, although the smaller area does have an effect, the ion current data produced in the simulation, before dividing by the area, show that there is still a discrepancy between the inward and outward moving ions. As discussed in Section 6.3.2, there are about twice as many inward moving ions at 50 mm,  $10^\circ$ , for example. This suggests that geometry effects (i.e., symmetric beam expansion) account for about 1/3 of the current in the Hall thruster plume, and that design factors (i.e., internal magnetic field and potential profile) account for the rest.

As previously discussed, analysis of the simulated probe data found that asymmetry in the simulated plasma potential leads to asymmetry in the ion density, with more ions being pushed towards the thruster centerline than away from it. This was seen in the averaged HPHall data, for all simulated cases. What has not been discussed yet is the reason for the asymmetry in the simulated plasma potential. As mentioned in Section 3.3.2, the plasma potential contours should primarily follow the magnetic field lines, since the mobility of electrons parallel to the field lines is high, while the mobility perpendicular to the field lines is low. Looking at Figures 3.6 and 3.7, it is clear that the magnetic field lines in the SPT-70 hall thruster are not symmetric about the channel centerline. An asymmetric magnetic field leads to a slightly asymmetric potential, which the simulation results shows is sufficient to lead to the formation of the central jet, as well as a greater number of ions being accelerated inward than outward. This suggests that the central jet formation can be controlled to some extent by the design of the thruster.

### **8.3 High Velocity High Angle Ions**

The other major Hall thruster plume phenomenon investigated in this study was the presence of high velocity ions at high angles off the thruster centerline. These ions have energies near the primary beam energy, but are found at angles up to  $80^\circ$  off the thruster centerline. These ions were seen in both the experimental ExB traces and the RPA traces. From the RPA traces, it was possible to determine the proportion of these ions relative to ions with lower energies.

The 200 W experimental data taken with the RPA revealed a peak at the primary beam energy for angles from 0 to  $80^\circ$ . The height and width of the peak varied with RPA

angle: at  $0^\circ$ , decreasing in height and becoming slightly wider as the angle was increased. For all angles, the high energy peak was centered at about 225 V, and the width of the peak was less than 50 V. Additionally, as the angle was increased, a peak centered at about 30 V started to grow in height.

Looking at the HPHall trajectories in the 200 W upstream simulation, one sees acceptable agreement with the experimental data until  $30^\circ$ . At  $40^\circ$ , the high energy ion peak essentially disappears, and at angles higher than  $40^\circ$ , there are almost no ions with energies above 100 eV/q. Overall, the matching between the 200 W upstream model and the 200 W experimental data is poor. Looking at the 200 W downstream case, one sees fairly good agreement with the experimental data until  $45^\circ$ . At this point, the high velocity peak seems to merge into the rest of the distribution, and at  $55^\circ$  there is no discernable peak in the distribution, just one broad “mound” that extends from 0 eV/q to about 275 eV/q. This trend continues for angles above  $55^\circ$  (with one exception at  $60^\circ$ , which was discussed in Section 6.4). The simulated results therefore show ions at 225 eV, but do not show a peak at this location. So the 200 W downstream model is better, but it still does not match the actual data at high angles.

Comparing the RPA experimental data at 650 W to the data from the simulated 650 W upstream case shows that the two data sets agree fairly well between  $0$  and  $30^\circ$ . At  $40^\circ$ , a clear peak in the experimental data can be seen at about 270 eV/q, whereas in the simulated case there is a small, very broad peak in the energy distribution. Whereas the experimental data shows a peak at the primary potential at angles out to  $60^\circ$ , the simulated data shows no such structure at angles greater than  $40^\circ$ . The 650 W downstream case does not do a much better job of matching the experimental data above  $30^\circ$ . Although it shows high energy peaks out to  $75^\circ$ , the peaks are much broader than in the experimental traces. Rather than a peak with a width of about  $30^\circ$ , centered at 270 V, a peak with a width of about 200 eV/q, centered at about 225 eV/q, is seen in the 650 W downstream data.

To understand what is causing the shapes of the simulated RPA traces, one must examine the plasma potential, electric field, and ion density distributions presented in Section 6.2. As was discussed in this section, in the “upstream” models the axial electric field is large relative to the radial electric field, except for a region within a few millimeters of the corners of the channel. Also, the region of high axial electric field occurs upstream of the exit plane. So, for an ion to obtain a kinetic energy that is close to the primary energy,

it must be created upstream of this region, and then be accelerated through the high field region. The only ions that can reach high angles in this situation are those that are born downstream of the region of high axial electric field, hence the tall low energy peaks and lack of high energy ions at high angles in the 650 and 200 W upstream simulated data.

In the “downstream” models, in contrast, the radial electric field was found to be comparable in magnitude to the axial electric field throughout most of the region near the exit plane. Near the corners of the channel, the magnitude of the radial electric field was almost an order of magnitude higher than the maximum value of the axial electric field in the simulation domain. This allows high energy ions to be created at all angles off of the thruster centerline. The reason that the energy distribution is mound-shaped at high angles is because the potential drop is spread out over a large axial distance. An ion that is created upstream of the potential drop can be accelerated out to high angles just as easily as an ion that is created in the middle of the potential drop.

If one compares the axial electric field in the 650 W downstream model to the 200 W downstream model (Figure 6.7 vs. 6.17), one sees that the potential drop, and thus the region of maximum axial electric field, occurs over a slightly shorter axial distance. This difference is reflected in the simulated RPA traces; in the 200 W case, at 70 to 80°, the ion energies span from 0 to 275 eV/q, while in the 650 W case, the distribution appears to be centered at about 200 eV/q and spans from about 100 to 300 eV/q. Since the potential drop occurs over a slightly shorter region in the 650 W downstream case, the distribution is slightly narrower and more peaked.

Clearly, none of the HPHall runs, even those in which a significant portion of the potential drop was moved downstream of the exit plane, do a particularly good job replicating the data seen in the experiment. Even though some primary energy ions are seen at high angles, these ions do not result in a peak in the energy distribution. Even if the erosion of the actual thruster were to be taken into account, the eroded region does not extend far enough back in the channel for the 650W and 200W upstream simulations to produce primary energy ions at high angles.

To reproduce the results seen in the experiment, the potential drop would need to look similar to the right-most drawing in Figure 8.1, i.e., the axial distance over which it occurs would have to be small, and most of the potential drop would need to occur downstream of the exit plane. In this case, any ion created upstream of the exit plane would

be accelerated through the full potential drop of the thruster. Most of the ions would be accelerated axially, since the highest density of ions would be along the centerline, where the electric field would be primarily axial. However, ions originating near the corner could be accelerated out to high angles, and because of the shape of the field at the corner, would be accelerated primarily in the radial direction, through the full potential drop of the thruster.

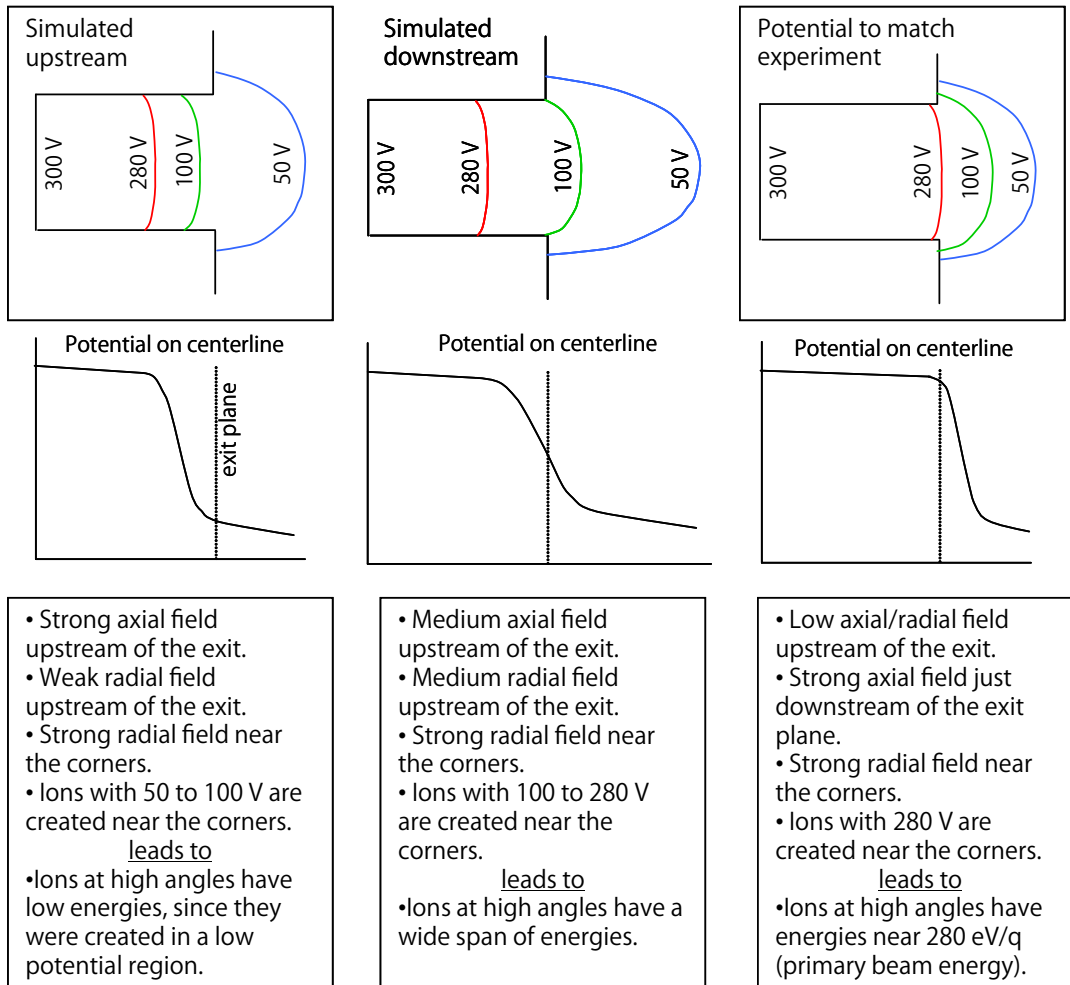


Figure 8.1: Potential profiles from HPHall versus the theoretical profile needed to match the experiment. The right-most potential profile could accelerate ions to high angles and high velocities, since ions created near the corner would be created in a high-potential region.

If the potential drop did look like the one pictured in Figure 8.1, at low angles off the thruster centerline, one would expect to see a large, high energy peak in the simulated data, as is seen in the experimental data. As the angle is increased, one would expect to see the peak get shorter in magnitude, but also become more narrow. The peak would become

more narrow due to the potential drop occurring over a shorter distance. At all angles, one would expect to see very few low energy ions in the simulated data, because most of the ions would be created upstream of the potential drop, even those that reach high angles. The lack of low energy ions in the simulated traces would not match the experimental results, since a large, low energy peak, as well as a tail of mid-range energy ions was seen in the experimental data. However, as was noted earlier, the version of HPHall that was used in the present study does not take into account the effects of charge exchange collisions or elastic scattering collisions. Collision phenomena would increase the number of low energy and mid-range ions present in the traces at high angles [48].

Despite the best efforts of the author (over 100 different HPHall cases were run), the mobility coefficients and transition locations could not be sensibly changed in such a way that resulted in a simulated potential profile that looks like the one pictured in Figure 8.1. This does not necessarily mean that the potential profile in Figure 8.1 is non-physical. In fact, recent internal measurements of a 6kW laboratory Hall thruster by B. M. Reid show that for this thruster most of the potential drop does occur downstream of the thruster exit plane [10, 35]. Accurate internal measurements of the SPT-70 thruster potential profile are not, to the author's knowledge, available, due to the difficulty of probing a small diameter thruster (the 6 kW thruster used in Reid's experiments has a diameter about 10 times larger than the SPT-70 thruster).

One of the conclusions that can be drawn from the comparison of the RPA experimental and simulated data sets is that if high angle ions are indeed created by a potential profile that looks like the one in Figure 8.1, then HPHall is doing a poor job of modeling the potential field of the SPT-70. Since the magnetic field was directly measured, the error in the potential profile is likely due to the electron-mobility sub-model. The way the electron mobility has been treated in HPHall has been the subject of much scrutiny [51, 52], however, the creation of a new electron mobility sub-model was beyond the scope of this thesis.

By applying the corner sheath model, it was possible to determine what effect the non-neutral sheath has on ion trajectories. Overall, the model results showed that the change in angle that could be achieved ranged from 10 to 20°, depending on the axial location at which an ion entered the sheath, and its velocity. Although this is a significant angle change and should not be discounted in future work, it is not enough to fully explain the high velocity, high angle ion peaks seen in the experimental data. Nor does it account for the

discrepancy between the simulated HPHall RPA traces and the actual RPA data.

## Chapter 9

# Conclusions and Recommendations

The research detailed in this thesis provides several contributions to the field of Hall thruster near-field and plume research. In addition to providing detailed measurements of the ion current density and ion velocities within the near-field region, this research offers insight into the specific physical mechanisms that govern the development of high velocity ion trajectories. Ultimately, the information contained in this thesis can be applied to the development of better Hall thruster simulations and thruster integration techniques.

### 9.1 Conclusions

In the investigation of the central jet, several notable conclusions were drawn from both the experimental and numerical data. The jet was found to be made up of ions traveling at angles between  $0$  and  $10^\circ$  off of the thruster centerline. The simulated data suggested that ions are able to obtain trajectory angles of about  $10^\circ$  due to the shape of the plasma potential. The experimental data show that as the ions converge on the thruster centerline to form the jet, they experience a decrease in radial velocity, producing a jet that not only contains ions with  $10^\circ$  trajectories, but also a substantial population of ions with purely axial  $0^\circ$  trajectories. To what degree this deceleration in the radial direction can be attributed to collisions, versus an elevated potential on the thruster centerline, is a subject for future study.

The high velocity trajectory investigation also showed a significantly greater proportion of inward moving ions versus outward moving ions, thus revealing that the beam development is not strictly due to symmetrical expansion from the channel. This observation was made for both the experimental and simulated data, and was attributed to a

plasma potential profile that is slightly asymmetric about the channel centerline. This is in line with previous experimental findings which showed how the shape of the magnetic field could influence the performance parameters of a Hall thruster [21]. In this previous study, it was seen that the internal magnetic field could have a large impact on the overall beam divergence; however, ion trajectories were not directly tracked in this previous case, nor was a direct link made between the magnetic field shape, the potential profile, and the ensuing ion trajectories, as was done here.

Additionally, a large amount of headway was made in discovering the mechanism that creates high angle, high energy ion trajectories. Because the theoretical potential profile shown in Figure 8.1 would explain the presence of these ions in the experimental data, and could match the RPA measurements if CEX and elastic scattering were taken into account, it is considered the most promising explanation for the high angle, high energy ions. Oscillations, at least those of the “breathing mode” and “transit-time” variety, are not likely to be the cause of these ions because the peaks and troughs in the potential oscillations do not line up with the peaks and troughs in the ion density oscillations. Therefore, the potential oscillations are more likely to broaden peaks in the energy spectrum, rather than generate them. Additionally, although the corner sheath model suggests that the sheath can increase ion trajectory angle by 10 to 20°, the sheath alone is not enough to create the high angle trajectories seen in the experiment.

One interesting implication of the study of the high angle, high energy ions is that these ions seem to be a direct reflection of the internal physics of the Hall thruster, and in particular the location of the acceleration region. The study showed what the RPA profiles would look like, given the potential profiles seen in the simulated cases. This suggests that RPA measurements could be treated as “signatures” for the internal shape of the potential. Since RPA measurements in the far-field of the thruster are much easier to obtain than internal measurements of potential, this might be a logical first step for any researcher seeking to determine what the potential profile looks like inside a given thruster.

## 9.2 Recommendations for Future Work

In terms of future study of the central jet, the next step to take is to determine to what degree collisions and the elevated plasma density along the thruster centerline affect the radial

deceleration of ions. Charge exchange collisions have already been implemented in HPHall, although some work is required to get them running more efficiently. Elastic scattering could be implemented in the code as well. An experimental survey of the potential on the thruster centerline would be fairly easy to conduct, to determine whether the rise in potential at the thruster centerline due to converging ions is large enough to produce the deceleration seen in the experiment.

In terms of future investigations of the high angle, high energy ions, there are a few approaches that could be taken to prove that the shape of the internal/near-field potential profile of the thruster does in fact look like the theoretical case required to produce them. One way would be to take internal measurements of an SPT-70 Hall thruster. Due to the small size of the SPT-70, it would be a challenge to take accurate internal measurements of the thruster without significantly disturbing the plasma. Another method would be to add a better electron mobility sub-model to HPHall, or to create a model independent of HPHall that includes accurate mobility physics. However, even if this is done, there is no guarantee that this will result in the desired potential profile. Probably the simplest approach is to do an extensive ion trajectory survey of a Hall thruster for which internal data is readily available. If high angle, high energy ions were found, combined with a measured potential profile that looks like the one in Figure 8.1, then that would be strong evidence for the conclusions made here.

Future SPT-70 measurements, a better electron mobility model, or HPHall studies and ion trajectory measurements on thrusters for which internal data is available, could reveal that the internal/near-field potential profile is capable of creating the RPA traces seen in the experiment. If this is the case, then one recommendation to Hall thruster modelers is to consider ion trajectory data, such as RPA measurements, when validating one's code. Up until now, Hall thruster codes have primarily been developed and tested by comparing the performance parameters such as thrust and specific impulse to experimental values. (One exception is an effort being made at the Air Force Research Laboratory to match HPHall outputs to internal LIF velocity measurements and external RPA measurements). However, as is suggested by the results of the present study, this method of validation is limited when it comes to the prediction of accurate ion trajectories by the code. If one's goal is to create a fully-integrated Hall thruster code, which combines internal, near-field, and far-field physics, it is important to understand how ion trajectories reflect the plasma parameters inside the

thruster channel.



## **Appendix A**

# **Additional Experimental ExB Data**

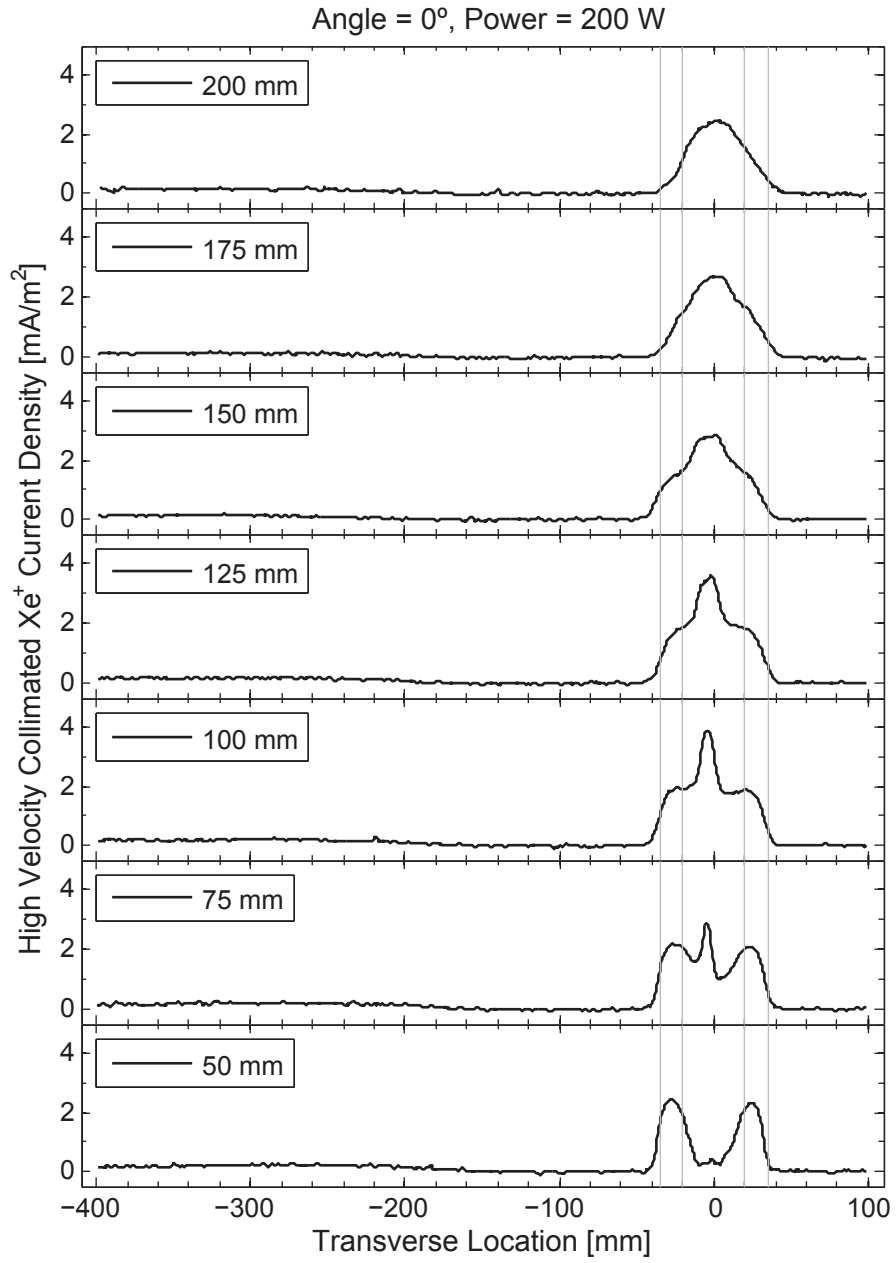


Figure A.1: ExB results, 200 W case, at 0°.

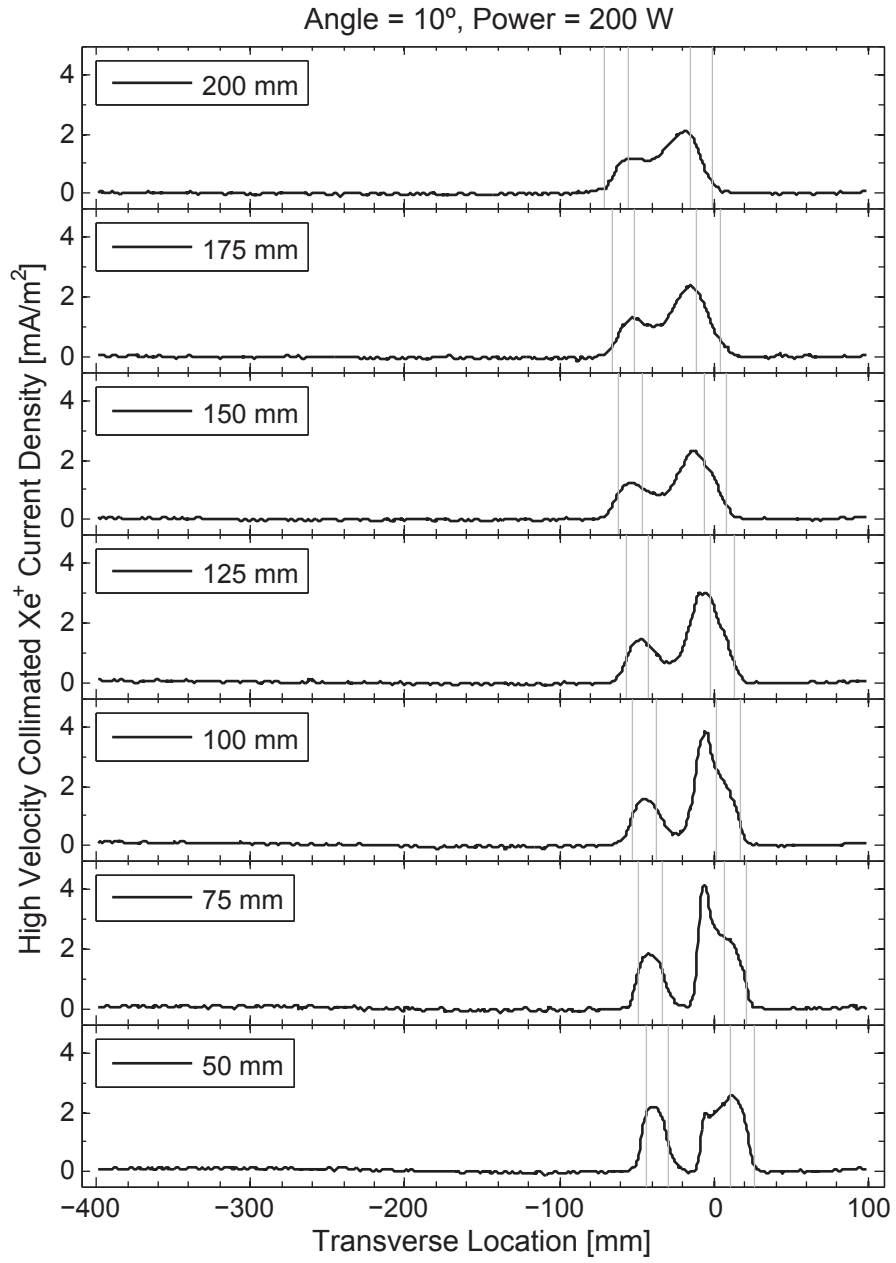


Figure A.2: ExB results, 200 W case, at 10°.

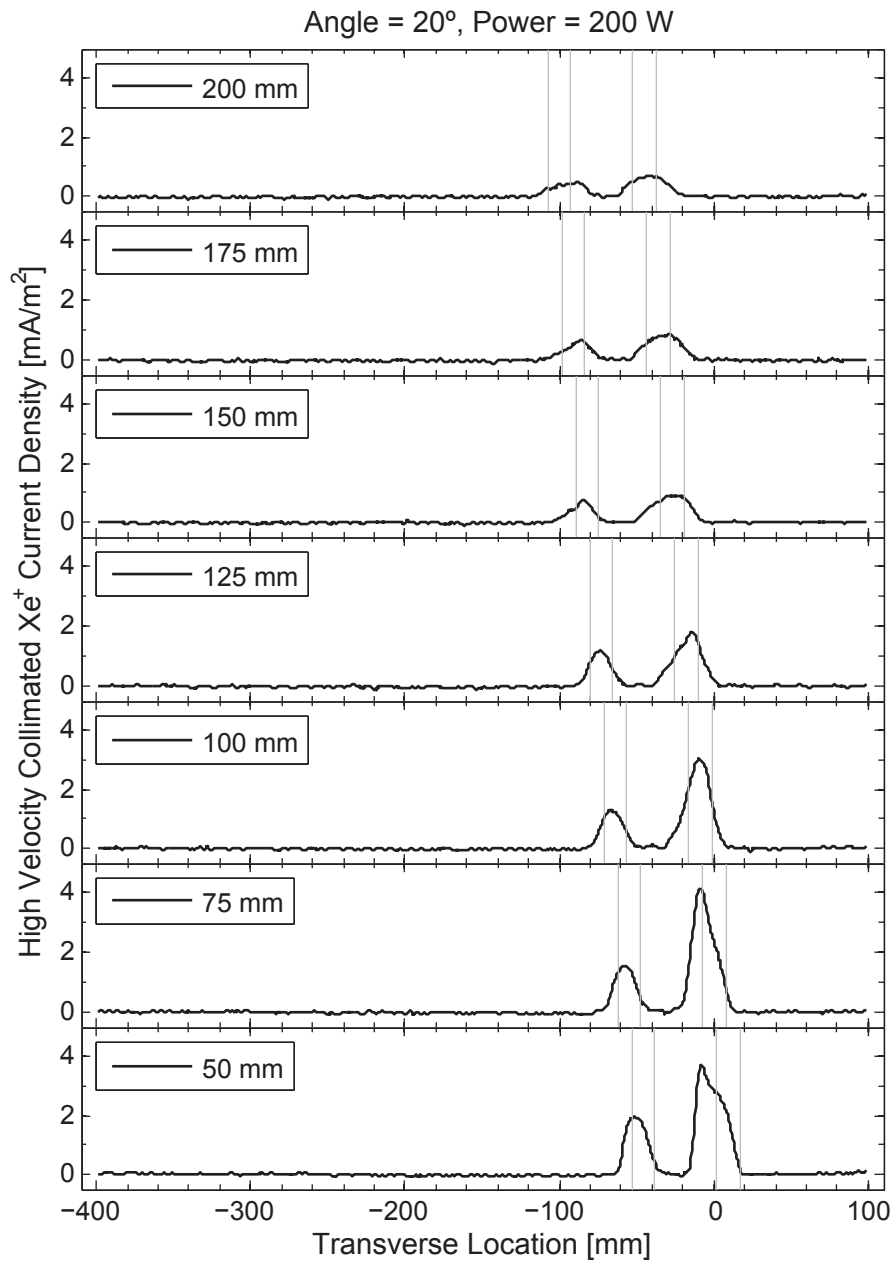


Figure A.3: ExB results, 200 W case, at 20°.

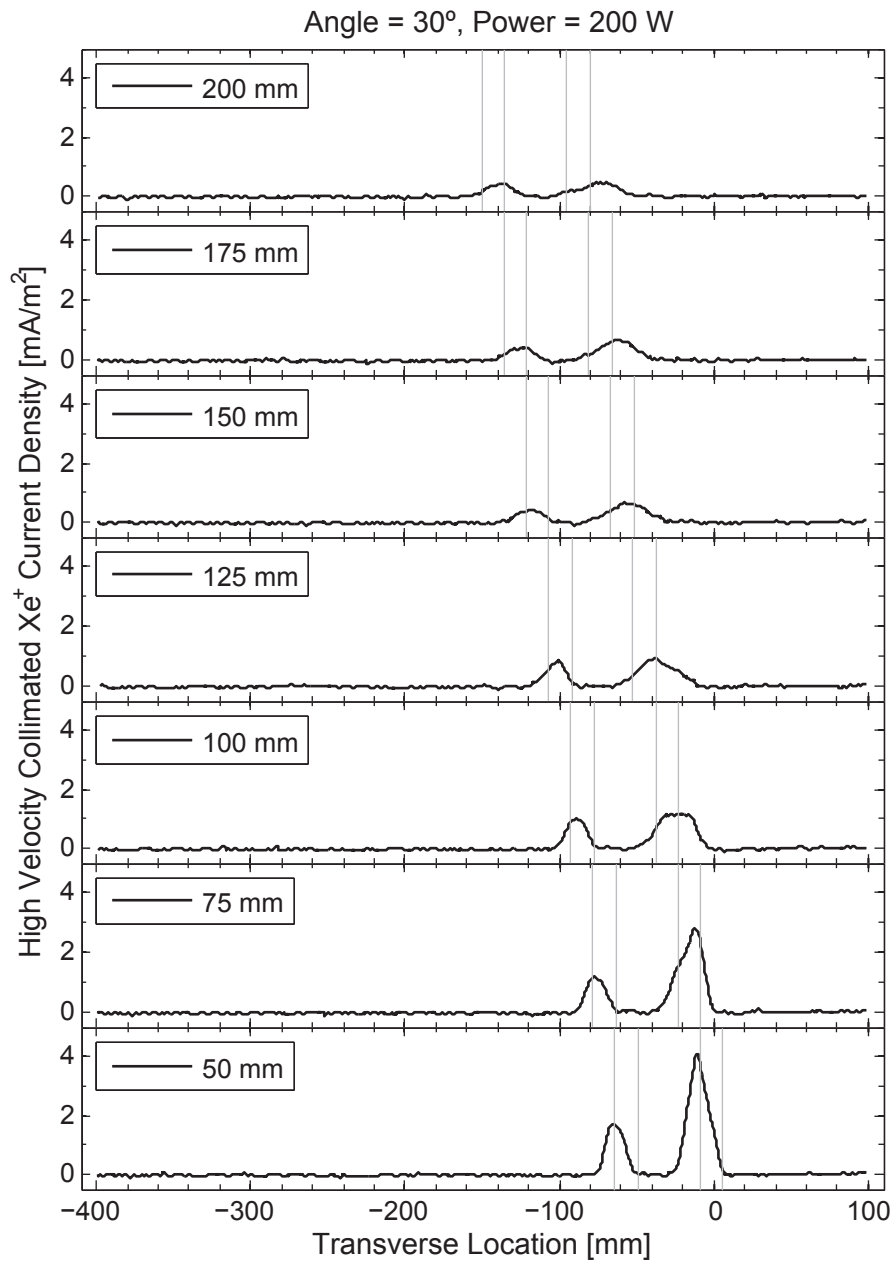


Figure A.4: ExB results, 200 W case, at 30°.

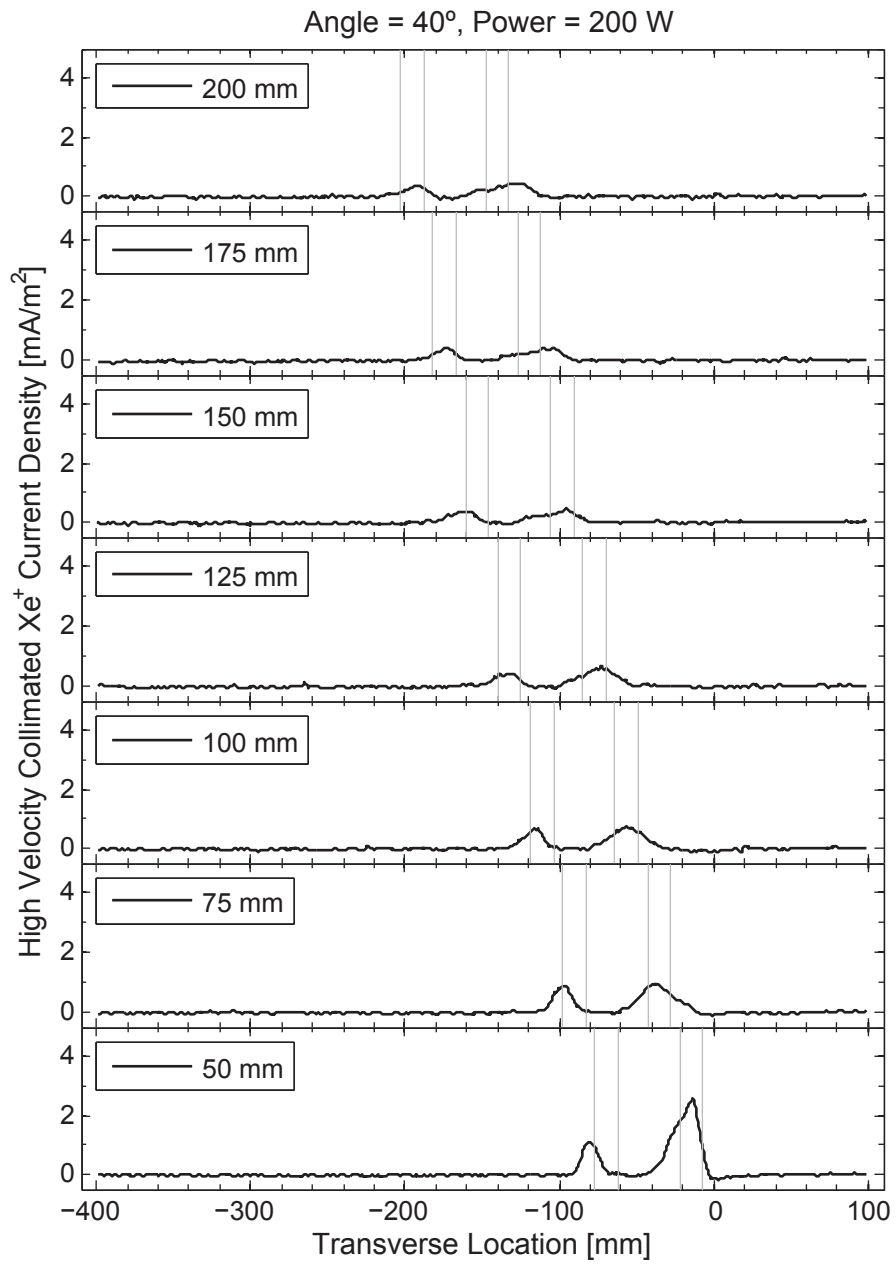


Figure A.5: ExB results, 200 W case, at 40°.

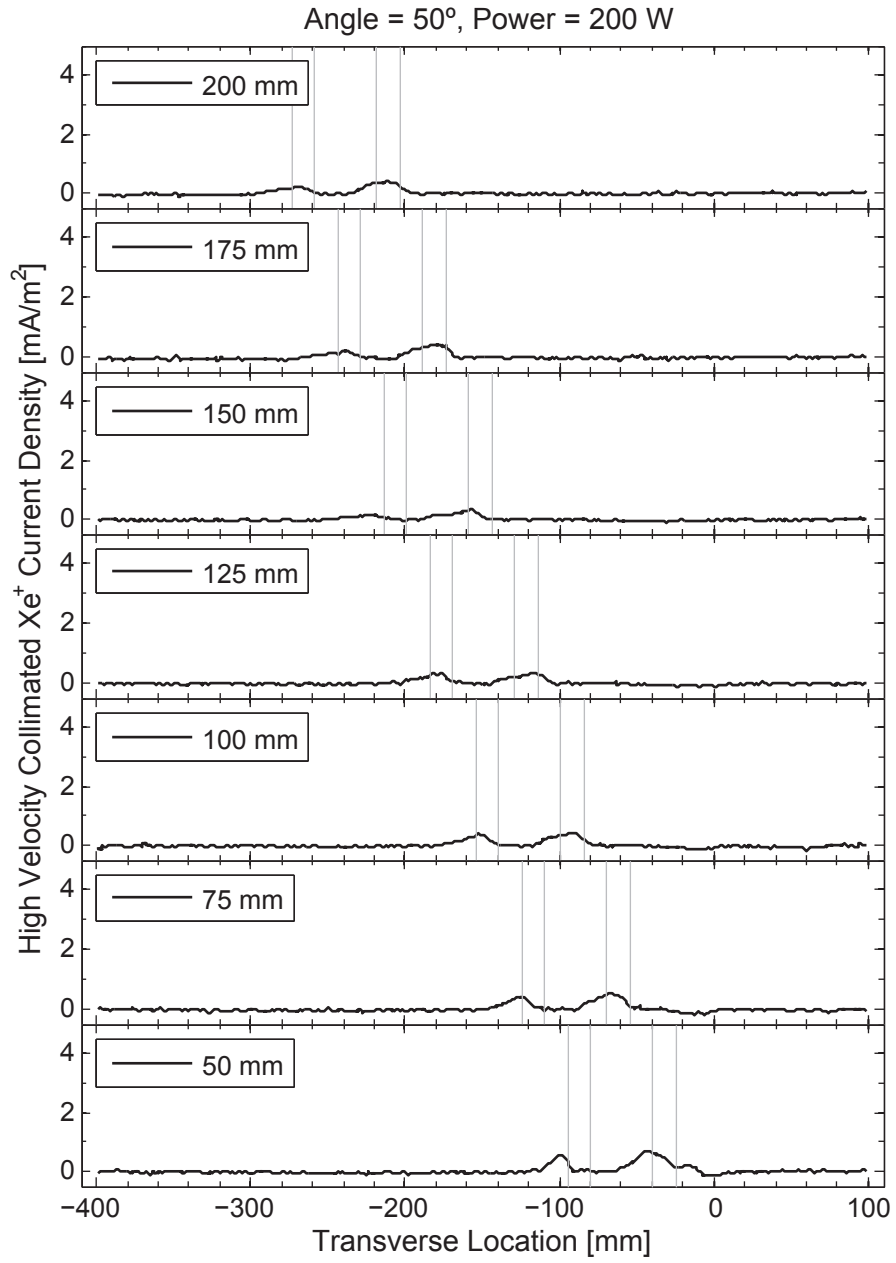


Figure A.6: ExB results, 200 W case, at 50°.

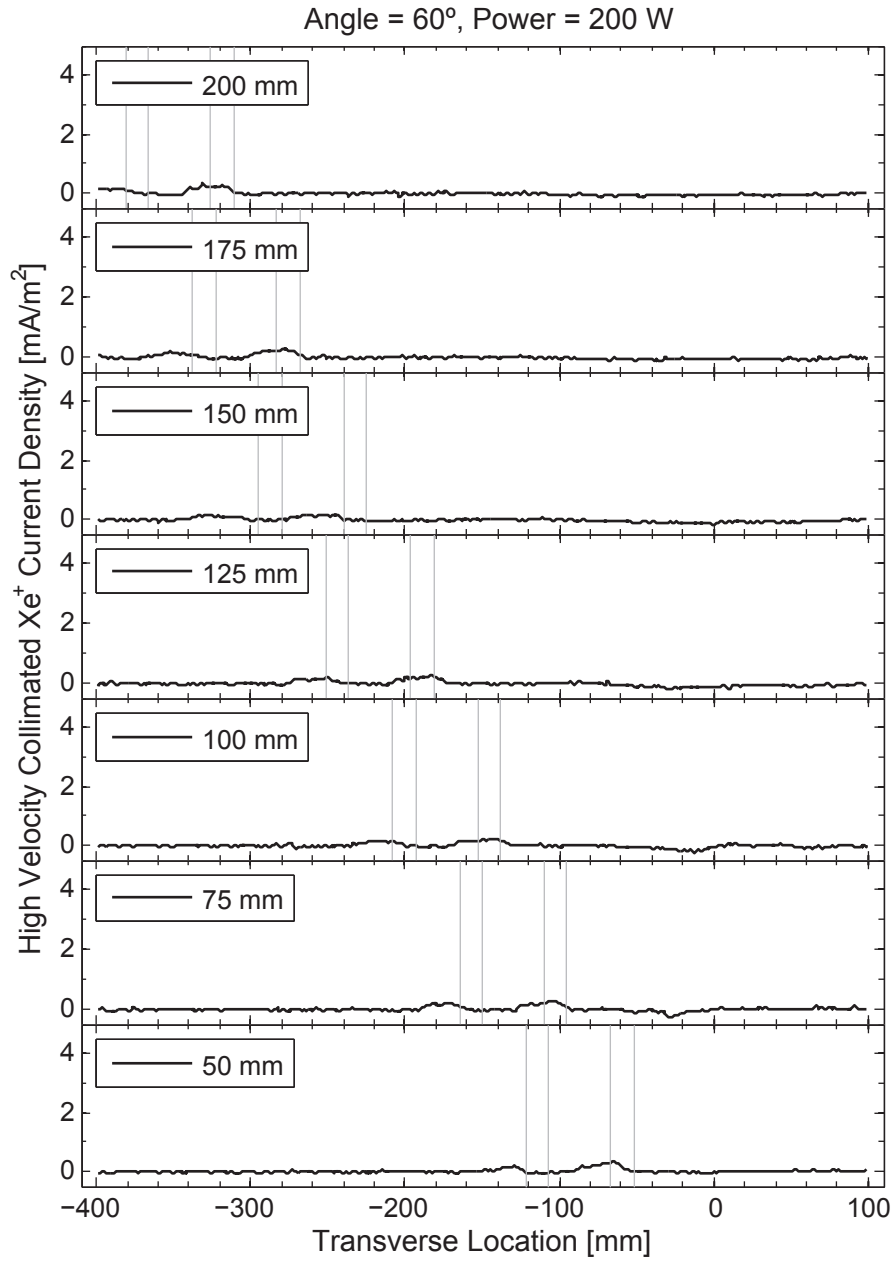


Figure A.7: ExB results, 200 W case, at 60°.

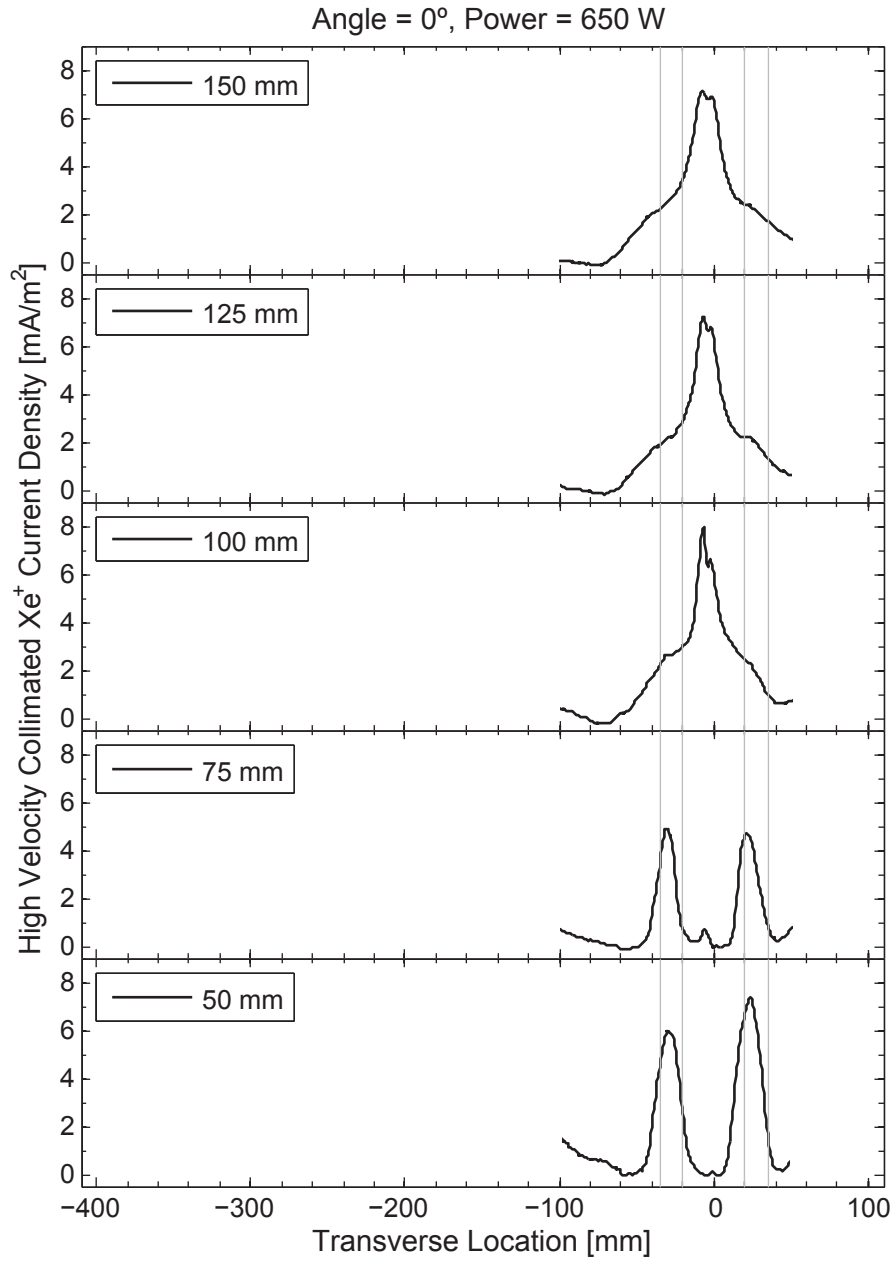


Figure A.8: ExB results, 650 W case, at 0°.

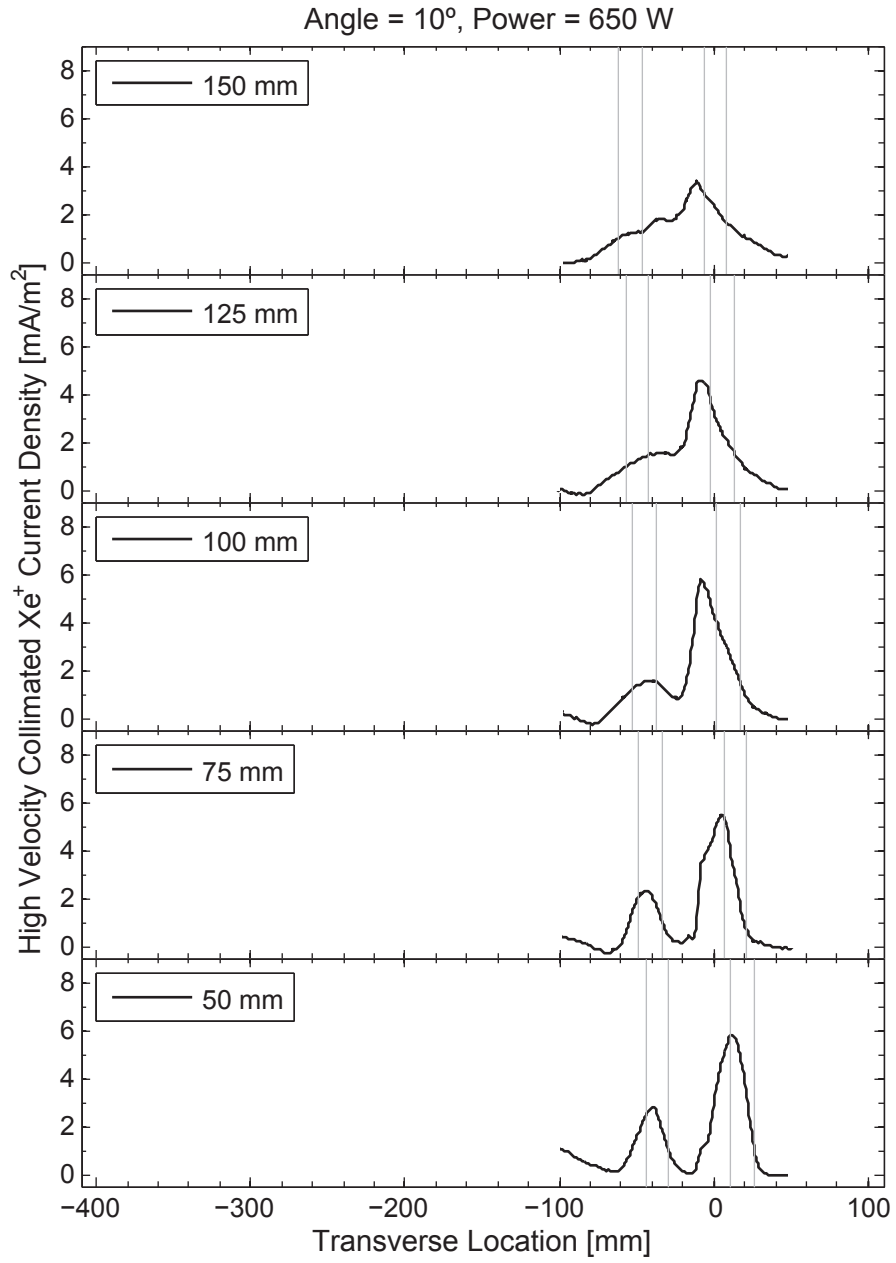


Figure A.9: ExB results, 650 W case, at 10°.

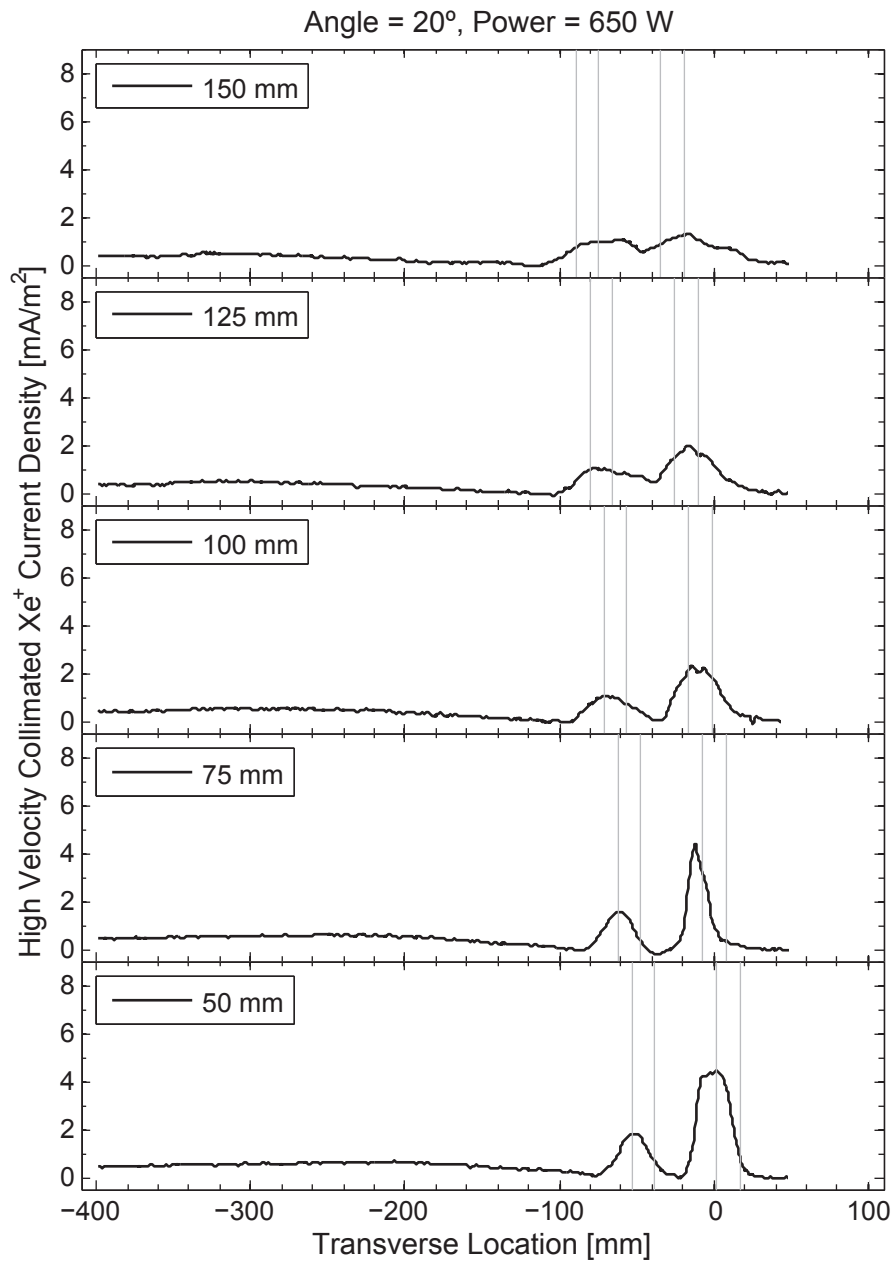


Figure A.10: ExB results, 650 W case, at 20°.

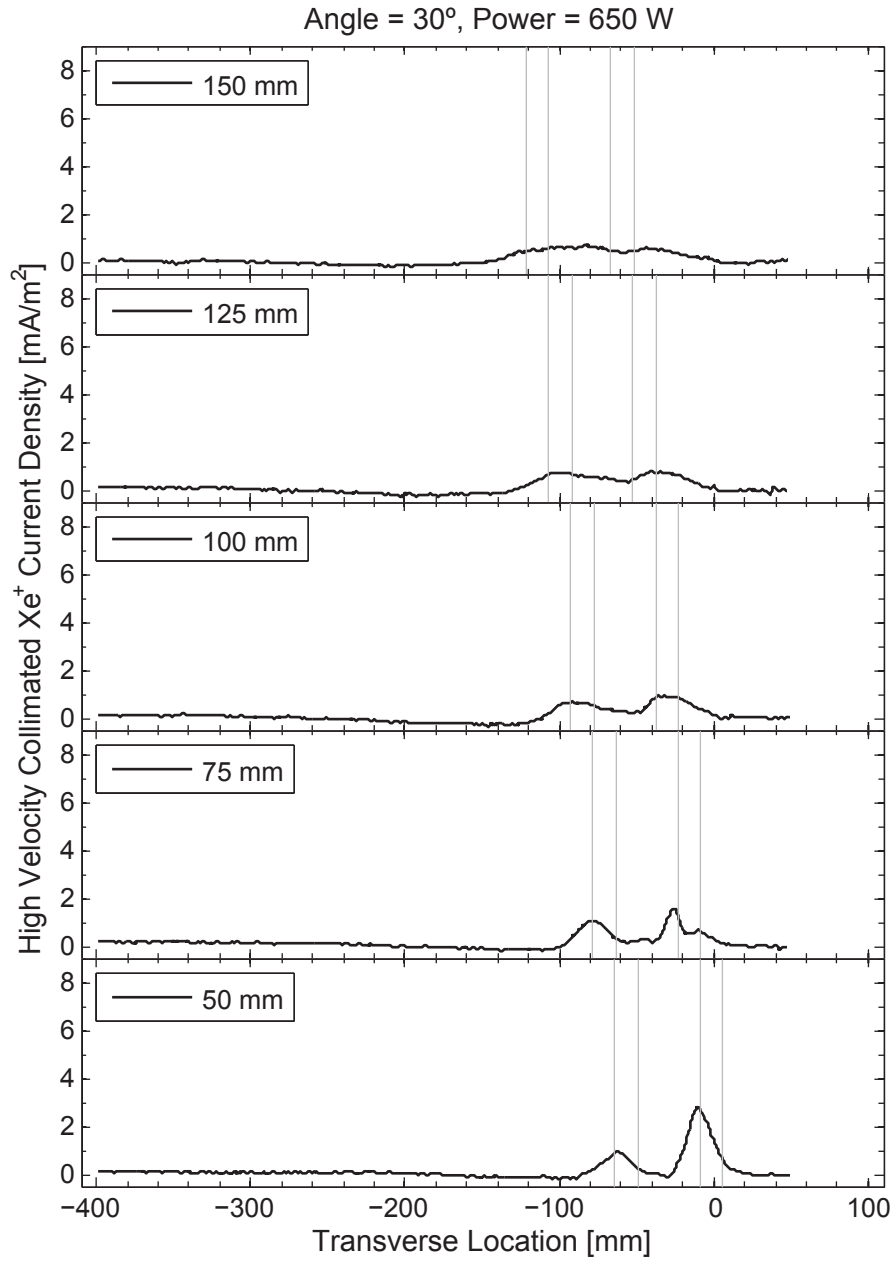


Figure A.11: ExB results, 650 W case, at 30°.

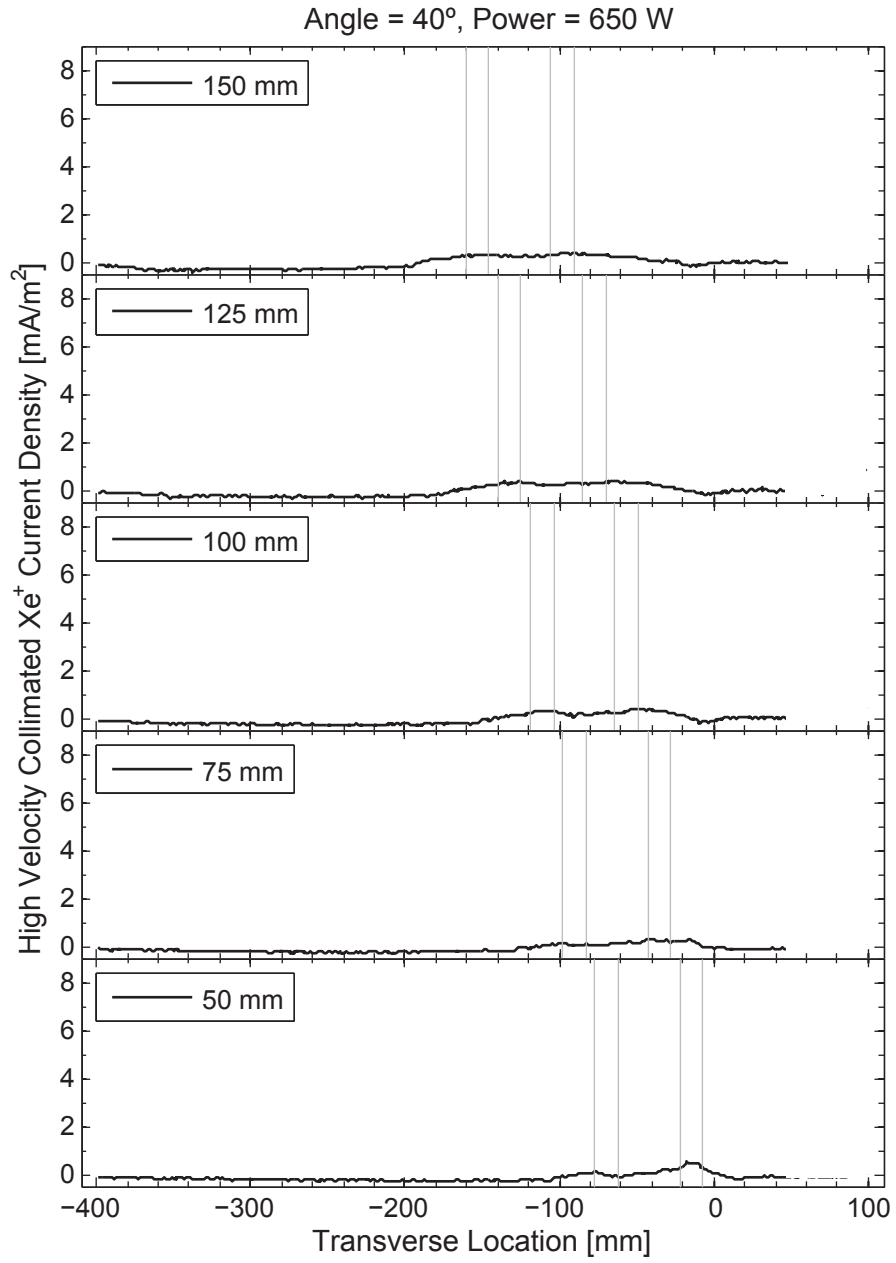


Figure A.12: ExB results, 650 W case, at 40°.



## **Appendix B**

# **Additional Experimental RPA Data**

### **B.1 Raw RPA Data**

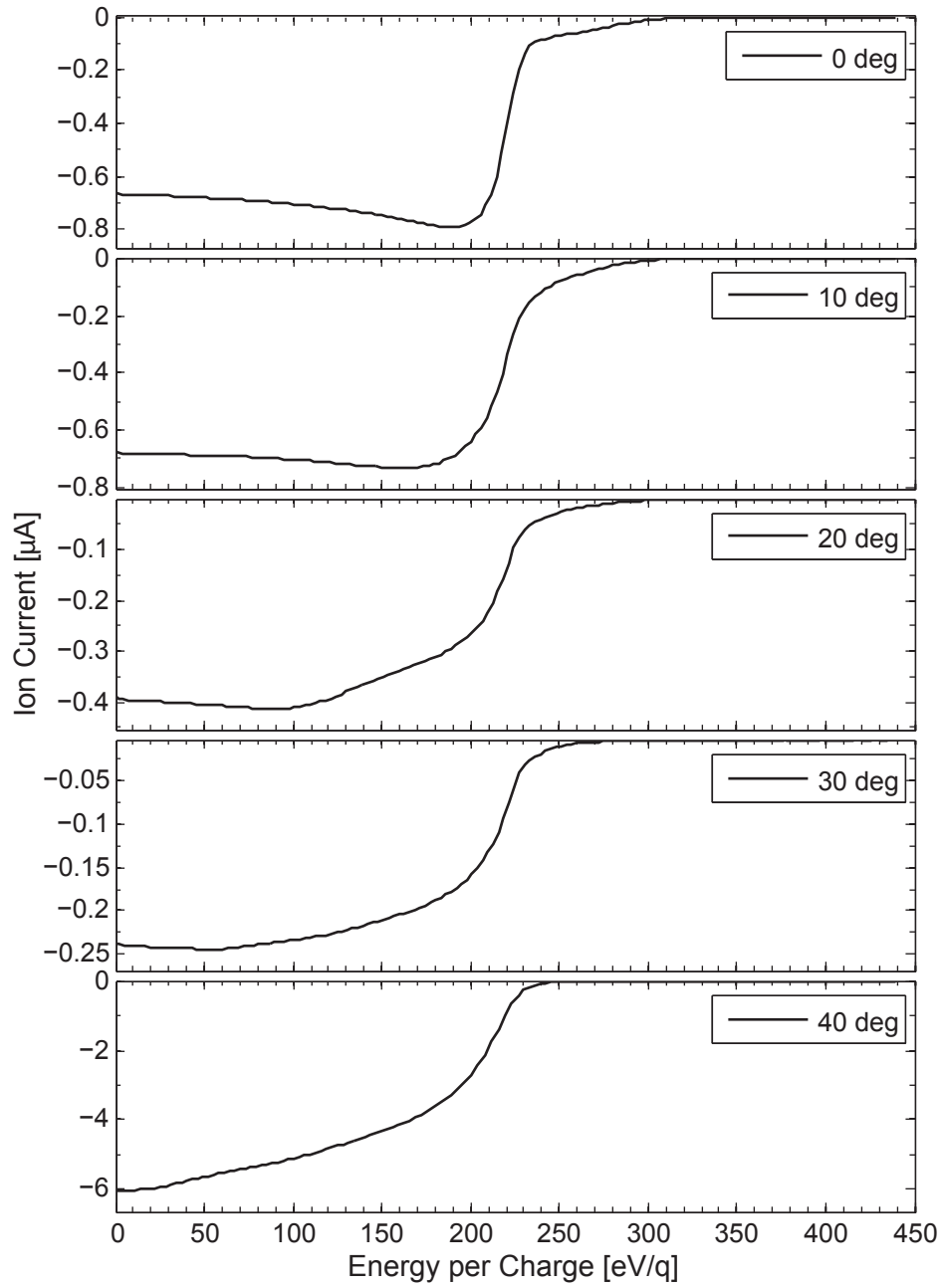


Figure B.1: RPA raw data, 200W, from 0 to 40°.

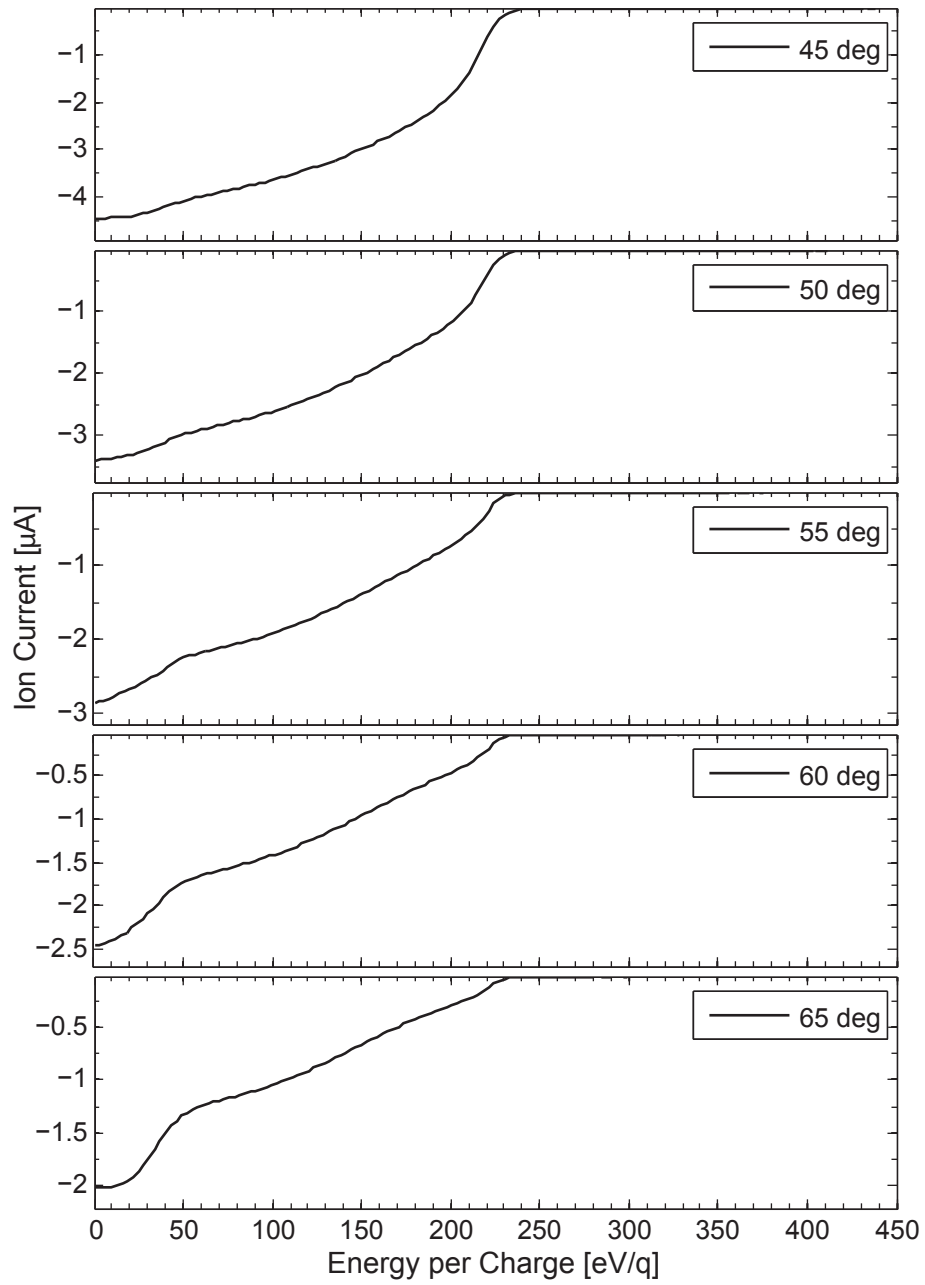


Figure B.2: RPA raw data, 200W, from 45 to 65°.

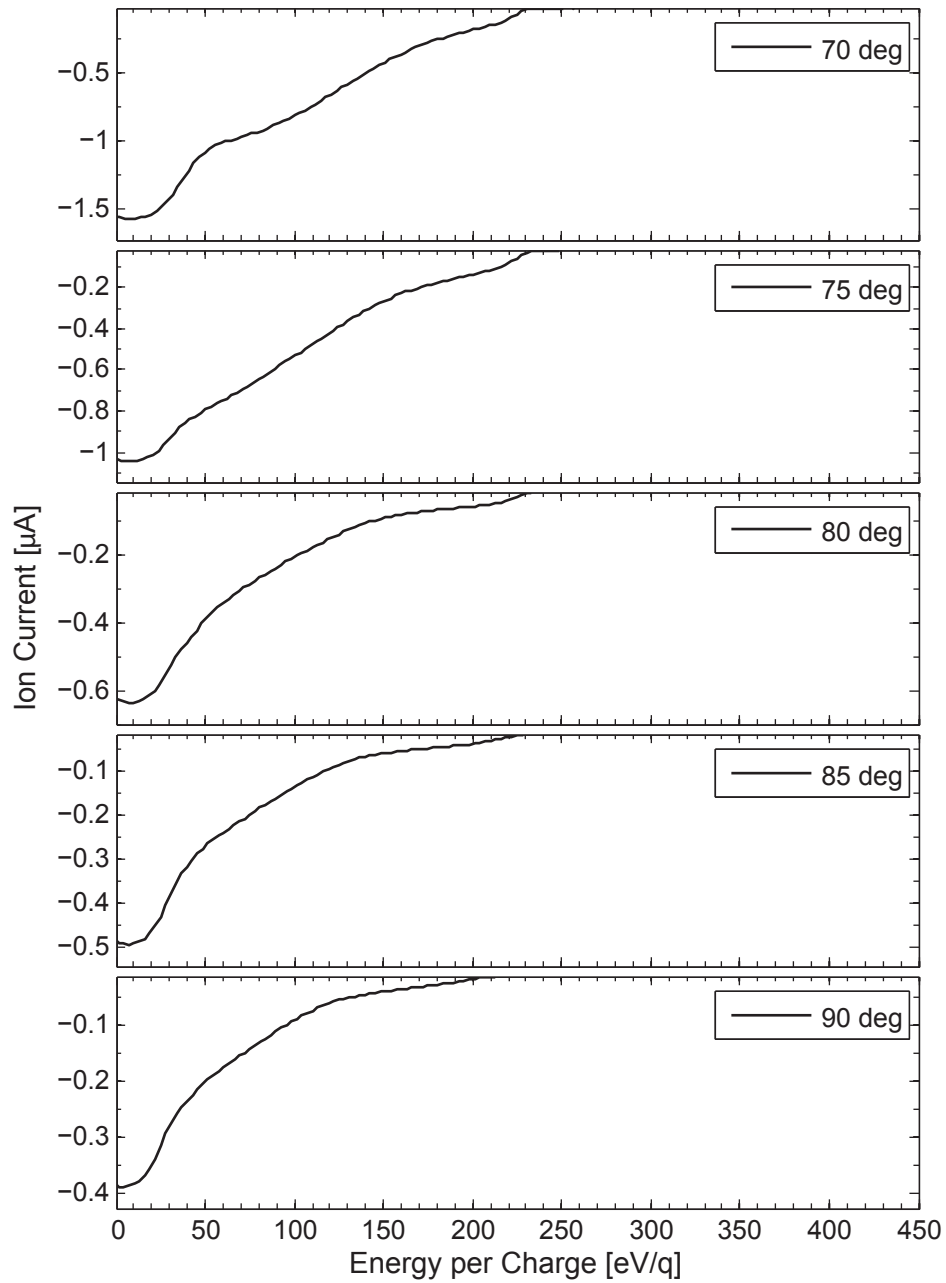


Figure B.3: RPA raw data, 200W, from 70 to 90°.

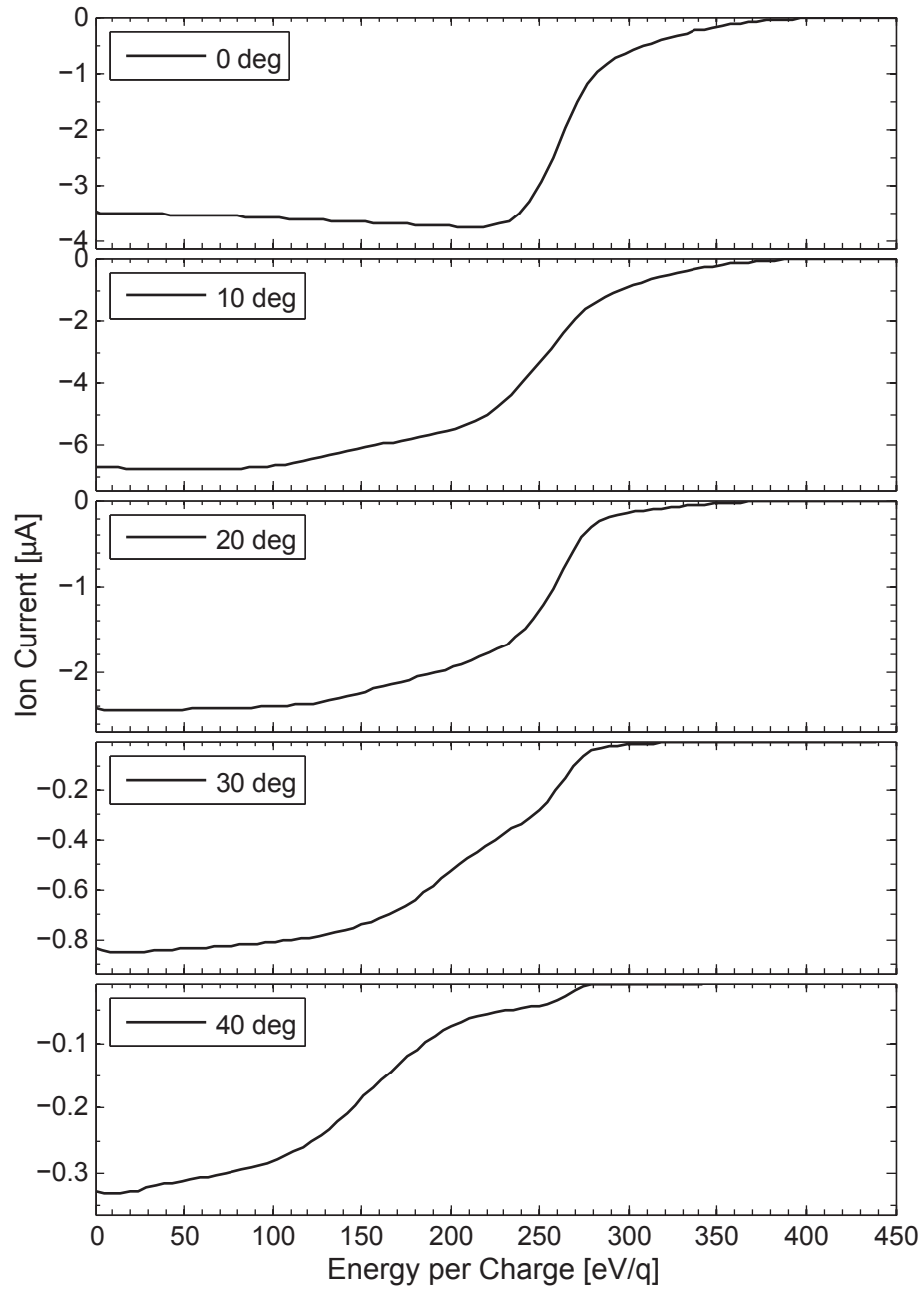


Figure B.4: RPA raw data, 650W, from 0 to 40°.

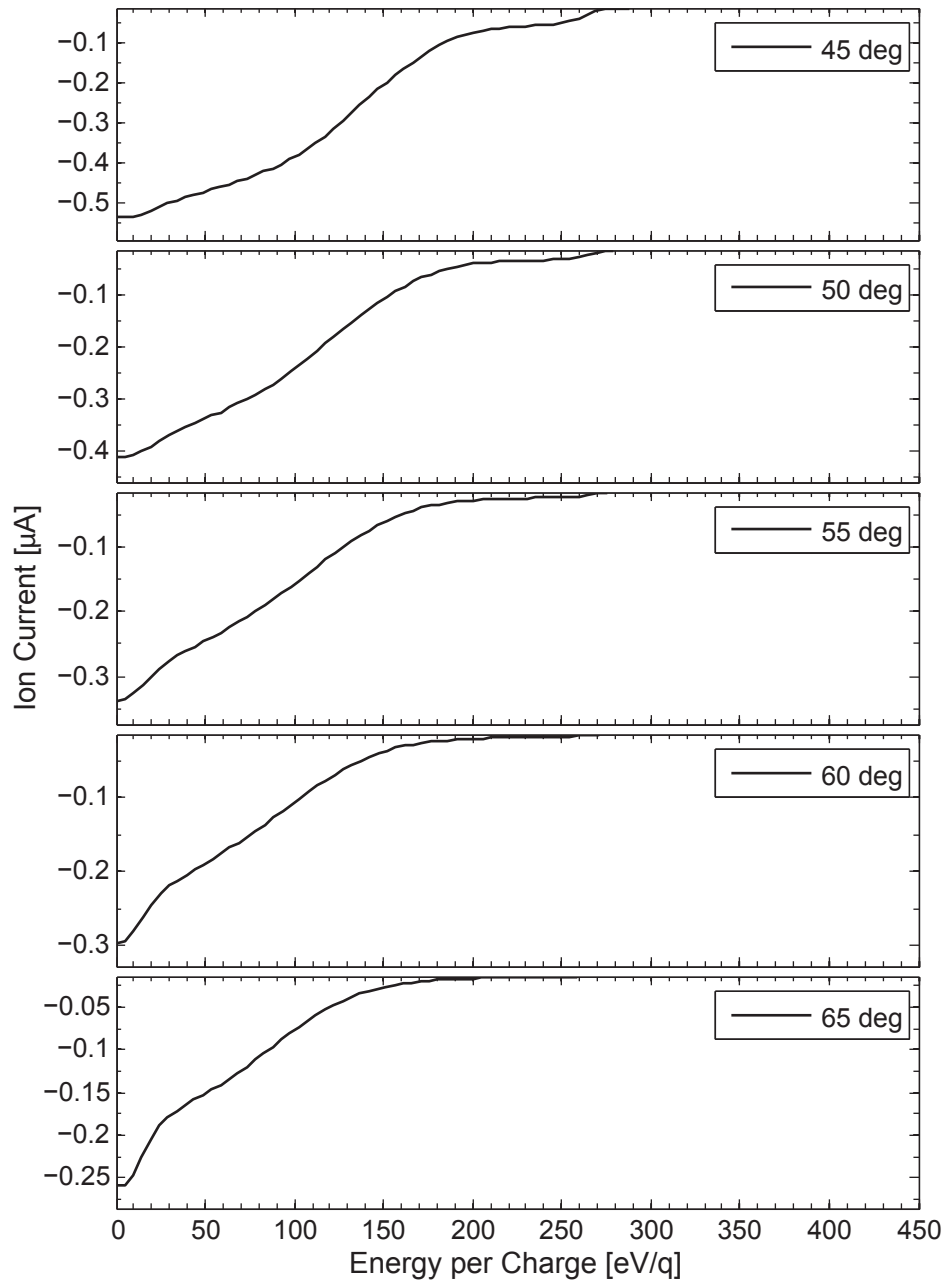


Figure B.5: RPA raw data, 650W, from 45 to 65°.

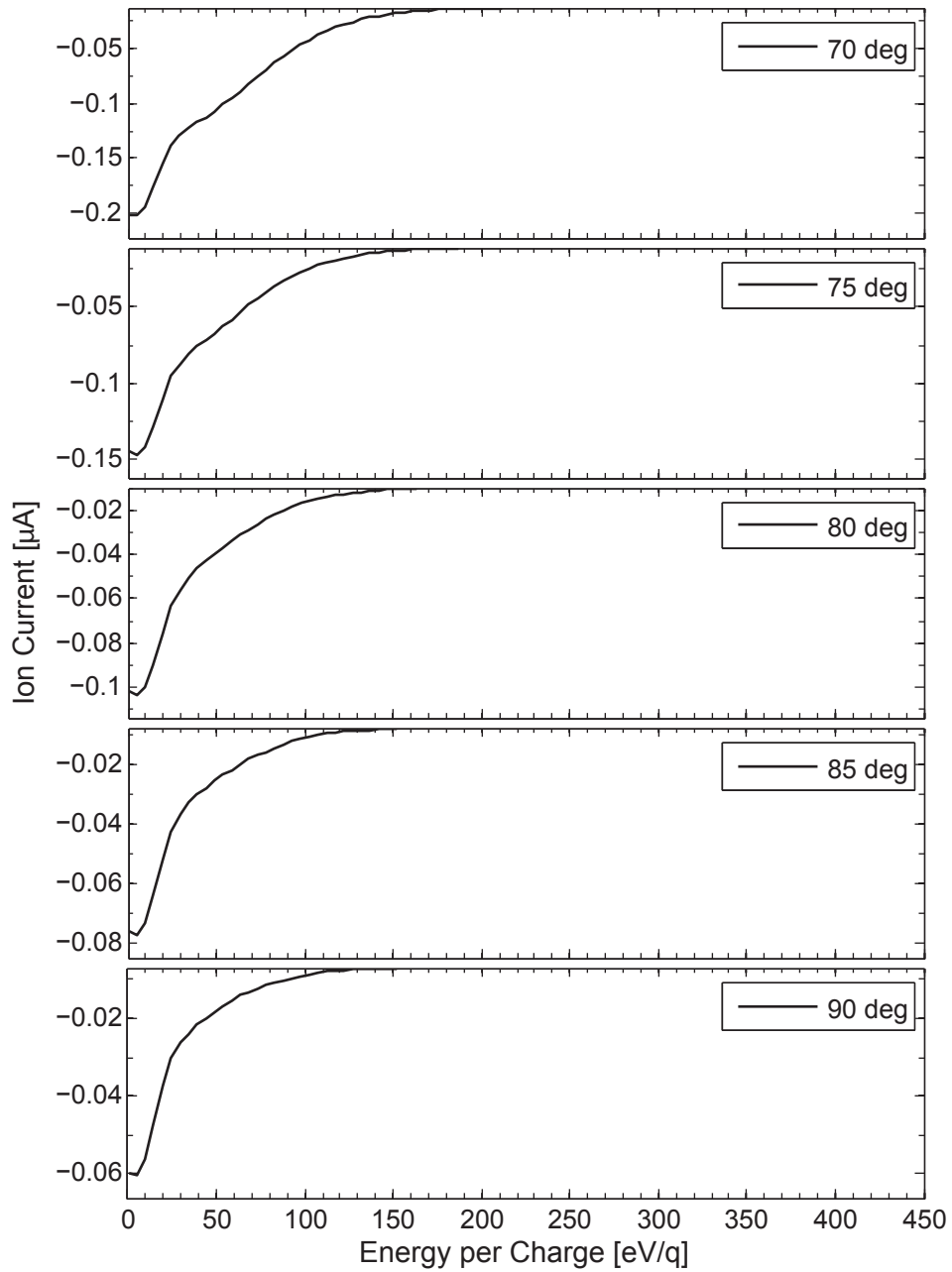


Figure B.6: RPA raw data, 650W, from 70 to 90°.

## **B.2 Differentiated RPA Data (not normalized)**

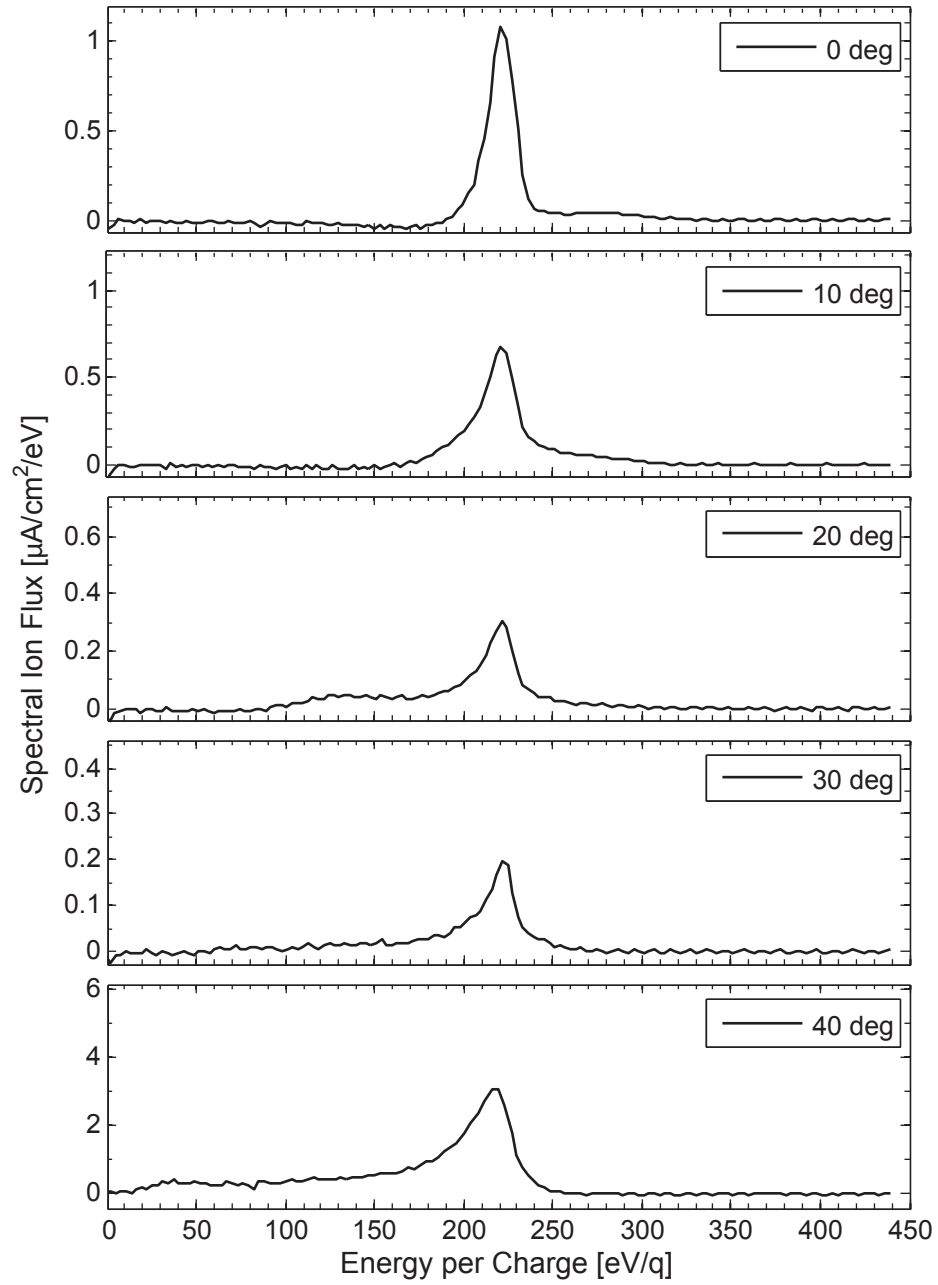


Figure B.7: RPA differentiated data, 200W, from 0 to 40°.

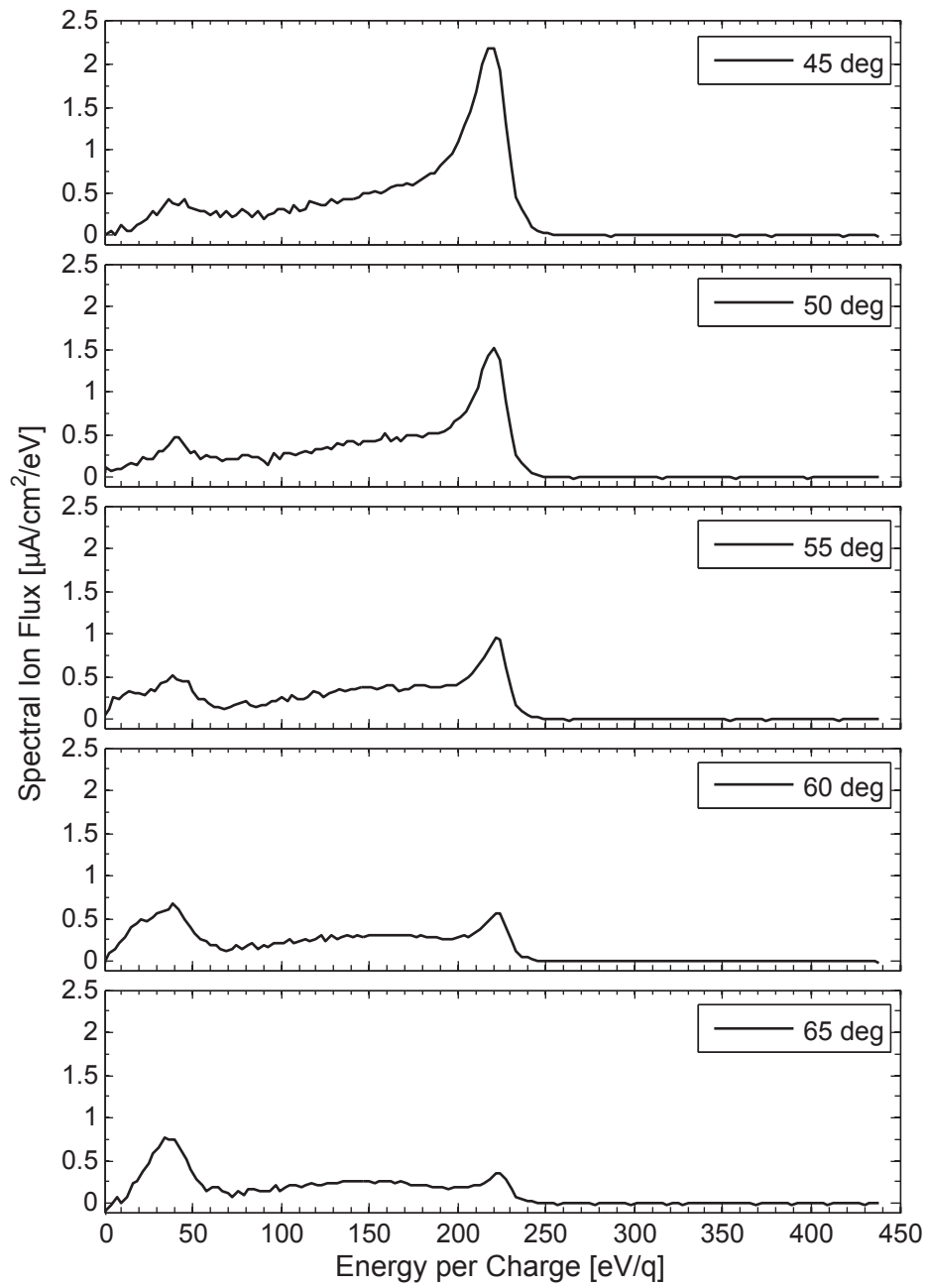


Figure B.8: RPA differentiated data, 200W, from 45 to 65°.

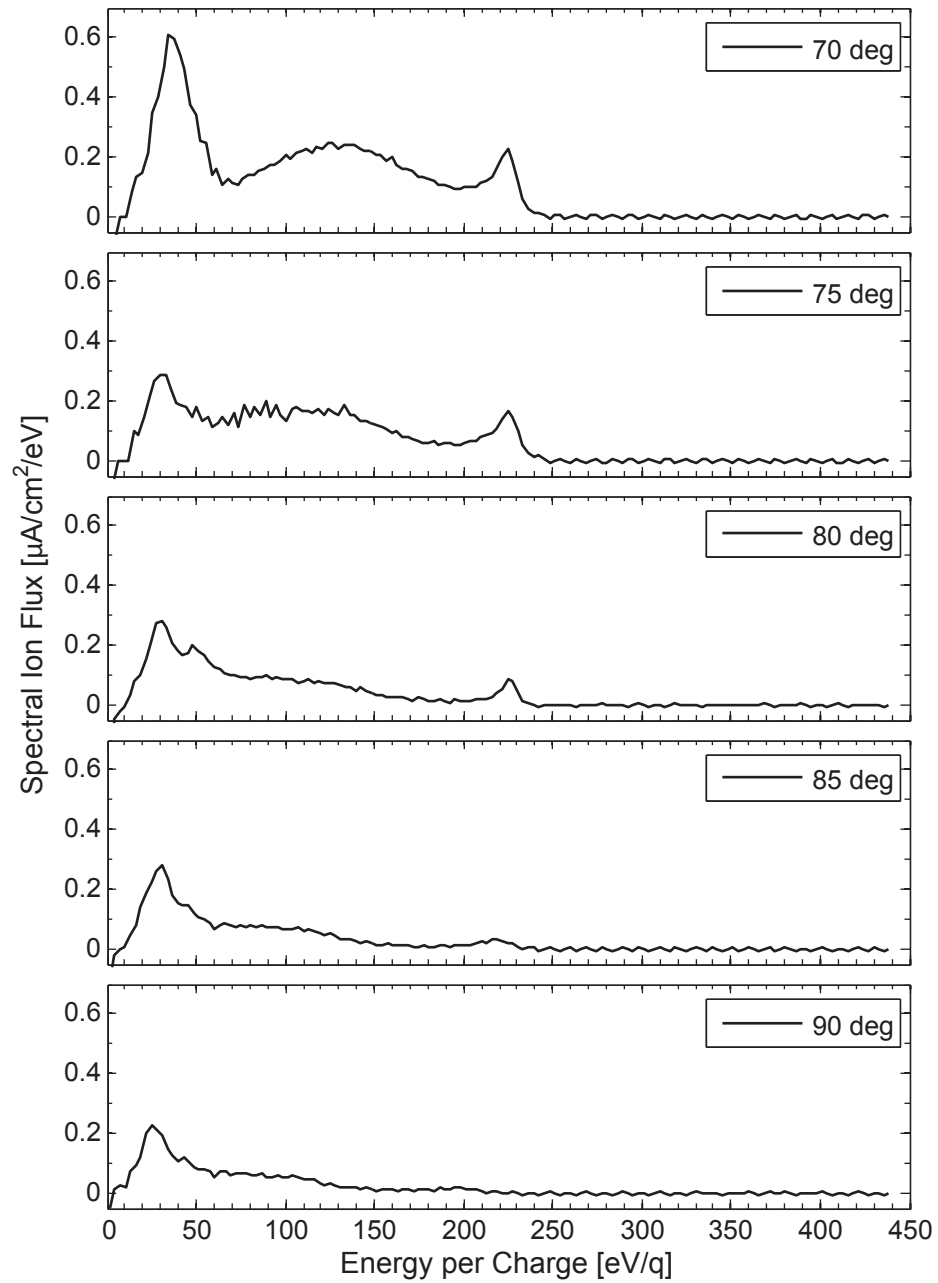


Figure B.9: RPA differentiated data, 200W, from 70 to 90°.

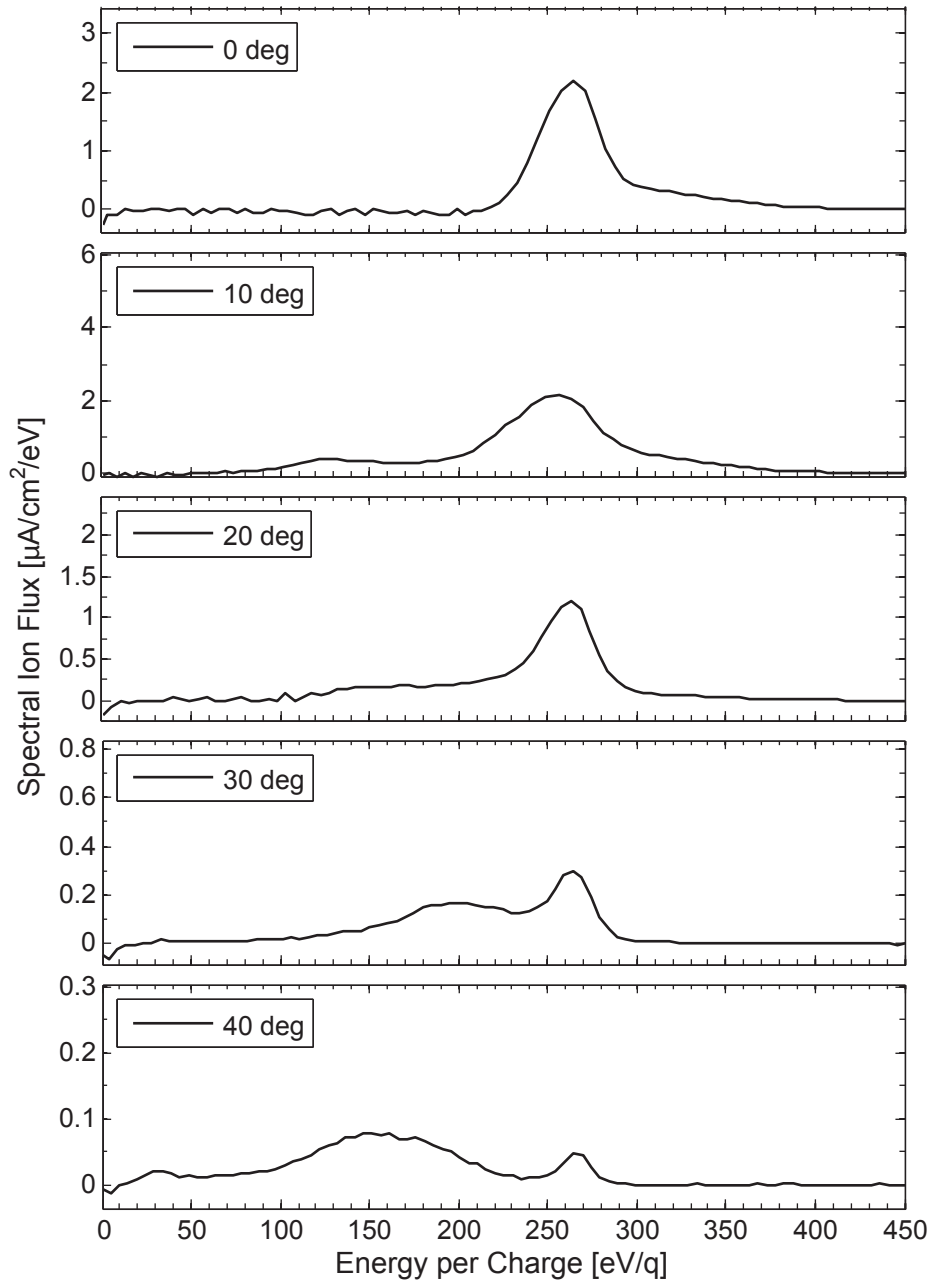


Figure B.10: RPA differentiated data, 650W, from 0 to 40°.

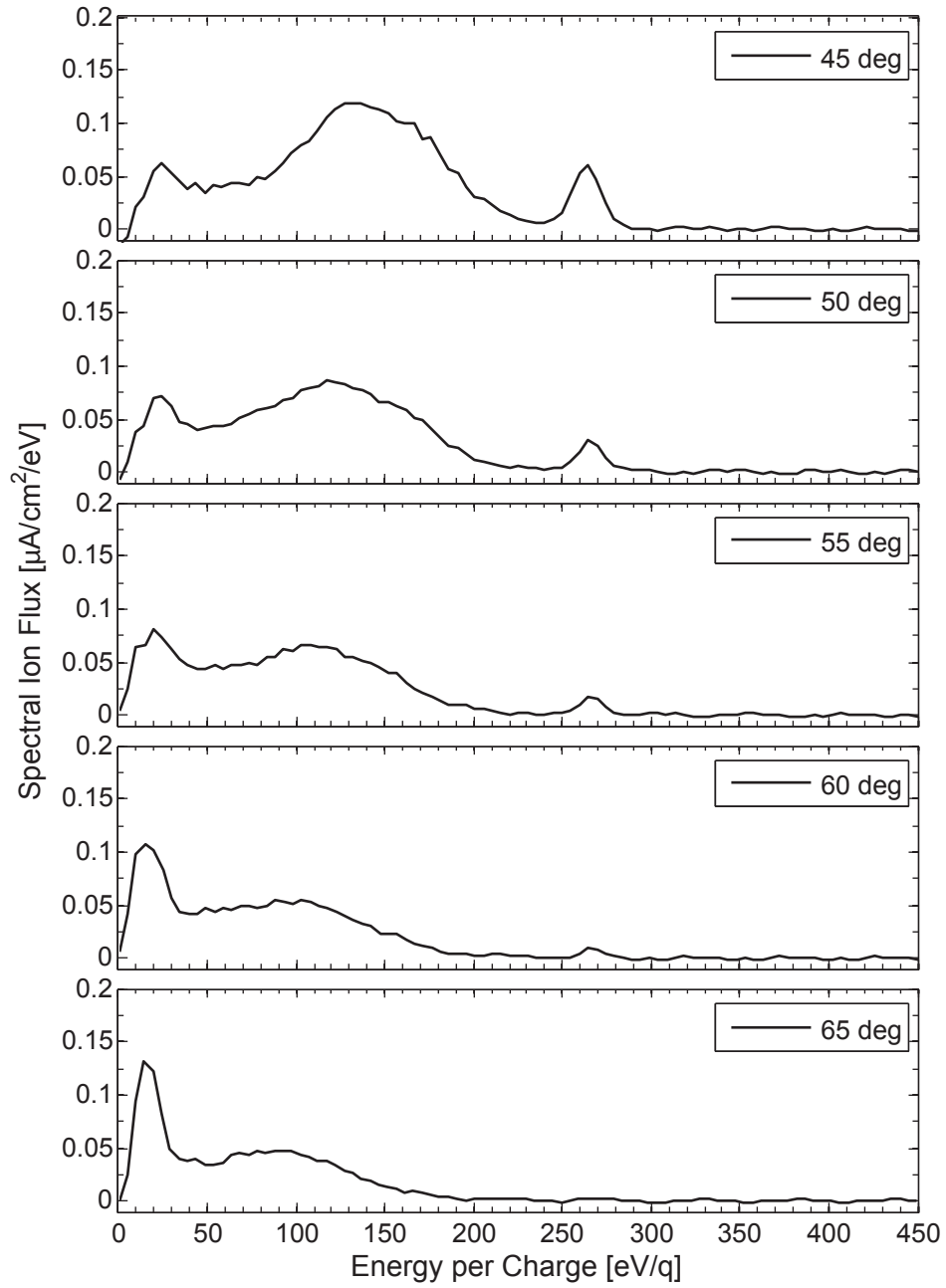


Figure B.11: RPA differentiated data, 650W, from 45 to 65°.

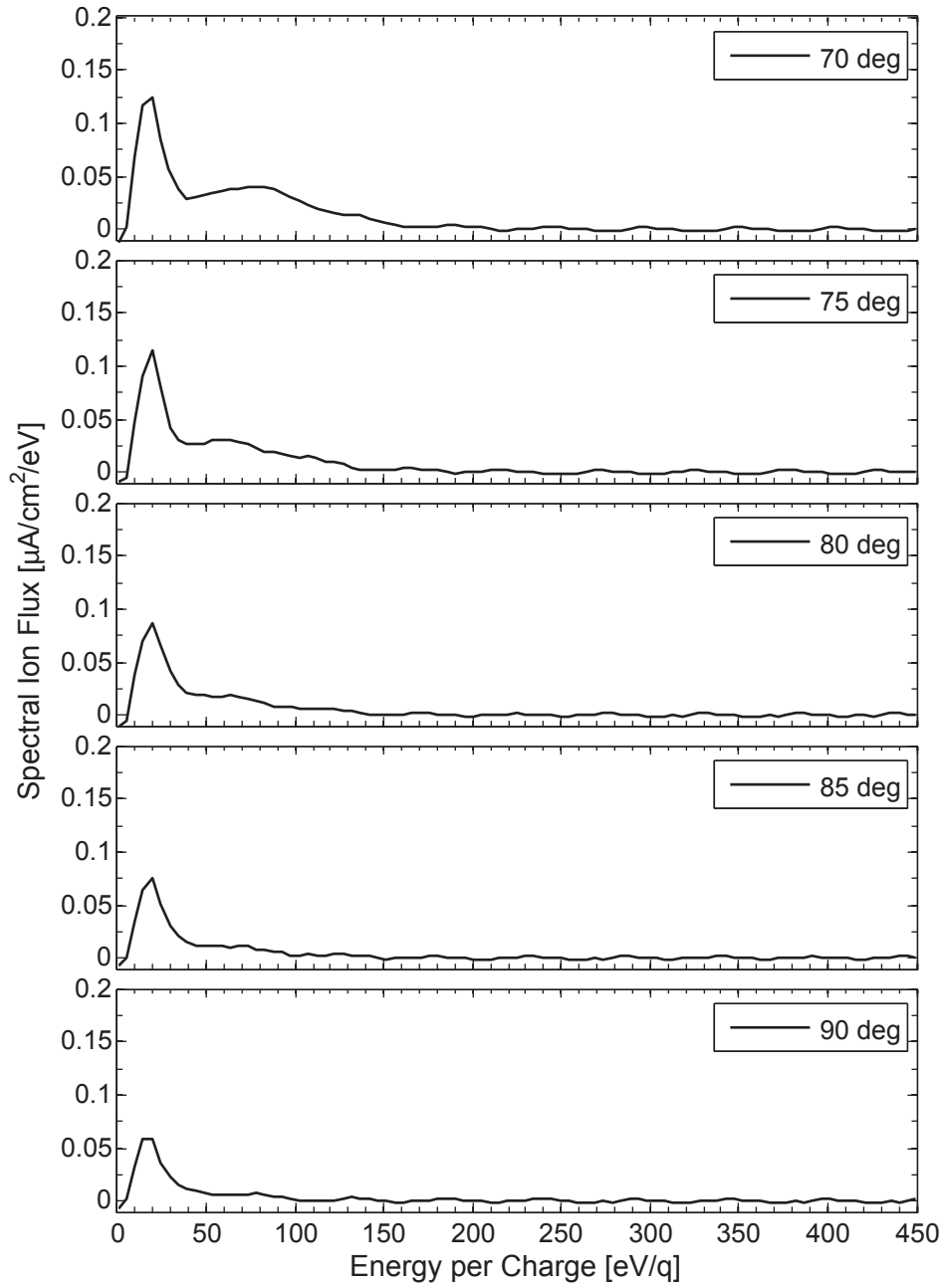


Figure B.12: RPA differentiated data, 650W, from 70 to 90°.

### B.3 Sputter Yield Data

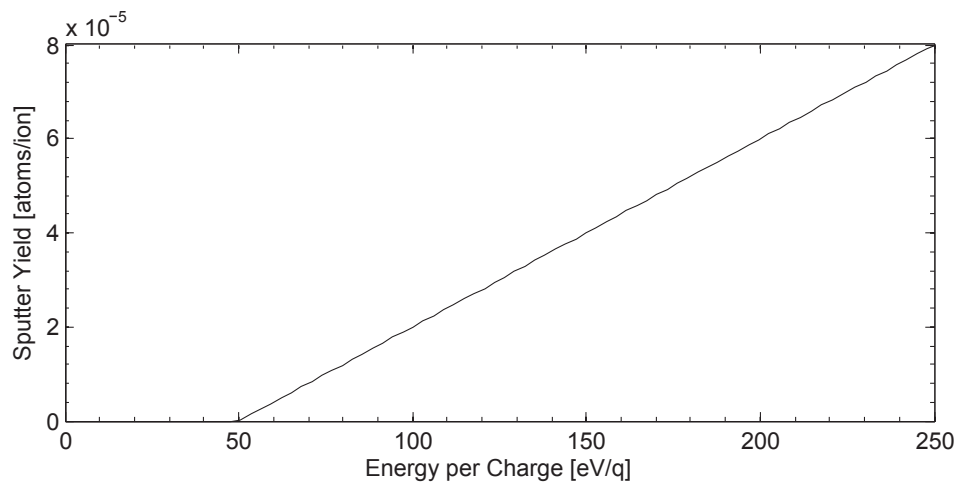


Figure B.13: Sputter yield for Carbon, fitted to data in [50].

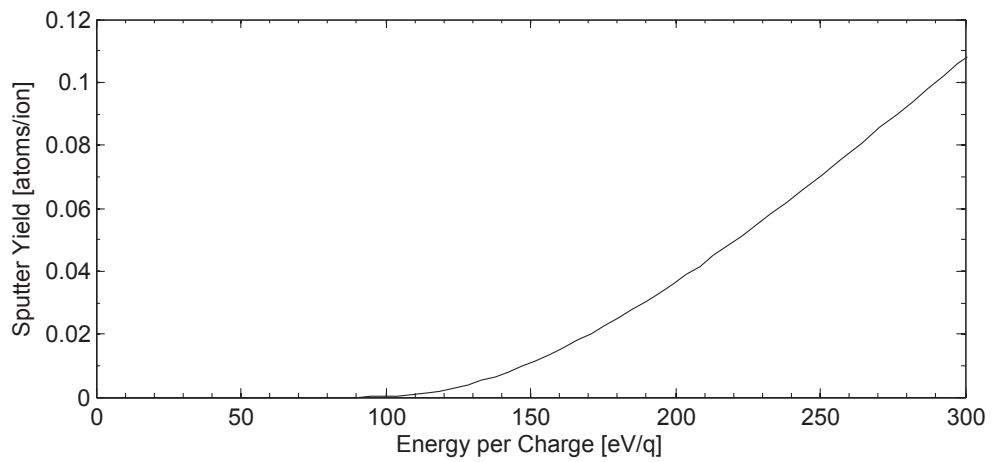


Figure B.14: Sputter yield for Silicon, from [49].

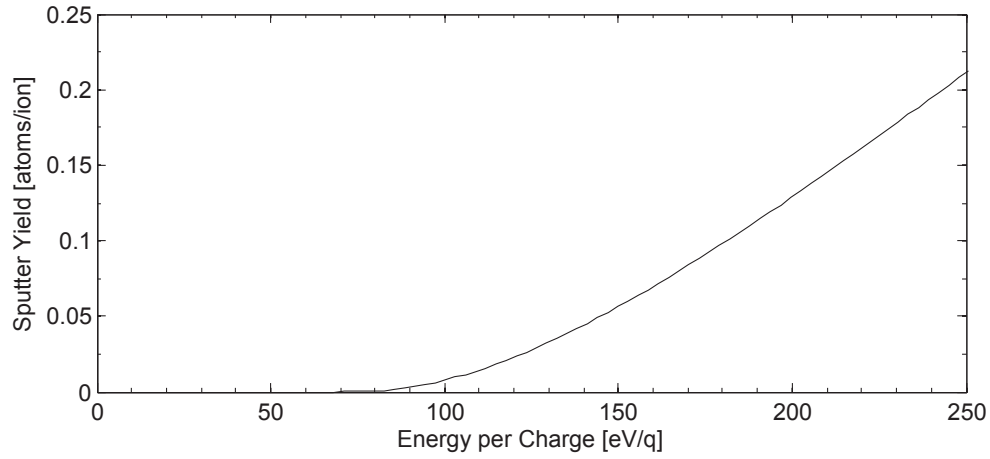


Figure B.15: Sputter yield for Aluminum, from [49].

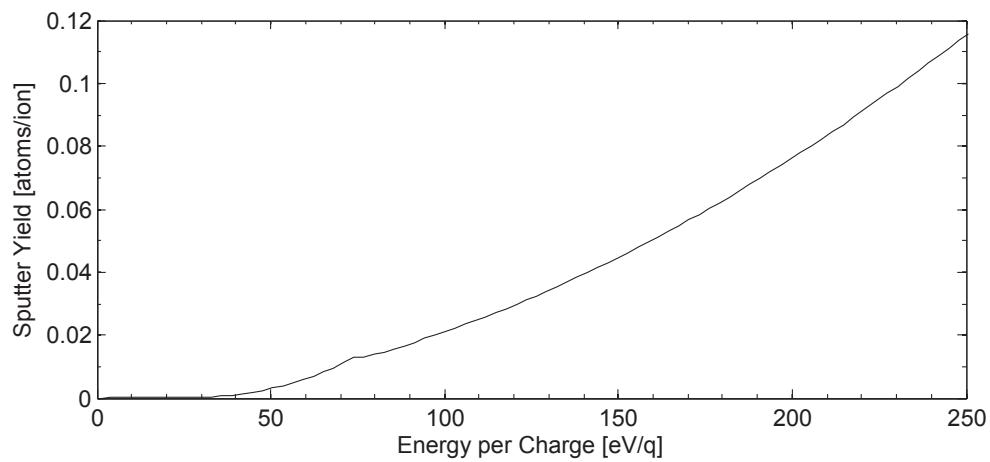


Figure B.16: Sputter yield for Titanium, fitted to data in [50].

## **Appendix C**

# **Additional HP Hall Oscillation Results**

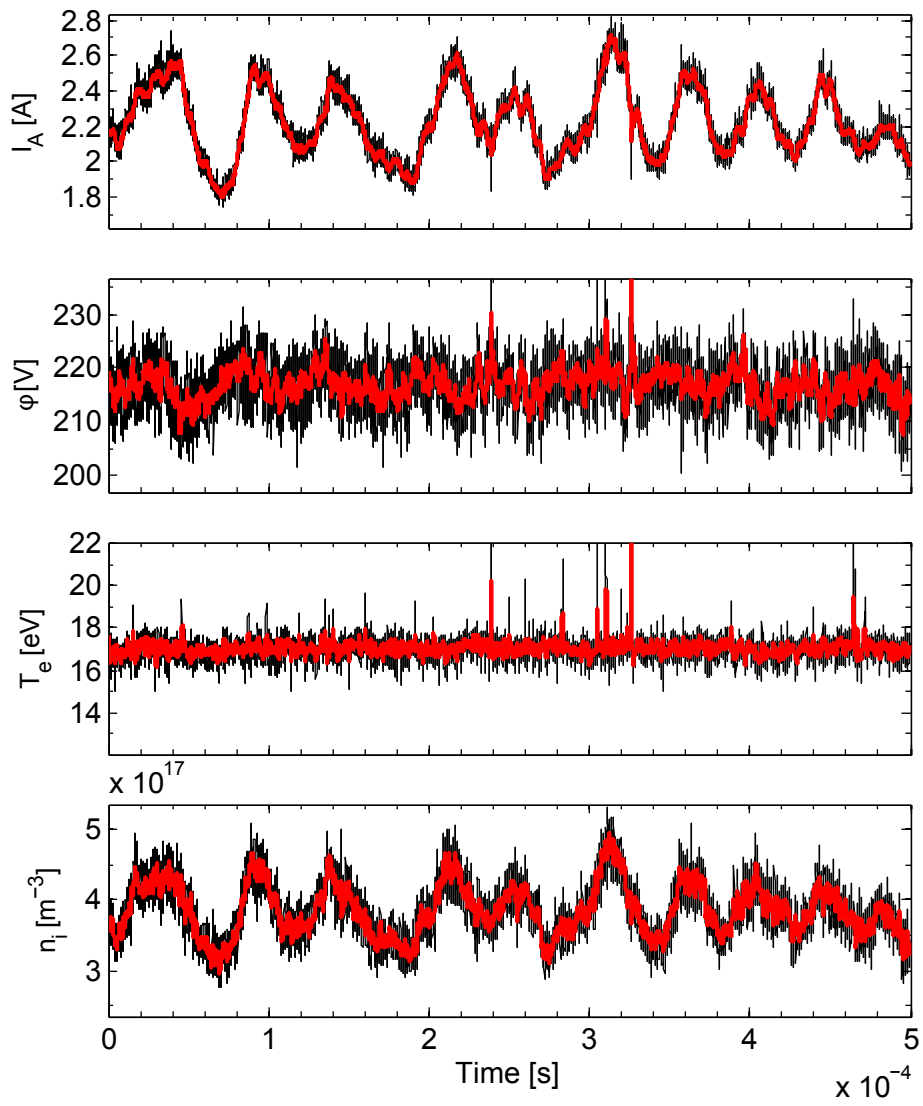


Figure C.1: Oscillation tracking in HPHall for the 650 W downstream run.

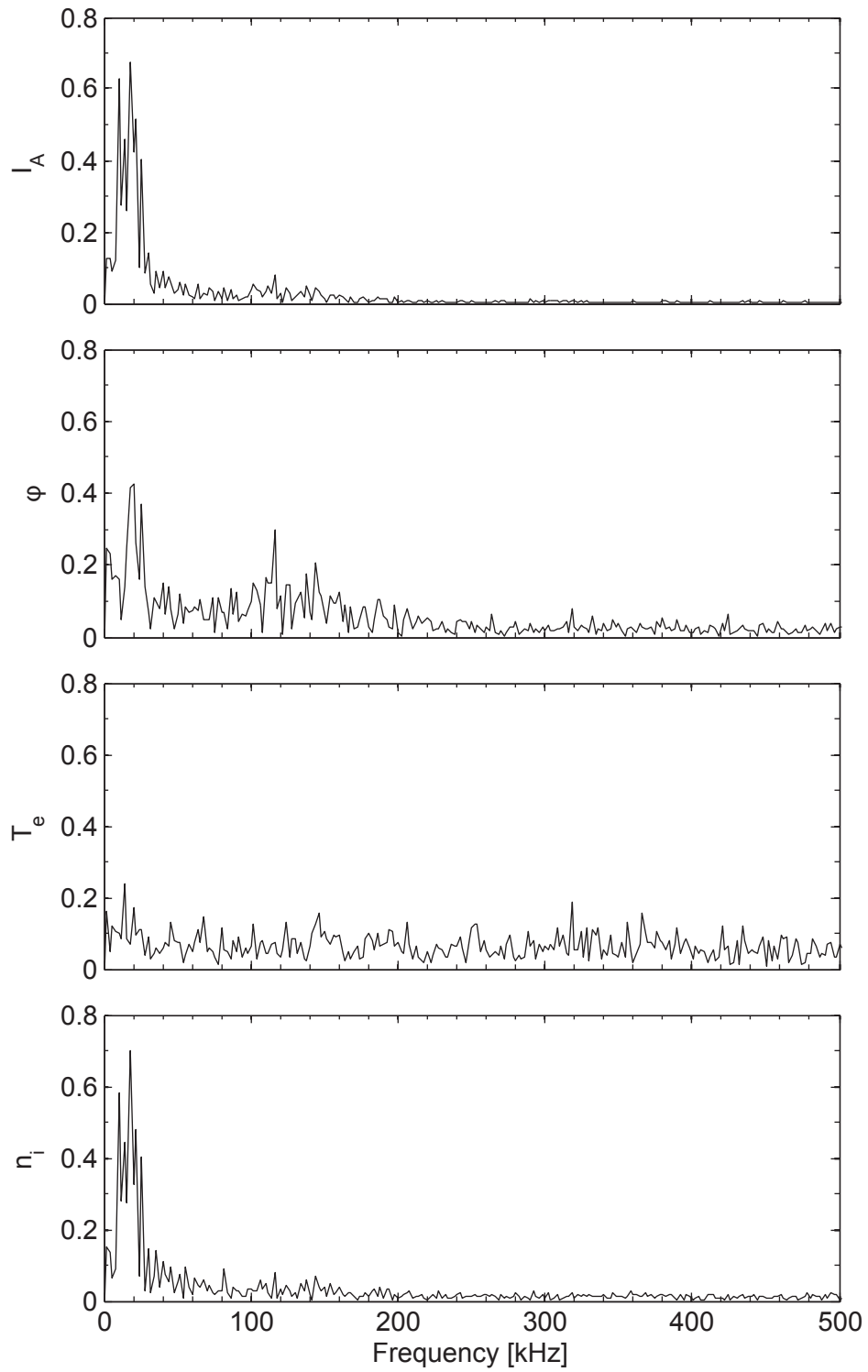


Figure C.2: Frequency spectrum for the 650 W downstream run.

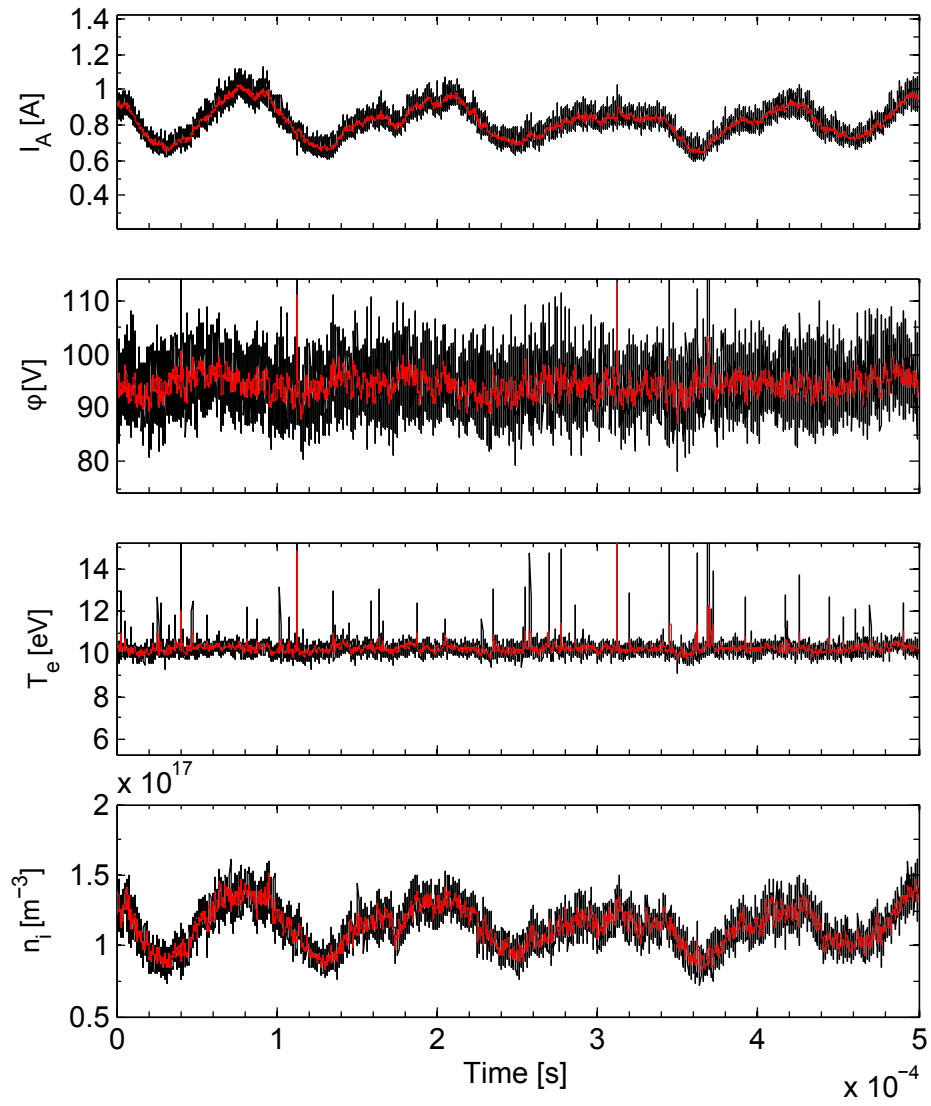


Figure C.3: Oscillation tracking in HPHall for the 200 W upstream run.

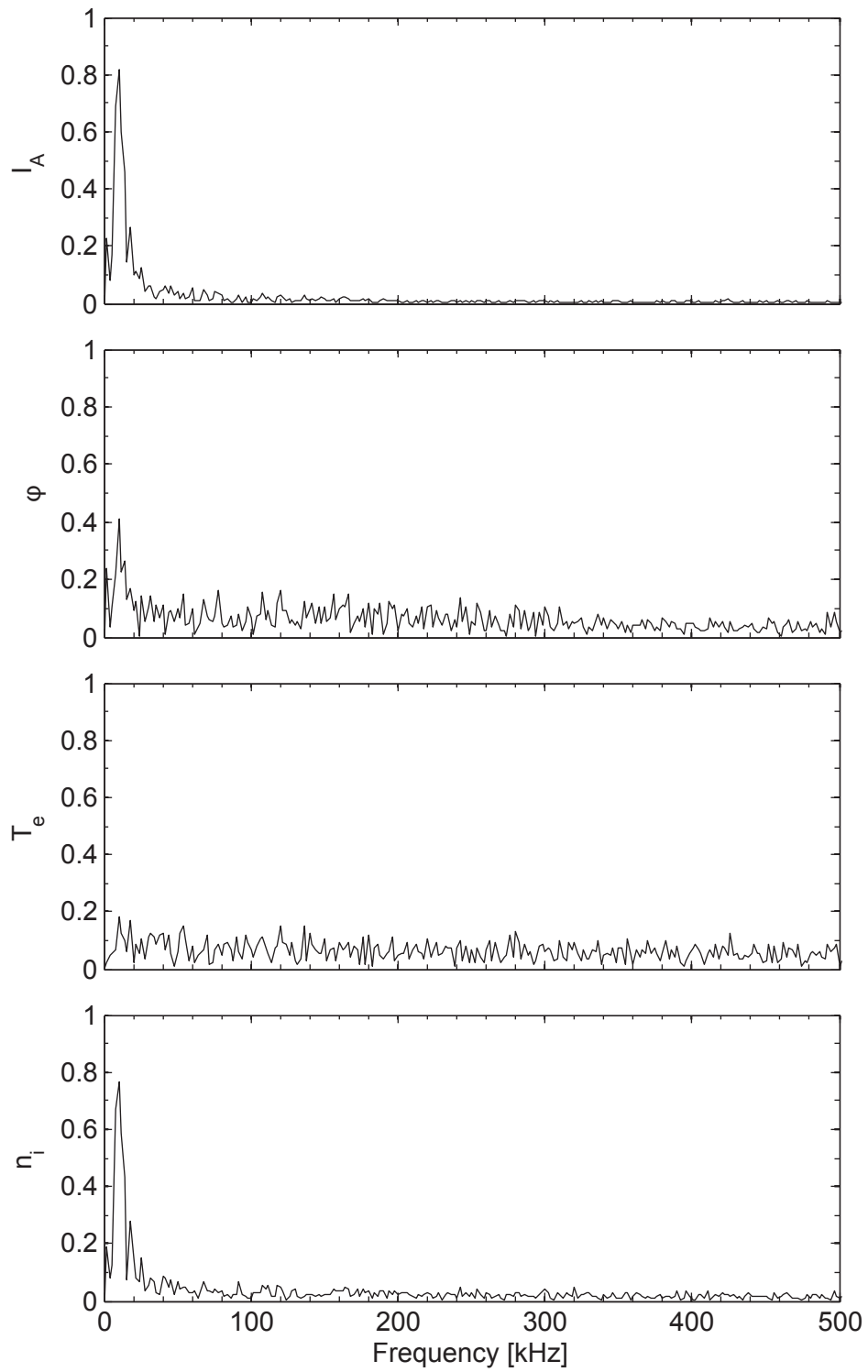


Figure C.4: Frequency spectrum for the 200 W upstream run.

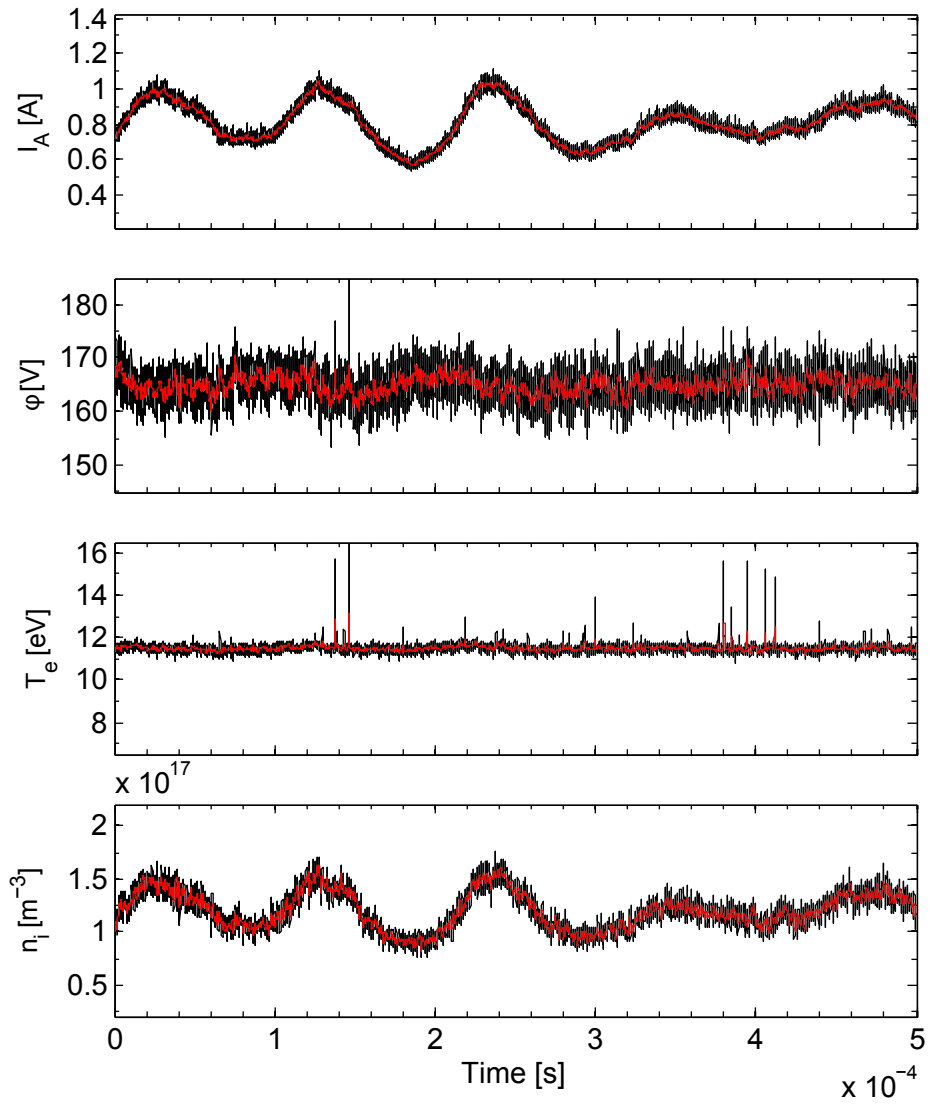


Figure C.5: Oscillation tracking in HPHall for the 200 W downstream run.

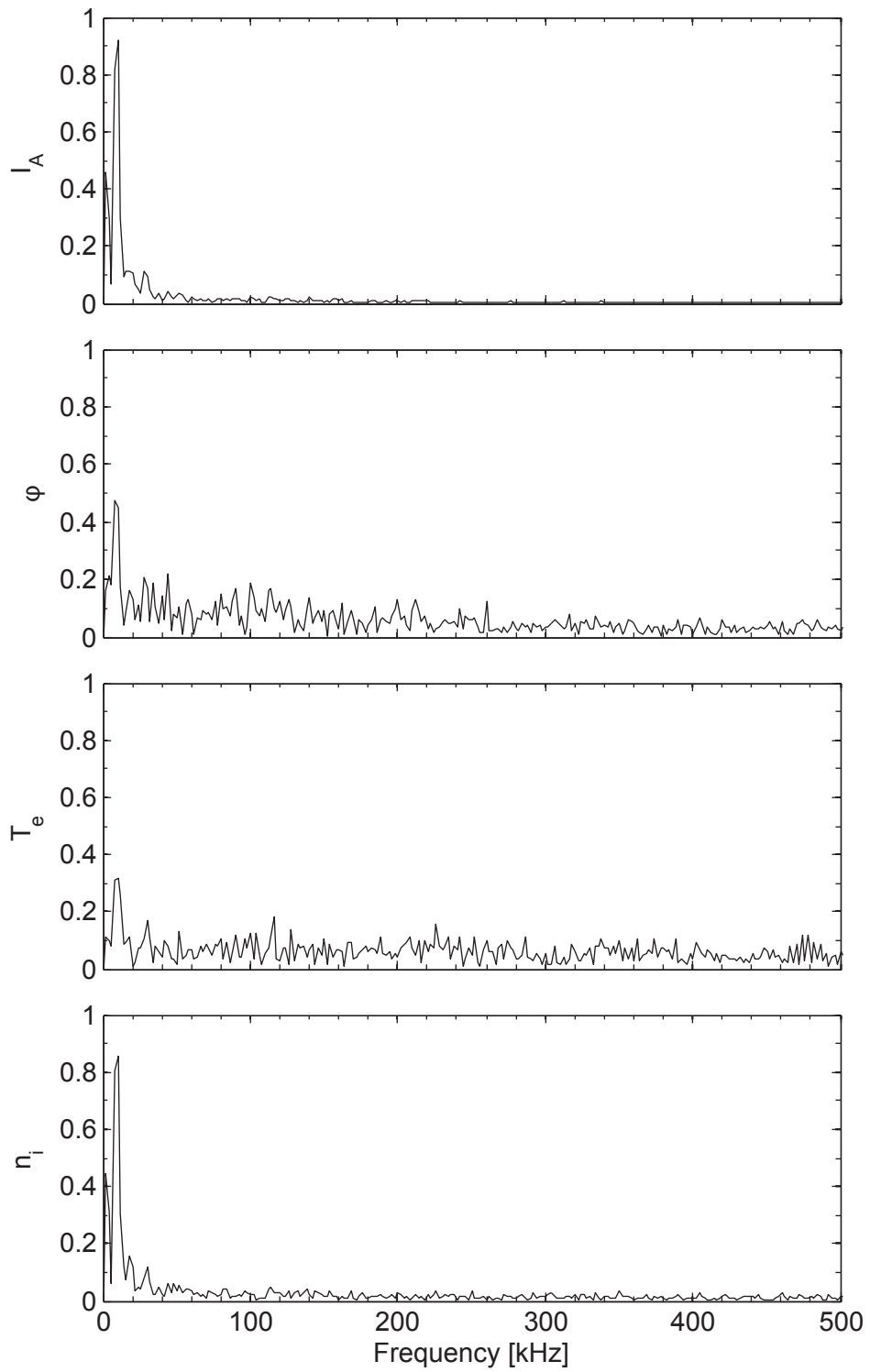


Figure C.6: Frequency spectrum for the 200 W downstream run.



## **Appendix D**

# **Additional HPHall Simulated ExB Probe Results**

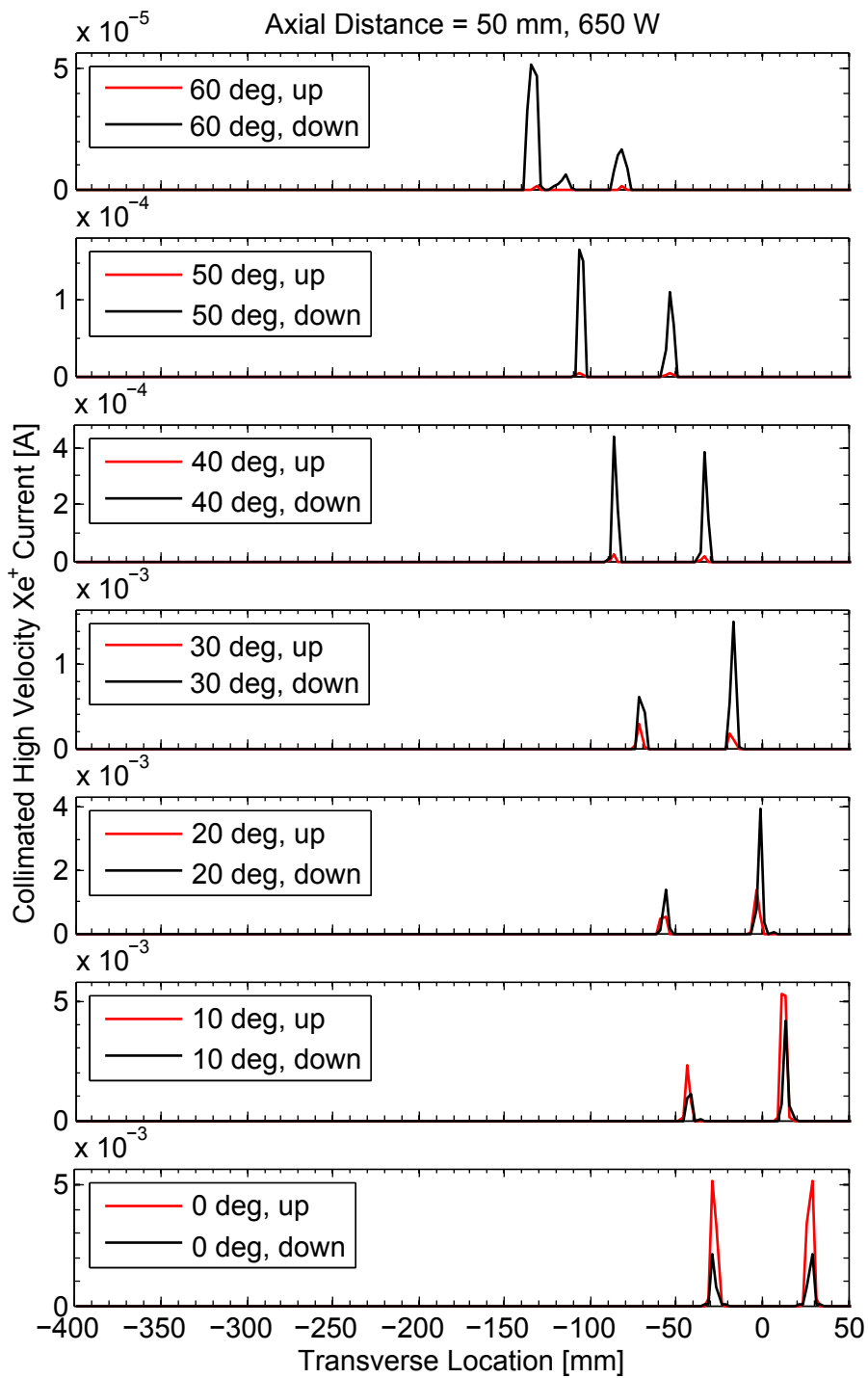


Figure D.1: ExB probe traces created from HPHall data at 50 mm, 650 W upstream and downstream runs, ion current (not ion current density).

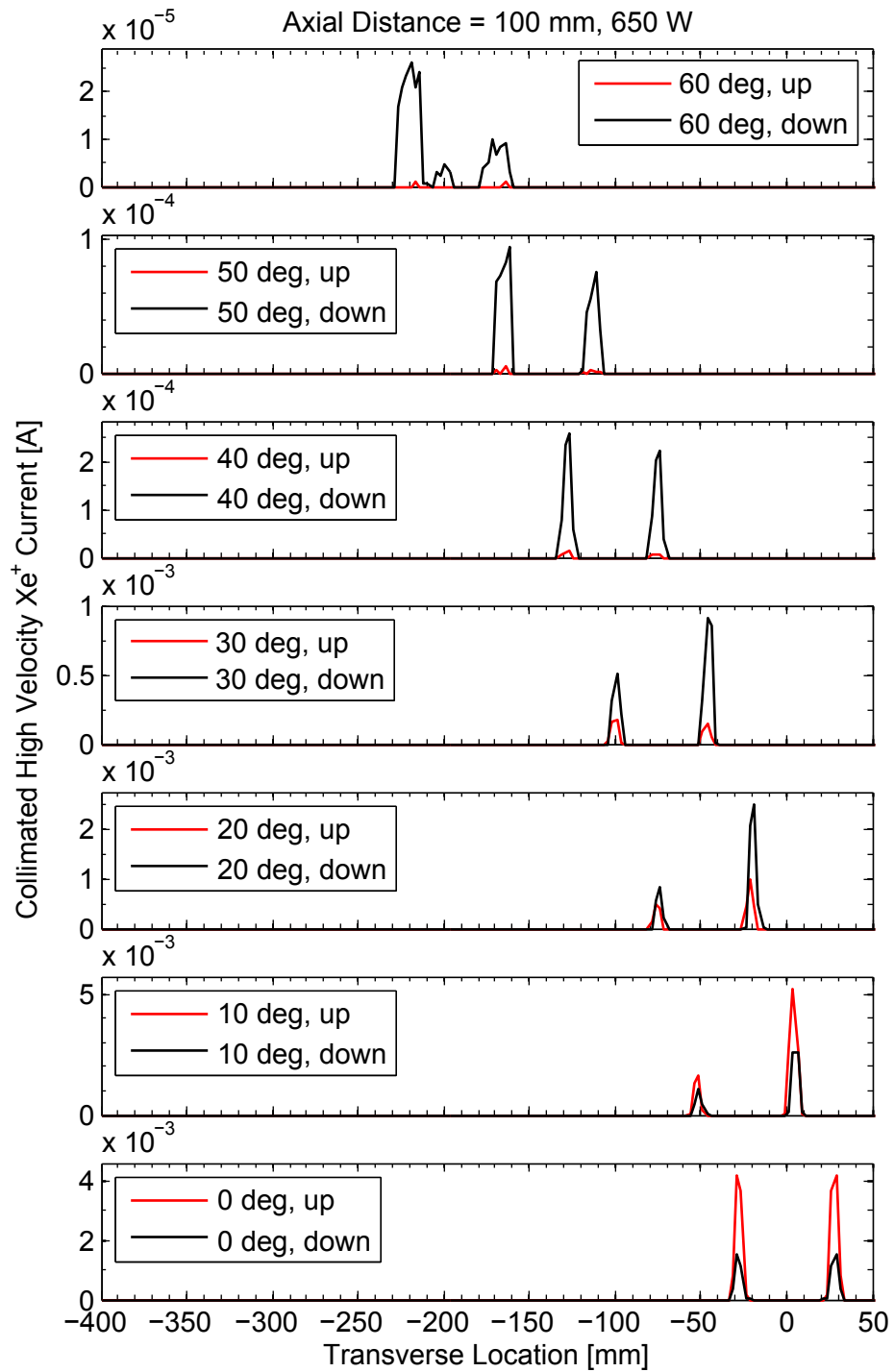


Figure D.2: ExB probe traces created from HPHall data at 100 mm, 650 W runs, ion current (not ion current density).

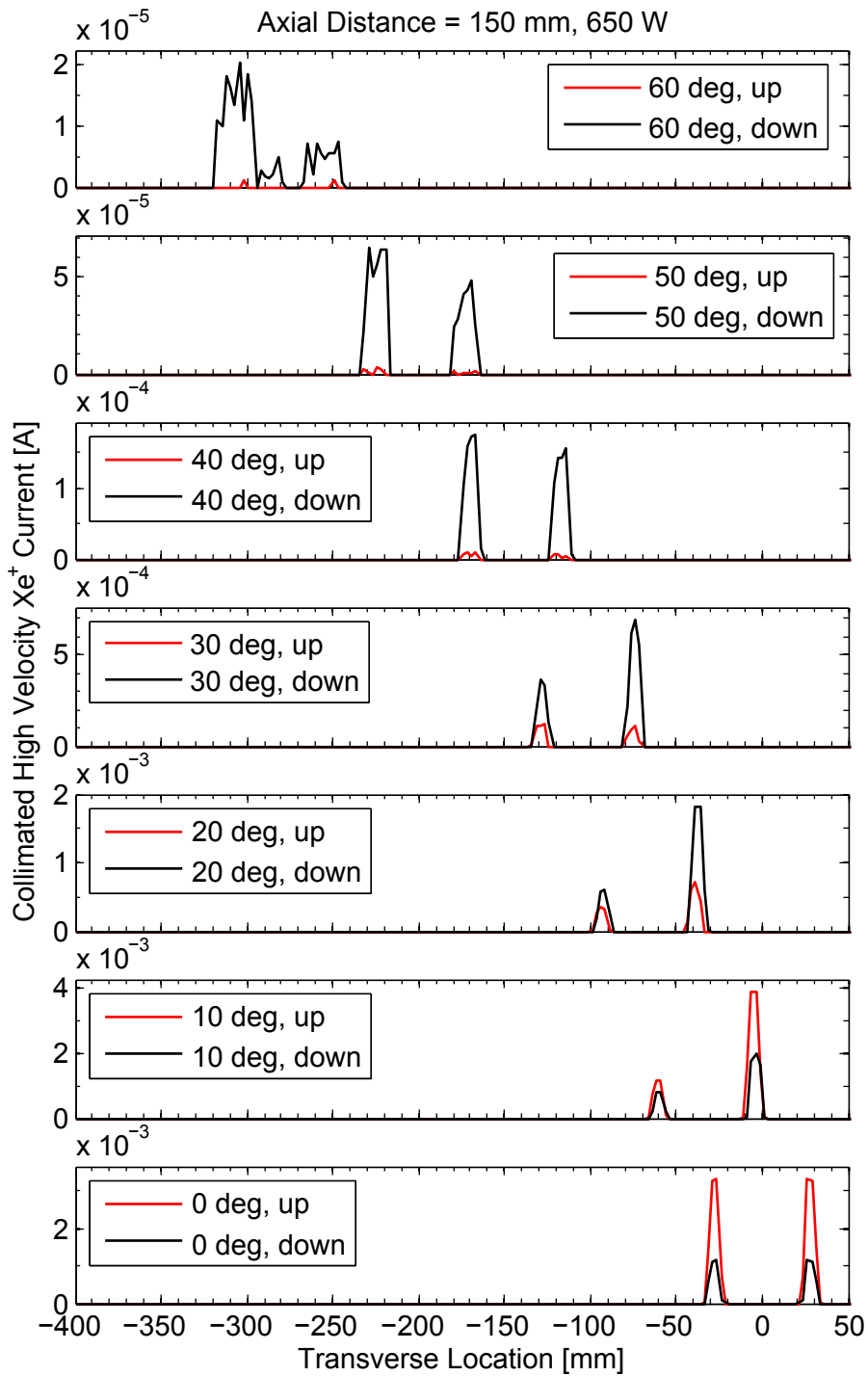


Figure D.3: ExB probe traces created from HPHall data at 150 mm, 650 W upstream and downstream runs, ion current (not ion current density).

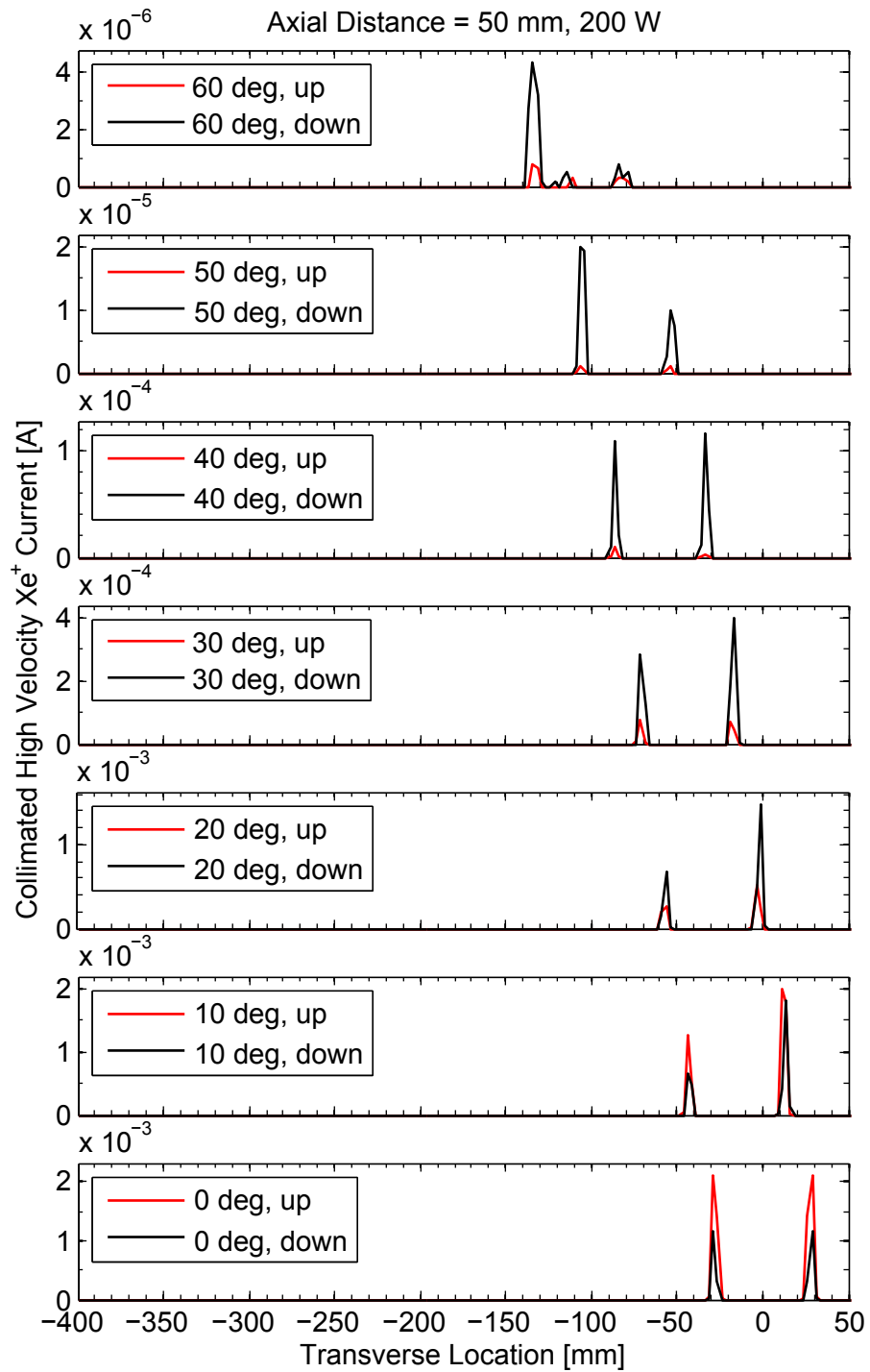


Figure D.4: ExB probe traces created from HPHall data at 50 mm, 200 W upstream and downstream runs, ion current (not ion current density).

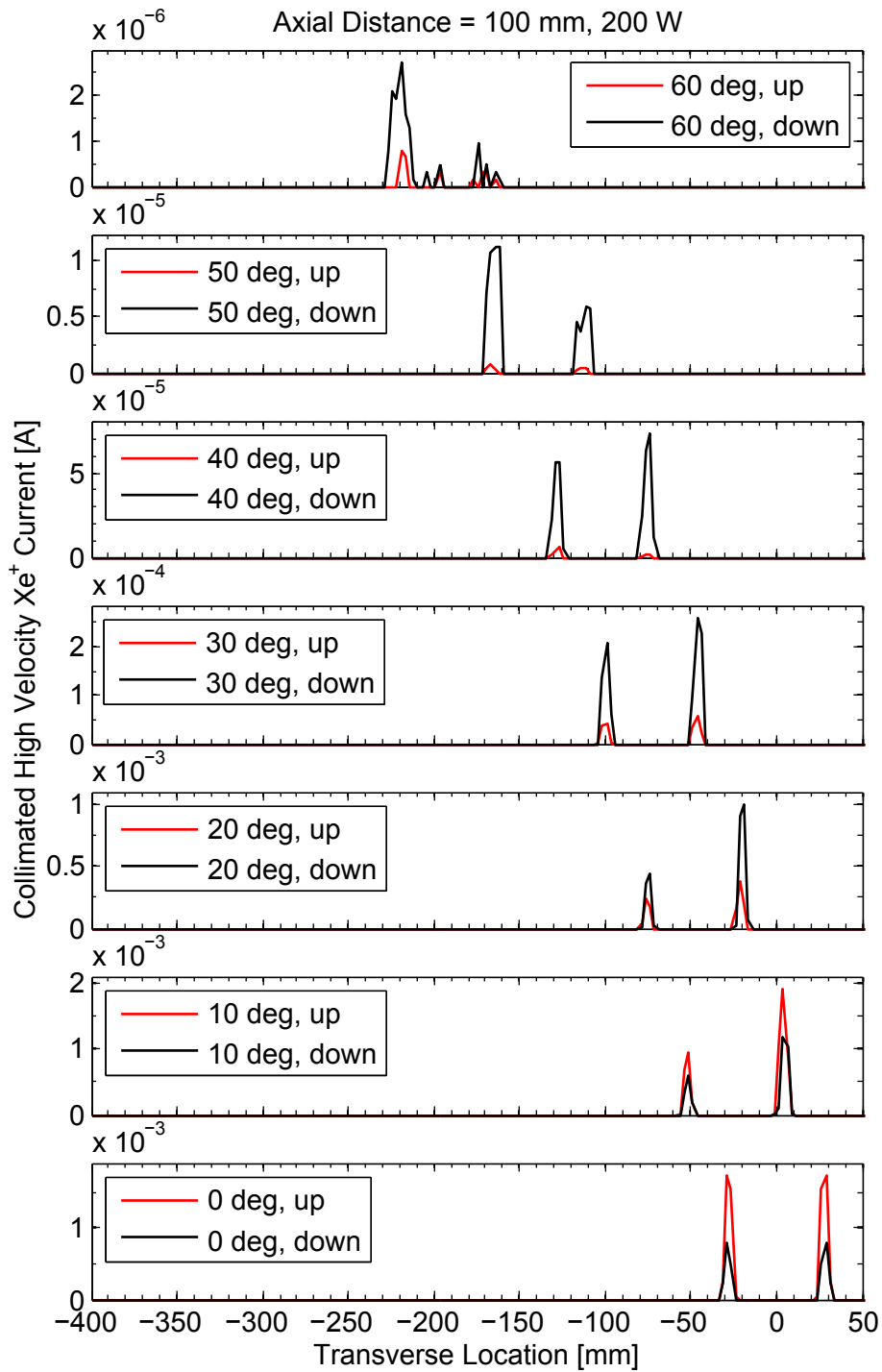


Figure D.5: ExB probe traces created from HPHall data at 100 mm, 200 W runs, ion current (not ion current density).

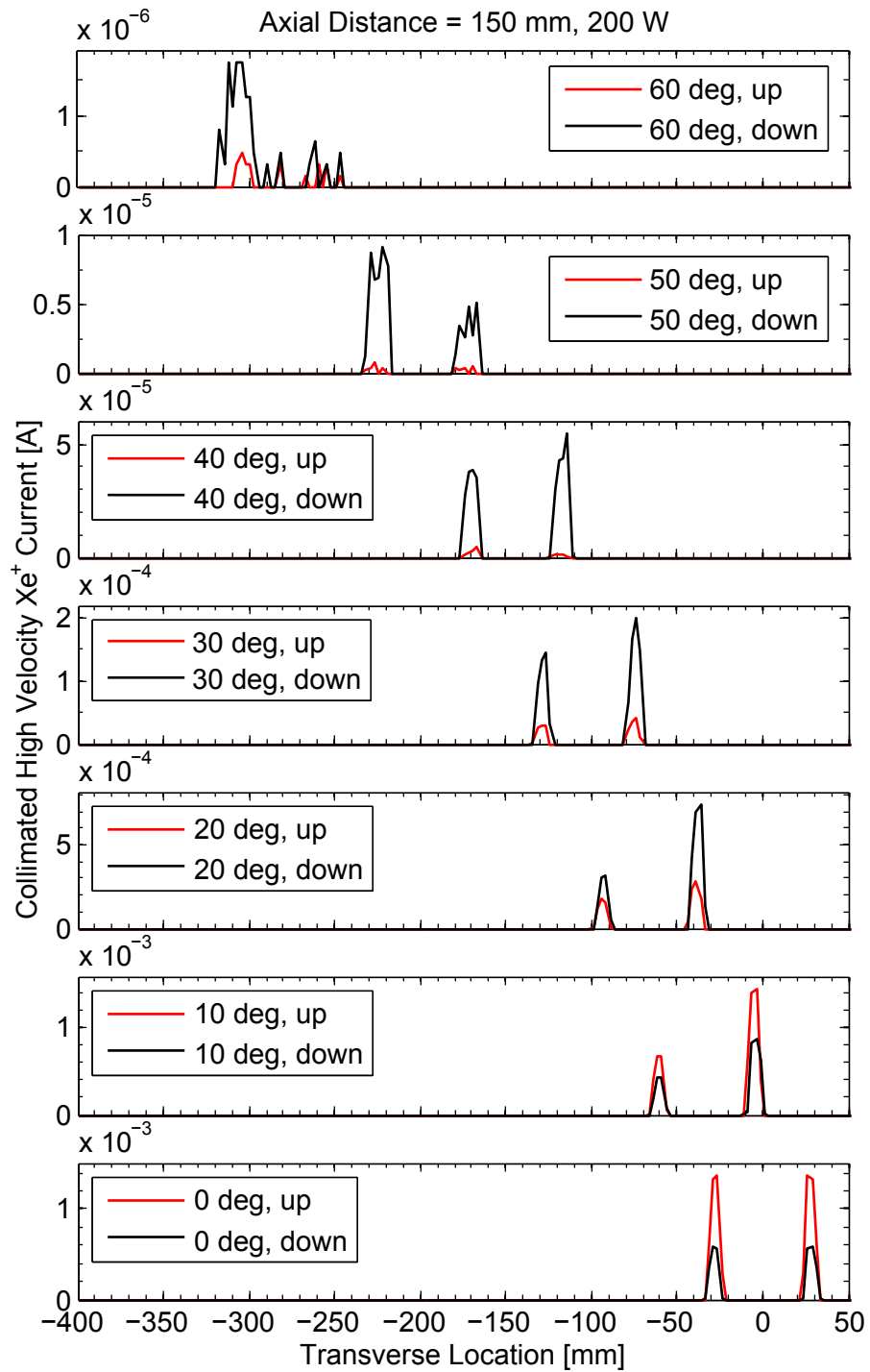


Figure D.6: ExB probe traces created from HPHall data at 150 mm, 200 W upstream and downstream runs, ion current (not ion current density).



## Appendix E

# Additional Corner Sheath Model Trajectory Results

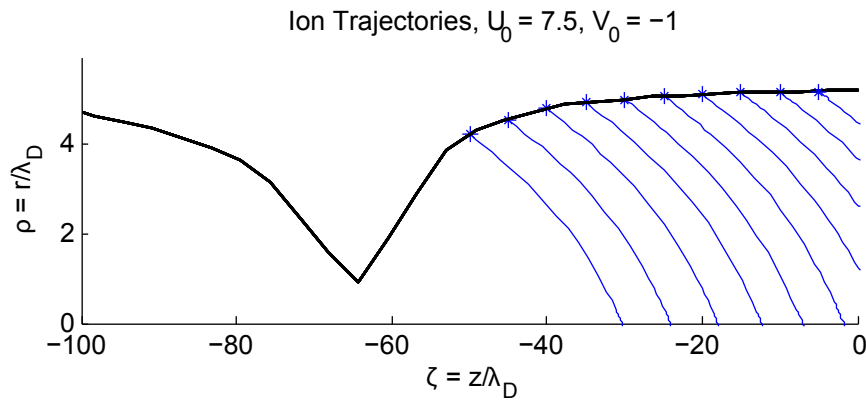


Figure E.1: Trajectories from the corner sheath model,  $U_0 = 7.5$ , 650 W upstream run.

Table E.1: Trajectories through sheath,  $U_0 = 7.5$ , 650 W upstream run.

$\zeta_0$	$\rho_0$	$\theta_0$ [°]	$\theta_f$ [°]	$\Delta\theta$ [°]
-50	4.2	-7.6	-20.7	-13.1
-45	4.5	-7.6	-21.2	-13.7
-40	4.8	-7.6	-21.6	-14.0
-35	4.9	-7.6	-21.8	-14.2
-30	5.0	-7.6	-21.9	-14.3
-25	5.0	-7.6	-22.1	-14.5
-20	5.1	-7.6	-20.0	-12.4
-15	5.1	-7.6	-14.4	-6.8
-10	5.1	-7.6	-10.8	-3.2
-5	5.2	-7.6	-8.6	-1.0

Table E.2: Trajectories through sheath,  $U_0 = 10.0$ , 650 W upstream run.

$\zeta_0$	$\rho_0$	$\theta_0$ [°]	$\theta_f$ [°]	$\Delta\theta$ [°]
-50	4.2	-5.7	-16.0	-10.2
-45	4.5	-5.7	-16.4	-10.7
-40	4.8	-5.7	-16.7	-10.9
-35	4.9	-5.7	-16.8	-11.0
-30	5.0	-5.7	-16.9	-11.2
-25	5.0	-5.7	-13.8	-8.1
-20	5.1	-5.7	-10.8	-5.0
-15	5.1	-5.7	-8.5	-2.8
-10	5.1	-5.7	-7.0	-1.3
-5	5.2	-5.7	-6.1	-0.4

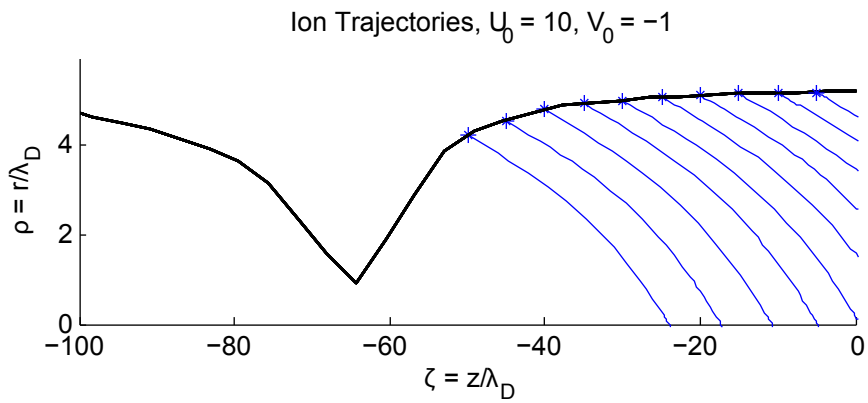
Figure E.2: Trajectories from the corner sheath model,  $U_0 = 10.0$ , 650 W upstream run.

Table E.3: Trajectories through sheath,  $U_0 = 7.5$ , 650 W downstream run.

$\zeta_0$	$\rho_0$	$\theta_0$ [°]	$\theta_f$ [°]	$\Delta\theta$ [°]
-50	4.7	-7.6	-19.8	-12.2
-45	4.6	-7.6	-19.5	-11.9
-40	4.5	-7.6	-19.1	-11.5
-35	4.4	-7.6	-18.9	-11.3
-30	4.4	-7.6	-18.6	-11.0
-25	4.3	-7.6	-18.4	-10.8
-20	4.2	-7.6	-18.3	-10.8
-15	4.2	-7.6	-14.4	-6.9
-10	4.1	-7.6	-11.1	-3.5
-5	4.1	-7.6	-8.9	-1.3

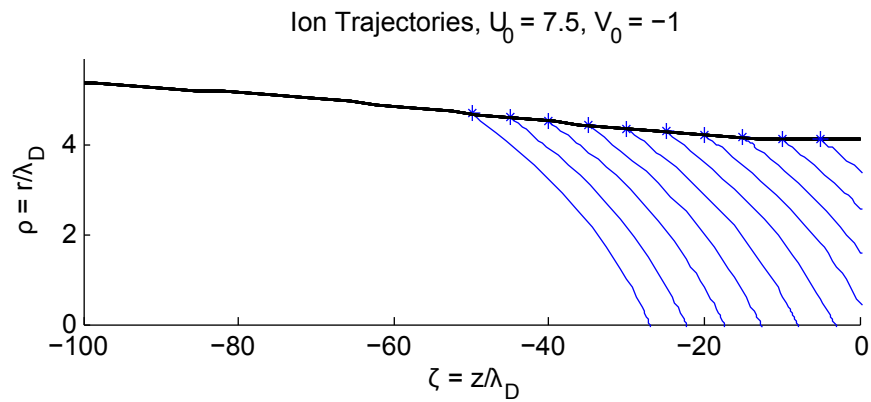
Figure E.3: Trajectories from the corner sheath model,  $U_0 = 7.5$ , 650 W downstream run.

Table E.4: Trajectories through sheath,  $U_0 = 10.0$ , 650 W downstream run.

$\zeta_0$	$\rho_0$	$\theta_0$ [°]	$\theta_f$ [°]	$\Delta\theta$ [°]
-50	4.7	-5.7	-14.8	-9.1
-45	4.6	-5.7	-14.6	-8.8
-40	4.5	-5.7	-14.4	-8.7
-35	4.4	-5.7	-14.1	-8.4
-30	4.4	-5.7	-14.1	-8.4
-25	4.3	-5.7	-12.5	-6.8
-20	4.2	-5.7	-10.1	-4.4
-15	4.2	-5.7	-8.3	-2.6
-10	4.1	-5.7	-7.2	-1.5
-5	4.1	-5.7	-6.4	-0.7

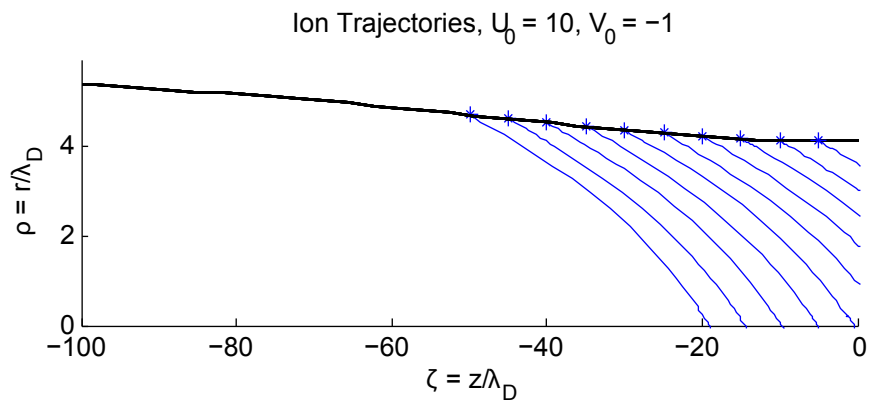
Figure E.4: Trajectories from the corner sheath model,  $U_0 = 10.0$ , 650 W downstream run.

Table E.5: Trajectories through sheath,  $U_0 = 7.5$ , 200 W upstream run.

$\zeta_0$	$\rho_0$	$\theta_0$ [°]	$\theta_f$ [°]	$\Delta\theta$ [°]
-50	4.7	-7.6	-21.3	-13.7
-45	4.8	-7.6	-21.5	-13.9
-40	4.9	-7.6	-21.8	-14.2
-35	4.9	-7.6	-22.0	-14.4
-30	5.0	-7.6	-22.2	-14.6
-25	5.1	-7.6	-22.2	-14.6
-20	5.1	-7.6	-19.1	-11.5
-15	5.2	-7.6	-13.8	-6.2
-10	5.2	-7.6	-10.4	-2.8
-5	5.3	-7.6	-8.4	-0.8

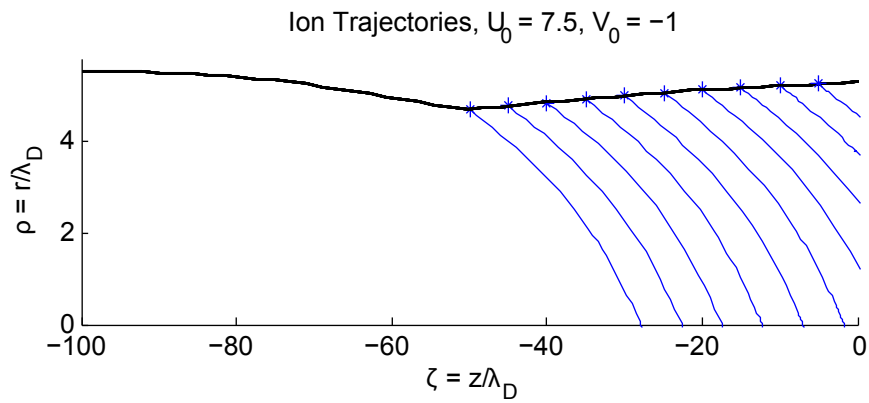
Figure E.5: Trajectories from the corner sheath model,  $U_0 = 7.5$ , 200 W upstream run.

Table E.6: Trajectories through sheath,  $U_0 = 10.0$ , 200 W upstream run.

$\zeta_0$	$\rho_0$	$\theta_0$ [°]	$\theta_f$ [°]	$\Delta\theta$ [°]
-50	4.7	-5.7	-16.5	-10.7
-45	4.8	-5.7	-16.7	-11.0
-40	4.9	-5.7	-16.8	-11.1
-35	4.9	-5.7	-16.9	-11.2
-30	5.0	-5.7	-17.0	-11.3
-25	5.1	-5.7	-13.5	-7.8
-20	5.1	-5.7	-10.3	-4.6
-15	5.2	-5.7	-8.3	-2.6
-10	5.2	-5.7	-6.9	-1.2
-5	5.3	-5.7	-5.9	-0.2

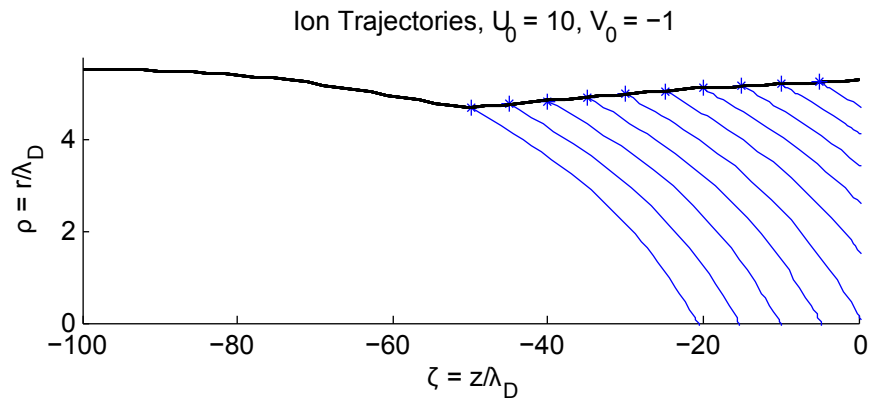
Figure E.6: Trajectories from the corner sheath model,  $U_0 = 10.0$ , 200 W upstream run.

Table E.7: Trajectories through sheath,  $U_0 = 7.5$ , 200 W downstream run.

$\zeta_0$	$\rho_0$	$\theta_0$ [°]	$\theta_f$ [°]	$\Delta\theta$ [°]
-50	5.15	-7.6	-21.9	-14.3
-45	5.10	-7.6	-21.9	-14.3
-40	5.08	-7.6	-22.0	-14.4
-35	5.08	-7.6	-21.9	-14.3
-30	5.08	-7.6	-21.9	-14.3
-25	5.08	-7.6	-22.0	-14.4
-20	5.08	-7.6	-18.9	-11.3
-15	5.09	-7.6	-13.7	-6.1
-10	5.11	-7.6	-10.4	-2.8
-5	5.12	-7.6	-8.4	-0.8

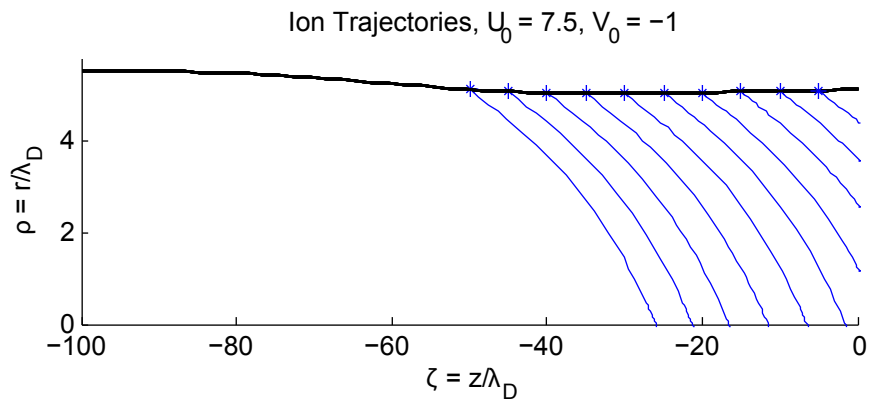
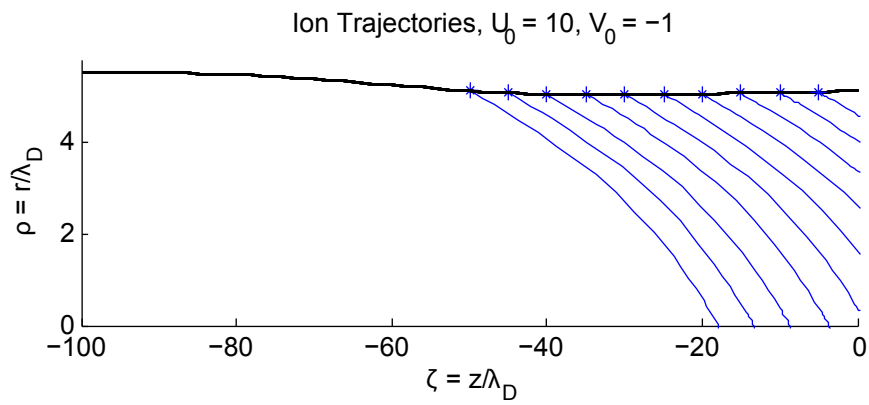
Figure E.7: Trajectories from the corner sheath model,  $U_0 = 7.5$ , 200 W downstream run.

Table E.8: Trajectories through sheath,  $U_0 = 10.0$ , 200 W downstream run.

$\zeta_0$	$\rho_0$	$\theta_0$ [°]	$\theta_f$ [°]	$\Delta\theta$ [°]
-50	5.15	-5.7	-16.8	-11.1
-45	5.10	-5.7	-16.8	-11.1
-40	5.08	-5.7	-16.8	-11.1
-35	5.08	-5.7	-16.8	-11.1
-30	5.08	-5.7	-16.6	-10.9
-25	5.08	-5.7	-13.1	-7.4
-20	5.08	-5.7	-10.2	-4.5
-15	5.09	-5.7	-8.3	-2.6
-10	5.11	-5.7	-6.8	-1.1
-5	5.12	-5.7	-6.1	-0.4

Figure E.8: Trajectories from the corner sheath model,  $U_0 = 10.0$ , 200 W downstream run.

# Bibliography

- [1] M. Martinez-Sanchez and J. E. Pollard. "Spacecraft electric propulsion - an overview". *Journal of Propulsion and Power*, 14(5):688–699, 1998.
- [2] D. J. Pidgeon, R. L. Corey, and B. Sauer. "Two years on-orbit performance of SPT-100 electric propulsion". *Proceedings of the 24th AIAA International Communications Satellite Systems Conference, San Diego, CA*, 2006.
- [3] D. R. Bromaghim et al. "200 W Hall thruster propulsion subsystem development for microsatellite missions". *Proceedings of the 53rd JANNAF Propulsion Meeting, Monterey, CA*, 2005.
- [4] G. D. Racca et al. "SMART-1 mission description and development status". *Planetary and Space Science*, 50(14-15):1323–1337, 2002.
- [5] D. M. Goebel and I. Katz. *Fundamentals of Electric Propulsion*. John Wiley and Sons, Inc., Hoboken, U.S.A., 2008.
- [6] W. A. Hargus and C. S. Charles. "Near exit plane velocity field of a 200 W Hall thruster". *Proceedings of the 39th AIAA/ASME/SAE/ASEE Joint Propulsion Conference and Exhibit, Huntsville, AL*, 2003.
- [7] W. A. Hargus and M. R. Nakles. "Evolution of the ion velocity distribution in the near field of the BHT-200-X3 Hall thruster". *Proceedings of the 42nd AIAA/ASME/SAE/ASEE Joint Propulsion Conference and Exhibit, Sacramento, CA*, 2006.
- [8] W. A. Hargus and M. R. Nakles. "Background pressure effects on internal and near-field ion velocity distribution of the BHT-600 Hall thruster". *Proceedings of the*

44th AIAA/ASME/SAE/ASEE Joint Propulsion Conference and Exhibit, Hartford, CT, 2008.

- [9] W. A. Hargus and C. S. Charles. "Near exit plane velocity field of a 200 W Hall thruster". *Journal of Propulsion and Power*, 24(1):127–133, 2002.
- [10] B. M. Reid. *The Influence of Neutral Flow Rate in the Operation of Hall Thrusters*. PhD thesis, University of Michigan, 2009.
- [11] K. K. Jameson. *Investigation of Hollow Cathode Effects on Total Thruster Efficiency in a 6 kW Hall Thruster*. PhD thesis, University of California Los Angeles, 2008.
- [12] S. W. Kim. *Experimental Investigations of Plasma Parameters and Species-dependent Ion Energy Distribution in the Plasma Exhaust Plume of a Hall Thruster*. PhD thesis, University of Michigan, 1999.
- [13] L. B. King. *Transport-Property and Mass Spectral Measurements in the Plasma Exhaust Plume of a Hall-effect Space Propulsion System*. PhD thesis, University of Michigan, 1998.
- [14] J. M. Fife. *Hybrid-PIC Modeling and Electrostatic Probe Survey of Hall Thrusters*. PhD thesis, Massachusetts Institute of Technology, 1998.
- [15] M. K. Allis et al. "A comparison of 2-D hybrid Hall thruster model to experimental measurements". *Proceedings of the 40th AIAA/ASME/SAE/ASEE Joint Propulsion Conference and Exhibit, Fort Lauderdale, FL*, 2004.
- [16] G. J. Bareilles et al. "Critical assessment of a two-dimensional hybrid Hall thruster model: Comparisons with experiments". *Physics of Plasmas*, 11(6):3035–3046, 2004.
- [17] I. Maqueda, D. Escobar, and E. Ahedo. "Advances on a Hall thruster hybrid code,". *Proceedings of the 27th International Electric Propulsion Conference, Pasadena, CA*, 2001.
- [18] F. I. Parra et al. "A two-dimensional hybrid model of the Hall thruster discharge". *Journal of Applied Physics*, 100(2):023304–1–023304–11, 2006.

- [19] L. Brieda et al. "Development of the draco code for modeling electric propulsion plume interactions". *Proceedings of the 40th AIAA/ASME/SAE/ASEE Joint Propulsion Conference and Exhibit, Fort Lauderdale, FL, 2004.*
- [20] M. Celik et al. "Hybrid-PIC simulation of a Hall thruster plume on an unstructured grid with DSMC collisions". *Proceedings of 28th International Electric Propulsion Conference Toulouse, France, 2003.*
- [21] R. R. Hofer, P. Y. Peterson, and A. D. Gallimore. "a high specific impulse two-stage Hall thruster with plasma lens focusing". *Proceedings of the 27th International Electric Propulsion Conference, Pasadena, CA, 2001.*
- [22] V. V. Zhurin, H. R. Kaufman, and R. S. Robinson. "Physics of closed drift thrusters". *Plasma Sources Science and Technology*, 8(1):R1–R20, 1999.
- [23] B. A. Arhipov et al. "Development and application of electric thrusters at EDB Fakel". *Proceedings of the 25th International Electric Propulsion Conference, Cleveland, OH, 1997.*
- [24] V. Kim et al. "Electric propulsion activity in Russia". *Proceedings of the 27th International Electric Propulsion Conference, Pasadena, CA, 2001.*
- [25] R. R. Hofer, M. L. R. Walker, and A. D. Gallimore. "A comparison of nude and collimated Faraday probes for use with Hall thrusters". *Proceedings of the 27th International Electric Propulsion Conference, Pasadena, CA, 2001.*
- [26] R. R. Hofer, J. M. Haas, and A. D. Gallimore. "Ion voltage diagnostics in the far-field plume of a high-specific impulse Hall thruster". *Proceedings of the 39th AIAA/ASME/SAE/ASEE Joint Propulsion Conference and Exhibit, Huntsville, AL, 2003.*
- [27] D. G. Conroy and L. K. Johnson. "Thruster plasma diagnostics for spacecraft". *Proceedings of the 53rd JANNAF Propulsion Meeting, 2005.*
- [28] D. A. Dahl. *Simion 3D Version 7.0 User's Manual*. SIMION, Idaho Falls, U.S.A., 2000.

- [29] I. G. Mikellides et al. "Hall-effect thruster simulations with 2-D electron transport and hydrodynamic ions". *Proceedings of the 30th International Electric Propulsion Conference, Ann Arbor, MI, 2009*.
- [30] J. J. Szabo. *Fully Kinetic Numerical Modeling of a Plasma Thruster*. PhD thesis, Massachusetts Institute of Technology, 2001.
- [31] J. C. Adam, A. Aeron, and G. Laval. "Study of stationary plasma thrusters using two-dimensional fully kinetic simulations". *Physics of Plasmas*, 11(1):295–305, 2004.
- [32] F. I. Parra and E. Ahedo. "Fulfillment of the Bohm condition on the 'hphall' fluid-PIC code". *Proceedings of the 40th AIAA/ASME/SAE/ASEE Joint Propulsion Conference and Exhibit, Fort Lauderdale, FL, 2004*.
- [33] R. R. Hofer et al. "Heavy particle velocity and electron mobility in hybrid-PIC Hall thruster simulations". *Proceedings of the 42nd AIAA/ASME/SAE/ASEE Joint Propulsion Conference and Exhibit, Sacramento, CA, 2006*.
- [34] R. R. Hofer et al. "Wall sheath and electron mobility modeling in hybrid-PIC Hall thruster simulations". *Proceedings of the 43rd AIAA/ASME/SAE/ASEE Joint Propulsion Conference and Exhibit, Cincinnati, OH, 2007*.
- [35] R. R. Hofer et al. "Efficacy of electron mobility models in hybrid-PIC Hall thruster simulations". *Proceedings of the 44th AIAA/ASME/SAE/ASEE Joint Propulsion Conference and Exhibit, Hartford, CT, 2008*.
- [36] S. Barral. "Theoretical analysis of the influence of the power supply on breathing oscillations in Hall thrusters". *Proceedings of the 30th International Electric Propulsion Conference, Florence, Italy, 2007, 2007*.
- [37] E. Y. Choueiri. "Plasma oscillations in Hall thrusters". *Physics of Plasmas*, 8(4):1411–1426, 2001.
- [38] P. M. Bellan. *Fundamentals of Plasma Physics*. Cambridge University Press, New York, U.S.A., 2006.
- [39] M. Hong and G. A. Emmert. "Two-dimensional fluid simulation of expanding plasma sheaths". *Journal of Applied Physics*, 78(12):6967–6973, 1995.

- [40] E. Ahedo. "Presheath/sheath model with secondary electron emission from two parallel walls". *Physics of Plasmas*, 9(10):4340–4347, 2002.
- [41] E. Ahedo. "Radial macroscopic model of a plasma flowing along annular dielectric walls". *Physics of Plasmas*, 9(7):3178–3186, 2002.
- [42] G. D. Hobbs and J. A. Wesson. "Heat flow through a langmuir sheath in the presence of electron emission". *Plasma Physics*, 9(1):85–87, 1966.
- [43] A. Dunaevsky, Y. Raitses, and N. J. Fisch. "Secondary electron emission from dielectric materials of a Hall thruster with segmented electrodes". *Physics of Plasmas*, 10(6): 2574–2577, 2003.
- [44] R. Peyret and T. D. Taylor. *Computational Methods for Fluid Flow*. Springer-Verlag, New York, U.S.A., 1983.
- [45] H. Press et al. *Numerical Recipes*. Cambridge University Press, Cambridge, U.K., 1986.
- [46] S. A. Self. "Exact solution of the collisionless plasma-sheath equation". *Physics of Fluids*, 6(12):1762–1768, 1963.
- [47] N. Sternberg and V. Godyak. "Patching collisionless plasma and sheath solutions to approximate the plasma-wall problem". *IEEE Transactions on Plasma Science*, 31(6): 1395–1401, 2003.
- [48] I. G. Mikellides et al. "Elastic scattering of ions in electrostatic thruster plumes". *Journal of Propulsion and Power*, 21(1):111–118, 2005.
- [49] N. Matsunami et al. "Energy dependence of the ion-induced sputtering yields of man-atomic solids". *Atomic Data and Nuclear Tables*, 31(1):1–80, 1984.
- [50] R. P. Doerner, D. G. Whyte, and Gebel D. M. "Sputtering yield measurements during low energy xenon plasma bombardment". *Journal of Applies Physics*, 93(9):5816–5823, 2003.
- [51] C. Thomas. *Anomalous Electron Transport in the Hall-Effect Thruster*. PhD thesis, Stanford University, 2006.

- [52] M. K. Scharfe. *Electron Cross-Field Transport Modeling in Radial-Axial Hybrid Hall Thruster Simulations*. PhD thesis, Stanford University, 2009.